
Supramolecular Synthesis of Novel Organic and Hybrid Materials of π -Systems for Optoelectronic Functions

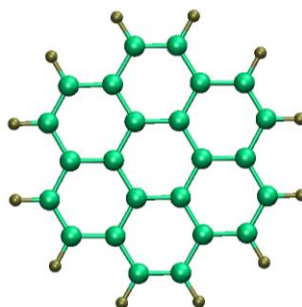
A Thesis

Submitted for the Degree of

Doctor of Philosophy

By

VENKATA RAO K



New Chemistry Unit

Jawaharlal Nehru Centre for Advanced Scientific Research

(A Deemed University)

Bangalore - 560064 (INDIA)

JUNE 2013

Supramolecular Synthesis of Novel Organic and Hybrid Materials of π -Systems for Optoelectronic Functions

A Thesis

Submitted for the Degree of

Doctor of Philosophy

By

VENKATA RAO K

UNDER THE SUPERVISION OF

Dr. SUBI J. GEORGE

New Chemistry Unit

Jawaharlal Nehru Centre for Advanced Scientific Research

(A Deemed University)

Bangalore-560064 (INDIA)

JUNE 2013

Dedicated to My Beloved Parents

DECLARATION

I hereby declare that the thesis entitled “*Supramolecular Synthesis of Novel Organic and Hybrid Materials of π -Systems for Optoelectronic Functions*” is an authentic record of research work carried out by me at the New Chemistry Unit, Jawaharlal Nehru Centre for Advanced Scientific Research, Bangalore, India under the supervision of **Dr. Subi J. George** and that it has not been submitted elsewhere for the award of any degree or diploma.

In keeping with the general practice in reporting scientific observations, due acknowledgment has been made whenever the work described is based on the findings of other investigators. Any omission that might have occurred due to oversight or error in judgment is regretted.

Venkata Rao K



**Jawaharlal Nehru Centre for
Advanced Scientific Research**

Dr. Subi J. George
New Chemistry Unit
Jawaharlal Nehru Centre for Advanced
Scientific Research (JNCASR)
Bangalore-560064, India
Phone : +91 80 2208 2964
Fax: + 91 80 22082627
E-mail: george@jncasr.ac.in

Date

June 24, 2013

CERTIFICATE

I hereby certify that the work described in this thesis titled “**Supramolecular Synthesis of Novel Organic and Hybrid Materials of π -Systems for Optoelectronic Functions**” has been carried out by **Venkata Rao K** at the New Chemistry Unit, Jawaharlal Nehru Centre for Advanced Scientific Research, Bangalore, India under my supervision and it has not been submitted elsewhere for the award of any degree or diploma.

Dr. Subi J. George
(Research Supervisor)

ACKNOWLEDGEMENTS

First and foremost, I would like to thank my research supervisor **Dr. Subi J. George** for introducing me to the field of supramolecular self-assembly and for giving the freedom to work on various problems. I am grateful to him for constant guidance, encouragement and support, leading to the successful completion of this work.

I would like to express my sincere gratitude to **Prof. C. N. R. Rao, FRS** for his guidance and for being a constant source of inspiration. I am also grateful to him for providing necessary facilities for carrying this work.

I am thankful to all the faculty members of NCU and CPMU for their guidance and support.

I have also received immense support from Professor M. R. S. Rao, President, JNCASR, which I gratefully acknowledge.

It is a great pleasure to thank all my collaborators,

Prof. C. N. R. Rao, FRS and his students; Dr. A. Ghosh, Dr. Rakesh Voggu, Dr. K. S.

Subramanyam, Dr. Ramakrishna Matte-CPMU/NCU

Prof. M. Eswaramoorthy and his students; Dr. K. K. R. Datta, Amrit, Pavan Kumar-CPMU

Prof. T. K. Maji and his students; K. Jayaramulu, Dr. S. Mohapatra, Ritesh Halder-CPMU

Prof. G. U. Kulkarni and his students; Dr. Abhay A. S., Umesh M. -CPMU

Prof. K. S. Narayan and his students; C. S. Ravichandran, Satyaprasad -CPMU

Prof. A. Saeki, Prof. Shu Seki, University of Osaka, Japan

for fruitful collaborations.

I great fully acknowledge Mr. K. Narendra (CPMU) for encouraging me to join in NCU with Dr. Subi J. George.

I am thankful to Dr. Subi J. George, Dr. T. Govindaraju, Prof. T. K. Maji and Prof. M. Eswaramoorthy from JNCASR and, Prof. P. Balaram and Prof. S. P. Sharma from IISc for their coursework.

I express my sincere thanks to all my teachers, especially from School of Chemistry, University of Hyderabad for their encouragement at various stages of my academic career.

I am grateful to my lab mates, The SupraChem Group, Mohit, Ankj, Chidambar, Bhawani, Krishnendu for their support and creating friendly atmosphere in the lab.

I am thankful to the following people for timely assistance in various measurements: NCUFP, Chennai, Dr. Ranjani V., G. K. Moorthy and Vishnu (lifetime); Prof. G. U. Kulkarni (Veeco Lab); Dr. S. Basavaraja (AFM); Mrs. Usha (TEM); Mrs. Selvi (FESEM); Mrs. Suma (Confocal microscopy); Mr. Anil (XRD); Mr. Mahesh (SEM and NMR); Mr. Vasu (UV, IR, PL, TGA); School of Chemistry, University of Hyderabad (solid-state NMR); Piyush and Amrit (DLS); Dr. Rajesh Ganapathy, H. K. Nagamanasa and Dr. J. D. Sudha (Rheology).

I am grateful to Ankita (R&D assistant), POCE students: Amrita, Hitesh and Ravinder; and SRFP students: Rajesh M., Subhadeep G., Soumya Mukharjee, Anjana George, Swetha for working with me on various projects.

I am thankful to academic and administrative staff of JNCASR for their assistance.

I thank all my friends Narendra, Subbu, Sandeep, Srinu, Dasari, Arjun, Malli, Matte, Leela, Rakesh, Pavan, Jayaram, Moses, Sharma, Satya, Shivaprasad, Yugandhar, Venki, Ganga, Nagarjun, Suresh, Saraiah, Anand, Ramana, Lingampally, Moorthy, Satish, Debu, Govind, LHN Reddy, Subbareddy and all other friends of JNCASR.

Besides the research life, I am thankful to Dr. Subi J. George and his family members for their hospitality and affection.

I am deeply grateful to my parents, sister and uncle for their support, love and affection throughout my life.

Financial assistance from Council of Scientific and Industrial Research (CSIR), India and Department of Science and Technology (DST), Government of India is gratefully acknowledged.

Venkat

Preface

This thesis presents the design, synthesis and properties of novel organic and organic-inorganic hybrid supramolecular assemblies of π -conjugated chromophores for improved optical and electronic functions.

The thesis is majorly divided into five parts.

Part-1 presents the introduction, which aim to summarize the state of the art strategies employed in the field of functional organic and hybrid materials derived via self-assembly. We have mainly focused on the design principles of various amphiphilic and charge-transfer π -conjugated assemblies and organic-inorganic light-harvesting hybrid assemblies.

Part-2 describes the synthesis and self-assembly of novel n-type coronene bisimide (**CBI**) amphiphiles and bolaamphiphiles. This part is divided into two sections. In **Part-2.1**, self-assembly and optoelectronic properties of various amphiphilic coronene bisimide (**CBI**) derivatives are discussed. The optical properties and morphology of these molecules have been fine-controlled by the composition of good/poor solvent mixture. The amphiphilic design of these molecules triggered a bilayer self-assembly in water, with tightly π -stacked chromophores in J-type fashion. The enhanced structural order in these nanostructures is further evident from their decent n-type mobility in the order of 10^{-2} cm²/V.s. In **Part-2.2**, mechanistic insights into the self-assembly process of **CBI** amphiphiles have been investigated using chirality as a probe. For this purpose, chirality was introduced to the **CBI** core via covalent and non-covalent functionalization with chiral side chains. Helical self-assembly and self-assembly mechanisms of these chiral **CBI** derivatives have been probed via circular dichroism spectroscopy and various microscopic techniques. Temperature dependent circular dichroism measurements provide insights into self-assembly mechanism and significant chiral amplification was observed in the co-assembly of chiral and achiral **CBI** derivatives.

In **Part-3**, synthesis of charge-transfer (CT) nanofibers through a non-covalent amphiphilic design strategy is described. Charge-transfer (CT) crystals formed from donor (D) and acceptor (A) molecules, which are organized either in a segregated (orthogonal, ..D-D-D.. and ..A-A-A..) or mixed (alternate, ...D-A-D...) fashion have gathered immense attention because of their excellent conducting properties. In this context, the supramolecular one-dimensional analogues of these binary CT complexes would provide novel conducting nanostructures through inherent doping and hence can provide new opportunities for nano-sized electronics. We have constructed various CT

nanostructures with alternate and orthogonal D-A organization using a non-covalent amphiphilic design of appropriately functionalized donor and acceptor molecules. These results are compiled in three sections. In **Part-3.1**, design, synthesis and properties of CT-nanofibers and nanotubes with mixed D-A organization is presented. In this construct, the D and A molecules are designed in such a way that the face-to-face CT pair resembles surfactant structure, which ensures its extended self-assembly in polar solvents. In **Part-3.2**, we have described a novel supramolecular cross-linking strategy for the alignment of CT-columns in solution and on surface. **Part-3.3** demonstrates the supramolecular synthesis of photoconductive nanostructure having non-covalently connected bi-continuous D-A heterojunctions with wide donor-acceptor interface and high charge-carrier mobility.

Part-4 presents the design and synthesis of novel, solution processable, luminescent soft-hybrids via an organic-inorganic hybrid co-assembly. **Part-4** is divided into two sections based on two different strategies that have been employed for achieving solid-state luminescent soft-hybrids. **Part-4.1** presents the electrostatic co-assembly of ionic donor and acceptor molecules with aminoclay (**AC**) are described. The resultant hybrids are water soluble and forms hydrogels with amplified fluorescence via Förster Resonance Energy Transfer (FRET), which can be efficiently transferred on to solid substrates by drop-casting. This concept was further extended to achieve highly pure solid-state white light emission. In **Part-4.2**, alternate co-assembly of charged chromophores and laponite (**LP**) nano particles is demonstrated for controlling the molecular organization of π -conjugated molecules from non-fluorescent aggregated state to fluorescent state in order to construct processable luminescent hybrids.

In **Part-5**, functional properties of superabsorbent dynamic microporous polymers derived from pyrene are described. Owing to their dynamic framework, these polymers showed reversible swelling and fluorescence response in most of the organic solvents. This has been further used for rapid encapsulation of various chromophoric guests such as C_{60} and fluorescent dyes, and investigated for photoinduced electron/energy transfer process.

TABLE OF CONTENTS

| | |
|-------------------|------|
| Declaration | i |
| Certificate | iii |
| Acknowledgments | v |
| Preface | viii |
| Table of contents | xi |

PART-1

| | |
|---------------------|----------|
| Introduction | 1 |
|---------------------|----------|

PART-1.1 *Amphiphilic and Charge-Transfer Designs for Self-Assembled Organic Nanostructures of π -Systems*

| | |
|--|----|
| Abstract | 3 |
| 1.1.1 Why Self-Assembly of π -Conjugated Systems? | 4 |
| 1.1.2 Amphiphilic Approach | 4 |
| 1.1.2a Amphiphilic PBIs | 5 |
| 1.1.2b Amphiphilic HBCs | 10 |
| 1.1.2c Amphiphilic Oligo(p-phenylenevinylene)s (OPVs) and Thiophenes | 12 |
| 1.1.3 Mixed Stack Charge-Transfer D-A Assemblies | 16 |
| 1.1.4 Conclusions and Outlook | 21 |
| 1.1.5 References | 22 |

PART-1.2 *Organic-Inorganic Light-Harvesting Scaffolds for Luminescent Hybrids*

| | |
|--|----|
| Abstract | 27 |
| 1.2.1 Introduction | 28 |
| 1.2.2 Periodic Mesoporous Silica (PMO) | 29 |
| 1.2.3 Dye Loaded Zeolites | 31 |
| 1.2.4 Dye Loaded MIMs | 35 |
| 1.2.5 Metal Organic Frameworks (MOFs) | 37 |
| 1.2.6 Conclusions and Outlook | 39 |
| 1.2.7 References | 40 |

PART-2

Self-Assembly of Coronene Bisimide Amphiphiles

PART-2.1 *Synthesis, Controllable Self-Assembly and Optoelectronic Properties of Novel n-Type Coronene Bisimide Amphiphiles*

| | |
|--------------------|----|
| Abstract | 45 |
| 2.1.1 Introduction | 46 |

| | | |
|-----------------|---|----|
| 2.1.2 | Design, Synthesis and Characterization | 48 |
| 2.1.3 | Self-assembly in Solution | 48 |
| 2.1.4 | Morphology Studies | 51 |
| 2.1.5 | OFET Device Characteristics | 53 |
| 2.1.6 | Conclusions | 55 |
| 2.1.7 | Experimental Section | 55 |
| 2.1.7a | Synthesis | 56 |
| 2.1.8 | References | 57 |
| PART-2.2 | <i>Mechanistic Insights into the Self-Assembly Process of Coronene Bisimide Amphiphiles</i> | |
| Abstract | | 61 |
| 2.2.1 | Introduction | 62 |
| 2.2.2 | Design Strategy and Synthesis | 63 |
| 2.2.3 | Self-Assembly in Solution | 64 |
| 2.2.4 | Mechanisms of Self-Assembly | 69 |
| 2.2.5 | Conclusions | 74 |
| 2.2.6 | Experimental Section | 74 |
| 2.2.6a | Synthesis | 75 |
| 2.2.7 | Analysis of the cooling curves | 75 |
| 2.2.7a | Isodesmic Model | 75 |
| 2.2.7b | Nucleation-Elongation Model | 76 |
| 2.2.8 | References | 76 |

PART-3

Charge-Transfer Nanostructures

PART-3.1 *Charge-Transfer Nanofibers with Mixed Donor-Acceptor Organization via Non-Covalent Amphiphillic Strategy*

| | | |
|----------|----------------------------------|----|
| Abstract | | 81 |
| 3.1.1 | Introduction | 82 |
| 3.1.2 | Non-Covalent Amphiphillic Design | 83 |
| 3.1.3 | CS-viologen D-A System | 84 |
| 3.1.3a | Design Strategy | 84 |
| 3.1.3b | Synthesis and Optical Studies | 84 |
| 3.1.3c | Gelation Studies | 85 |
| 3.1.3d | Face-to-Face D-A Organization | 86 |
| 3.1.3e | Morphology Studies | 89 |

| | | |
|-----------------|--|-----|
| 3.1.4 | PS-Viologen D-A System | 91 |
| 3.1.5 | OPV-PBI CT-System | 92 |
| 3.1.5a | Design Strategy | 92 |
| 3.1.5b | Gelation and Rheology Experiments | 92 |
| 3.1.5c | Optical Studies | 94 |
| 3.1.5d | Morphology Studies | 97 |
| 3.1.5e | Conductive AFM Studies | 98 |
| 3.1.6 | Conclusions | 99 |
| 3.1.7 | Experimental Section | 99 |
| 3.1.7a | Synthesis | 100 |
| 3.1.8 | References | 101 |
| PART-3.2 | <i>Autonomous Alignment of Charge-Transfer Fibers via Two-Dimensional Donor-Acceptor Self-Assembly</i> | |
| | Abstract | 107 |
| 3.2.1 | Introduction | 108 |
| 3.2.2 | Design Strategy | 109 |
| 3.2.3 | Optical Studies and Gelation Experiments | 110 |
| 3.2.4 | Morphology Studies | 111 |
| 3.2.5 | Linear Dichroism and Powder XRD Studies | 113 |
| 3.2.6 | Cross-linking Experiments | 115 |
| 3.2.7 | Conclusions | 116 |
| 3.2.8 | Experimental Section | 117 |
| 3.2.8a | Synthesis | 117 |
| 3.2.9 | References | 118 |
| PART-3.3 | <i>High Charge Carrier Mobility in Non-Covalently Tailored D-A Heterojunction Nanostructures</i> | |
| | Abstract | 123 |
| 3.3.1 | Introduction | 124 |
| 3.3.2 | Design Strategy | 124 |
| 3.3.3 | Characterization of D and A Co-Assembly | 125 |
| 3.3.4 | Transient Absorption Measurements | 129 |
| 3.3.5 | Morphology | 130 |
| 3.3.6 | Transient Photocurrent Measurements | 132 |
| 3.3.7 | Conclusions | 133 |
| 3.3.8 | Experimental Section | 134 |
| 3.3.8a | Transient photocurrent measurements | 134 |

| | | |
|--------|------------|-----|
| 3.3.8b | Synthesis | 135 |
| 3.3.9 | References | 135 |

PART-4**Luminescent Soft-Hybrids****PART-4.1** *Light-Harvesting Organic-Inorganic Soft-Hybrids: Energy Transfer Induced Amplified Fluorescence and Highly Pure Solid-State White-Light Emission*

| | | |
|----------|-----------------------------------|-----|
| Abstract | | 141 |
| 4.1.1 | Introduction | 142 |
| 4.1.2 | Design Strategy | 143 |
| 4.1.3 | Organic-Inorganic Co-Assembly | 145 |
| 4.1.4 | Energy Transfer in Solution | 150 |
| 4.1.5 | Energy Transfer in Gels and Films | 154 |
| 4.1.6 | White-Light Emission | 156 |
| 4.1.7 | Dynamics in solution | 162 |
| 4.1.8 | Conclusions | 163 |
| 4.1.9 | Experimental Section | 164 |
| 4.1.9a | Synthesis | 165 |
| 4.1.10 | References | 165 |

PART-4.2 *Controlling the Molecular Organization of π - Systems via Hybrid Co-Assembly: A Non-Covalent Strategy towards Solution Processable Luminescent Hybrids*

| | | |
|----------|---|-----|
| Abstract | | 169 |
| 4.2.1 | Introduction | 170 |
| 4.2.2 | Design Strategy and Synthesis | 172 |
| 4.2.3 | H-Aggregates to Fluorescent Hybrid Dye-LP Monomers | 173 |
| 4.2.4 | Fluorescent Dye J-aggregates-LP Hybrids | 175 |
| 4.2.5 | Rheology Studies on Hybrid Hydrogels | 179 |
| 4.2.6 | Transparent and Luminescent Films of Dye J-Aggregate-LP Hybrids | 180 |
| 4.2.7 | Alternate Organic-Inorganic Hybrid Arrays | 182 |
| 4.2.8 | Conclusions | 183 |
| 4.2.9 | Experimental Section | 183 |
| 4.2.9a | Synthesis | 184 |
| 4.2.10 | References | 185 |

PART-5

Conjugated Microporous Polymers*Super-Absorbent Dynamic Microporous Polymers: Guest-Responsive Reversible Swelling, Enhanced Fluorescence, and Light-Harvesting*

| | |
|--|-----|
| Abstract | 191 |
| 5.1 Introduction | 192 |
| 5.2 Preliminary Work on POPs | 194 |
| 5.3 Functional Properties of Pyrene Based Microporous Polymers | 195 |
| 5.3a Synthesis and Structural Characterization | 195 |
| 5.3b Dynamic and Swelling Nature | 198 |
| 5.3c Oil Removal and Recovery from Water | 202 |
| 5.3d Encapsulation of C ₆₀ and Photoinduced Electron Transfer | 203 |
| 5.3e Fluorescence as a Probe for Guest Encapsulation | 204 |
| 5.3f POPs as Light-Harvesting Scaffolds | 205 |
| 5.4 Conclusions | 209 |
| 5.5 Experimental Section | 209 |
| 5.5a Synthesis | 211 |
| 5.6 References | 211 |
| Curriculum Vitae | 215 |
| List of Publications | 217 |

PART-1

Introduction

PART-1.1 Amphiphilic and Charge-Transfer Designs for Self-Assembled Organic Nanostructures of π -Systems

PART-1.2 Organic-Inorganic Light-Harvesting Scaffolds for Luminescent Hybrids

Controlling the molecular organization of π -conjugated systems is of paramount importance in the design of functional optoelectronic materials. Self-assembly offers a simple and innovative way to control the hierarchical organization of π -systems under thermodynamic control. On the other hand, organization of π -conjugated systems with the aid of inorganic components is also an efficient approach for the design of functional organic-inorganic hybrid materials. However, self-assembled nanostructures of π -conjugated systems often showed poor performance on devices, whereas hybrid materials suffer from their solution processability. This thesis presents our attempts to improve the optoelectronic functions of organic materials and solution processability of organic-inorganic hybrid materials constructed from self-assembled π -conjugated systems. The first half of this thesis presents our molecular designs to improve the optoelectronic functions of self-assembled π -systems using amphiphilic and charge-transfer approaches. The second half of the thesis provides our strategies to construct solution processable organic-inorganic hybrid materials via non-covalent co-assembly between π -systems and inorganic clays (soft-hybrid approach).

This introduction part provides an overview on the various design principles of wide variety of self-assembled organic and hybrid materials reported in literature for improved optoelectronic functions. Since this research area is very vast, we restrict ourselves to the examples related to designs presented in this thesis. This introduction Part is divided into two sections. Part-1.1 presents amphiphilic and charge-transfer (CT) approaches for the design of self-assembled organic nanostructures. Part-1.2 concentrates on various luminescent organic-inorganic light-harvesting hybrids.

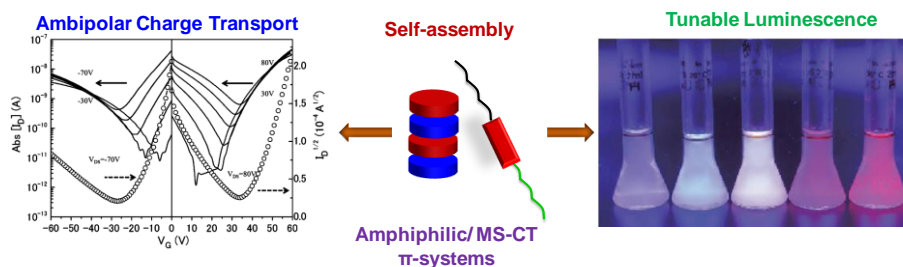
PART-1.1

Amphiphilic and Charge-Transfer Designs for Self-Assembled Organic Nanostructures of π -Systems

Abstract

The performance of organic electronic devices not only depends on the chemical structure of organic molecules but also on different hierarchies of their supramolecular organization. Thus, the self-assembly of π -conjugated systems has been a topic of immense interest for supramolecular chemists. In this context, self-assembly of wide variety of π -conjugated molecules have been investigated in detail to control their supramolecular organization. However, these self-assembled structures often showed poor device performance. The first half of this thesis presents our attempts to improve the optoelectronic functions of various self-assembled π -systems. We have mainly employed two strategies, namely, amphiphilic and charge-transfer (CT) approaches, towards this objective. In this section of introduction, we provide an overview on the design principles and optoelectronic functions of various self-assembled π -systems based on amphiphilic and charge-transfer (CT) approaches reported in literature.

First we discuss about the optoelectronic functions of self-assembled amphiphilic π -conjugated oligomers. Amphiphilic self-assembly of π -systems results in nanostructures with well defined supramolecular ordering and with high association constants. Recent advances in the amphiphilic self-assembly of well known n-type and p-type semiconductors such as perylene bisimides (PBIs), hexabenzocoronenes (HBCs), oligo(p-phenylenevinylene)s (OPVs) and oligothiophenes are mainly discussed. Next, we discuss about the CT-assemblies of π -systems having mixed stack (MS) electron donor (D) and acceptor (A) organization. Our discussion is centred on ferroelectric, luminescence and ambipolar charge transport properties of various MS-CT crystals and CT- nanostructures.



1.1.1 Why Self-Assembly of π -Conjugated Systems?

Semiconducting, π -conjugated oligomers/polymers are the promising candidates for optoelectronic functions in the context of cost-effective and flexible plastic electronic devices.¹ The performance of these devices not only depends on the chemical structure of π -systems but also on their different hierarchies of supramolecular organization.² In this context, self-assembly offers an efficient way to control the hierarchical organization of π -systems under thermodynamic control.³ Enormous efforts have been performed in the last decade to obtain ordered structures of π -systems with anisotropic electronic coupling and to have control over their performance on devices.⁴ Moreover these self-assembled nanostructures can be used as conducting components in nanosized (5-100 nm) electronic devices.

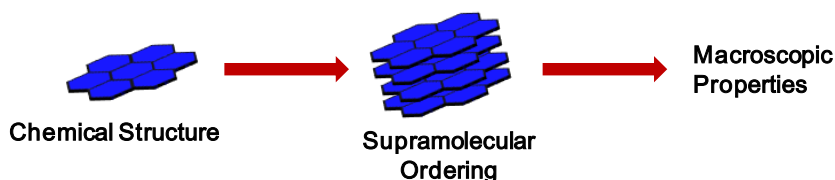


Figure 1.1.1. Schematic representation on how the macroscopic properties of materials are related to chemical structure and supramolecular organization.

In the last decade, significant progress has been achieved in the supramolecular self-assembly of π -conjugated oligomers in the view of nanosized electronics.⁵ The challenges for using conjugated polymers in devices are their poor charge transport, luminescence and photovoltaic performances. This could be due to low π - π ordering between polymer chains on devices. This can be addressed by self-assembly of well defined small conjugated oligomers without sacrificing the ease of solution processability. In this section, some of the recent advances in the supramolecular design principles of various p-type and n-type π -conjugated oligomers towards improved optoelectronic functions are discussed. This section is mainly focused on amphiphilic and charge-transfer approaches which are featured as two promising strategies to achieve self-assembled nanostructures with high efficient transport and luminescence suitable for optoelectronics.

1.1.2 Amphiphilic Approach

One of the reasons for low efficiencies in supramolecular chromophoric systems could be the molecular design with solubilizing side chains, which hamper the molecular order and disrupt the extended π - π stacking in the assemblies. In this regard, an amphiphilic design for self-assembly of chromophores can be of particular interest. Moreover, it has been shown that hydrophobic interactions between the amphiphilic systems can give rise to less dynamic

assemblies with high association constants. Hence, an amphiphilic design combined with the electroactive chromophores can give rise to highly ordered assemblies with stronger π - π interactions and hence better mobilities. In this section we summarize the design principles and optoelectronic functions of self-assembled nanostructures of various p-type and n-type amphiphilic π -conjugated oligomers. Although, various other non-covalent interactions such as hydrogen bonding have also been extensively used for the supramolecular organization these π -systems,^{2,3,6} we restrict ourselves to the amphiphilic design, keeping in mind the theme of this thesis.

1.1.2a Amphiphilic PBIs

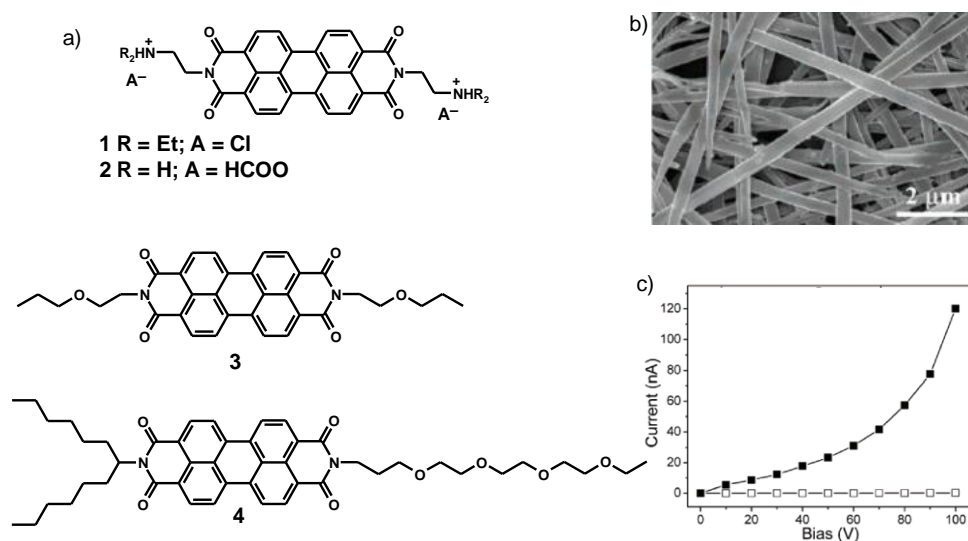


Figure 1.1.2. a) Molecular structures of amphiphilic PBIs. b) SEM image of nanobelts of **3** [reproduced from ref. 14]. c) I-V curves measured on a nanobelt of **3** in air (open rectangle) and in saturated hydrazine vapour (closed rectangle) [reproduced from ref. 15].

Perylene bisimides (PBIs), also known as perylene diimides (PDIs) are one of the well studied organic semiconductors in organic electronics owing to their elegant molecular structure and outstanding optoelectronic functions (Figure 1.1.2a).⁷ Considering their efficient electron transport, PBI dyes are one of the prime choices for n-type organic field effect transistors (OFETs)⁸ and in organic photovoltaics as alternatives to fullerene acceptors.⁹ In this context various non-covalent strategies have been employed to improve the supramolecular ordering of PBIs in devices for efficient optoelectronic functions.¹⁰ Würthner et al. have extensively investigated the supramolecular self-assembly of PBI dyes in water¹¹ and organic solvents¹² by employing various non-covalent interactions in addition to strong π - π interactions between PBI chromophores. They observed that π - π stacking of PBIs in water is very efficient with an association constant of $K > 10^8 M^{-1}$; as a result, self-assembly of PBI amphiphiles in water would be a potential approach for the creation of n-type materials, with improved

optoelectronic functions.

Chang et al. first studied the self-organization of water soluble cationic PBI amphiphiles (**1** and **2**, Figure 1.1.2a).¹³ Both these molecules form lyotropic phases in water at appropriate concentrations, resulting in highly aligned assemblies on substrates with dichroic ratios comparable with that of commercial polarizers. Zang et al. prepared the self-assembled nanobelts of propoxyethyl PBI (**3**) by injecting its molecularly dissolved solution in chloroform into methanol (Figure 1.1.2b).¹⁴ Upon exposure to hydrazine vapours nanobelts of **3** displayed high conductivity of 10^{-3} S cm^{-1} at room temperature, due to the formation of PBI radical anions (Figure 1.1.2c).¹⁵ They have also achieved millimeter long nanobelts by the self-assembly of asymmetric PBI amphiphile (**4**) in ethanol-water mixtures, with π -stacked PBIs oriented along the length of nanobelt.¹⁶ Two probe device made from a single nanobelt of **4** also showed three orders of magnitude increase in current after reduction with hydrazine vapours than pristine nanobelts.

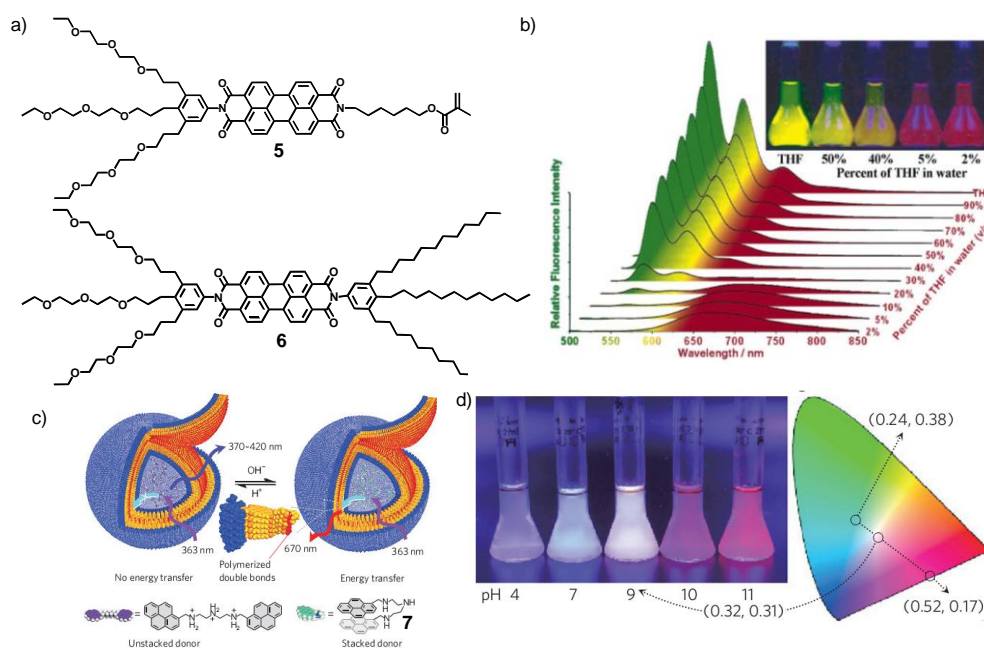


Figure 1.1.3. a) Molecular structures of wedge shaped amphiphilic PBIs (**5** and **6**). b) Emission spectra and corresponding solution photographs of **5** in THF-water mixtures [reproduced from ref. 17]. c) Schematic illustration of the donor (**7**)-loaded polymerized vesicles with pH-tunable energy transfer. d) Photograph of donor-loaded polymerized vesicles in aqueous solution at different pH under an ultraviolet lamp (366 nm) and corresponding CIE 1931 chromaticity diagram [Figure 1.1.3c and d, reproduced from ref. 18].

Würthner et al. reported the self-assembly and co-assembly of various glycol functionalized PBI amphiphiles (**5** and **6**) in THF-water mixtures (Figure 1.1.3a). The solution state emission colours of these amphiphiles were tuned from green to red by modulating the extent of aggregation with THF-water mixture (Figure 1.1.3b).¹⁷ Interestingly, the co-assembly

of **5** and **6** resulted in the formation of supramolecular vesicles, which were further stabilized by covalent cross linking of hydrophobic segments through photopolymerization (Figure 1.1.3c). These membrane vesicles are further loaded with pH responsive bispyrene derivative (**7**) and fluorescence of these vesicles was tuned through pH controlled resonance energy transfer from **7** to membrane PBIs (Figure 1.1.3d).¹⁸ Interestingly, at pH 9 white light emission was observed due to partial energy transfer. In basic conditions (pH > 9) **7** shows excimer emission having overlap with PBI absorption, as a result efficient resonance energy transfer is feasible from **7** to PBI aggregates which becomes less efficient in acidic conditions due to poor overlap of monomeric emission of **7** with PBI absorption, as it prefers unstacked conformation (Figure 1.1.3c).

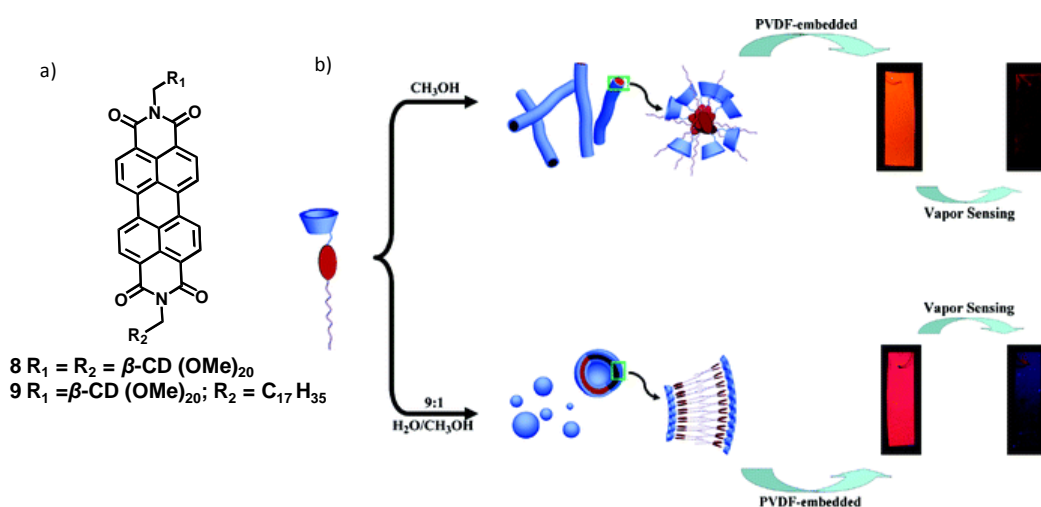


Figure 1.1.4. a) Molecular structures of β -cyclodextrin functionalized PBI amphiphiles. b) Schematic illustration of self-assembly and vapour sensing of organic amines by nanostructures of **9** embedded in PVDF matrix [reproduced from ref. 19b].

Liu and coworkers explored the emission properties of supramolecular aggregates of β -cyclodextrin functionalized PBI amphiphiles (**8** and **9**, Figure 1.1.4) formed in water for sensing of various organic amine vapours (Figure 1.1.4).¹⁹ Interestingly, **8** self-assembles in water to form fluorescent 1D nanorods due to weak π - π interactions between PBI units as a result of steric repulsions caused by β -cyclodextrin pendants.^{19a} Asymmetric amphiphile **9** also self-assembles into fluorescent nanorods and vesicles in methanol and 9:1 water/methanol mixtures, respectively (Figure 1.1.4b).^{19b} Furthermore, these fluorescent supramolecular aggregates were embedded in polyvinylidene fluoride (PVDF) membranes for turn-off fluorescence sensing of organic amine vapours via both photoinduced electron transfer from amines to PBIs and disturbing the exciton migration among PBIs in the aggregate through amine inclusion (Figure 1.1.4b).

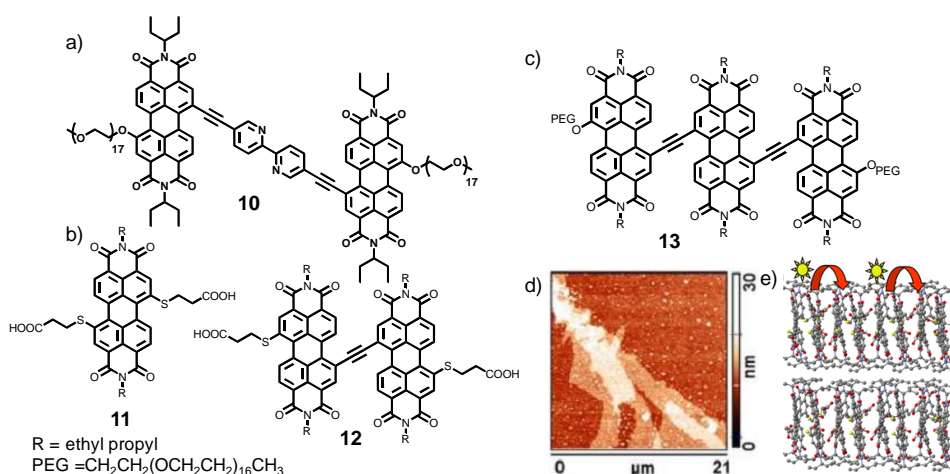


Figure 1.1.5. *a-c) Molecular structures of oligo PBI amphiphiles. d) Self-assembled nanosheets of 13 formed in water and e) schematic representation of exciton migration in these nanosheets [Figure 1.1.5d and e, reproduced from ref. 22].*

Rybtchinski et al. extensively investigated the self-assembly oligo PBI amphiphiles in water (Figure 1.1.5).²⁰ Remarkably, self-assembled networks of polyethylene glycol (PEG) functionalized oligo PBI amphiphile (**10**) were very robust like covalent systems and demonstrated their application as nano filtration membranes (Figure 1.1.5a).²¹ Interestingly, PBIs **11-13**, self-assemble in water into crystalline 2D structures and showed efficient exciton migration up to 120 nm length scales (Figure 1.1.5b-e).²² Moreover exciton diffusion coefficients of these crystalline assemblies are better than PTCDA (perylene tetracarboxylic dianhydride)²³ crystalline films. Furthermore, wide spectral coverage and 2D morphology of this class of PBIs would be advantageous for the fabrication of efficient artificial light-harvesting systems.

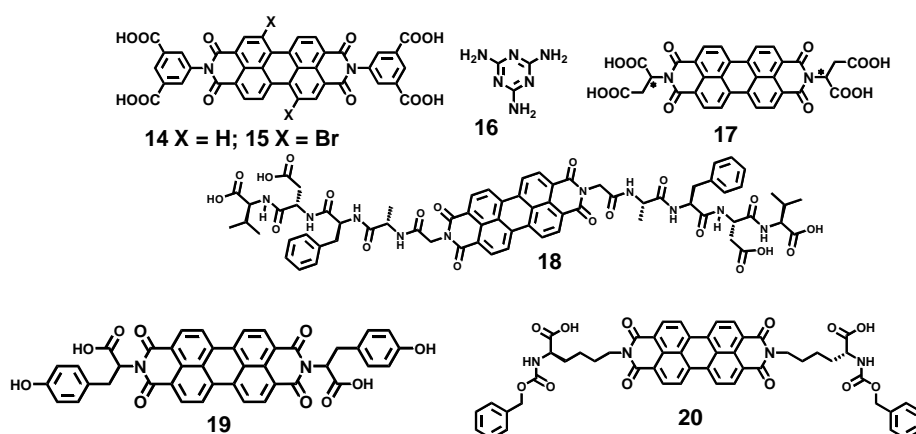


Figure 1.1.6. *Molecular structures of acid/peptide functionalized PBI amphiphiles and melamine (16).*

Hydrogels through supramolecular assembly of PBI chromophores guided by hydrogen bonding have been made by Malik et al. and Tovar et al. (Figure 1.1.6, **14-18**). Malik's group

showed the spontaneous formation of hydrogels by acid functionalized PBIs (**14** and **15**) when treated with melamine (**16**) due to intermolecular H-bonding.²⁴ In these hydrogels, PBIs exist as H-aggregates and fluorescence of these aggregates is probably due to excimer formation. Later they have also found that, aspartic acid functionalized PBIs (**17**) are also efficient gelators for water, under acidic conditions and gelation is promoted through inter molecular H-bonding and J-aggregation of PBIs.²⁵ Tovar et al. functionalized PBIs with β -sheet forming peptides to make PBI-peptide (**18**) hydrogels.²⁶ However the resultant hydrogels are non-fluorescent probably due to strong H-aggregation of PBI units. Banerjee et al. showed the multifunctional behaviour of peptide functionalized PBI (**19**) assemblies.²⁷ L-tyrosine functionalized PBI (**19**) amphiphiles, self-assemble in water and form pH responsive luminescent hydrogels.^{27a} Interestingly, these gel networks showed photo-switchable conductivity when shined with visible/white light with high on/off ratios. Recently Li et al. also reported the fine tuning of L-lysine-functionalized PBI (**20**) nanostructures by varying the ratio between acetone and water.²⁸

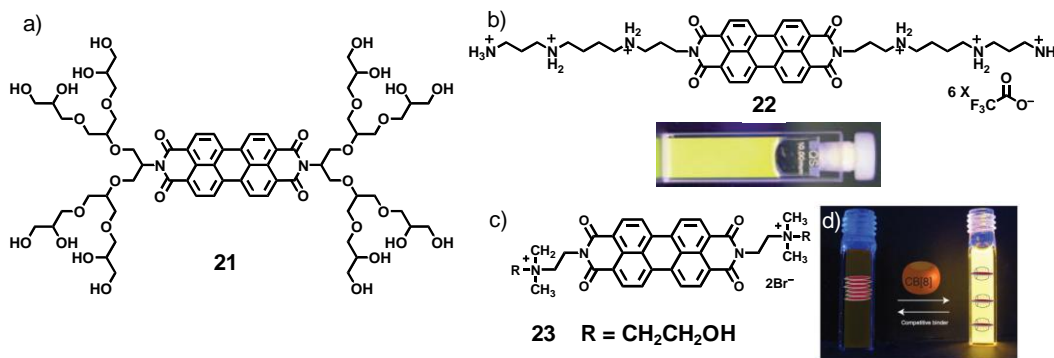


Figure 1.1.7. a) Molecular structure of polyglycerol dendron functionalized PBI amphiphile (**21**). b) Molecular structure of spermine functionalized PBI amphiphile (**22**) and photograph showing its monomeric fluorescence in acidic water [reproduced from ref. 30]. c) Molecular structures of dicationic PBI amphiphile (**23**). d) Photographs of **23** (left) and **23**-CB[8] (right) complex in water upon irradiation with a 450 nm light source [reproduced from ref. 31].

Monomeric form of PBIs often exhibits fluorescence quantum yield close to unity, which will be often suppressed by many orders of magnitude in their aggregates. Moreover, this is inevitable in water due to their high association constants (*vide supra*). In this context, Würthner and co-workers showed that quantum yields of PBIs in water can be improved by suppressing PBI aggregation through modification on imide side chains with water soluble functional groups (Figure 1.1.7). For this purpose, several PBI derivatives functionalized with different generations of polyglycerol dendrons (Figure 1.1.7a, **21**) were made and increase in the quantum yield of these derivatives in water was observed with increase in the dendron generation and reached near to unity with fourth generation dendron due to effective suppression PBI aggregation by dendron fences.²⁹ This approach was further demonstrated in spermine functionalized PBIs (**22**) where the electrostatic repulsion between spermines in

acidic water enhances the PBI fluorescence quantum yield while hindering π - π stacking between PBI units (Figure 1.1.7b).³⁰ Scherman et al. used host-guest interactions to amplify the fluorescence quantum yield of PBIs in water (Figure 1.1.7c and d).³¹ The simple dicationic PBI (**23**) alone in water has poor quantum yield due to its H-aggregation, which was amplified near to unity by spatially separating PBI molecules through complexation with CB[8] (Figure 1.1.7d). These highly fluorescent PBI dyes in water can be potential candidates for bioimaging owing to their high photo-stability and tunable emission.

1.1.2b Amphiphilic HBCs

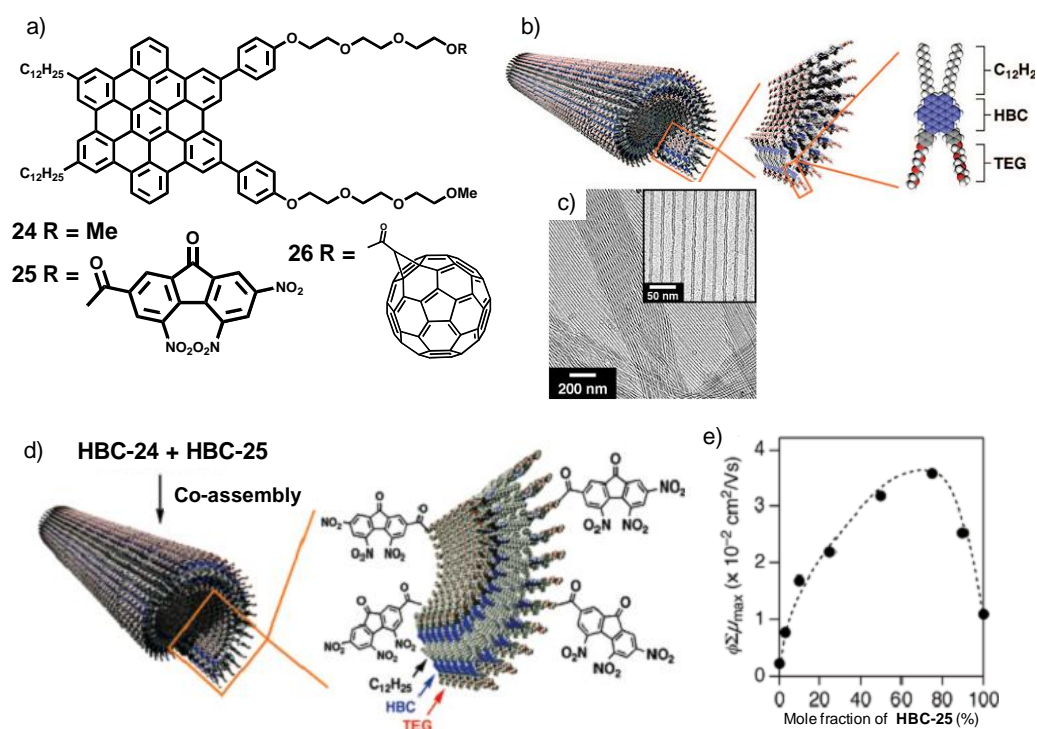


Figure 1.1.8. a) Molecular structures of various HBC amphiphiles. b) Schematic illustrations of the hierarchical structures of a nanotube formed from **HBC-24** and c) TEM images of amphiphilic HBC (alkyl chain is C₁₃H₂₇) nanotubes at different magnifications [reproduced from ref. 33b]. d) Schematic illustration for the formation of a co-assembled graphitic nanotube from **HBC-24** and **HBC-25**. TEG is triethylene glycol. e) Plot of transient photoconductivity maximum values versus mole fractions of **HBC-25** in **HBC-24** nanotubes [Figure 1.1.8d and e, reproduced from ref. 35c].

Hexa-peri-hexa-benzocoronenes (HBCs), are another class of well studied organic semiconductors owing to their efficient hole transporting behaviour and strong tendency to self-organize through π - π stacking (Figure 1.1.8a). Müllen et al. extensively investigated the self-organization of hydrophobic HBCs and their charge carrier mobility in the liquid crystalline state.³² Aida et al. described a bottom up synthesis of supramolecular graphitic nanotubes by the self-assembly of amphiphilic HBCs (Figure 1.1.8a and b, **24**).³³ In solution these nanotubes

are formed by hierarchical self-assembly of HBC chromophores driven by π - π stacking between HBC units and bilayer formation by partial interdigitation of alkyl chains (Figure 1.1.8b and c). The resultant nanotubes are redox active and a single nanotube exhibits resistivity of 2.5 megohms at 285 K after oxidation with NOBF_4 . Recently, they have shown that HBC nanotubes made from chiral derivative form macroscopic fibers via unidirectional alignment of nanotubes and they can be processed with a glass hook.³⁴ As a result, these macroscopic fibers exhibit high anisotropic conductivity upon iodine doping.

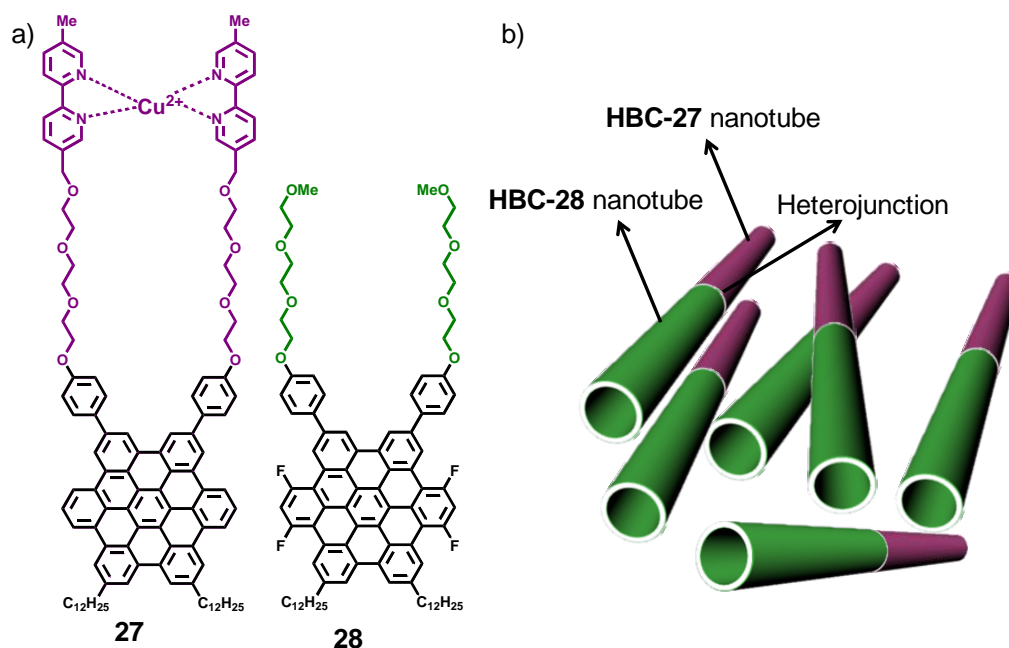


Figure 1.1.9. a) Molecular structures of amphiphilic HBCs used in supramolecular construction of linear heterojunction nanotubes. b) Schematic representation of non-covalently connected **HBC-27** and **HBC-28** nanotubes to form a linear heterojunction.

The glycol chains of these amphiphilic HBC derivatives were further covalently functionalized with various electron deficient acceptor (A) molecules to have nanoscale phase segregation between covalently linked electron rich donor (D, HBC core) and A molecules for efficient photocurrent generation.³⁵ In this design, amphiphilic interactions provided by glycol chains are crucial for segregation of D and A molecules without any ground state charge-transfer (CT) interactions. In this context amphiphilic HBC was covalently linked with one of the two well known A molecules, trinitrofluorenone (TNF)/ C_{60} at triethylene glycol termini (Figure 1.1.8a, **25** and **26**). The resultant covalent D-A amphiphile self-assembles to form coaxial nanotubes in which p-type HBC stacks in the tubular wall are laminated by the n-type TNF/ C_{60} at the outer and inner surfaces of the nanotube. Efficient photoinduced electron transfer and charge separation was observed in these coaxial nanotubes owing to their spatially isolated nanoscale p-n heterojunction configuration and efficient exciton migration along HBC

stacks. As a result, these nanotubes showed fast photoconductivity response with high on/off ratios. High charge carrier mobilities ($\sim 3 \text{ cm}^2/\text{V.s}$) along a single nanotube was observed in flash-photolysis time-resolved microwave conductivity (FP-TRMC) measurements when D-A HBC amphiphile was co-assembled with HBC amphiphile, compared to the homoassembly of D-A-HBC alone (Figure 1.1.8d and e). This is attributed to the suppression of defects in HBC stacks caused by clustering of TNF/ C_{60} layers in homotropically assembled D-A HBC nanotube.³⁶ This covalent amphiphilic D-A strategy was further demonstrated for nanoscale tailoring of various p-type and n-type heterojunction assemblies such as oligothiophene- C_{60} ,³⁷ porphyrin- C_{60} ,³⁸ oligothiophene-PBI³⁹ dyads and dibenzo[a,c]phenazines.⁴⁰ We have achieved segregation of D and A stacks with a non-covalent approach in which D and A molecules are non-covalently connected through ionic interactions to form a heterojunction. The self-assembly of this ionic complex results in the formation of heterojunction nanostructures with wide D-A interface and high charge carrier mobility ($1.2 \text{ cm}^2/\text{V.s}$) which is discussed in Part-3.3 of this thesis. On the other hand, recently Aida et al. demonstrated for the first time a non-covalent synthesis of supramolecular linear p-n heterojunctions through the supramolecular growth of an electron deficient HBC (**28**) amphiphile nanotube on the seed of electron rich amphiphilic HBC (**27**) nanotube (Figure 1.1.9).⁴¹ These non-covalently connected p-n junction nanotubes communicate electronically through the heterojunction interface and showed five times longer lifetime for photogenerated carriers than their homotropic nanotubes (Figure 1.1.9b).

1.1.2c Amphiphilic Oligo(p-phenylenevinylene)s (OPVs) and Thiophenes

OPVs are another important class of p-type semiconductors and their polymer counter parts (PPVs) are widely utilized in photovoltaics and electroluminescent devices owing to their excellent luminescence properties.⁴² Amphiphilic design strategy is also employed in OPV chromophores to improve their supramolecular ordering as it plays crucial role in their device performance. In this context, Stupp et al. investigated the self-assembly of amphiphilic OPV (**29**) derivatives asymmetrically substituted with PEG (polyethylene glycol) and hydrophobic alkyl chains (Figure 1.1.10a).⁴³ These molecules self-assemble in water and in other polar solvents by forming both thermotropic and lyotropic liquid crystalline mesophases, while forming luminescent gels at high concentrations (Figure 1.1.10b). The optoelectronic properties of these amphiphiles are sensitive to the length of PEG chain. Interestingly, films of OPV molecule with longest PEG chain retain its monomer emission in the solid state with high fluorescence quantum yield due to suppression of OPV aggregation by PEG chains.

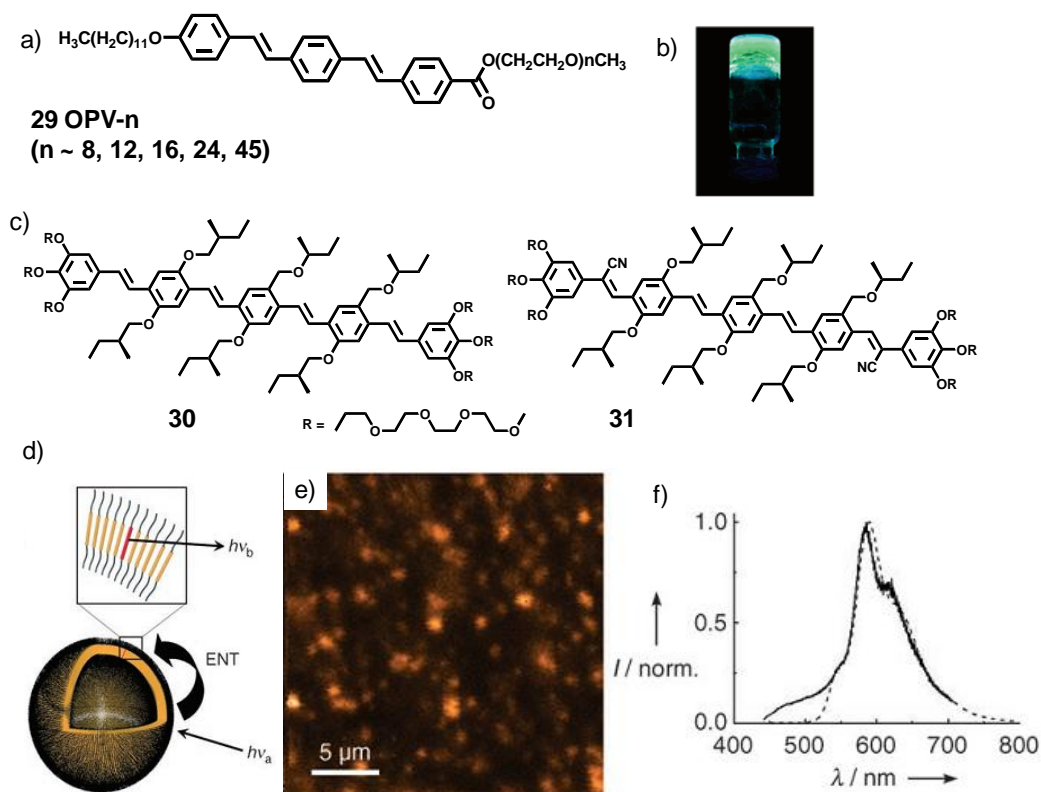


Figure 1.1.10. a) Molecular structures of OPV amphiphiles functionalized with PEGs having different chain lengths. b) OPV amphiphile (**29**, $n = 24$) derived hydrogel irradiated under 365 nm UV light [reproduced from ref. 43]. c) Molecular structures of OPV amphiphiles having oligo(ethylene glycol) functionalized gallic wedges. d) Schematic representation of energy transfer process from **30** to **31** in single co-assembled vesicles. e) Scanning confocal microscopy images and f) resulting fluorescence spectra ($\lambda_{\text{exc}} = 411$ nm) of mixtures of **30** and **31** (2 mol% of **31**). The fluorescence of these single vesicles (solid lines) is compared to the corresponding solution spectra (dashed lines) [Figure 1.1.10d-f, reproduced from ref. 44a].

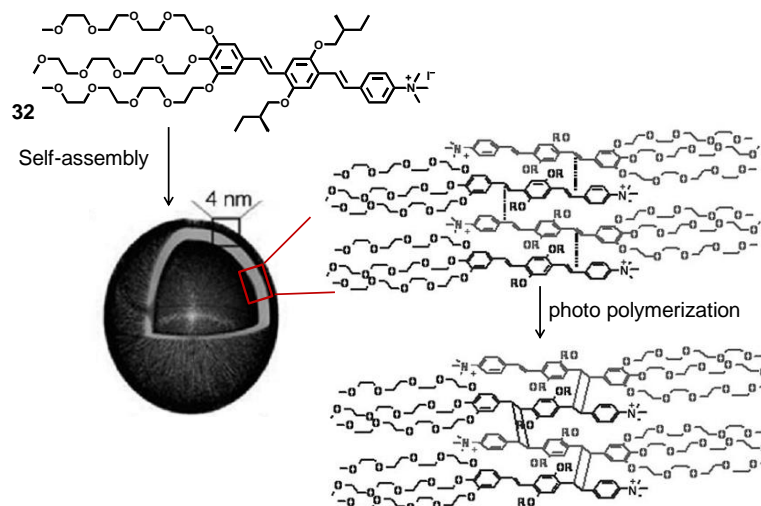


Figure 1.1.11. Proposed head-to-tail organization of **32** in the vesicles formed in water and the resulting photocycloaddition [reproduced from ref. 44b].

Meijer and co-workers studied the solution state self-assembly and optoelectronic functions of various amphiphilic OPVs linked with gallic wedges (**30-32**).⁴⁴ All these amphiphiles self-assemble to form vesicles in water through synergistic π -stacking between OPV chromophores and amphiphilic interactions. Since self-assembled π -stacks are versatile scaffolds for excitation energy/electron transfer process,⁴⁵ energy transfer from **30** to **31** was investigated in their co-assembled vesicles state (Figure 1.1.10c-f).^{44a} In the co-assembled form, efficient energy transfer was observed from **30** to **31** which can be visualized using scanning confocal microscopy images (Figure 1.1.10e and f). Interestingly, energy transfer was also observed (after 48 h) in the mixed individual vesicular assemblies of **30** and **31** owing to their dynamic nature. In an interesting study, Meijer et al. found that cationic OPV amphiphile (**32**) self-assembles in a head-to-tail fashion to form supramolecular vesicles due to interaction between ammonium and glycol chains (Figure 1.1.11).^{44b} This special organization facilitates the photo-induced [2+2] cycloaddition between OPVs under ambient conditions, resulting in covalently polymerized vesicle membranes.

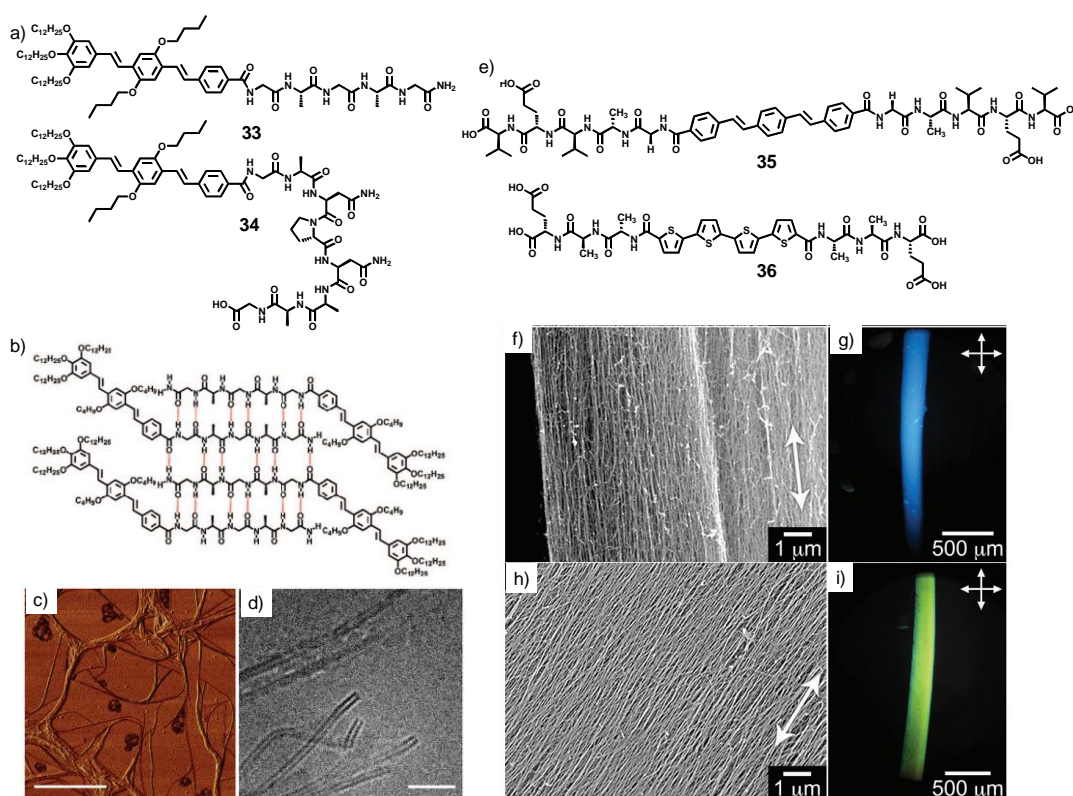


Figure 1.1.12. a) Molecular structures of OPV peptide amphiphiles (**33** and **34**). b) Molecular structure of an antiparallel β -sheet conformation of a monolayer of **33**. c) AFM image of nanofibers of **33** formed in water. d) cryo-TEM image of **34** in water [Figure 1.1.12b-d, reproduced from ref. 46]. e) Molecular structures of OPV and oligothiophene peptide amphiphiles that form hydrogels. Representative SEM images of aligned structures composed of f) **35** and h) **36**. Optical birefringence of macroscale peptide fibers composed of g) **35** and i) **36** as seen under crossed polarizers [Figure 1.1.12f-i, reproduced from ref. 47].

Amphiphilic self-assembly of OPV chromophores is also promoted by conjugating them with β -sheet forming peptides (Figure 1.1.12, **33-35**). Scanning tunnelling microscopy (STM) at the submolecular level on OPV-peptide conjugates reported by Meijer's group reveals the formation of bilayers with antiparallel orientation of OPVs in a β -sheet conformation of peptide chains and in water they self-assemble to form various 1D nanostructures such as nanofibers and nanotubes (Figure 1.1.12b-d).⁴⁶ On the other hand, the class of OPV-peptide conjugates reported by Tovar et al. form hydrogels and highly aligned nanowires on substrate were obtained via extrusion from syringe (Figure 1.1.12e-g).⁴⁷ This design was further extended to oligothiophene-peptide (**36**) conjugate to achieve aligned nanowires with high anisotropic mobility ($\sim 0.03 \text{ cm}^2/\text{V}\cdot\text{s}$) (Figure 1.1.12h and i).

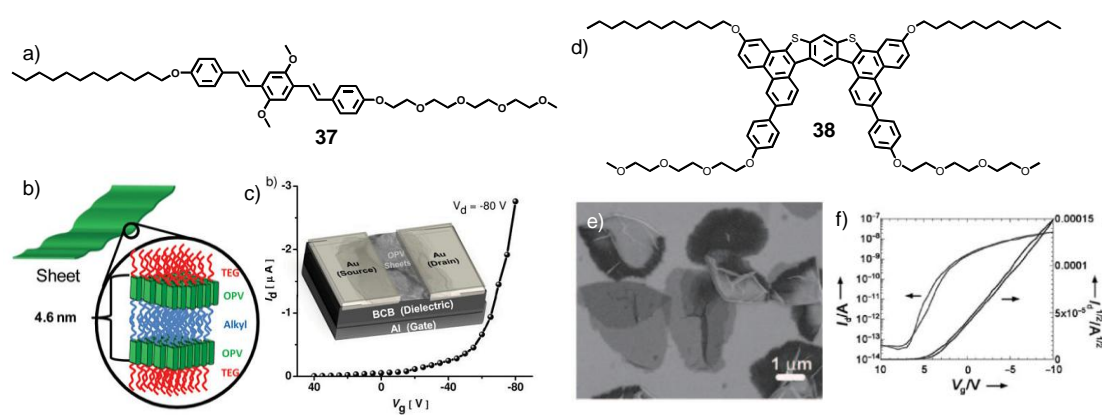


Figure 1.1.13. a) Molecular structure of OPV amphiphile (**37**) and b) schematic representation of its molecular organization in the sheets. c) Transconductance curves for sheets made from **37** in top contact bottom gate FET and inset shows the schematics of the device structure with these sheets as active layer [Figure 1.1.13b and c, reproduced from ref. 48]. d) Molecular structure of butterfly shaped amphiphile (**38**). d) SEM image of 2D nano sheets of **38**. f) Transfer characteristics of a 2D film transistor of **38** nanosheets [Figure 1.1.13e and f, reproduced from ref. 50].

Recently our group investigated the self-assembly of amphiphilic OPV chromophores for improved electronic functions (Figure 1.1.13a-c).⁴⁸ For this purpose, OPV chromophore is asymmetrically functionalized with tetraethylene glycol and hydrophobic alkyl chains (Figure 1.1.13a). In THF-water mixture, **37** self-assemble into 2D sheets through a combination of π - π and solvophobic interactions with well defined supramolecular ordering between the chromophores (Figure 1.1.13b). As a result, these nanosheets shows hole mobility up to $0.008 \text{ cm}^2/\text{V}\cdot\text{s}$ which is three orders magnitude higher than non-amphiphilic OPV assemblies (Figure 1.1.13c).⁴⁹ Similar design was also reported by Pei et al. for a butterfly shaped thiophene derivative (**38**) which also self-assembles into free standing nanosheets in chloroform-methanol mixtures and exhibit hole mobility as high as $0.02 \text{ cm}^2/\text{V}\cdot\text{s}$ (Figure 1.1.13d-f).⁵⁰ We further extended this amphiphilic approach to new n-type coronene bisimide based nanostructures,

with efficient electron transport properties which are discussed in Part-2.1 of this thesis.

1.1.3 Mixed Stack Charge-Transfer D-A Assemblies

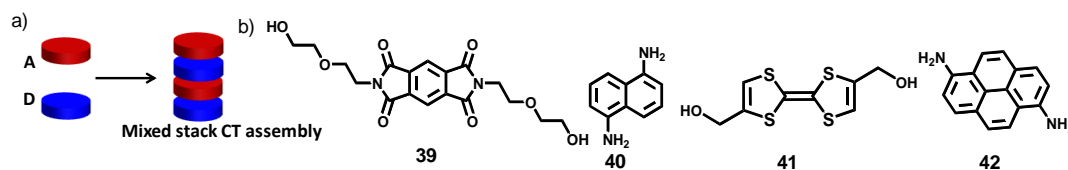


Figure 1.1.14. a) Schematic representation showing the face-to-face orientation of D and A in mixed stack CT assembly. b) Molecular structures of A (**39**) and D (**40-42**) molecules that show room temperature ferroelectricity in their MS-CT crystal state.

Mixed stack (MS) charge-transfer (CT) assemblies,⁵¹ in which D and A molecules are organized in a face-to-face manner, have attracted attention in recent years due to their applications in optoelectronic and ferroelectric materials (Figure 1.1.14a). On the other hand, one-dimensional (1D) supramolecular nanowires obtained by the self-assembly of single component π -conjugated oligomers showed significant charge transport only after external doping (*vide supra*). In this context, 1D stacks of MS-CT complexes from the co-assembly of D and A molecules have gathered immense attention since this concept would furnish highly conducting nanowires through inherent doping and hence can be a viable tool for nanoelectronics. Although rich amount of literature exists on MS-CT crystals in last four decades, only recent attempts have been focused on their optoelectronic functions. In this session, we focus on the ferroelectric and optoelectronic functions of MS-CT assemblies reported recently.

MS-CT crystals exhibiting strong CT interactions are proposed as potential candidates for ferroelectric applications owing to their ability to show displacive-type ferroelectricity.⁵² One dimensional (1D) ferroelectricity was first observed in MS-CT complexes of tetrathiafulvalene (TTF) with *p*-bromanil⁵³ or *p*-chloranil.⁵⁴ However, these complexes show ferroelectric transition only under cryogenic conditions. With an elegant molecular design, Stupp et al. synthesized MS-CT crystals that can show ferroelectric polarization switching at room temperature.⁵⁵ These are made from pyromellitic diimide (**39**) based acceptor and TTF/naphthalene/pyrene (**40-42**) based donors in which 1D D-A stacks are interconnected by H-bonding interactions.

On the other hand, Brédas et al. predicted high ambipolar mobility in MS-CT crystals using density functional theory calculations and mixed quantum/classical dynamics simulations.⁵⁶ They propose that, similar charge transport characteristics of hole and electron along D-A stacking directions are responsible for their ambipolar charge transport while

featuring them as potential candidates for organic electronics. This is quite remarkable because high mobilities in organic polymers or self-assembled nanostructures of π -systems have been achieved majorly through external doping which is often tedious and may not be uniform throughout the sample.⁵⁷ Experimental reports on various MS-CT-pairs indeed showed enhanced charge transport in their CT state. Saito et al. first experimentally showed the metallic conductivity in the MS-CT crystals formed between tellurafulvalene (**43**) donor and diethyltetracyanoquinodimethane (DE-TCNQ, **44**) acceptor (Figure 1.1.15a).⁵⁸ Interestingly, Brédas's prediction of ambipolar mobility is experimentally proved in MS-CT crystals of various D-A pairs, investigated in recent years. For example, high ambipolar mobility ($\mu_h = 0.13 \text{ cm}^2/\text{V}\cdot\text{s}$ and $\mu_e = 0.04 \text{ cm}^2/\text{V}\cdot\text{s}$) are observed in MS-CT crystalline microrods of dibenzotetrathiafulvalene (**45**) and TCNQ (**46**) pair (Figure 1.1.15a).⁵⁹ Similarly, Wakahara et al. reported MS-CT crystalline nanosheets composed of C_{60} (**48**) and ferrocene or cobalt porphyrin (**47**) (Figure 1.1.15a and b).⁶⁰ Nanosheets of latter CT pair showed ambipolar mobility of $10^{-5} \text{ cm}^2/\text{V}\cdot\text{s}$ and $10^{-6} \text{ cm}^2/\text{V}\cdot\text{s}$ for holes and electrons respectively (Figure 1.1.15c).

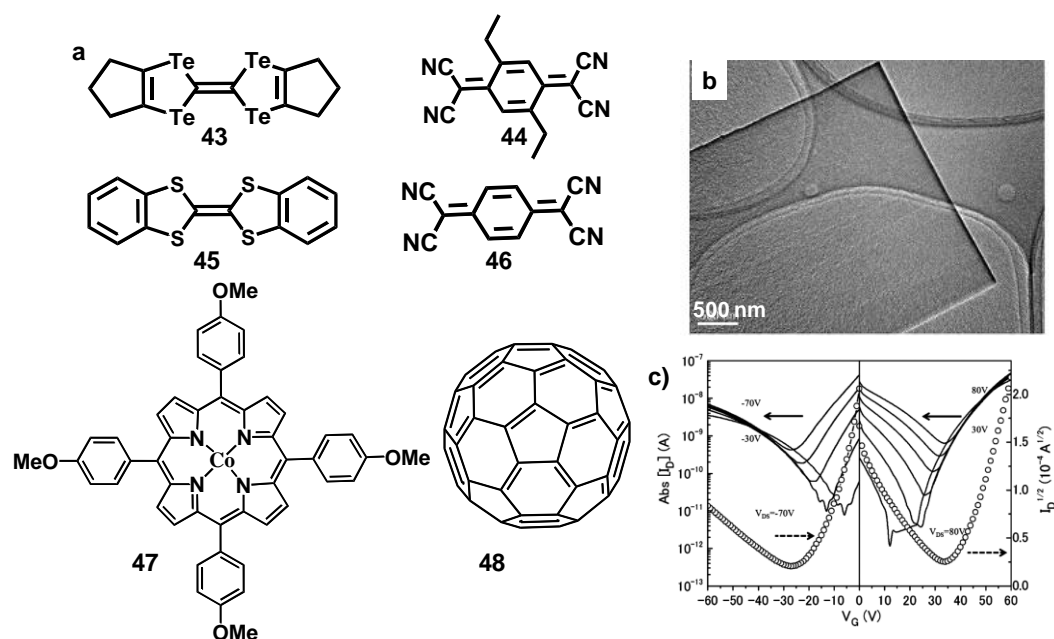


Figure 1.1.15. a) Molecular structures of various D (**43**, **45** and **47**) and A (**44**, **46** and **48**) molecules. b) TEM image of a single crystalline nanosheet of **47** and **48** CT complex. c) The transfer characteristics of **47-48** nanosheets in the dark for positive and negative gate biases. The solid lines show the drain current versus gate voltage for various V_{DS} , and the open symbols show the square root of drain current [Figure 1.1.15b and c, reproduced from ref. 60a].

Interestingly, MS-CT crystals of distyrylbenzene (**49**) and dicyanodistyrylbenzene (**50**) chromophores reported by Park et al. showed much higher ambipolar mobility ($\mu_h = 0.0067 \text{ cm}^2/\text{V}\cdot\text{s}$ and $\mu_e = 0.067 \text{ cm}^2/\text{V}\cdot\text{s}$) than C_{60} -cobalt porphyrin system with remarkable luminescent properties (Figure 1.1.16a-c).⁶¹ The CT complex emission is red shifted than individual D or A

molecules emission with a quantum yield of 0.31. Authors attribute this high fluorescence of CT complex to the non-negligible oscillator strength of S_1 state and low non-radiative decay in the CT crystal state. Wilson et al. also observed strong fluorescence from aqueous suspensions/solid-state powders of MS-CT complexes formed between hydrophobic naphthalene diimide (NDI) derivative (**51**) and various π -conjugated D molecules (**52-57**) which are non fluorescent in organic solvents (Figure 1.1.16d and e).⁶² Moreover, the CT emission is more red-shifted compared to the individual D or A emissions and can be tuned by changing the energy of the HOMO of the D molecules (Figure 1.1.16e). Authors proposed that exclusion of solvent from D-A molecules is the main driving force for fluorescent CT complex formation in water or solid-state. These fluorescent CT complexes self-assemble in water into nanoparticles which are further exploited for bio-imaging owing to their emission above 550 nm. Similarly, Lee et al. synthesized luminescent crystalline microtubes utilizing MS-CT interactions of tetracyanobenzene (**60**) with various π -conjugated molecules (**58** and **59**) (Figure 1.1.17a).⁶³ In this case, authors attribute CT emission to aggregation-induced emission enhancement (AIEE) effect. Interestingly, by doping **60** and **58** CT microtubes with different concentrations of **59**, tunable solid-state emission including white light was achieved due to controlled energy transfer from TCNB-naphthalene (blue emission) CT state to TCNQ-pyrene (yellow emission) CT state (Figure 1.1.17b-d).^{63a} In an interesting study, Pei et al. reported the luminescent photoconductive crystalline CT microwires composed of truxene (D, **61**) and truxenone (A, **62**) derivatives (Figure 1.1.17e-g).⁶⁴ Though this pair shows ground state CT interactions, orientation of D and A molecules in these microwires is not well documented.

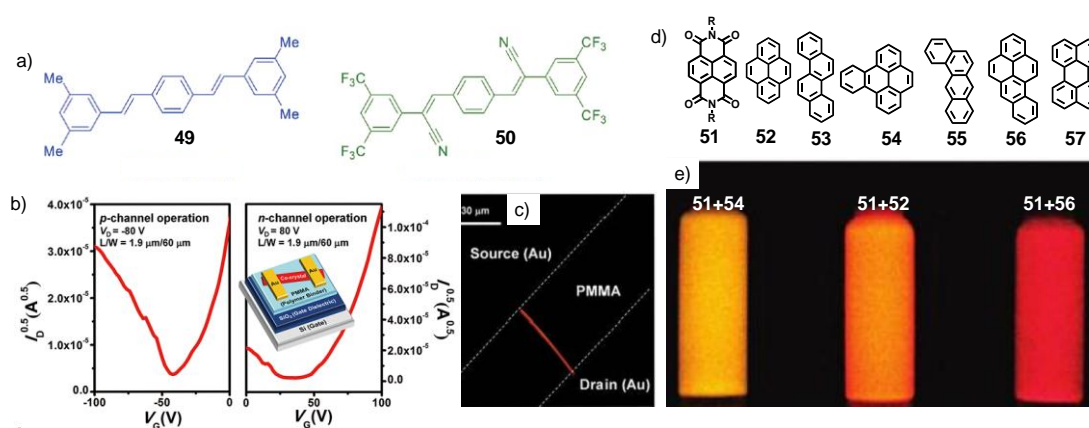


Figure 1.1.16. a) Chemical structures of D (**49**) and A (**50**) molecules studied by Park et al. b) Transfer and output characteristics of the **49-50** single CT crystal OFET, fabricated by solvent vapor annealing. Inset shows the schematic drawing of the device. c) Optical microscope image of a single-crystal OFET under UV light [Figure 1.1.16a-c, reproduced from ref. 61]. d) Chemical structures of naphthalene diimide A (**51**) and various polyaromatic D (**52-57**) molecules. R = isoamyl. e) Photographs of particle dispersions of CT complexes of **51** with various pyrene derivatives (**52**, **54** and **56**) under 365 nm UV light irradiation [reproduced from ref. 62].

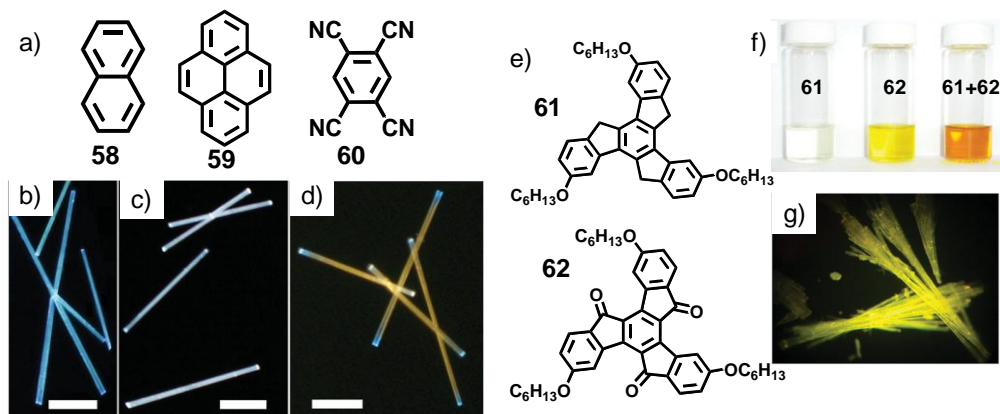


Figure 1.1.17. a) Molecular structures of D (**58** and **59**) and A (**60**) molecules used in the synthesis of luminescent CT microtubes. Fluorescence microscopy images of mixed **58** and **60** CT complex microtubes with a doping concentration of b) 0, c) 0.015%, and d) 0.1% of **59** excited with unfocused UV light (330–380 nm) [Figure 1.1.17b-d, reproduced from ref. 63a]. All scale bars are 30 μm . e) Molecular structures of truxene (**61**) and truxenone (**62**) derivatives and f) the photographs of **61**, **62** and their 1:1 mixture in CH_2Cl_2 . g) Fluorescence microscopy images of CT microwires of **61** and **62** precipitated from hexane [Figure 1.1.17f and g, reproduced from ref. 64b].

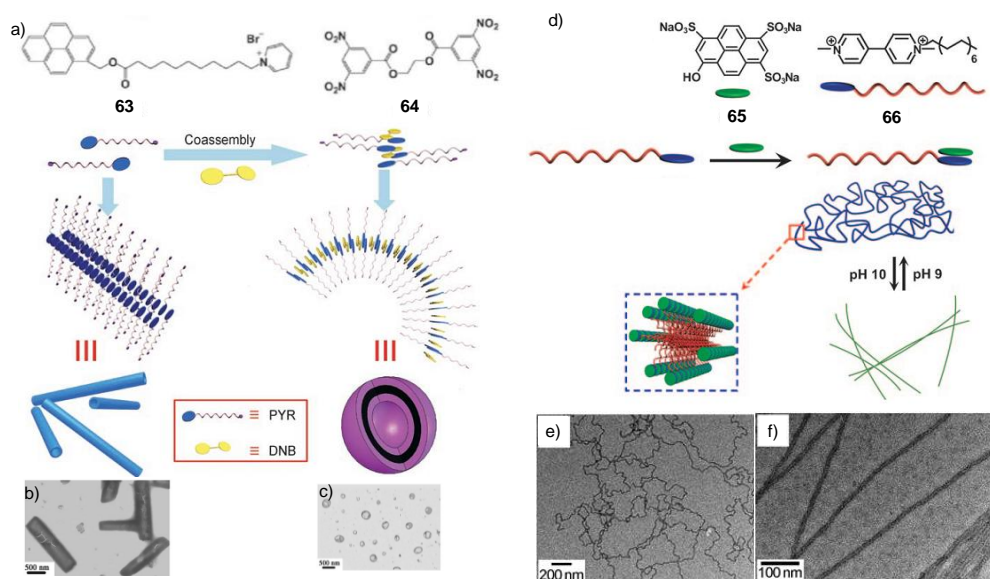


Figure 1.1.18. a) Molecular structures of pyrene derived D (**63**) and nitro derived A (**64**) and schematic representation of the transformation of **63** from b) tubes to c) vesicles due to CT interactions [Figure 1.1.18a-c, reproduced from ref. 67]. d) Molecular structures of anionic D (**65**) and cationic A (**66**) and schematic representation of the preparation of the pH-responsive nanofibers through self-assembly of **65-66** supramolecular amphiphile. TEM images of **65-66** amphiphile in e) pH 9 buffer and in f) pH 10 buffer solution [Figure 1.1.18d-f, reproduced from ref. 68].

Despite having interesting optoelectronic functions, CT crystals/microwires are very difficult to process for thin film based large area device fabrication. To address this issue Percec et al. investigated the optoelectronic functions of various dendrimer attached D-A CT

complexes in their liquid crystalline (LC) state.⁶⁵ Remarkably, LC state of these CT complexes exhibits good electron and hole mobility which are two to five orders of magnitude higher than their amorphous state and better than many conjugated polymers. On the other hand, recent advances in self-assembly resulted in the non-covalent synthesis of 1D nanowires having MS-CT D-A organization (Figure 1.1.18). In this context, Zhang et al. extensively investigated the self-assembly and morphological features of various D-A supra-amphiphiles in water (Figure 1.1.18 and 1.1.19).⁶⁶ Zhang et al. observed that, when amphiphilic pyrene (**63**) derivative treated with electron deficient nitro (**64**) derivative, it forms a supramolecular CT amphiphile with self-assembly and morphological features that are completely different from homotropic assembly of pyrene donor (Figure 1.1.18a-c).⁶⁷ When this design was extended to anionic pyrene derivatives (**65**) and viologen (**66**), the resultant CT complex self-assembled in water like classical surfactants and formed wormlike like micelles whose stiffness can be tuned with pH (Figure 1.1.18d-f).⁶⁸ Latter this design was extended to alkoxy naphthol (**67**) and naphthalene diimide (**68**) CT pair and control over dimensionality of morphologies such as 2D nanosheets and 1D nanofibers of these CT amphiphiles was achieved by changing the size and shape of D/A molecule and through introduction of dual CT interactions with pyrene donor (**65**) (Figure 1.1.19).⁶⁹ However, performance of these soft CT nanostructures on devices is not yet known.

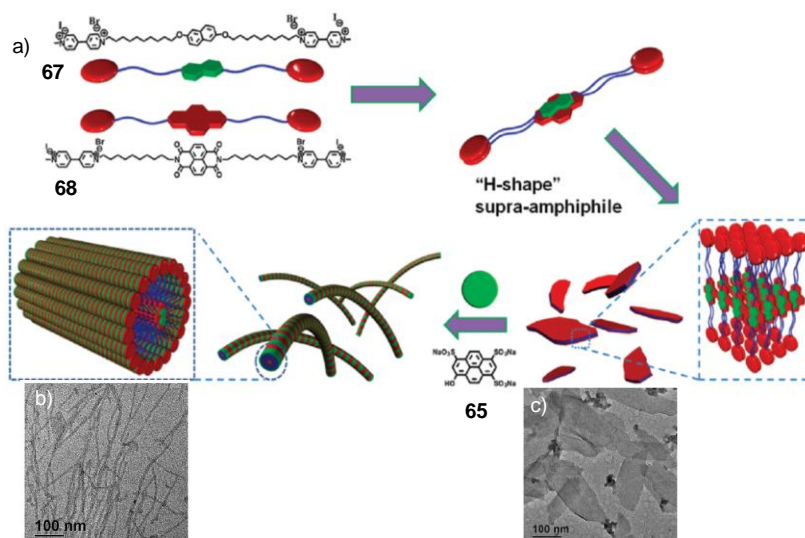


Figure 1.1.19. a) Molecular structures of D (**67** and **65**) and A (**68**) molecules and schematic representation of the rational fabrication and programmable evolution of well-defined nanofibers and nanosheets by supramolecular engineering of supra-amphiphiles having dual CT interactions. TEM images of b) **67-68-65** mixed CT nanofibers and b) **67-68** CT nanosheets in pH 9 buffer solution [reproduced from ref. 69c].

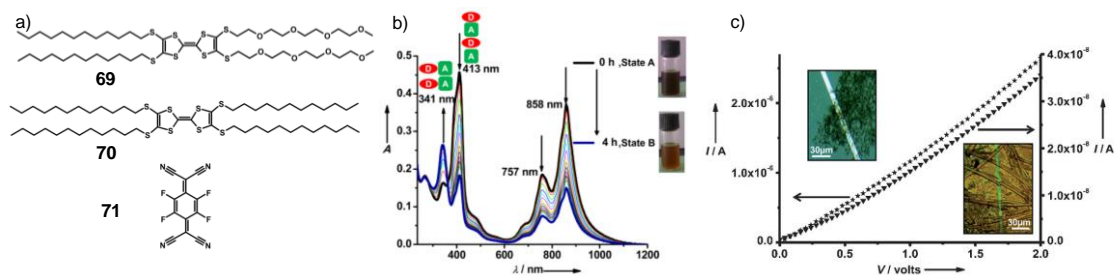


Figure 1.1.20. a) Molecular structures of TTF donor (**69** and **71**) derivatives and F_4TCNQ acceptor (**70**). b) Time-dependent UV/Vis spectra of 1:1 mixture of **70** and **71** in 50% chloroform-methanol solvent mixture (0.1 mM). Inset shows the photo-graph of solution color changes of CT complex at 0 and 4 h. c) I–V curves of state A (star) and state B (triangle) respectively. Inset shows the respective optical microscopy images (transmittance mode) of the nanostructures between the gold electrodes [reproduced from ref. 70].

We have recently investigated the supramolecular self-assembly of non-covalent CT complexes of amphiphilic (**69**) and hydrophobic (**70**) TTF derivatives with F_4TCNQ (**71**) (Figure 1.1.20a).⁷⁰ In case of amphiphilic TTF (**69**), we have observed a morphology transition from spherical particles to nanorods upon co-assembly with **71**. On the other hand, **70** alone form nanofibers in chloroform-methanol mixture which is retained in its CT complex state with **71**. Interestingly, the latter CT complex showed spontaneous molecular reorganization between D and A molecules from MS (state A) to segregated (state B) stacks within 4 h owing to their dynamic behaviour (Figure 1.1.20b). Two probe electrical measurements on these CT fibers in both states showed conductivity in the order of 10^{-5} S/cm (Figure 1.1.20c). Latter, we have achieved MS-CT 1D nanostructures having high mobility/conductivity with improved molecular design of D and A molecules which are discussed in Part-3.1 of this thesis. Moreover, MS-CT interactions are also extensively utilized by Scherman et al. for supramolecular cross-linking of covalent polymers to create stimuli responsive supramolecular materials.⁷¹

1.1.4 Conclusions and Outlook

In conclusion, amphiphilic and MS-CT strategies are proved to be very useful to improve the optoelectronic functions of self-assembled π -systems. However, only few π -conjugated oligomers and polymers⁷² have been investigated in this direction and amphiphilic self-assembly can be extended to many potential π -systems. Most of the photovoltaic devices investigated so far were with non-amphiphilic π -conjugated oligomers/polymers and we believe that introducing amphiphilic interactions to these molecules can improve the morphology of active layers and thereby an increase in their photo-conversion efficiency. In addition, MS-CT combined with amphiphilic interactions can adopt the benefits from both the approaches and

can yield well defined self-assembled nanostructures with excellent charge-transport properties.

1.1.5 References

1. C. D. Dimitrakopoulos, P. R. L. Malenfant, *Adv. Mater.* **2002**, *14*, 99; b) D. Braun, *Mater. Today* **2002**, *5*, 32; c) R. H. Friend, R. W. Gymer, A. B. Holmes, J. H. Burroughes, R. N. Marks, C. Taliani, D. D. C. Bradley, D. A. dos Santos, J.-L. Brédas, M. Löglund, W. R. Salaneck, *Nature* **1999**, 397, 121-128; d) A. O. Patil, A. J. Heeger, F. Wudl, *Chem. Rev.* **1988**, *88*, 183; e) Kraft, A.; Grimsdale, A. C.; Holmes, A. B. *Angew. Chem. Int. Ed.* **1998**, *37*, 402-428; f) A. C. Grimsdale, K. L. Chan, R. E. Martin, P. G. Jokisz, A. B. Holmes, *Chem. Rev.* **2009**, *109*, 897.
2. F. J. M. Hoeben, P. Jonkheijm, E. W. Meijer, A. P. H. J. Schenning, *Chem. Rev.* **2005**, *105*, 1491.
3. a) E. W. Meijer, A. P. H. J. Schenning, *Nature* **2002**, *419*, 353; b) J.-M. Lehn, *Science* **2002**, *295*, 2400; c) G. M. Whitesides, B. Grzybowski, *Science* **2002**, *295*, 2418; d) T. Aida, E. W. Meijer, S. I. Stupp, *Science* **2012**, *335*, 813; d) E. Moulin, G. Cormos, N. Giuseppone, *Chem. Soc. Rev.* **2012**, *41*, 1031.
4. a) E. Moulin, F. Niess, M. Maaloum, E. Buhler, I. Nyrkova, N. Giuseppone, *Angew. Chem. Int. Ed.* **2010**, *49*, 6974; b) V. Faramarzi, F. Niess, E. Moulin, M. Maaloum, J.-F. Dayen, J.-B. Beaufrand, S. Zanettini, B. Doudin, N. Giuseppone, *Nat. Chem.* **2012**, *4*, 485; c) Y.-Y. Noh, J.-J. Kim, Y. Yoshida, K. Yase, *Adv. Mater.* **2003**, *15*, 699; d) X. L. Chen, A. J. Lovinger, Z. Bao, J. Sapjeta, *Chem. Mater.* **2001**, *13*, 1341.
5. E. Moulin, J.-J. Cid, N. Giuseppone, *Adv. Mater.* **2013**, *25*, 47787.
6. a) A. Ajayaghosh, V. K. Praveen, *Acc. Chem. Res.* **2007**, *40*, 644; b) A. Mishra, C.-Q. Ma, P. Bäuerle, *Chem. Rev.* **2009**, *109*, 1141.
7. a) F. Würthner, *Chem. Commun.* **2004**, 1564; b) M. R. Wasielewski, *Acc. Chem. Res.* **2009**, *42*, 1910.
8. a) H. Usta, A. Facchetti, T. J. Marks, *Acc. Chem. Res.*, **2011**, *44*, 501–510; b) R. R. Reghu, Hari K. Bisoyi, J. V. Grazulevicius, P. Anjukandi, V. Gaidelis, V. Jankauskas, *J. Mater. Chem.* **2011**, *21*, 7811.
9. S. Rajaram, R. Shivanna, S. K. Kandappa, K. S. Narayan, *J. Phys. Chem. Lett.* **2012**, *3*, 2405.
10. a) T. Seki, X. Lin, S. Yagai, *Asian J. Org. Chem.* **2013** (DOI: 10.1002/ajoc.201300025); b) Z. Chen, A. Lohr, C. R. Saha-Möller, F. Würthner, *Chem. Soc. Rev.* **2009**, *38*, 564.
11. D. Görl, X. Zhang, F. Würthner, *Angew. Chem. Int. Ed.* **2012**, *51*, 6328.
12. a) T. E. Kaiser, H. Wang, V. Stepanenko, F. Würthner, *Angew. Chem. Int. Ed.* **2007**, *46*, 5541–5544; b) X.-Q. Li, V. Stepanenko, Z. Chen, P. Prins, L. D. A. Siebbeles, F.

- Würthner, *Chem. Commun.* **2006**, 3871; c) F. Würthner, C. Bauer, V. Stepanenko, S. Yagai, *Adv. Mater.* **2008**, *20*, 1695.
13. I. K. Iverson, S.-W. Tam-Chang, *J. Am. Chem. Soc.* **1999**, *121*, 5801.
 14. K. Balakrishnan, A. Datar, R. Oitker, H. Chen, J. Zuo, L. Zang, *J. Am. Chem. Soc.* **2005**, *127*, 10496.
 15. Y. Che, A. Datar, X. Yang, T. Naddo, J. Zhao and L. Zang, *J. Am. Chem. Soc.* **2007**, *129*, 6354.
 16. Y. Che, A. Datar, K. Balakrishnan, L. Zang, *J. Am. Chem. Soc.* **2007**, *129*, 7234.
 17. X. Zhang, Z. Chen, F. Würthner, *J. Am. Chem. Soc.* **2007**, *129*, 4886.
 18. X. Zhang, S. Rehm, M. M. Safont-Sempere, F. Würthner, *Nat. Chem.* **2009**, *1*, 623.
 19. a) Y. Liu, K.-R. Wang, D.-S. Guo, B.-P. Jiang, *Adv. Funct. Mater.* **2009**, *19*, 2230; b) B.-P. Jiang, D.-S. Guo, Y. Liu, *J. Org. Chem.* **2010**, *75*, 7258.
 20. E. Krieg, B. Rybtchinski, *Chem. Eur. J.* **2011**, *17*, 9016.
 21. E. Krieg, H. Weissman, E. Shirman, E. Shimoni, B. Rybtchinski, *Nat. Nanotechnol.* **2011**, *6*, 141.
 22. C. Shahar, J. Baram, Y. Tidhar, H. Weissman, S. R. Cohen, I. Pinkas, B. Rybtchinski, *ACS Nano*, **2013**, *7*, 3547.
 23. E. Engel, K. Leo, M. Hoffmann, *Chem. Phys.* **2006**, *325*, 170.
 24. P. K. Sukul, D. Asthana, P. Mukhopadhyay, D. Summa, L. Muccioli, C. Zannoni, D. Beljonne, A. E. Rowan, S. Malik, *Chem. Commun.* **2011**, *47*, 11858.
 25. P. K. Sukul, P. K. Singh, S. K. Maji, S. Malik, *J. Mater. Chem. B*, **2013**, *1*, 153.
 26. G. S. Vadehra, B. D. Wall, S. R. Diegelmann, J. D. Tovar, *Chem. Commun.* **2010**, *46*, 3947.
 27. a) S. Roy, D. K. Maiti, S. Panigrahi, D. Basak, A. Banerjee, *RSC Adv.* **2012**, *2*, 11053; b) D. K. Maiti, A. Banerjee, *Chem. Commun.* **2013** (DOI: 10.1039/C3CC43371D).
 28. Y. Sun, C. He, K. Sun, Y. Li, H. Dong, Z. Wang, Z. Li, *Langmuir* **2011**, *27*, 11364.
 29. T. Heek, C. Easting, C. Rest, X. Zhang, F. Würthner, R. Haag, *Chem. Commun.* **2010**, *46*, 1884.
 30. S. Rehm, V. Stepanenko, X. Zhang, T. H. Rehm, F. Wrthner, *Chem. Eur. J.* **2010**, *16*, 3372.
 31. F. Biedermann, E. Elmalem, I. Ghosh, W. M. Nau, O. A. Scherman, *Angew. Chem. Int. Ed.* **2012**, *51*, 7739.
 32. M. D. Watson, A. Fechtenkötter, K. Müllen, *Chem. Rev.* **2001**, *101*, 1267.
 33. a) J. P. Hill, W. Jin, A. Kosaka,; T. Fukushima, H. Ichihara, T. Shimomura, K. Ito, T. Hashizume, N. Ishii, T. Aida, *Science*, **2004**, *304*, 1481; b) W. Jin, Y. Yamamoto, T.

- Fukushima, N. Ishii, J. Kim, K. Kato, M. Takata, T. Aida, *J. Am. Chem. Soc.* **2008**, *130*, 9434.
34. Y. Yamamoto, T. Fukushima, W. Jin, A. Kosaka, T. Hara, T. Nakamura, A. Saeki, S. Seki, S. Tagawa, T. Aida, *Adv. Mater.* **2006**, *18*, 1297.
35. a) W. Jin, T. Fukushima, M. Niki, A. Ko-saka, N. Ishii, T. Aida, *Proc. Natl. Acad. Sci. USA* **2005**, *102*, 10801; b) Y. Yamamoto, T. Fukushima, Y. Suna, N. Ishii, A. Saeki, S. Seki, S. Tagawa, M. Taniguchi, T. Kawai, T. Aida, *Science* **2006**, *314*, 1761; c) Y. Yamamoto, T. Fukushima, A. Saeki, S. Seki, S. Tagawa, N. Ishii, Aida, *J. Am. Chem. Soc.* **2007**, *129*, 9276.
36. A. Saeki, Y. Koizumi, T. Aida, S. Seki, *Acc. Chem. Res.* **2012**, *45*, 1193.
37. W.-S. Li, Y. Yamamoto, T. Fukushima, A. Saeki, S. Seki, S. Tagawa, H. Masunaga, S. Sasaki, M. Takata, T. Aida, *J. Am. Chem. Soc.* **2008**, *130*, 8886.
38. Y. Hizume, K. Tashiro, R. Charvet, Y. Yamamoto, A. Saeki, S. Seki, T. Aida, *J. Am. Chem. Soc.* **2010**, *132*, 6628–6629; b) R. Charvet, Y. Yamamoto, T. Sasaki, J. Kim, K. Kato, M. Takata, A. Saeki, S. Seki, T. Aida, *J. Am. Chem. Soc.* **2012**, *134*, 2524.
39. W.-S. Li, A. Saeki, Y. Yamamoto, T. Fukushima, S. Seki, N. Ishii, K. Kato, M. Takata, T. Aida, *Chem. Asian J.* **2010**, *5*, 1566.
40. M.-C. Yeh, Y.-L. Su, M.-C. Tzeng, C. W. Ong, T. Kajitani, H. Enozawa, M. Takata, Y. Koizumi, A. Saeki, S. Seki, T. Fukushima, *Angew. Chem. Int. Ed.* **2013**, *52*, 1031;
41. W. Zhang, W. Jin, T. Fukushima, A. Saeki, S. Seki, T. Aida, *Science*, **2011**, *334*, 340.
42. a) M. R. Robinson, S. J. Wang, A. J. Heeger, G. C. Bazan, *Adv. Funct. Mater.* **2001**, *11*, 413; b) Goodson, T. Li, W. Gharavi, A. Yu, L. *Adv. Mater.* **1997**, *9*, 639; c) V. Gebhardt, A. Bacher, M. Thelakkat, U. Stalmach, H. Meier, H.-W. Schmidt, D. Haarer, *Synth. Met.* **1997**, *90*, 123.
43. J. F. Hulvat, M. Sofos, K. Tajima, S. I. Stupp, *J. Am. Chem. Soc.* **2005**, *127*, 366.
44. a) F. J. M. Hoeben, I. O. Shklyarevskiy, M. J. Pouderoijen, H. Engelkamp, A. P. H. J. Schenning, P. C. M. Christianen, J. C. Maan, E. W. Meijer, *Angew. Chem. Int. Ed.* **2006**, *45*, 1232; b) S. J. George, T. F. A. de Greef, R. Bovee, van J. L. J. Dongen, A. P. H. J. Schenning, E. W. Meijer, *Chem. Asian J.* **2009**, *4*, 910.
45. a) A. Ajayaghosh, S. J. George, V. K. Praveen, *Angew. Chem. Int. Ed.* **2003**, *42*, 332; i) K. Sugiyasu, N. Fujita, S. Shinkai, *Angew. Chem. Int. Ed.* **2004**, *43*, 1229; b) A. D. Guerso, A. G. L. Olive, J. Reichwagen, H. Hopf, J.-P. Desvergne, *J. Am. Chem. Soc.* **2005**, *127*, 17984; c) A. Ajayaghosh, V. K. Praveen, C. Vijayakumar, S. J. George, *Angew. Chem. Int. Ed.* **2007**, *46*, 6260; d) A. Ajayaghosh, C. Vijayakumar, V. K. Praveen, S. S. Babu, R. Varghese, *J. Am. Chem. Soc.* **2006**, *128*, 7174; e) A. Ajayaghosh, V. K. Praveen, S.

- Srinivasan, R. Varghese, *Adv. Mater.* **2007**, *19*, 411; f) A. Ajayaghosh, V. K. Praveen, C. Vijayakumar, *Chem. Soc. Rev.* **2008**, *37*, 109.
46. R. Matmour, I. De Cat, S. J. George, W. Adriaens, P. Leclère, P. H. H. Bomans, N. A. J. M. Sommerdijk, J. C. Gielen, P. C. M. Christianen, J. T. Heldens, J. C. M. van Hest, D. W. P. M. Löwik, S. De Feyter, E. W. Meijer, A. P. H. J. Schenning, *J. Am. Chem. Soc.* **2008**, *130*, 14576.
47. B.D. Wall, S. R. Diegelmann, S. Zhang, T. J. Dawidczyk, W. L. Wilson, H. E. Katz, H.-Q. Mao, J. D. Tovar, *Adv. Mater.* **2011**, *23*, 5009.
48. B. Narayan, S. P. Senanayak, A. Jain, K. S. Narayan, S. J. George, *Adv. Funct. Mater.* **2013**, (DOI: 10.1002/adfm.201202298).
49. a) P. Jonkheijm, N. Stutzmann, Z. Chen, D. M. de Leeuw, E. W. Meijer, A. P. H. J. Schenning, F. Würthner, *J. Am. Chem. Soc.* **2006**, *128*, 9535; b) M. Mas-Torrent, P. Hadley, P. Jonkheijm, A. P. H. J. Schenning, E. W. Meijer, S. George, A. Ajayaghosh, *J. Chem. Phys.* **2006**, *124*, 154704.
50. J. Yin, Y. Zhou, T. Lei, J. Pei, *Angew. Chem. Int. Ed.* **2011**, *50*, 6320.
51. a) V. Balzani, M. G-Lopez, J. F. Stoddart, *Acc. Chem. Res.* **1998**, *31*, 405; b) C. A. Schalley, K. Beizai, F. Vögtle, *Acc. Chem. Res.* **2001**, *34*, 465.
52. S. Horiuchi, Y. Tokura, *Nat. Mater.* **2008**, *7*, 357.
53. Y. Tokura, S. Koshihara, Y. Iwasa, H. Okamoto, T. Komatsu, T. Koda, N. Iwasawa, G. Saito, *Phys. Rev. Lett.* **1989**, *63*, 2405.
54. H. Okamoto, T. Mitani, Y. Tokura, S. Koshihara, T. Komatsu, Y. Iwasa, T. Koda, G. Saito, *Phys. Rev. B* **1991**, *43*, 8224.
55. A. S. Tayi, A. K. Shveyd, A. C.-H. Sue, J. M. Szarko, B. S. Rolczynski, D. Cao, T. J. Kennedy, A. A. Sarjeant, C. L. Stern, W. F. Paxton, W. Wu, S. K. Dey, A. C. Fahrenbach, J. R. Guest, H. Mohseni, L. X. Chen, K. L. Wang, J. F. Stoddart, S. I. Stupp, *Nature* **2012**, *488*, 485.
56. L. Zhu, Y. Yi, Y. Li, E.-G. Kim, V. Coropceanu, J.-L. Brédas, *J. Am. Chem. Soc.* **2012**, *134*, 2340.
57. a) C. K. Chiang, M. A. Druy, S. C. Gau, A. J. Heeger, E. J. Louis, A. G. MacDiarmid, Y. W. Park, H. Shirakawa, *J. Am. Chem. Soc.*, **1978**, *100*, 1013; b) J. Puigmartí-Luis, V. Laukhin, Á. P. del Pino, J. Vidal-Gancedo, C. Rovira, E. Laukhina, D. B. Amabilino, *Angew. Chem. Int. Ed.* **2007**, *46*, 38.
58. G. Saito, S.-S. Pac, O. O. Drozdova, *Synthetic Metals*, **2001**, *120*, 667.
59. H.-D. Wu, F.-X. Wang, Y. Xiao, G.-B. Pan, *J. Mater. Chem. C*, **2013**, *1*, 2286.
60. a) T. Wakahara, P. D'Angelo, K. Miyazawa, Y. Nemoto, O. Ito, N. Tanigaki, D. D.C. Bradley, T. D. Anthopoulos, *J. Am. Chem. Soc.* **2012**, *134*, 7204; b) T. Wakahara, M.

- Sathish, K. Miyazawa, C. Hu, Y. Tateyama, Y. Nemoto, T. Sasaki, O. Ito, *J. Am. Chem. Soc.* **2009**, *131*, 9940.
61. S. K. Park, S. Varghese, J. H. Kim, S.-J. Yoon, O. K. Kwon, B.-K. An, J. Gierschner, S. Y. Park, *J. Am. Chem. Soc.* **2013**, *135*, 4757.
62. M. D. Gujrati, N. S. S. Kumar, A. S. Brown, B. Captain, J. N. Wilson, *Langmuir* **2011**, *27*, 6554.
63. Y.-Y. Lei, Y. Jin, D.-Y. Zhou, W. Gu, X.-B. Shi, L.-S. Liao, S.-T. Lee, *Adv. Mater.* **2012**, *39*, 5345; b) Y. L. Lei, L.-S. Liao, S.-T. Lee, *J. Am. Chem. Soc.* **2013**, *135*, 3744.
64. a) J. Luo, L. Chen, J.-Y. Wang, T. Lei, L.-Y. Li, J. Pei, Y. Song, *New J. Chem.* **2010**, *34*, 2530; b) J.-Y. Wang, J. Yan, L. Ding, Y. Ma, J. Pei, *Adv. Funct. Mater.* **2009**, *19*, 1746.
65. V. Percec, M. Glodde, T. K. Bera, Y. Miura, I. Shiyonovskaya, K. D. Singer, V. S. K. Balagurusamy, P. A. Heiney, I. Schne, A. Rapp, H.-W. Spiess, S. D. Hudson, H. Duan, *Nature* **2002**, *419*, 384.
66. a) C. Wang, Z. Wang, X. Zhang, *Acc. Chem. Res.* **2012**, *45*, 608; b) X. Zhang, C. Wang, *Chem. Soc. Rev.* **2011**, *40*, 94.
67. C. Wang, S. Yin, S. Chen, H. Xu, Z. Wang, X. Zhang, *Angew. Chem. Int. Ed.* **2008**, *47*, 9049.
68. C. Wang, Y. Guo, Y. Wang, H. Xu, R. Wang, X. Zhang, *Angew. Chem. Int. Ed.* **2009**, *48*, 8962.
69. a) K. Liu, C. Wang, Z. B. Li, X. Zhang, *Angew. Chem. Int. Ed.* **2011**, *50*, 4952; b) K. Liu, Y. Yao, C. Wang, Y. Liu, Z. Li, X. Zhang, *Chem. Eur. J.* **2012**, *18*, 8622; c) K. Liu, Y. Yao, Y. Liu, C. Wang, Z. Li, X. Zhang, *Langmuir*, **2012**, *28*, 10697.
70. A. Jain, K. V. Rao, U. Mogera, A. A. Sagade, S. J. George, *Chem. Eur. J.* **2011**, *17*, 12355.
71. a) U. Rauwald, O. A. Scherman, *Angew. Chem. Int. Ed.* **2008**, *47*, 3950; b) E. A. Appel, F. Biedermann, U. Rauwald, S. T. Jones, J. M. Zayed, O. A. Scherman, *J. Am. Chem. Soc.* **2010**, *132*, 14251; c) E. A. Appel, X. J. Loh, S. T. Jones, F. Biedermann, C. A. Dreiss, O. A. Scherman, *J. Am. Chem. Soc.* **2012**, *134*, 11767.
72. C. Kanimozhi, N. Yaacobi-Gross, K. W. Chou, A. Amassian, T. D. Anthopoulos, S. Patil, *J. Am. Chem. Soc.* **2012**, *134*, 16532.

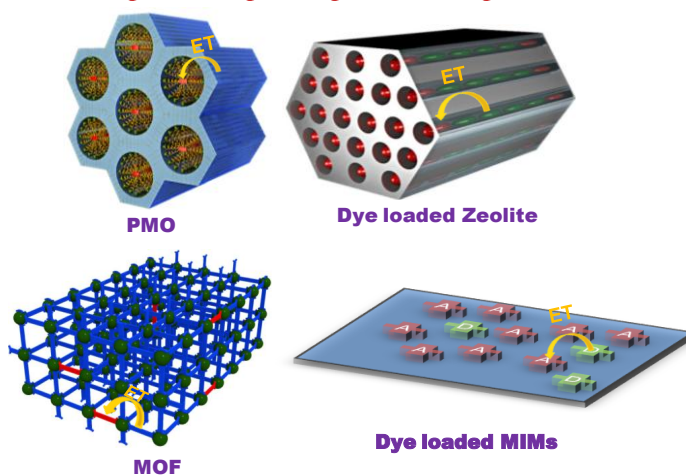
PART-1.2

Organic-Inorganic Light-Harvesting Scaffolds for Luminescent Hybrids

Abstract

In this section, a brief overview on organic-inorganic light-harvesting scaffolds for solid-state luminescence applications is provided. Luminescent light-harvesting organic-inorganic hybrid materials form a curious field not only because of its potential to deal with a variety of device related challenges but also because it breaks new ground with the current trend of merging both organic and inorganic functionality. This section is majorly focused on design principles and luminescence properties of four types of organic-inorganic light-harvesting scaffolds, Periodic Mesoporous Organosilica (PMO), dye loaded Zeolites, Multilayered Inorganic Minerals (MIMs) and Metal-Organic Frameworks (MOFs). The design principles and challenges associated with these materials motivated us to formulate the aim and scope of second half of this thesis towards luminescent soft-hybrids.

Organic-Inorganic Light-Harvesting Scaffolds



1.2.1 Introduction

Light-harvesting multi-chromophoric synthetic scaffolds offer a promising option for the design of functional materials with high and tunable luminescence.¹ These artificial photonic antennas made up of donor (D) chromophores can harvest the light to the acceptors (A), which are incorporated either covalently or non-covalently, via a Forster Resonance Energy Transfer mechanism (FRET). However, in order to parallel the nature's efficiency, well defined, hierarchically organized chromophores, analogous to the anisotropic chlorophyll arrays are crucial for efficient energy migration. Most studied among this has been the use of supramolecular assemblies of organic chromophores, in which the molecular organization is guided by the non-covalent forces.² Although, they have excellent solution processability, they lack in monodispersity and invariably lead to decrease in emission due to strong intermolecular π - π interactions. In this respect, scaffolding of organic fluorophores using structurally ordered inorganic materials has emerged recently as an attractive and efficient design for luminescent materials.³

Inorganic counterparts serve as ideal materials for the highly ordered scaffolding of organic chromophores, because of their characteristic nanoscopic periodicity and/or well-defined pore channels. The nanostructured periodicity present in the inorganic component can be translated for the spatial organization of the chromophores via co-polymerization or co-assembly, whereas the nano/micro channels can host non-covalently embedded organic chromophores in their channels. Thus in these organic-inorganic scaffolds inter-chromophoric interactions are minimized resulting in highly luminescent hybrids. In addition these multichromophoric hybrids provide highly organized arrays of donor and acceptor molecules for efficient light harvesting, which facilitate the tuning of emission colour. Advantages of synthetic simplicity and transparent nature (important for luminescent devices) compared with the organic assemblies are extra add ons.

In this section, various organic-inorganic light-harvesting hybrid scaffolds designed recently for tunable luminescence are described. This section is majorly focused on the luminescent hybrids based on Periodic Mesoporous Organosilica (PMO), dye loaded Zeolites, clay sheets (Multilayered Inorganic Minerals (MIMs)) and Metal-Organic Frameworks (MOFs). In PMOs the co-organization with organics is based on taking advantage of their periodic covalent arrays as well as mesoscopic channels. Whereas, in other materials like Zeolites, MOF or clay, nanopores, channels and interlayer galleries were used, respectively for incorporating chromophores.

1.2.2 Periodic Mesoporous Silica (PMO)

PMO is a product of a polycondensation between organosilane precursors.⁴ The whole process is soft-templated by a surfactant with its aggregate dimensions and packing giving the resultant silicate its porosity and periodicity.⁵ The structure of the final material contains hexagonally packed mesoporous channels (meso channels) surrounded by the silicate cross-linked organic moiety (walls). Co-condensation of more than one organosilane precursors has also been extensively employed for PMO synthesis to tailor the density of functionalization on its surface as well as to render them with multi-component features.^{6,7} The organization of chromophores in the PMO wall along with appropriate guest molecules in their meso-channels makes it a versatile donor scaffold for FRET process (Figure 1.2.1a).

One of the major challenges to achieve such a goal was to synthesize a crystalline wall structure with organic chromophores. This challenge was overcome by Inagaki and co-workers by making use of a directional supramolecular strategy where π -stacking in tandem with hydrophobic interactions of a benzene silane derivative has been used.⁶ This was a major breakthrough because it paved the path for densely and covalently embedded ordered chromophores in PMO wall. Also, despite having high density of chromophores, the structural versatility of PMO allows their spatial separation without giving any room for aggregation to yield high solid-state fluorescence quantum yield of these hybrids. Consequently, a plethora of chromophores⁷ such as oligophenylenevinyls (OPV), anthracene, divinylazo-benzene and benzoimines have been used to design luminescent PMOs. Lack of inter-chromophoric interactions in these hybrids is supported by the high rotational mobility around the Si-C bond which has been probed by NMR spin relaxation experiments. In naphthalene functionalized PMOs, monomeric emission was observed from the crystalline solid powder.⁸ Similarly, in OPV derived PMOs aggregation was discouraged by the alkoxy groups present on the chromophore.^{6b}

Apart from the chromophores embedded in PMO walls, their pores can host a variety of hydrophobic and hydrophilic molecules, their position in the pore however can vary. For example, hydrophilic dye molecules such as coumarin and rhodamine are concentrated near to the polar head of surfactant micelle (near to wall), whereas hydrophobic guests such as rubrene tend to be embedded in the hydrocarbon tails of micelle (at the pore centre).⁹

An intriguing single molecular diffusion study of dyes in the surfactant micelles inside porous channels of PMO films not only showed their 1-dimensional diffusion confirming presence of long channels, it also shows their size dependence on the diffusion distance. Importance of this study lies in the fact that photo processes like FRET are highly dependent on direction of molecular dipole, which in turn is caused by rotational dynamics.¹⁰

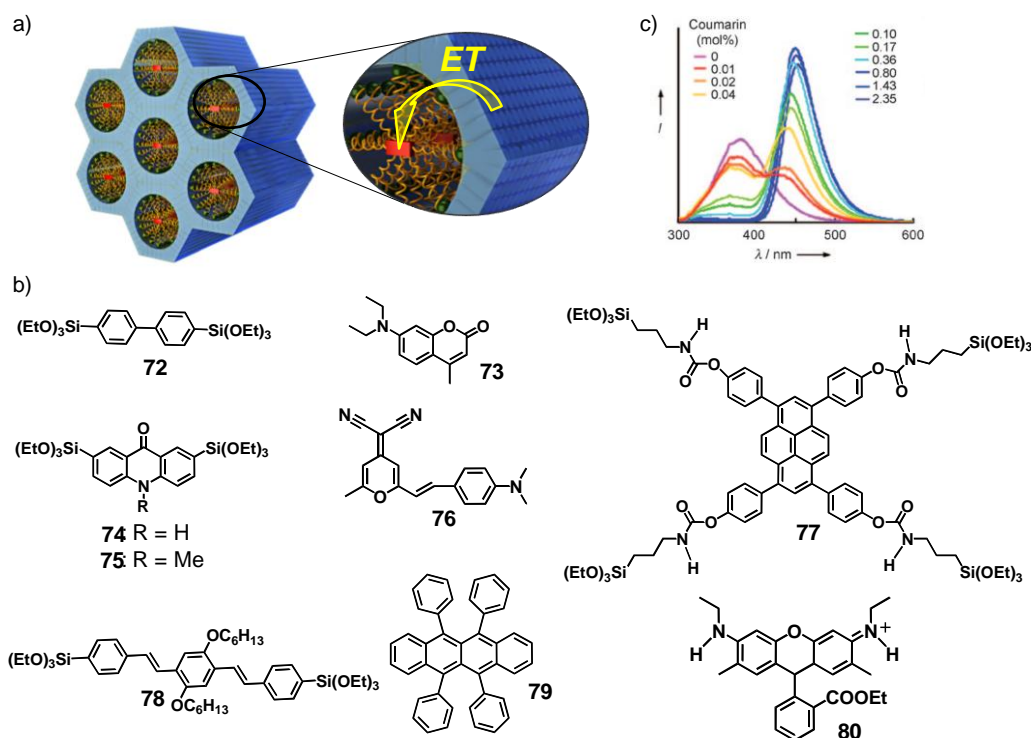


Figure 1.2.1 Schematic representation of energy transfer process in chromophore embedded PMO. b) Molecular structures of donor-silane precursors and acceptor dyes. c) Fluorescence spectra for **72/73**-PMO powders with 0–2.35 mol% of **73** [reproduced from ref. 11].

A powerful PMO derived light harvesting system can emerge combining their ability to have chromophores in two separate compartments (walls and mesochannels), which has been exploited by Inagaki and co-workers. D-A compartmentalization in PMOs was reported initially using biphenyl (**72**) bridges as donors and coumarin dye (**73**) encapsulated in the mesochannels as acceptors (Figure 1.2.1a and b).¹¹ FRET process was investigated in both film and powder forms loaded with different mol% of **73**. Increase in the percentage of **73** loading resulted in concomitant decrease in biphenyl emission and increase in intensity of **73** (Figure 1.2.1c). The quantum yield of the material doubled by addition of mere 0.8% of **73** with nearly 100% FRET efficiency. Similar strategy was later used to design visible light-harvesting PMO with acridone (**74**) bridges and DCM (**76**) dye channels. Use of n-methylated acridone silanes (**75**) further enhanced the transmittance (> 93%) of these PMOs by disrupting the intermolecular interactions mediated by H-bonding.¹² This concept has also been used for amplified metal sensing.¹³

Use of FRET in PMO subsequently has led to the development of materials with tunable emission so as to achieve multiple colours with an ideal combination of them to get even a white light emission. Partial energy transfer (ET) from PMOs bridged with highly blue emitting dyes such as tetraphenylpyrene (**77**) or oligophenylenevinyls (**78**) to yellow emitting dyes such as rhodamine (**80**) or rubrene (**79**) resulted in the white light.¹⁴

Light-harvesting process was investigated in dye doped PMOs prepared in two different methods. The first one is a pre-synthetic method where donor silane and acceptor molecules were

added together to the surfactant micelle solution followed by silica condensation reaction to make antenna PMOs. The second method is a post-synthetic approach where donor PMO scaffolds were soaked with acceptor solution to make antenna materials. Even though, ET efficiency was found to be more efficient in the later approach, former one is more preferred in the view of device fabrication. This is mainly due to its ease of solution processability, because the solution having all the precursors to make PMO antenna can be drop-casted on required substrate before condensation (Figure 1.2.2a). Using this pre-synthetic method, highly luminescent and transparent light-harvesting PMO films were made on glass substrates and prototype LEDs coated with PMOs were also demonstrated (Figure 1.2.2b).

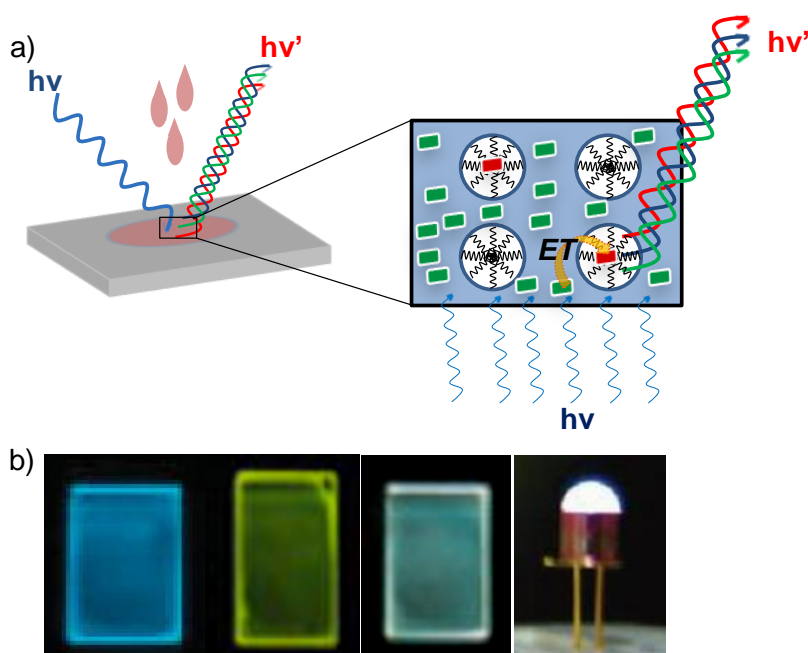


Figure 1.2.2. a) Schematic representation for the pre-synthetic method for the design of light-harvesting PMO films and b) photographs of multicoloured luminescent films and prototype white LED thus prepared [reproduced from ref. 14].

As summarised above PMOs are excellent materials for light harvesting and related applications. An added incentive however here is that apart from having great adaptability in terms of function, their morphology is very well controllable.

1.2.3 Dye Loaded Zeolites

Zeolites comprising of nanochannels with uniform pore diameters can act as a template for the 1-D end-to-end organization of fluorophores. This characteristic makes it a unique substrate that opens up many avenues in light-harvesting hybrids. Among a wide variety of zeolite materials, hexagonal Zeolite L crystals (ZLCs) have been extensively used due to their two major advantages. Firstly, because of their ability to organize both neutral and cationic dye molecules inside their anionic tubular nanochannels and secondly due to the ease of synthesis of these materials.¹⁵ To incorporate the dyes inside ZLCs methods like ion-exchange and vapour

deposition are used with latter being for neutral dyes and former for cationic. The well-defined diameter of 7.1 Å, of these nanochannels allows the dyes to organize in a longitudinal fashion without any π - π interaction even at high concentrations.¹⁶ This anisotropic organization of molecules is further responsible for efficient 1D hopping of excitons and polarized emission which can be further trapped at desired positions of ZLCs via FRET.

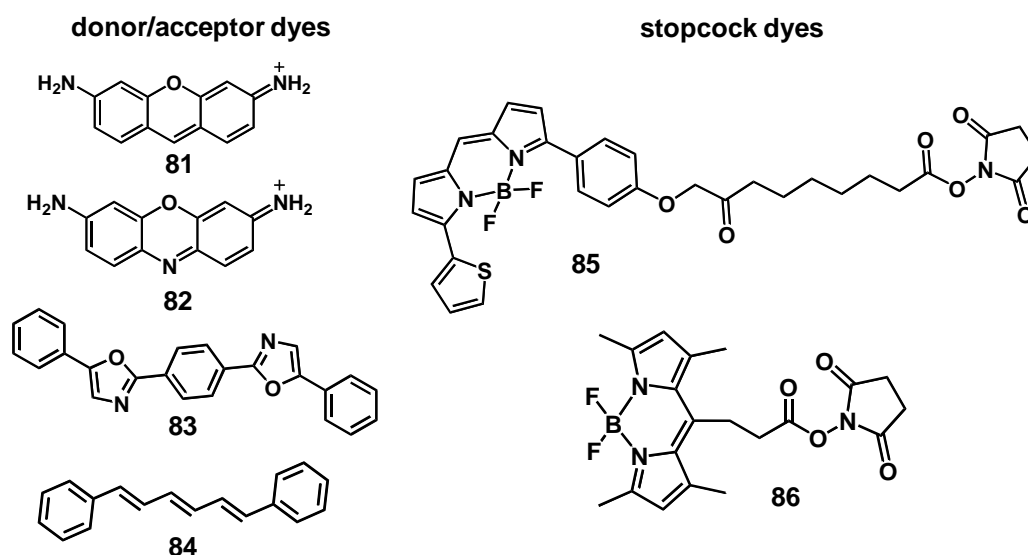


Figure 1.2.3. Molecular structures of various D, A and stopcock molecules used to load in ZLC channels.

One of the unique advantages of Zeolite based systems is that, different molecules can be sequentially encapsulated into the nano-channels, thereby providing the flexibility of placing the desired D and A chromophores at predetermined positions. One of the FRET pair extensively investigated in ZLCs are green emitting pyronine (**81**) and red emitting oxonine (**82**) owing to their cationic nature and efficient spectral overlap (Figure 1.2.3).¹⁷ ZLC nanochannels loaded with **81** in the middle and **82** at either ends showed a very fast energy migration from **81** to **82**, thereby amplifying its solid-state quantum yield close to unity (Figure 1.2.4a and b).¹⁸

Multicoloured luminescent materials ranging from green to red could also be obtained by the random loading of D (**81**) and A (**82**) molecules in different compositions, thereby controlling the extent of energy transfer. Taking again the advantage of the sequential incorporation of dyes in zeolite channels multiple acceptor molecules can also be loaded to facilitate a directional, cascade energy transfer.^{19,20} In order to construct one such systems, first nanochannels were loaded with neutral blue emissive **83** or **84** via gas phase double ampoule method followed by loading of **81** (green) and finally of **82** via ion exchange, thus locating red dyes (**82**) at the channel ends. In this three chromophoric hybrid system, intense red emission due to **82** was observed at the ends of ZLCs because of cascade energy transfer. Additionally they also showed

white luminescent regions due to the superposition of the fluorescence of all three dyes apart from the blue and red regions of individual dyes.

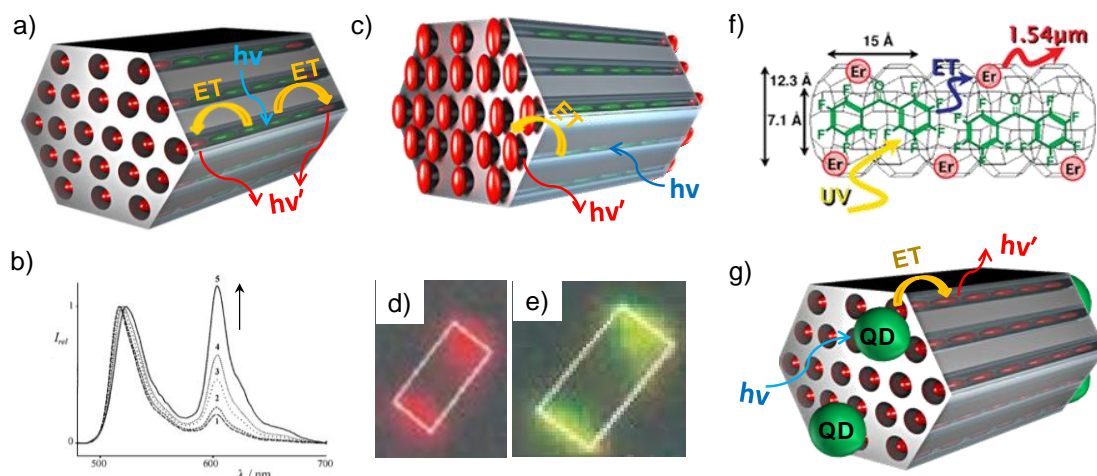


Figure 1.2.4. a) Schematic representation of ET process in ZLC loaded with D (green) and A (red) molecules. b) Emission spectra of **81**-ZLC crystals loaded with increasing amounts of **82** [reproduced from ref. 18a]. c) Schematic representation of stopcock plugged ZLC based antenna. FM images of 2 μm sized **82**-ZLC modified with two stopcocks (**85**) per channel upon exciting d) **85** and e) **82** [reproduced from ref. 21]. The emission spreading out of the crystals border is due the presence of stopcocks. Schematic illustration of the ET process in f) ZLCs loaded with fluoro benzophenone and the erbium (III) ions, and g) QDs modified **82**-ZLC channels [reproduced from ref. 23b].

A “stopcock” molecular design has been elegantly introduced to end-cap the ZLCs with a bulky chromophore which can further act as an extraction/injection point of excitation energy (Figure 1.2.3c). Stopcock molecules contain a large dye (D/A) molecular head appended by a flexible tail (**85** and **86**). The bulky chromophoric head cannot enter the ZLC channels, whereas the flexible tail ensures the anchoring of these molecules at the channel entrances. This concept was first demonstrated with two BODIPY derivatives **85** or **86** as stopcocks (Figure 1.2.3 and 1.2.4c-e).²¹ When **81**-ZLCs were end-capped with two **85** molecules per channel, emission from stopcock was observed, as a result of ET from **81**. Similarly, when **82**-ZLCs were modified with **86**, efficient injection of electronic excitation energy into the ZLCs was observed due to energy transfer from stopcock. Fluorescence microscopy images indeed showed the emission spreading out of the crystals border due to the presence of stopcock molecules (Figure 1.2.4d and e). This concept was extended with a variety of π -conjugated stopcock molecules.²²

The excellent light-harvesting properties of dye loaded ZLCs were further extended to create composite antenna materials by conjugating them with inorganic luminescent components such as lanthanide ions and quantum dots QDs. ZLCs loaded with fluoro benzophenone dyes and erbium (III) ions showed FRET induced NIR emission at 1.54 μm with a quantum yield of 2.5% (Figure 1.2.4f).²³ In another interesting approach by De Cola et al. QDs were conjugated on dye

loaded **ZLCs** for better spectral coverage and injection of excitation energy from **QDs** to the dye molecules (Figure 1.2.4g).²⁴ This has been demonstrated using **82** loaded **ZLCs** decorated with green emitting amine capped CdSe/ZnS core-shell **QDs** through non-covalent interactions on their surface.

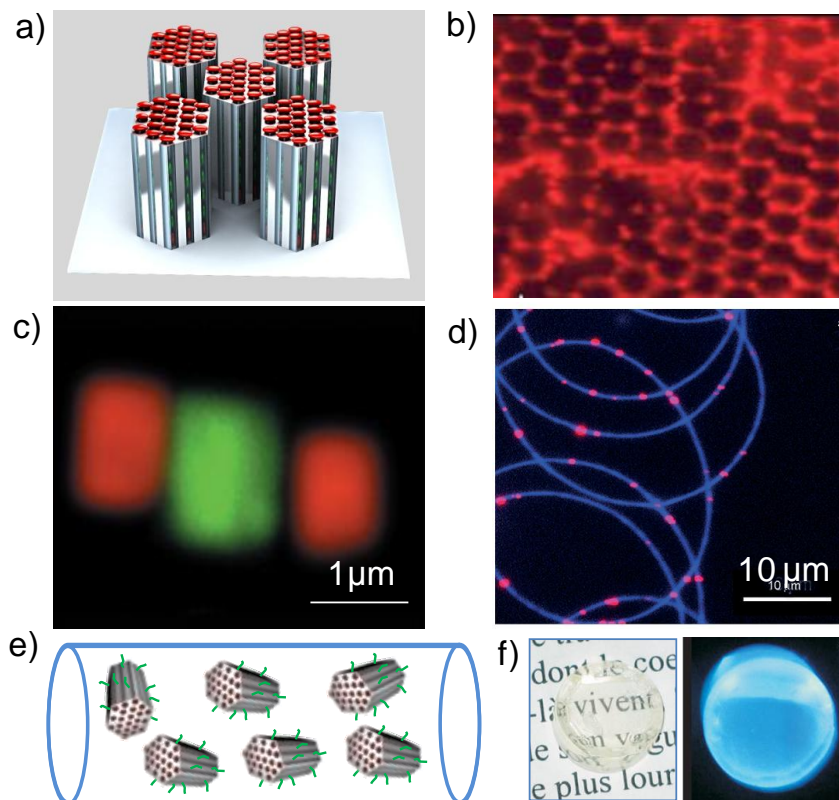


Figure 1.2.5. *a) Schematic representation of dye-ZLC organization in oriented monolayers. b) FM images of 82-ZLCs organized by a surface-tension-driven self-assembly process [reproduced from ref. 27]. c) FM images of the alternate longitudinal assembly of 82-ZLC and 81-ZLCs mediated by metal-coordination [reproduced from ref. 28]. d) FM images of red emitting ZLCs embedded in the polymer nanofibers [reproduced from ref. 29]. e) Schematic of ZLCs embedded in a polymer matrix for processability. f) Photographs of processable dimethyl derivative of 83 loaded ZLCs with CR39 polymer under ambient (left) and under UV illumination (right) [reproduced from ref. 31].*

Several efforts have been made to integrate and to improve the device performance of dye loaded Zeolite antenna materials by organising them on surfaces.²⁵ In this respect, oriented monolayers of dye-zeolite crystals in which the crystals are longitudinally aligned on a surface would be highly beneficial because of the anisotropic nature of the energy-transfer along the length of **ZLCs** (Figure 1.2.5a).²⁶ Covalent linking of **ZLCs** to the glass surfaces using C_{60} as a linker yielded stable monolayers with good mechanical strength. Furthermore, hexagonal arrays of **82-ZLCs** obtained by a surface-tension driven self-assembly, which exhibited bright polarized emission (Figure 1.2.5b).²⁷ Longitudinal end-to-end assembly of **ZLCs** have been achieved with anthracene derived stop-cock molecules due to the π - π interactions between the anthracene aromatics. Alternatively, zinc-terpyridine coordination bonds have also been used for the linear,

alternate co-assembly of green and red emitting ZLCs (Figure 1.2.5c).²⁸ These could be helpful in nano-barcode devices.

In order to address the solution processability of ZLCs, attempts such as conjugating them with organic polymer chains or embedding them in polymer matrixes have been made. Electrospinning the mixture of dye-loaded zeolites with polymers such as poly(ethylene oxide)²⁹ gave composite nanofibers (Figure 1.2.5d).³⁰ By conjugating ZLCs with Columbia Resin 39 (CR39), highly transparent and fluorescent monoliths of polymer-Zeolite composites have been made (Figure 1.2.5e-f).³¹

1.2.4 Dye Loaded MIMs

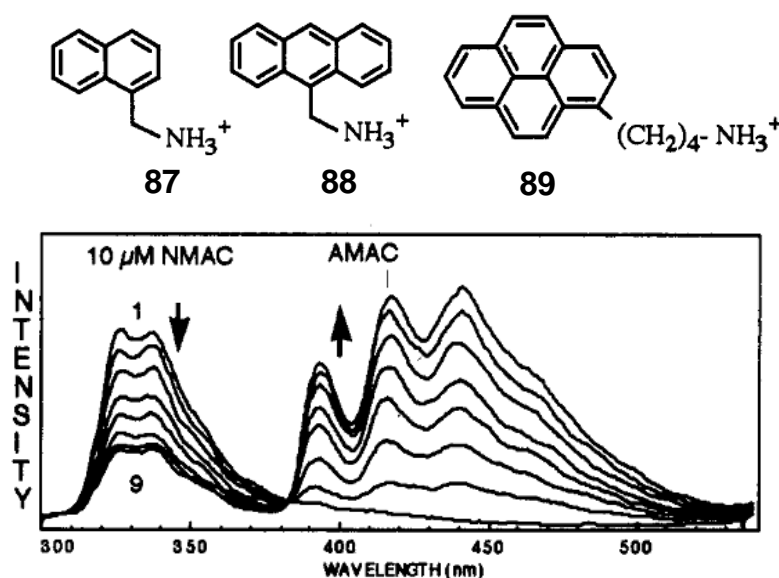


Figure 1.2.6. a) Molecular structures of cationic D and A molecules used in energy transfer experiments. b) Fluorescence spectra of **87** (10 μM) and **88** (0-6.36 μM) in the presence of **BAZrP** (0.00896 by weight) [reproduced from ref. 32].

Clays are the multilayered inorganic materials (MIMs) that can be synthesised so as to tune their surface charge characteristics. Moreover these layers act as a platform to organize the dye molecules in their interlayer galleries to facilitate light-harvesting among the organized components. However, only charged molecules can be incorporated into these MIMs via ion exchange. First demonstration on MIMs as energy transfer platforms was given by Kumar et al.³² using anionic α -zirconium phosphate (α -ZrP) layers and ammonium (cationic) derivatives of naphthalene, anthracene and pyrene (Figure 1.2.6). To enhance the binding of hydrophobic dyes, α -ZrP was absorbed with butylamine hydrochloride (**BAZrP**). Efficient excitation energy transfer was observed from **87** to **88/89** in the presence of **BAZrP** as evidenced from the efficient quenching of **87** emission with increase of **88** concentration (Figure 1.2.6b). In addition, amplification in **88** emission when **87** was excited further indicates the efficient energy migration

between D molecules in the present system. Interestingly, the absence energy transfer from **87** to **88/89** when there is no **BAZrP** due to the absence of spatial organization provided by inorganic platform (**BAZrP**).

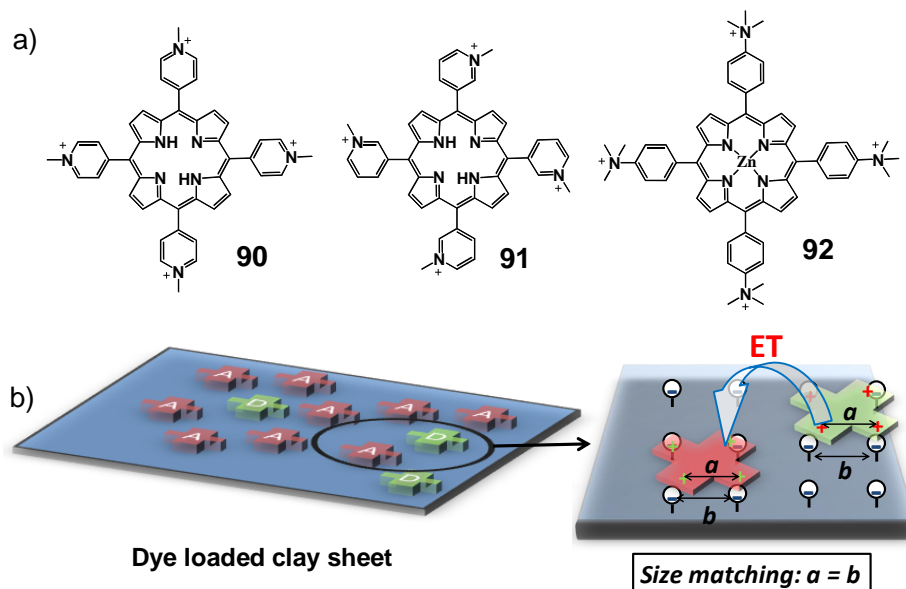


Figure 1.2.7. a) Molecular structures of D/A cationic porphyrins and b) schematic representation maximum adsorption of these molecules clay surface due to size matching effect.

Later Inoue and co-workers have utilized Sumecton SA (**SSA**), an anionic clay as host to promote energy transfer between various cationic porphyrins (**90/91** to **92**) (Figure 1.2.7).³³ To control the aggregation of the porphyrins, the surface charge density of clay has been modulated by using various ratios of inorganic precursors. The net charge on a clay sheet was determined by a factor called as cationic exchange capacity (CEC).³³ Experiments with clay of varied CEC suggested that a high density of dye organization on surface occurs when inter charge distance on the clay matches with the inter charge distance on the chromophores structure (size matching effect) (Figure 1.2.7b).³⁴ By using this size matching methodology, clay surfaces with densely packed D and A porphyrins exhibiting a very efficient energy transfer were obtained. Interestingly, in these hybrids the energy transfer mode differed for different loadings of the porphyrins.^{33a} At lower chromophores loadings (< 0.2%) intra sheet energy transfer was observed whereas with increased loadings (>20%), an inter sheet mechanism predominates because of the decreased distance between adjacent clays. An alternative explanation of dye exchange was ruled out due to the lack of dye dynamics after being adsorbed on the clay surface. Despite having excellent light-harvesting properties, these anionic clays tend to aggregate in water which hampers their solution processability. We have addressed this issue by selecting soluble clay sheets and their efficient solution state co-assembly with luminescent D and A dyes led to the

formation of solution processable luminescent light-harvesting hybrids which are discussed in Part-2 of this thesis.

1.2.5 Metal Organic Frameworks (MOFs)

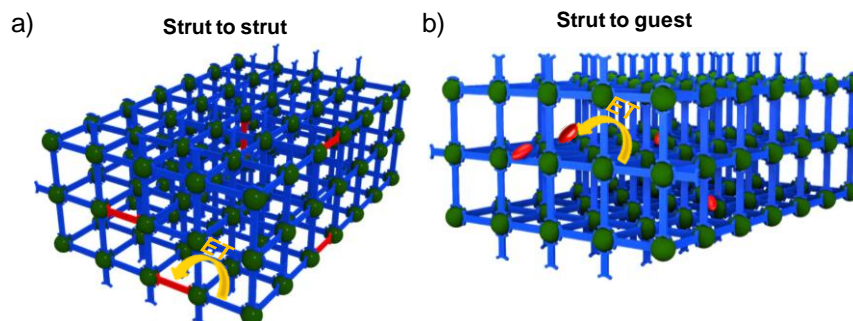


Figure 1.2.8. Schematic representation of a) strut to strut and b) strut to guest energy transfer process in MOFs.

MOFs are 3-D crystalline structures formed via the co-ordination between a metal ion and a multi-functional rigid organic spacer.³⁵ This design endows the MOFs with inherent porosity as one of the essential properties of these materials. MOFs have emerged recently as light-harvesting hybrid materials, because of the use of chromophores as linkers or struts between metal nodes. This organization, due to co-ordination, provides an efficient way to spatially disperse these chromophores hence creating a photoactive scaffold. Two design strategies have been used so far for the design of light-harvesting MOFs (Figure 1.2.8). Firstly, both D and A chromophores being a part of the structural framework as linkers in order to promote a strut-to-strut energy transfer and secondly, the exploitation of the inherent porosity of MOFs by incorporating an acceptor into the donor framework to facilitate strut to guest energy transfer.

Hupp et al. have extensively investigated light-harvesting properties of porphyrin derived MOFs. Elegantly designed pillar-paddle wheel structured MOF having zinc porphyrin-tetraacid (**93**) as a paddlewheel and pyridine functionalized boron dipyrromethene (**94**) as pillar showed very efficient energy transfer from pillar strut to paddlewheel strut (Figure 1.2.9, 1.2.10a and b).³⁶ The efficient energy transfer between these geometrically orthogonal struts is attributed to the slight deviation of their root-mean-square value of the angle from 90° . In addition the clever use of Zn^{II} with d^{10} configuration as metal nodes prevented the quenching of struts due to any ligand-to-metal charge transfer. Interestingly MOFs constructed from dipyridylporphyrins (**95** and **96**) as pillars showed very efficient exciton migration up to forty-five porphyrin struts.³⁷ Surface functionalization of these MOFs with CdSe/ZnS core/shell **QDs**³⁸ resulted in efficient energy-transfer (>80 %) from the later to the framework ligands, resulting in novel light-harvesting composite materials having broad spectral coverage in the entire visible region.

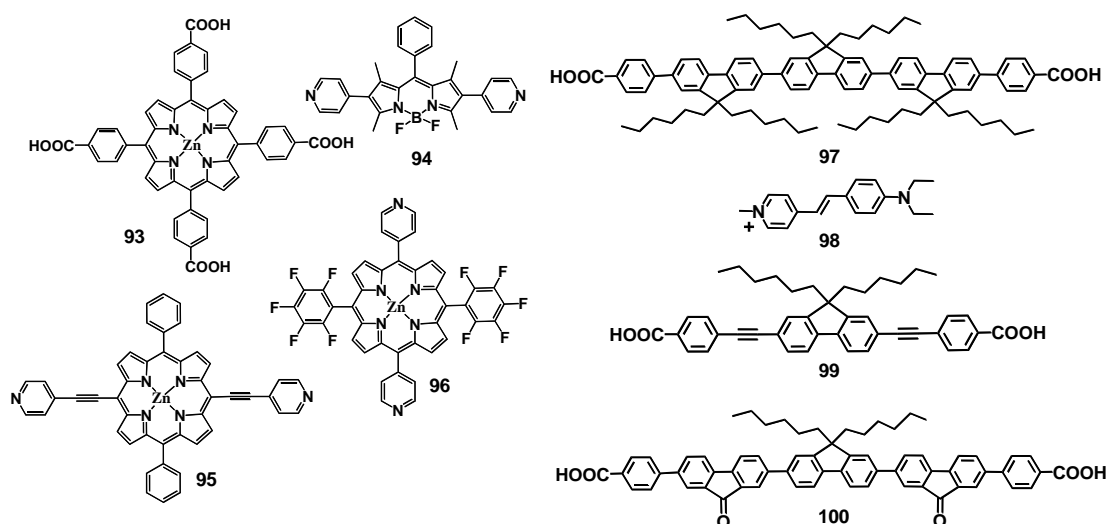


Figure 1.2.9. Structures of molecules used as struts and guests in the synthesis of light-harvesting MOFs.

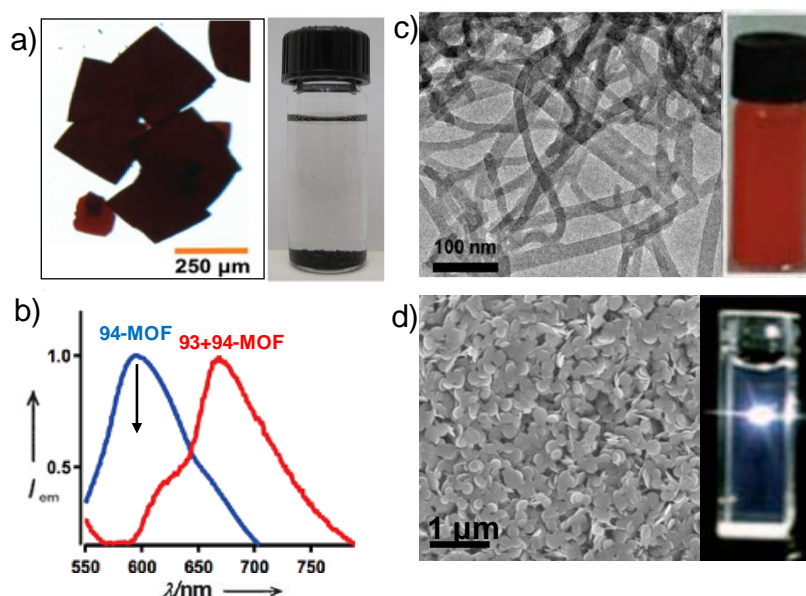


Figure 1.2.10. a) Photographs of 93+94-MOF crystals and their dispersion in ethanol. b) Emission spectra of 94-MOF with and without 93 [Figure 1.2.10a and b, reproduced from ref. 36]. c) TEM image of 97+98-Zn(OAc)₂ nMOFs and their dispersion in DMF [reproduced from ref. 39]. d) SEM image of Gd^{III} (97+2% 100) nMOFs and their dispersion in DMF [reproduced from ref. 40b].

Scaling down these MOF macrocrystals into nano-regime would be advantageous in order to increase their solution dispersibility (Figure 1.2.10c and d). Loh et al. first demonstrated nanoscale MOFs (nMOFs) by the use of ligands having flexible alkyl chains.³⁹ nMOFs, constructed from oligomeric fluorine diacid (97) having hexyl chains and zinc nodes, showed nanowire morphology with excellent dispersion ability (Figure 1.2.10c). These nanowires further showed efficient energy transfer to encapsulated red emitting trans-4-styryl-1-methylpyridiniumiodide (98) acceptor molecules. This approach was further extended by Uvdal et al.

with several derivatives as struts and lanthanide ions as nodes (Figure 1.2.9).⁴⁰ When **99** was treated with various Ln^{III} ions, crystalline thin nanodisks were obtained with long dispersion life time and excellent luminescence properties. nMOFs made from Gd^{III}, also showed efficient energy transfer to the entrapped **98** acceptors.^{40a} Antenna materials have also been made by using structurally similar D and A ligands during the nMOF synthesis with Gd^{III}. Mixed ligand nMOFs constructed from **97** donors and oligofluorenone (**100**) showed bright white-light emission due to partial strut-to-strut energy transfer (Figure 1.2.10d).^{40b}

1.2.6 Conclusions and Outlook

To summarize, we have given a detailed account of the various methodologies adopted to harness energy transfer in organic-inorganic hybrid materials. Even though single component materials are shown to have efficient luminescent properties, multicomponent light-harvesting systems provide easy access to tuneable emission and better spectral coverage. These hybrid materials are simple to synthesize and have a good control on their internal structure such as periodicity and surface charge. In order to address the solution processability of these hybrids, various ways have been exploited such as the formation of thin films in PMOs, polymer encapsulation in zeolites, and downsizing to nano level in case of MOFs. Though first three have reached a pretty convenient phase on this issue, we believe that similar strategies are to be employed in case of MOFs as well, which actually is the youngest member among the four. It would be unwise to believe that the tale ends here. There are many challenges, diversifications ahead awaiting these materials for example since organic-inorganic hybrids composed of ionic chromophores, they can be exploited for light-emitting electrochemical cells. Another big challenge is to couple this energy transfer process with an electron transfer and this can well be the next frontier for these materials. The high solid state quantum yield and aqueous stability (except MOFs) of these materials would be advantageous for use in photocatalysis and water splitting. This would be further helpful for improving the efficiencies of solar-cells by an appropriate coupling with the light-harvesting system.⁴¹ Also, fluorescence detection of analytes can be achieved with greater selectivity by using the amplified fluorescence of acceptor via energy-transfer as in light-harvesting hybrids.⁴² This has been achieved in case of PMOs but is yet to be translated in other hybrids.

Since the inorganic hosts used in the design of light-harvesting hybrids are environmental friendly, readily available and takes major weightage of the total material, these systems can serve the purpose of pure organic materials in a cost effective and eco friendly manner. Also, recent development on soft-luminescent hybrids seems to be a potential test-bed for various optical applications and it is worth extending this strategy to other functional chromophores.

1.2.7 References

1. a) A. Ajayaghosh, V. K. Praveen, C. Vijayakumar, *Chem. Soc. Rev.* **2008**, *37*, 1090; b) S. S. Babu, K. K. Kartha, A. Ajayaghosh, *J. Phys. Chem. Lett.* **2010**, *1*, 3413; c) P. D. Frischmann, K. Mahata, F. Würthner, *Chem. Soc. Rev.* **2013**, *42*, 1847; d) A. Adronov, J. M. J. Fréchet, *Chem. Commun.* **2000**, 1701; e) C. Devadoss, P. Bharathi, J. S. Moore, *J. Am. Chem. Soc.* **1996**, *118*, 9635; f) D.-L. Jiang, T. Aida, *Nature* **1997**, *388*, 454; g) L. Chen, Y. Honsho, S. Seki, D. Jiang, *J. Am. Chem. Soc.* **2010**, *132*, 6742.
2. a) W. Li, T. Aida *Chem. Rev.* **2009**, *109*, 6047; b) M. D. Ward *Chem. Soc. Rev.* **1997**, *26*, 365; c) F. J. M. Hoeben, L. M. Herz, C. Daniel, P. Jonkheijm, A. P. H. J. Schenning, C. Silva, S. C. J. Meskers, D. Beljonne, R. T. Phillips, R. H. Friend, E. W. Meijer, *Angew. Chem. Int. Ed.* **2004**, *43*, 1976; d) A. Ajayaghosh, S. J. George, V. K. Praveen, *Angew. Chem. Int. Ed.* **2003**, *42*, 332.
3. a) K. V. Rao, K. K. R. Datta, M. Eswaramoorthy and S. J. George, *Chem. Eur. J.* **2012**, *18*, 2184; b) D. Brühwiler, G. Calzaferri, T. Torres, J. H. Ramm, N. Gartmann, L.-Q. Dieu, I. López-Duarte, M. V. Martínez-Díaz, *J. Mater. Chem.* **2009**, *19*, 8040.
4. a) P. V. Der Voort, D. Esquivel, E. De Canck, F. Goethals, I. Van Driessche, F. J. Romero-Salguero, *Chem. Soc. Rev.* **2013**, *42*, 3913; b) L. Han, S. Che, *Chem. Soc. Rev.* **2013**, *42*, 3740.
5. a) A. Mehdi, C. Reye, R. Corriu, *Chem. Soc. Rev.* **2011**, *40*, 563; b) L. Han, S. Che, *Chem. Soc. Rev.* **2013**, *42*, 3740; c) J. Y. Ying, C. P. Mehnert, M. S. Wong *Angew. Chem. Int. Ed.* **1999**, *38*, 56.
6. S. Inagaki, S. Guan, T. Ohsuna, O. Terasaki, *Nature* **2002**, *416*, 304.
7. a) M. Cornelius, F. Hoffmann, B. Ufer, P. Behrens, M. Fröba, *J. Mater. Chem.* **2008**, *18*, 2587; b) N. Mizoshita, Y. Goto, T. Tani, S. Inagaki, *Adv. Funct. Mater.* **2008**, *18*, 3699; c) D. Chandra, T. Yokoi, T. Tatsumi, A. Bhaumik, *Chem. Mater.* **2007**, *19*, 5347.
8. N. Mizoshita, Y. Goto, M. P. Kapoor, T. Shimada, T. Tani, S. Inagaki, *Chem. Eur. J.* **2009**, *15*, 219.
9. T. Tani, N. Mizoshita, S. Inagaki, *J. Mater. Chem.* **2009**, *19*, 4451.
10. S. Ito, S. Fukuya, T. Kusumi, Y. Ishibashi, H. Miyasaka, Y. Goto, M. Ikai, T. Tani, S. Inagaki, *J. Phys. Chem. C* **2009**, *113*, 11884.
11. S. Inagaki, O. Ohtani, Y. Goto, K. Okamoto, M. Ikai, K. Yamanaka, T. Tani, T. Okada, *Angew. Chem. Int. Ed.* **2009**, *48*, 4042.
11. a) Y. Maegawa, N. Mizoshita, T. Tani, S. Inagaki, *J. Mater. Chem.* **2010**, *20*, 4399; b) H. Takeda, Y. Goto, Y. Maegawa, T. Ohsuna, T. Tani, K. Matsumoto, T. Shimada, S. Inagaki, *Chem. Commun.* **2009**, 6032.

13. M. Waki, N. Mizoshita, Yoshifumi Maegawa, T. Hasegawa, T. Tani, T. Shimada, S. Inagaki, *Chem. Eur. J.* **2012**, *18*, 1992.
14. a) N. Mizoshita, Y. Goto, T. Tani, S. Inagaki, *Adv. Mater.* **2009**, *21*, 4798; b) N. Mizoshita, Y. Goto, Y. Maegawa, T. Tani, S. Inagaki, *Chem. Mater.* **2010**, *22*, 2548.
15. a) G. Calzaferri, M. Pauchard, H. Maas, S. Huber, A. Khatyr, T. Schaafsma, *J. Mater. Chem.* **2002**, *12*, 1; b) C. Minkowski, R. Pansu, M. Takano, G. Calzaferri, *Adv. Funct. Mater.* **2006**, *16*, 273.
16. G. Calzaferri, N. Gfeller, *J. Phys. Chem.* **1992**, *96*, 3428.
17. N. Gfeller, S. Megelski, G. Calzaferri, *J. Phys. Chem. B* **1998**, *102*, 2433.
18. a) N. Gfeller, S. Megelski, G. Calzaferri, *J. Phys. Chem. B* **1999**, *103*, 1250; b) M. M. Yatskou, M. Meyer, S. Huber, M. Pfenniger, G. Calzaferri, *ChemPhysChem* **2003**, *4*, 567.
19. K. Lutkouskaya, G. Calzaferri, *Phys. Chem. B* **2006**, *110*, 5633.
20. M. Pauchard, A. Devaux, G. Calzaferri, *Chem. Eur. J.* **2000**, *6*, 3456.
21. H. Maas, G. Calzaferri, *Angew. Chem. Int. Ed.* **2002**, *41*, 2284.
22. a) C. Minkowski, G. Calzaferri, *Angew. Chem. Int. Ed.* **2005**, *44*, 5325; b) S. Huber, G. Calzaferri, *Angew. Chem. Int. Ed.* **2004**, *43*, 6738; c) O. Bossart, L. De Cola, S. Welter, G. Calzaferri, *Chem. Eur. J.* **2004**, *10*, 5771.
23. a) A. Monguzzi, G. Macchi, F. Meinardi, R. Tubino, M. Burger, G. Calzaferri, *Appl. Phys. Lett.* **2008**, *92*, 123301; b) A. Mech, A. Monguzzi, F. Meinardi, J. Mezyk, G. Macchi, R. Tubino, *J. Am. Chem. Soc.* **2010**, *132*, 4574.
24. S. Ramachandra, Z. D. Popović, K. C. Schuermann, F. Cucinotta, G. Calzaferri, L. De Cola, *Small* **2011**, *7*, 1488.
25. G. Calzaferri, H. Li, D. Brühwiler, *Chem. Eur. J.* **2008**, *14*, 7442.
26. a) A. Z. Ruiz, H. Li, G. Calzaferri, *Angew. Chem. Int. Ed.* **2006**, *45*, 5282; b) H. Li, Y. Wang, W. Zhang, B. Liu, G. Calzaferri, *Chem. Commun.* **2007**, 2853.
27. S. Yunus, F. Spano, G. Patrinoiu, A. Bolognesi, C. Botta, D. Brühwiler, A. Z. Ruiz, *Adv. Funct. Mater.* **2006**, *16*, 2213.
28. Z. Popović, M. Busby, S. Huber, G. Calzaferri, L. De Cola, *Angew. Chem. Int. Ed.* **2007**, *46*, 8898.
29. I. Cucchi, F. Spano, U. Giovanella, M. Catellani, A. Varesano, G. Calzaferri, C. Botta, *Small* **2007**, *3*, 305.
30. V. Vohra, G. Calzaferri, S. Destri, M. Pasini, W. Porzio, C. Botta, *ACS Nano* **2010**, *4*, 1409.
31. S. Suárez, A. Devaux, J. Bañuelos, O. Bossart, A. Kunzmann, G. Calzaferri, *Adv. Funct. Mater.* **2007**, *17*, 2298.
32. C. V. Kumar, A. Chaudhari, *J. Am. Chem. Soc.* **1994**, *116*, 403.

33. a) S. Takagi, D. A. Tryk, H. Inoue, *J. Phys. Chem. B* **2002**, *106*, 5455; b) S. Takagi, M. Eguchi, D. A. Tryk, H. Inoue, *Langmuir* **2006**, *22*, 1406.
34. a) S. Takagi, T. Shimada, M. Eguchi, T. Yui, H. Yoshida, D. A. Tryk, H. Inoue, *Langmuir* **2002**, *18*, 2265; b) Y. Ishida, T. Shimada, D. Masui, H. Tachibana, H. Inoue, S. Takagi, *J. Am. Chem. Soc.* **2011**, *133*, 14280.
35. a) O.K. Farha, J. T. Hupp, *Acc. Chem. Res.* **2008**, *41*, 1782; b) S. Kitagawa, R. Kitaura, S.-i. Noro, *Angew. Chem. Int. Ed.* **2004**, *43*, 2334.
36. C. Y. Lee, O. K. Farha, B. J. Hong, A. A. Sarjeant, S. T. Nguyen, J. T. Hupp, *J. Am. Chem. Soc.* **2011**, *133*, 15858.
37. H.-J. Son, S. Jin, S. Patwardhan, S. J. Wezenberg, N. C. Jeong, M. So, C. E. Wilmer, A. A. Sarjeant, G. C. Schatz, R. Q. Snurr, O. K. Farha, G. P. Wiederrecht, J. T. Hupp, *J. Am. Chem. Soc.* **2013**, *135*, 862.
38. S. Jin, H.-J. Son, O. K. Farha, G. P. Wiederrecht, J. T. Hupp, *J. Am. Chem. Soc.* **2013**, *135*, 955.
39. X. Zhang, Z.-K. Chen, K. P. Loh, *J. Am. Chem. Soc.* **2009**, *131*, 7210.
40. a) X. Zhang, M. A. Ballem, M. Ahrén, A. Suska, P. Bergman, K. Uvdal, *J. Am. Chem. Soc.* **2010**, *132*, 10391; b) X. Zhang, M. A. Ballem, Z.-J. Hu, P. Bergman, K. Uvdal, *Angew. Chem. Int. Ed.* **2011**, *50*, 5729.
41. A. Das, K. S. Narayan *Adv. Mater.* **2013**, *25*, 2193.
42. M. Waki, N. Mizoshita, Y. Maegawa, T. Hasegawa, T. Tani, T. Shimada, S. Inagaki *Chem. Eur. J.* **2012**, *18*, 1992.

PART-2

Self-Assembly of Coronene Bisimide Amphiphiles

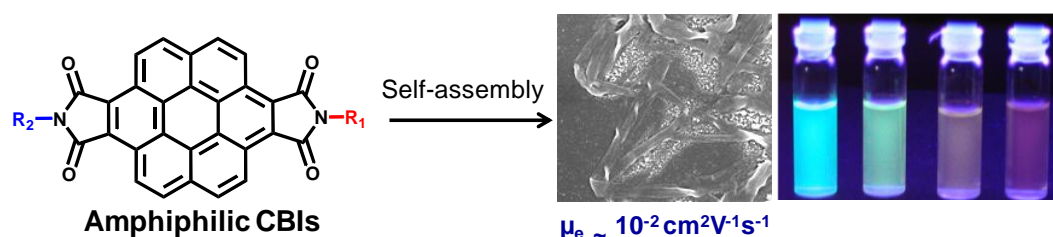
- PART-2.1** Synthesis, Controllable Self-Assembly and Optoelectronic Properties of Novel n-Type Coronene Bisimide Amphiphiles
- PART-2.2** Mechanistic Insights into the Self-Assembly Process of Coronene Bisimide Amphiphiles

PART-2 . 1

Synthesis, Controllable Self-Assembly and Optoelectronic Properties of Novel *n*-Type Coronene Bisimide Amphiphiles*

Abstract

In this section, an amphiphilic design strategy for an efficient electron transporting chromophore based nanostructures is described. For this purpose, we have designed and synthesized two new *n*-type coronene bisimide (CBI) amphiphilic derivatives, **Amph-CBI** and **Bamph-CBI** decorated with polar glycol and non-polar dodecyl chains to trigger amphiphilic self-assembly in polar solvents such as water and methanol. This ensures efficient π - π interaction between chromophores in the self-assembled nanostructures due to the strong hydrophobic interactions. Amphiphilic self-assembly of both the derivatives showed the formation of well defined nanostructures with tunable morphology and luminescence depending on the ratio between good and poor solvents. Field effect transistor (FET) devices made from these self-assembled nanostructures showed high electron mobility in the order of $10^{-2} \text{ cm}^2/\text{V}\cdot\text{s}$, suggesting the importance of amphiphilic design strategy to create nanostructures with efficient charge transport suitable for nanoelectronics.



*A Paper based on this work has appeared in *Org. Lett.* 2010, 12, 2656-2659; Manuscript under preparation.

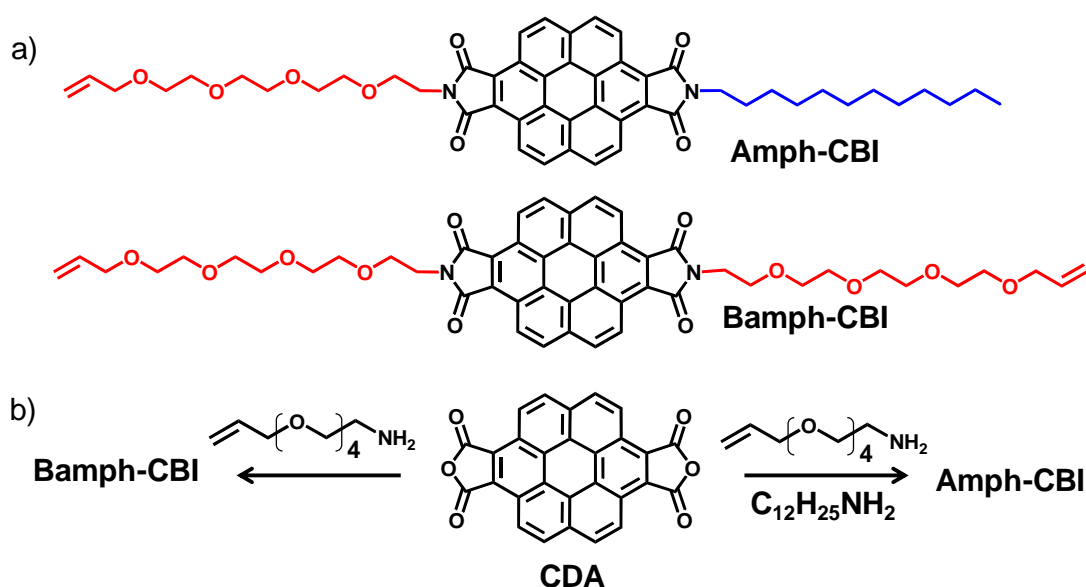
2.1.1 Introduction

Ever since the advent of organic semiconductors in optoelectronic devices, the effect of structure and organization of the functional π -conjugated components on the performance of these devices has received continuous attention.¹ In this context, several attempts have been made in recent years to synthesize new π -conjugated systems and to control their self-assembly by utilizing various non-covalent interactions such as H-bonding, π - π stacking and solvophobic interactions.² However, self-assembled nanowires of these π -conjugated oligomers³ often showed poor performance on devices than their single crystals and vacuum deposited thin films⁴ due to the absence of the long-range molecular ordering. Moreover the presence of solubilizing side groups often disturbs the supramolecular order and π - π stacking between the chromophores thereby making them less efficient for hole/electron transport. In this context, self-assembly of π -conjugated oligomers through amphiphilic interactions would be more promising for improving mesoscopic order.⁵ These amphiphilic π -conjugated molecules can self-assemble in polar solvents such as water like a classical surfactant to yield well defined nanostructures with tunable morphology.⁶ Moreover, to overcome repulsive interactions with polar solvents, chromophores stack efficiently with smaller π - π distances. This further would give rise to less dynamic and stable self-assembled stacks.⁷

Although, several efforts have been made to self-assemble electron-rich aromatic cores to generate *p*-type semiconducting supramolecular stacks,⁸ only a limited number of electron-acceptor molecules such as perylene bisimides⁹ and fullerenes,¹⁰ are exploited for the design of assemblies with *n*-type mobility.¹¹ Recently amphiphilic self-assembly of *p*-type oligo(*p*-phenylenevinylene)s and butterfly shaped thiophene oligomer are shown to form well ordered free standing sheets with enhanced mobilities.¹² Moreover, self-assembled nanotubes of hole transporting amphiphilic hexabenzocoronene (HBC) are known to have excellent charge transport properties.¹³ Hence, we envisaged that an amphiphilic design of *n*-type chromophore would be an ideal choice to achieve highly ordered self-assembled nanostructures for improved electron transport. Self-assembled nanostructures of amphiphilic *n*-type perylene bisimides (PBIs) have been well studied, however they are shown to have significant electron transport only after external doping.^{9c} Therefore, the synthesis and organization of novel new *n*-type organic semiconductor materials is crucial for the development of organic and supramolecular electronics.^{2a}

In this regard, coronene bisimides (CBIs) can be potential *n*-type semiconductors owing to their large planar π -surface, ability to have strong π - π interactions and can be made solution processable through functionalization.¹⁴ Strong intermolecular interactions between the extended planar aromatic cores of these derivatives are expected to result in higher charge

carrier mobilities and hence can emerge as an alternative to the well-studied class of *n*-type perylene bisimide (PBI) molecules as potential electron transport materials. Interestingly, diimide, tetraester and imidoester derivatives of coronene are known to be liquid crystalline.^{14b} Although various *p*-type coronene derivatives such as hexabenzocoronenes (HBCs) have been exploited for the design of supramolecular one-dimensional nanostructures,^{8j-m} there is no report pertaining to *n*-type coronene derivatives self-assembly.



Scheme 2.1.1. a) Molecular structures of amphiphilic CBIs (**Amph-CBI** and **Bamph-CBI**). b) Scheme for the synthesis of amphiphilic CBIs.

In this section we describe the synthesis, self-assembly and optoelectronic functions of a novel class of soluble *n*-type coronene bisimide amphiphiles (Scheme 2.1.1a). We have rendered the coronene bisimide (CBI) amphiphile (**Amph-CBI**), with a dodecyl and a tetraethylene glycol chain, and bolaamphiphile (**Bamph-CBI**) with tetraethylene glycol chains on both sides in order to promote a surfactant-like self-assembly in polar solvents.¹⁵ The optical properties and the morphology of the self-assembled coronene bisimide nanostructures are controlled by the solvent composition. Depending on the ratio between good and poor solvent, various self-assembled nanostructures such as nanotapes, nanotubes, nanorods and nanoparticles were obtained. Field effect transistors (FETs) made from these amphiphilic nanostructures showed electron mobilities in the order of $10^{-2} \text{ cm}^2/\text{V}\cdot\text{s}$, which is one of the highest values reported so far for *n*-type self-assembled nanostructures. More importantly, these FET devices are found to be operative at ambient conditions, whereas many of the reported *n*-type semiconductors are shown to be responsive to electric field, only under vacuum or inert atmosphere.¹⁶

2.1.2 Design, Synthesis and Characterization

The amphiphilic CBI derivatives were synthesized by condensation reaction between respective amines and coronene dianhydride (**CDA**) (Scheme 2.1.1b and see experimental section). In the case of **Amph-CBI**, we have performed statistical reaction on **CDA** with glycol and dodecyl amines and obtained **Amph-CBI** as the major product. All the products were purified by a combination of column chromatography on silica gel and size exclusion chromatography (Bio-beads, SX-3, chloroform). Both amphiphilic CBI derivatives have been fully characterized by ^1H and ^{13}C NMR spectroscopy, matrix-assisted laser desorption ionization mass spectrometry (MALDI-TOF-MS), high resolution mass spectrometry (HRMS) and elemental analysis. Both amphiphiles are molecularly soluble in THF and chloroform, and tend to form supramolecular aggregates in THF-water and chloroform-methanol solvent mixtures. The UV/Vis absorption as well as fluorescence spectra of molecularly dissolved **Amph-CBI** and **Bamph-CBI** in THF (1×10^{-5} M) showed all the typical spectral features of substituted coronene bisimides, reported in literature (Figure 2.1.1).^{14b} For both the derivatives, an absorption band with a vibronic fine structure was observed between 425-500 nm, whereas the absorption and fluorescence maxima appears at 339 nm and 486 nm, respectively.

2.1.3 Self-assembly in Solution

The self-assembly behavior of amphiphilic CBIs in solution was first probed by optical spectroscopic studies in THF-water solvent mixtures (Figure 2.1.1). Absorption and emission spectra of amphiphilic CBIs in THF-water mixtures of different compositions showed significant changes, consistent with the presence of aggregates at higher water percentages. For example, addition of an increasing amount of water (20-90 %) to a molecularly dissolved solution of amphiphilic CBIs in THF ($c = 1 \times 10^{-5}$ M) led to a gradual decrease in the intensities of the absorption bands at 339, 452 and 481 nm with a simultaneous increase in the intensity of the red-shifted bands at 355, 474 and 502 nm for **Amph-CBI** and 355, 472 and 506 nm for **Bamph-CBI** (Figure 2.1.1a and b). In addition, for both the derivatives, a gradual decrease in fluorescence intensity at 450-550 nm with the appearance of a new red-shifted, broad and structure-less bands at higher wavelengths were observed upon the addition of the bad solvent (water) into the THF solution of amphiphilic CBIs (Figure 2.1.1c and d). These features are diagnostic of the π - π interactions of the CBI chromophores as a result of the self-assembly of the amphiphiles and are similar to the J-aggregates of analogous perylene bisimide dyes.^{9h,i} Self-assembly induced changes in fluorescence could also be monitored by naked-eye, which showed different emission ranging from the green emission of molecularly dissolved chromophores in 100 % THF to the orange-red emission of the aggregates in solvent mixtures containing 90 % water (inset, Figure 2.1.1a). In case of **Bamph-CBI** significant aggregation

was observed only above 60% of water, whereas **Amph-CBI** showed the formation aggregates even at 50% water indicating better aggregation tendency of the latter CBI derivative. Interestingly, UV/Vis spectra of **Amph-CBI** at 50:50 ratio and **Bamph-CBI** at 30:70 THF-water compositions showed significant scattering, characteristic of large aggregates which gradually disappeared at higher water percentages (80-98 %) indicating the presence of two-different self-assembled structures for both CBI derivatives (*vide infra*). This is more evident from the different emission maxima observed for **Bamph-CBI** in 30:70 ($\lambda_{em} = 542$ nm) and 10:90 ($\lambda_{em} = 527$ nm) THF-water mixtures (Figure 2.1.1d).

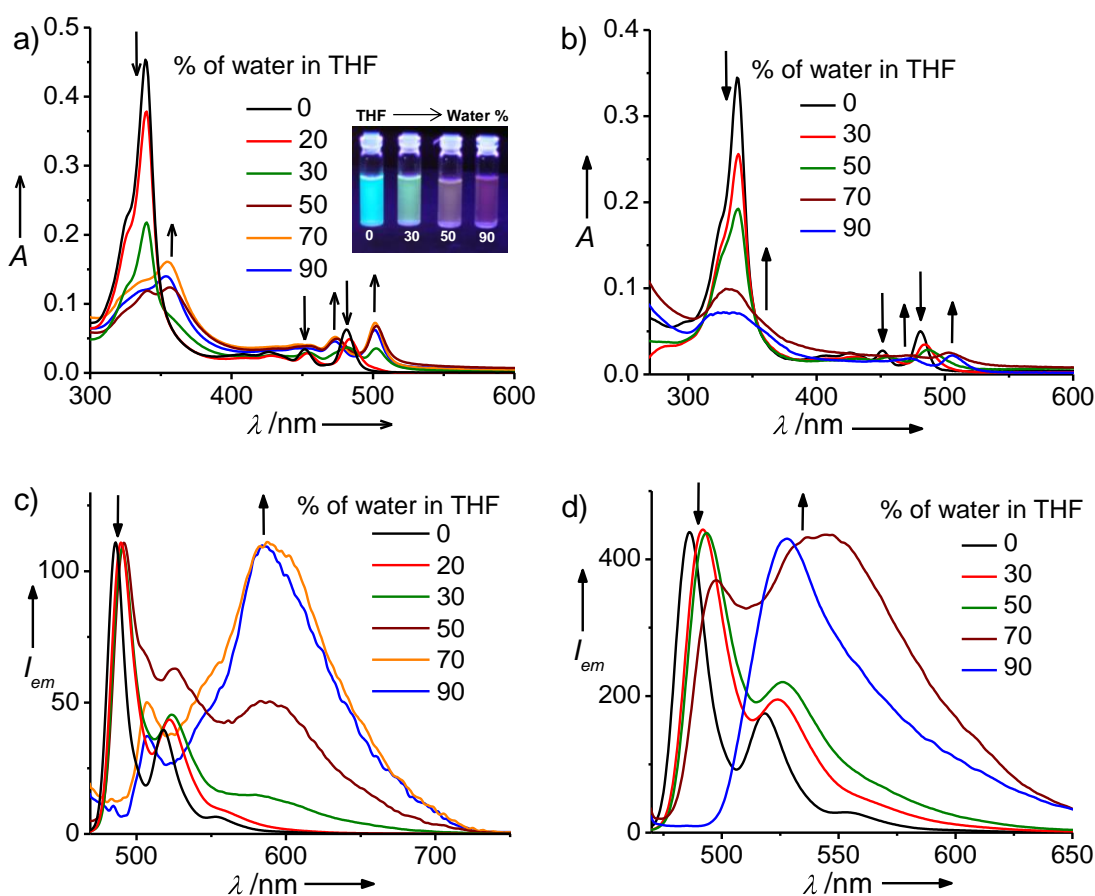


Figure 2.1.1. Absorption spectra of a) **Amph-CBI** and b) **Bamph-CBI** in THF-water mixtures. Inset of Figure 2.1.1a shows the photographs of **Amph-CBI** in THF-water mixtures under 365 nm UV light. Normalized emission spectra of c) **Amph-CBI** and d) **Bamph-CBI** in THF-water mixtures ($c = 0.01$ mM, $l = 4$ mm, $\lambda_{exc} = 450$ nm).

Dynamic light scattering (DLS) studies further supported the self-assembly and different types of aggregates for amphiphilic CBIs in THF-water solvent mixtures (Figure 2.1.2a and b). In the case of **Amph-CBI**, at 50% of water in THF, large aggregates with average hydrodynamic radius of 7 μ m were obtained, consistent with the scattering observed in the absorption spectra (Figure 2.1.2a). However, further increase in water composition resulted in significant decrease in the size of the aggregate, thus showing an average diameter of 75 nm

in 90% of water. Similarly, in case of **Bamph-CBI**, hydrodynamic radius of aggregates at 70% of water (~400 nm) is two times higher than at 90% of water (~150 nm) in THF (Figure 2.1.2b). Since, the increase in water composition is generally expected to result in more efficient and higher-order self-assembly, thereby an increase in the aggregate size, the unexpected decrease in the DLS dimensions at higher water percentages could be attributed to a completely different self-assembly (*vide infra*).

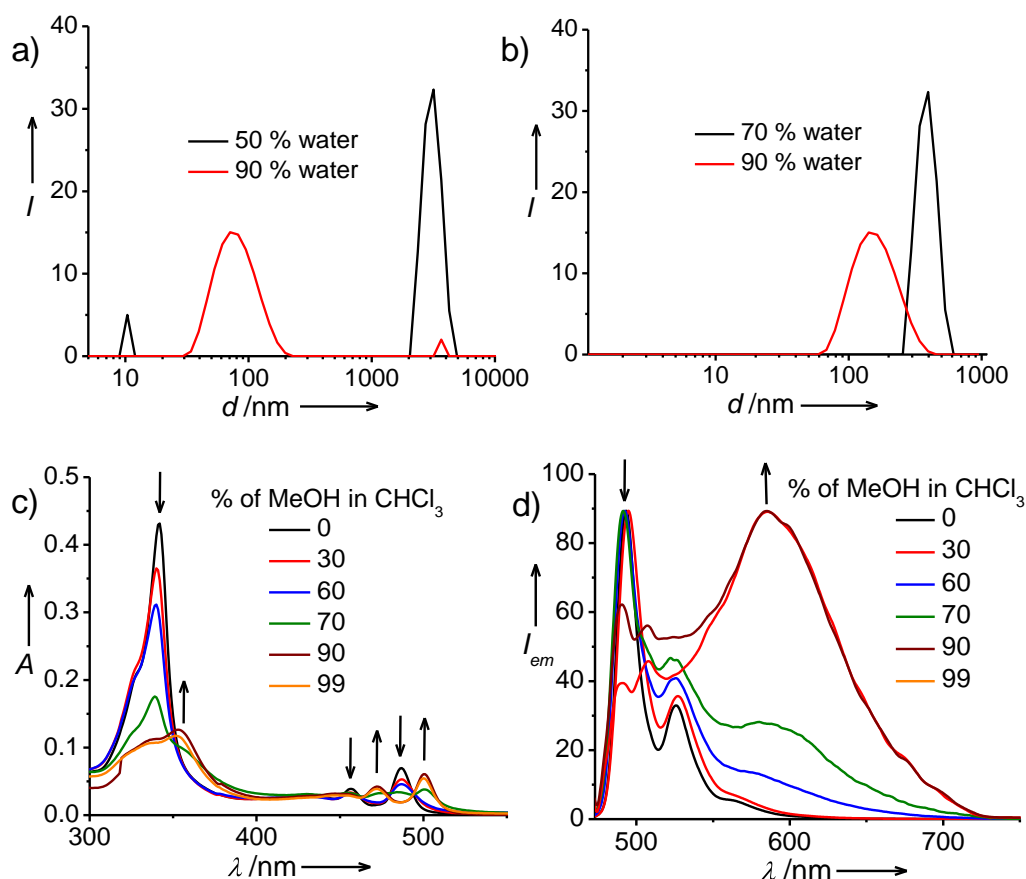


Figure 2.1.2. DLS size distribution profiles of a) **Amph-CBI** ($c = 0.1$ mM) and b) **Bamph-CBI** ($c = 0.1$ mM) with different amounts of water in THF. c) Absorption and d) normalized emission spectra of **Amph-CBI** in CHCl_3 -MeOH mixtures ($c = 0.01$ mM, $l = 4$ nm).

We have also studied the self-assembly of **Amph-CBI** in chloroform-methanol mixtures (Figure 2.1.2c and d). Similar to THF-water mixtures, increase in the methanol content in chloroform induced the J-aggregation, as evident from the red-shifted absorption and emission features at above 70% of methanol. However, compared to THF-water solvent mixture, in chloroform-methanol solvent mixture more amount of poor solvent (methanol) was required to induce significant aggregation in **Amph-CBI** due to its more solubility in this solvent mixture. Moreover, we have not observed two-different self-assembled structures in chloroform-methanol solvent mixture as in THF-water solvent mixture.

2.1.4 Morphology Studies

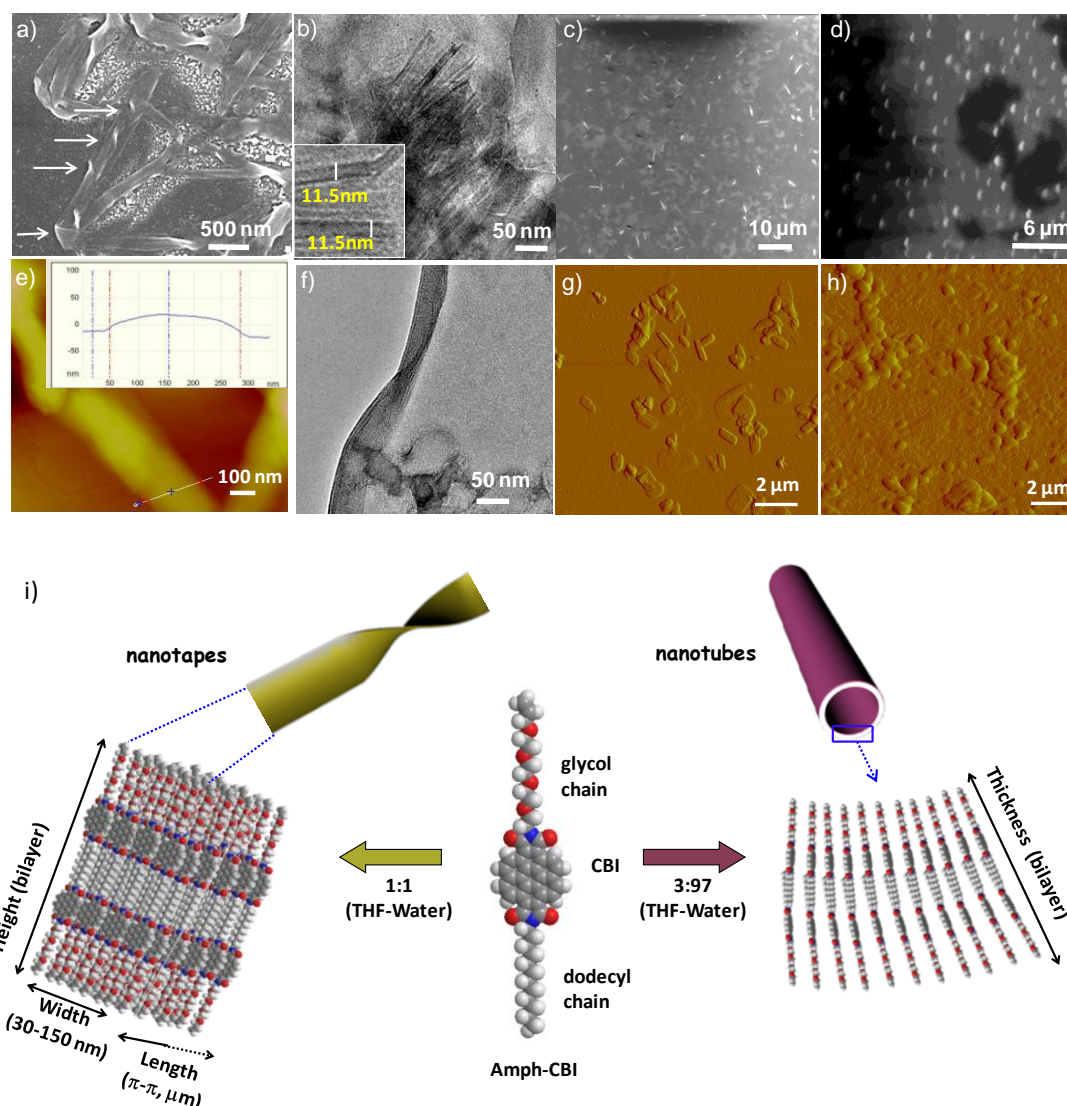


Figure 2.1.3. a) FE-SEM image of **Amph-CBI** nanotapes formed in 1:1 THF-water. b) TEM image of **Amph-CBI** nanotubes formed in 3:97 THF-water. FE-SEM images of **Bamph-CBI**; c) nanorods formed in 30:70 THF-water and d) nanoparticles formed in 10:90 THF-water mixtures. e) AFM and f) TEM images of **Amph-CBI** nanotapes formed in 1:1 THF-water. AFM images of **Bamph-CBI** g) nanorods formed in 30:70 THF-water and h) nanoparticles formed in 10:90 THF-water mixtures. i) Schematic representation of the bilayer self-assembly of **Amph-CBI** to nanotapes (left) and nanotubes (right). All morphology studies were performed with 0.1 mM solutions of amphiphilic CBIs.

In order to get insight into the morphology of the self-assembled amphiphilic CBIs, detailed microscopic studies have been performed (Figure 2.1.3). Remarkably, the observed differences in the dimensions of aggregates from DLS measurements is clearly reflected in the microscopic images, where large nanostructures were observed for both amphiphilic CBIs from the samples made from the lower percentages of water than the high percentage (Figure 2.1.3a-d). **Amph-CBI** in 50% THF-water solvent mixture showed long twisted nanotapes whereas the

corresponding 90% water in THF solvent mixture showed the formation of small nanotubes (Figure 2.1.3a and b). Similarly, **Bamph-CBI** also showed the formation nanorods at 70% of water and small nanoparticles at 90% water in THF (Figure 2.1.3c,d,g and h). The differences in the dimensions of these nanostructures are consistent with the observed changes in the hydrodynamic radius from the DLS measurements. This unambiguously suggest the formation different nanostructures in solution via self-assembly and not due to any surface drying effects.

The supramolecular nanostructures of **Amph-CBI** were further investigated in detail to understand the molecular packing in the self-assembled nanostructures. In case of **Amph-CBI**, the self-assembly can be envisaged to involve the stacking of bilayers of the **Amph-CBI** along the π - π stacking direction of the chromophore, characteristic of surfactant-like molecules. Detailed AFM investigation of the nanotapes showed a thickness of 30-40 nm, which could be due to the presence of multi-bilayers along the height of the tapes (Figure 2.1.3e). The presence of multi-bilayers is further supported by the TEM analysis of the self-assembled tapes that are negatively stained with uranyl acetate which showed a clear contrast for different layers with a thickness of 3.5 nm, at the twisted edges of the nanotapes (Figure 2.1.3f). These dimensions are in good correlation with the bilayer packing of the amphiphiles (excluding the hydrophilic part), in which the two hydrophobic chains are fully interdigitated at the interior, implying that the molecules are positioned with its long axis perpendicular to the π - π direction in the bilayer. Based on these observations the proposed molecular organization in the supramolecular tapes are schematically shown in Figure 2.1.3i, in which the CBI amphiphiles are arranged in a side-wise manner with its short-axis along the width of the nanotapes. The nanotubes **Amph-CBI** formed at high percentages of water (90-99 %) showed the presence of uniform width having an average diameter of ~12 nm (Figure 2.1.3b). Thickness of the nanotube side-walls is approximately 3.8 nm, which also matches with the interdigitated bilayer arrangement of **Amph-CBI** (4 nm), indicating that most of the nanotubes are single-walled (Figure 2.1.3i). These nanotubes might have been formed by the rolling of CBI bilayer sheets, as frequently observed in the case of surfactant molecules. It is evident that the morphology of the self-assembled **Amph-CBI** depends on THF-water solvent composition, although the molecular arrangement in both cases favors typical bilayers.

The self-assembled nanorods and nanoparticles of **Bamph-CBI** in solution are further studied using confocal laser microscopy (Figure 2.1.4a and b). The measurements were carried out by sealing the nanostructures solutions formed in THF-water mixtures between two glass cover slips. When samples were exposed to 453 nm laser, bright green fluorescent nanorods and nanoparticles were observed in THF-water mixtures. This further confirm the existence of **Bamph-CBI** nanostructures with distinct morphology in solution which are formed due to

differences in the packing/process of self-assembly by chromophores in different ratios of good (THF) and poor (water) solvents. Interestingly, FESEM images of **Amph-CBI** in 90:10 chloroform-methanol mixtures showed the formation of short nanorods having width of 30-50 nm and length of 500-800 nm (Figure 2.1.4c). In addition, TEM images of these rods stained with uranyl acetate showed the presence of uniform nanoscale striations of ~4 nm (Figure 2.1.4d). This clearly indicates that, these nanorods are formed by lateral association of **Amph-CBI** bilayers (4 nm) having interdigitated alkyl chains.

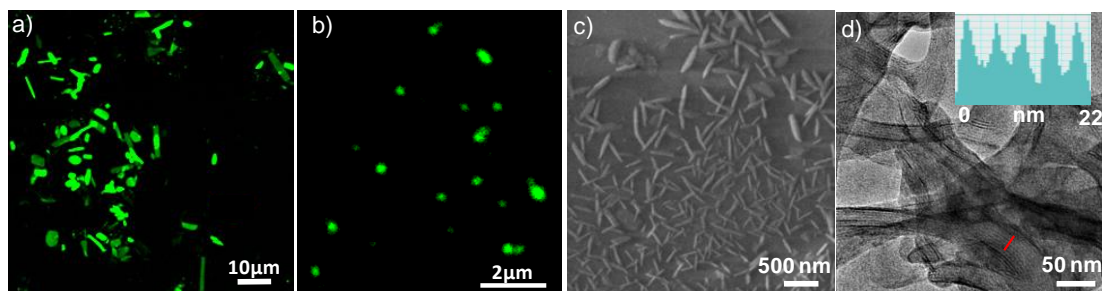


Figure 2.1.4. Confocal fluorescence microscopy images of **Bamph-CBI**; a) nanorods formed in 30:70 THF-water and b) nanoparticles formed in 10:90 THF-water mixtures. c) FE-SEM and d) TEM images of **Amph-CBI** nanorods formed in 10:90 CHCl_3 -MeOH solvent mixtures. Intensity profile in the inset of Figure 2.1.4d indicates the lateral association of **Amph-CBI** bilayers in the nanorods. All morphology studies were done with 0.1 mM solutions of amphiphilic CBIs.

2.1.5 OFET Device Characteristics

To validate the amphiphilic self-assembly of chromophores for enhanced charge transport, we have fabricated organic field effect transistor (OFET) devices using both amphiphilic CBI nanostructures as transport layers (Figure 2.1.5). CBI nanostructures formed in solution were directly introduced on the dielectric layer to form top-contact, bottom-gated FET structures. The observed positive output and transconductance curve with the applied positive gate voltage indicates the n-type transport in these self-assembled nanostructures. The estimated mobility is as high as $0.95\text{-}0.93 \times 10^{-2} \text{ cm}^2/\text{V}\cdot\text{s}$ for self-assembled nanotapes and nanotubes of **Amph-CBI** with an average mobility of $0.8 \times 10^{-2} \text{ cm}^2/\text{V}\cdot\text{s}$ (obtained from a set of 10 devices) (Table 2.1.1). Similarly nanorods of **Bamph-CBI** also displayed a high mobility of $0.75 \times 10^{-2} \text{ cm}^2/\text{V}\cdot\text{s}$ (Table 2.1.1). The current on/off ratios of all these nanostructures are good, typically in the order of 10^2 (Table 2.1.1). However, nanoparticles of **Bamph-CBI** showed poor mobilities typically in the order of $10^{-4} \text{ cm}^2/\text{V}\cdot\text{s}$, probably due to the lack of long range 1D π -stacking order (Table 2.1.1). Though electron mobility¹⁷ is more sensitive to defects and external factors than hole mobility, the observed high electron mobility in amphiphilic CBI nanostructures while operating at ambient conditions is probably due to their well defined order as a result of amphiphilic self-assembly. This amphiphilic self-assembly approach is also

recently employed in NIR absorbing diketopyrrolopyrrole polymers to improve their molecular ordering, as a result these polymers exhibit high field effect electron mobilities ($>1 \text{ cm}^2/\text{V.s}$).¹⁸

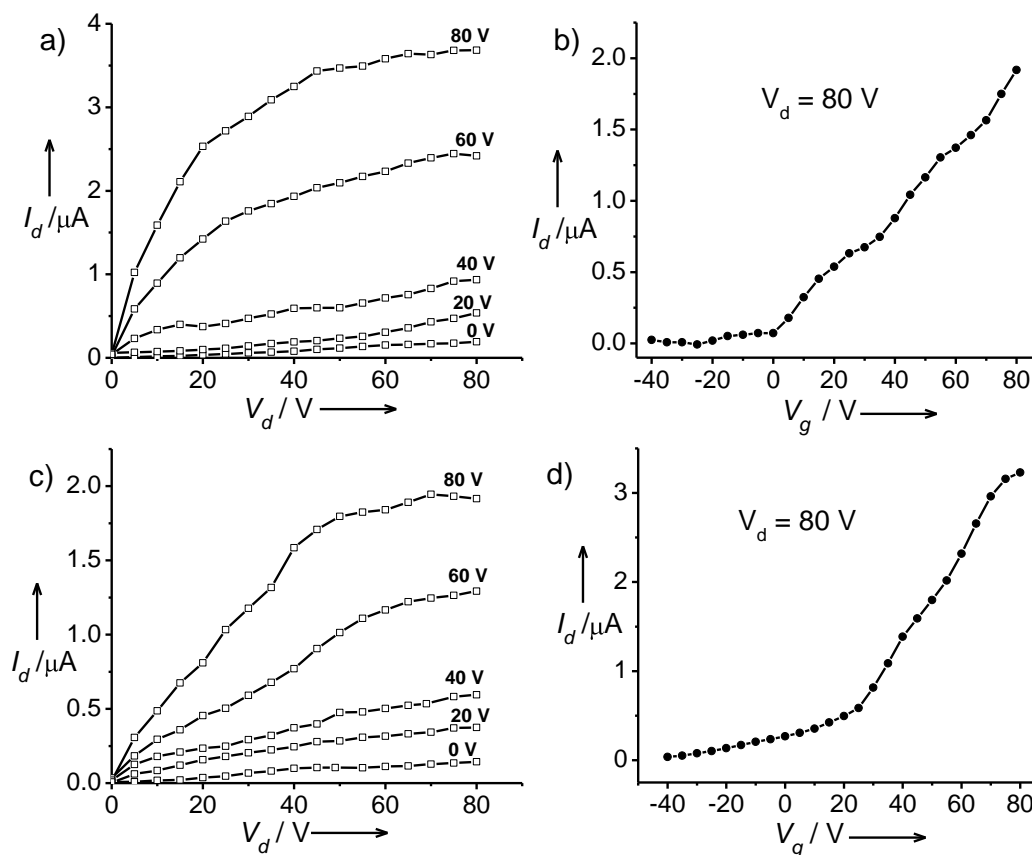


Figure 2.1.5. a) and b) Typical output and transconductance curves for **Amph-CBI** tubes in top contact bottom gate FET with L (channel length) $\approx 20 \mu\text{m}$, W (channel width) $\approx 1 \text{ mm}$ and C (capacitance per unit area of the gate insulator layer) $\approx 4 \text{ nF/cm}^2$. c) and d) Typical output and transconductance curves for **Bamph-CBI** nanorods in top contact bottom gate FET with $L \approx 20 \mu\text{m}$, $W \approx 1 \text{ mm}$ and $C \approx 4 \text{ nF/cm}^2$.

Table 2.1.1. Electron mobilities and on/off ratios of various nanostructures of amphiphilic CBIs

| Morphology | $\mu_{max} (\text{cm}^2/\text{V.s})$ | I_{on}/I_{off} |
|------------------------------------|--------------------------------------|------------------|
| Nanotapes (Amph-CBI) | 0.0095 | 100 |
| Nanotubes (Amph-CBI) | 0.0093 | 100 |
| Nanorods (Bamph-CBI) | 0.00756 | 100 |
| Nanoparticles (Bamph-CBI) | 10^{-4} | 100 |

2.1.6 Conclusions

In conclusion, we have described the synthesis and self-assembling properties of new *n*-type coronene bisimide amphiphiles, decorated with polar glycol and non-polar dodecyl chains. The amphiphilic nature of these molecules allowed their self-assembly in water similar to classical surfactants, while promoting strong π - π interactions between hydrophobic coronene aromatic cores, to result in stable nanostructures. Interesting features of the present systems are their diverse optical properties and self-assembled morphology of the self-assembly, which can be fine-controlled by the solvent-composition. The OFET devices made from these self-assembled CBI nanostructures of amphiphilic CBIs displayed high electron mobility in the order of 10^{-2} cm²/V.s. Moreover, these functional chromophores could be further exploited for efficient energy and electron transfer processes and are promising functional components for mesoscopic optoelectronics.

2.1.7 Experimental Section

General Methods: Field Emission Scanning Electron Microscopy (FE-SEM) measurements were performed on a NOVA NANO SEM 600 (FEI) by drop casting the solutions on glass substrate followed by drying in vacuum and were operated with an accelerating voltage of 30 kV. Transmission Electron Microscopy (TEM) measurements were performed on a JEOL, JEM 3010 operated at 300 kV. Samples were prepared by placing a drop of the solution on carbon coated copper grids followed by drying at room temperature. The images were recorded with an operating voltage 300 kV. In order to get a better contrast, some samples were stained with uranyl acetate (1 wt % in water) before the measurements. Atomic Force Microscopy (AFM) measurements were performed on a Veeco diInnova SPM operating in tapping mode regime. Micro-fabricated silicon cantilever tips doped with phosphorus and with a frequency between 235 and 278 kHz and a spring constant of 20-40 Nm⁻¹ were used. The samples were prepared by drop casting aggregate solutions on glass substrate and dried in air followed by vacuum drying at 40 °C. Electronic absorption spectra were recorded on a Perkin Elmer Lambda 900 UV-Vis-NIR Spectrometer and emission spectra were recorded on Perkin Elmer Ls 55 Luminescence Spectrometer. UV-Vis and emission spectra were recorded in a 4 mm path length cuvette. Fluorescence spectra of solutions were recorded with 450 nm excitation wavelength. NMR spectra were obtained with a Bruker AVANCE 400 (400 MHz) Fourier transform NMR spectrometer with chemical shifts reported in parts per million (ppm) with respect to TMS. Matrix-assisted laser desorption ionization time-of-flight (MALDI-TOF) spectra were obtained on a Bruker ultraflex 2 MALDI-TOF mass spectrometer with α -cyano-4-hydroxycinnamic acid matrix. Dynamic light scattering Experiments (DLS) measurements were carried out using a NanoZS (Malvern UK) employing a 532 nm laser at a back scattering angle

of 173°. Confocal Microscopy imaging was done at room temperature using a Zeiss LSM 510 META laser scanning confocal microscope. The microscope objective of 63X (NA 1.4) and 20X (NA 0.5) were employed. Sample was prepared by sealing the solution between two glass plates.

Field Effect Mobility Measurements: Field effect mobility measurements were performed on top contact bottom gate transistor structures. The fabrication of the FET device involved coating of Al electrode (10^{-6} mbar, 40 nm thick) by physical vapour deposition on standard RCA treated clean glass substrates. This was followed by coating of the dielectric layer of hydroxyl free divinyl tetramethylsiloxane bis (benzocyclobutene) at 800 rpm for 1 min and annealed in a glove box atmosphere at 290 °C. The effective capacitance per unit area (C) of the dielectric films measured using Keithley 4200 semiconductor parameter analyser was found to be ≈ 4 nF/cm² for films of thickness 0.5–0.6 μ m. The surface of the dielectric was further treated with hexamethyldisilazane in liquid by spin coating at 1500 rpm for 30 s and annealing at 110 °C for 2 h in N₂ atmosphere. This was followed by solution casting the nanostructures of CBI amphiphiles in appropriate THF and water compositions to obtain the films of thickness ≈ 300 nm. The source-drain Au electrode was also vapour deposited (10^{-6} mbar, 40 nm thick). The electrical characterization of the FETs were done using a standard set up of Keithley 2400 Source meters and a high impedance electrometer (Keithley 6514). The measurements were also cross checked with Keithley 2400 semiconductor parameter analyser. The performance parameters of the devices were extracted in the saturation regime from the transconductance characteristics curves by using the equation: $I_{ds} = (\mu_{FET}WC/2L)(V_g - V_{th})^2$, where I_{ds} is the drain current, W and L are respectively the channel width and length, C is the capacitance per unit area of the gate insulator layer, and V_g and V_{th} are the gate voltage and the threshold voltage, respectively. The mobility values reported are the median values obtained from the measurements performed on 10–15 devices in each case which are representative of the general trends in these molecules.

2.1.7a Synthesis

CDA^{14b} and 3,6,9,12-tetraoxapentadec-14-en-1-amine¹⁹ were synthesized according to the literature methods and dodecyl amine was purchased from Merck.

Amph-CBI: Coronene dianhydride (**CDA**) (500 mg, 1.14 mmol), dodecylamine (320 mg, 1.73 mmol), 3,6,9,12-tetraoxapentadec-14-en-1-amine (410 mg, 1.73 mmol), imidazole (20 g) and zinc acetate (317 mg, 1.73 mmol) were thoroughly mixed and heated with stirring at 140 °C for overnight. Then the reaction mixture was transferred under hot conditions to a 1M HCl solution and it was extracted with chloroform. The organic layer was repeatedly washed with 1M HCl

followed by saturated NaCl solution and dried over anhydrous Na₂SO₄ and then filtered. After evaporating the chloroform the obtained brown colour crude product was purified by column chromatography (silica gel, 100% chloroform to 5% MeOH in chloroform) and Bio-Beads (S-X3) column chromatography to yield 23% of **Amph-CBI** (243 mg) as yellowish orange powder. ¹H NMR (400 MHz, CDCl₃): δ 8.53 (d, *J* = 8 Hz, 2H, ArH), 8.44 (d, *J* = 8 Hz, 2H, ArH), 7.57 (d, *J* = 9 Hz, 2H, ArH), 7.54 (d, *J* = 9 Hz, 2H, ArH), 5.85-5.92 (m, 1H, CH=CH₂), 5.14-5.26 (m, 2H, CH=CH₂), 3.97-3.99 (m, 4H), 4.1 (m, 2H), 3.73-3.55 (m, 10H, OCH₂), 3.89-3.88 (m, 4H), 1.88-1.90 (m, 2H, CH₂), 1.32-1.42 (m, 18H, CH₂), 0.91 (t, *J* = 7 Hz, 3H, CH₃); ¹³C NMR (100 MHz, CDCl₃): δ 168.5, 168.3, 134.7, 127.2, 126.8, 123.0, 122.8, 121.9, 121.8, 119.9, 119.8, 117.1, 116.5, 72.2, 70.7, 70.7, 70.6, 70.6, 70.2, 69.4, 68.2, 38.1, 37.2, 31.9, 29.79, 29.7, 29.7, 29.6, 29.4, 29.3, 28.9, 27.1, 22.7, 14.2; MALDI-TOF MS *m/z* 845.41 [M+Na]⁺, 862.09 [M+K]⁺; Analytical calculation for C₅₁H₅₄N₂O₈·0.5H₂O: C 73.62 H 6.66, N 3.37. Found: C 73.99, H 6.55, N 3.10.

Bamph-CBI: CDA (300 mg, 0.682 mmol), 3,6,9,12-tetraoxapentadec-14-en-1-amine (476 mg, 2.04 mmol), imidazole (16 g) and zinc acetate (188 mg, 1.024 mmol) were thoroughly mixed and heated with stirring to reflux (150 °C) for overnight. Then the reaction mixture was transferred under hot conditions to a 1M HCl solution and subsequently it was extracted with chloroform. The organic layer was repeatedly washed with 1M HCl. Then the organic layer was washed with saturated NaCl solution, dried using anhydrous Na₂SO₄ and then filtered. After evaporating the solvent under reduced pressure the crude product, which was reddish orange in colour was purified by column chromatography (silica gel, started with 3% methanol in chloroform to 10% methanol in chloroform) and Bio-beads (S-X3) column chromatography to yield, 40% of **Bamph-CBI** as yellowish orange powder. ¹H NMR (400 MHz, CDCl₃): δ 9.48 (d, *J* = 7.6 Hz, 4H, ArH), 8.51 (d, *J* = 7.6 Hz, 4H, ArH), 5.86-5.79 (m, 2H, CH=CH₂), 5.21-5.09 (m, 4H, CH=CH₂), 4.286 (t, *J* = 6 Hz, 4H), 4.079 (t, *J* = 5.6 Hz, 4H), 3.93-3.48 (m, 28H, OCH₂); ¹³C NMR (100 MHz, CDCl₃): δ 168.9 134.7, 127.6, 123.7, 122.6, 121.2, 120.8, 117.1, 72.2, 70.8, 70.7, 70.6, 70.5, 70.2, 69.4, 68.3, 37.4, 29.7; HRMS (ESI): Calculated for C₅₀H₅₀N₂O₁₂Na- 893.3261 [M+Na]⁺ and found 893.3191.

2.1.8 References

1. a) F. Würthner, *Angew. Chem. Int. Ed.* **2001**, *40*, 1037; b) F. J. M. Hoeben, P. Jonkheijm, E.W. Meijer, A. P. H. J. Schenning, *Chem. Rev.* **2005**, *105*, 1491.
2. a) A. P. H. J. Schenning, E. W. Meijer, *Chem. Commun.* **2005**, 3245; b) A. Ajayaghosh, S. J. George, A. P. H. J. Schenning, *Top. Curr. Chem.* **2005**, *258*, 83; c) T. Ishi-i, S. Shinkai, *Top. Curr. Chem.* **2005**, *258*, 119; d) J. Wu, W. Pisula, K. Müllen, *Chem. Rev.* **2007**, *107*,

- 718; e) A. Ajayaghosh, V. K. Praveen, *Acc. Chem. Res.* **2007**, *40*, 644; f) A. Mishra, C.-Q. Ma, P. Bäuerle, *Chem. Rev.* **2009**, *109*, 1141; g) Z. Chen, A. Lohr, C. R. Saha-Möller, F. Würthner, *Chem. Soc. Rev.* **2009**, *38*, 564.
3. a) A. Saeki, Y. Koizumi, T. Aida, S. Seki, *Acc. Chem. Res.* **2012**, *45*, 1193; b) M. Hasegawa, M. Iyoda, *Chem. Soc. Rev.* **2010**, *39*, 2420; c) T. Lei, J. Pei, *J. Mater. Chem.* **2012**, *22*, 785.
4. a) C. D. Dimitrakopoulos, P. R. L. Malenfant, *Adv. Mater.* **2002**, *14*, 99; b) P. T. Herwig, K. Müllen, *Adv. Mater.* **1999**, *11*, 480; c) T. Yasuda, M. Saito, H. Nakamura, T. Tsutsui, *Appl. Phys. Lett.* **2006**, *89*, 182108.
5. a) Y. Yamamoto, T. Fukushima, Y. Suna, N. Ishii, A. Saeki, S. Seki, S. Tagawa, M. Taniguchi, T. Kawai, T. Aida, *Science* **2006**, *314*, 1661; b) H. J. Kim, T. Kim, M. Lee, *Acc. Chem. Res.* **2011**, *44*, 72; c) H. Shao, J. Seifert, N. C. Romano, M. Gao, J. J. Helmus, C. P. Jaronec, D. A. Modarelli, J. R. Parquette, *Angew. Chem. Int. Ed.* **2010**, *49*, 7688; d) C. Wang, Z. Wang, X. Zhang, *Acc. Chem. Res.* **2012**, *45*, 608; e) M. Kumar, S. J. George, *Chem. Eur. J.* **2011**, *17*, 11102; f) K. V. Rao, K. Jayaramulu, T. K. Maji, S. J. George, *Angew. Chem. Int. Ed.* **2010**, *49*, 4218.
6. a) T. Shimizu, M. Masuda, H. Minamikawa, *Chem. Rev.* **2005**, *105*, 1401; b) L. A. Estroff, A. D. Hamilton, *Chem. Rev.* **2004**, *104*, 1201.
7. a) F. J. M. Hoeben, I. O. Shklyarevskiy, M. J. Pouderoijen, H. Engelkamp, A. P. H. J. Schenning, P. C. M. Christianen, J. C. Maan, E. W. Meijer, *Angew. Chem. Int. Ed.* **2006**, *45*, 1232; b) X. Zhang, Z. Chen, F. Würthner, *J. Am. Chem. Soc.* **2007**, *129*, 4886; c) L. C. Palmer, S. I. Stupp, *Acc. Chem. Res.* **2008**, *41*, 1674; d) S. J. George, T. F. A. de Greef, R. Bovee, van J. L. J. Dongen, A. P. H. J. Schenning, E. W. Meijer, *Chem. Asian J.* **2009**, *4*, 910.
8. ***For phenylenevinylene based self-assembly, see:*** a) A. Ajayaghosh, S. J. George, *J. Am. Chem. Soc.* **2001**, *123*, 5148; b) A. P. H. J. Schenning, P. Jonkheijm, E. Peeters, E. W. Meijer, *J. Am. Chem. Soc.* **2001**, *123*, 409; c) S. J. George, A. Ajayaghosh, P. Jonkheijm, A. P. H. J. Schenning, E. W. Meijer, *Angew. Chem. Int. Ed.* **2004**, *43*, 3422; d) J. F. Hulvat, M. Sofos, K. Tajima, S. I. Stupp, *J. Am. Chem. Soc.* **2005**, *127*, 366; e) P. Jonkheijm, P. van der Shoot, A. P. H. J. Schenning, E. W. Meijer, *Science* **2006**, *313*, 80; ***For porphyrin and phthalocyanine based self-assembly, see:*** f) H. Engelkamp, S. Middelbeek, R. J. M. Nolte, *Science* **1999**, *284*, 785; g) T. Ishi-i, R. Iguchi, E. Snip, M. Ikeda, S. Shinkai, *Org. Lett.* **2001**, *3*, 3634; h) M. Shirakawa, N. Fujita, S. Shinkai, *J. Am. Chem. Soc.* **2003**, *125*, 13934; i) R. van Hameren, P. Schön, A. M. van Buul, J. Hoogboom, S. V. Lazarenko, J. W. Gerritsen, H. Engelkamp, P. C. M. Christianen, H. A. Heus, J. C. Maan, T. Rasing, S. Speller, A. E. Rowan, J. A. A. W. Elemans, R. J. M. Nolte,

- Science* **2006**, *314*, 1433; **For HBC based self-assembly, see:** j) J. P. Hill, W. Jin, A. Kosaka, T. Fukushima, H. Ichihara, T. Shimomura, K. Ito, T. Hashizume, N. Ishii, T. Aida, *Science* **2004**, *304*, 1481; k) S. Xiao, J. Tang, T. Beetz, X. Guo, N. Tremblay, T. Siegrist, Y. Zhu, M. Steigerwald, C. Nuckolls, *J. Am. Chem. Soc.* **2006**, *128*, 10700; l) W. Jin, Y. Yamamoto, T. Fukushima, N. Ishii, J. Kim, K. Kato, M. Takata, T. Aida, *J. Am. Chem. Soc.* **2008**, *130*, 9434; m) X. Feng, W. Pisula, T. Kudernac, D. Wu, L. Zhi, S. De Feyter, K. Müllen, *J. Am. Chem. Soc.* **2009**, *131*, 4439; **For thiophene based self-assembly, see:** n) I. O. Shklyarevskiy, P. Jonkheijm, P. C. M. Christianen, A. P. H. J. Schenning, E. W. Meijer, O. Henze, A. F. M. Kilbinger, W. J. Feast, A. D. Guerso, J.-P. Desvergne, J. C. Maan, *J. Am. Chem. Soc.* **2005**, *127*, 1112; o) Jatsch, A.; Kopyshchev, A.; Mena-Osteritz, E.; Bäuerle, P. *Org. Lett.* **2008**, *10*, 961; p) S. Schmid, E. Mena-Osteritz, A. Kopyshchev, P. Bäuerle, *Org. Lett.* **2009**, *11*, 5098; **For TTF based self-assembly, see:** q) T. Kitahara, M. Shirakawa, S. Kawano, U. Beginn, N. Fujita, S. Shinkai, *J. Am. Chem. Soc.* **2005**, *127*, 14980; r) J. Puigmartí-Luis, V. Laukhin, A. P. del Pino, J. Vidal-Gancedo, C. Rovira, E. Laukhina, D. B. Amabilino, *Angew. Chem., Int. Ed.* **2007**, *46*, 238; s) J. Puigmartí-Luis, Á. P. del Pino, V. Laukhin, L. N. Feldborg, C. Rovira, E. Laukhina, D. B. Amabilino, *J. Mater. Chem.* **2010**, *20*, 466; **For Miscellaneous p-type self-assembly, see:** s) M. Ikeda, M. Takeuchi, S. Shinkai, *Chem. Commun.* **2003**, 1354; t) P. Babu, N. M. Sangeetha, P. Vijayakumar, U. Maitra, K. Rissanen, A. R. Raju, *Chem. Eur. J.* **2003**, *9*, 1922; u) A. Ajayaghosh, R. Varghese, S. Mahesh, V. K. Praveen, *Angew. Chem. Int. Ed.* **2006**, *45*, 7729; v) A. Ajayaghosh, R. Varghese, V. K. Praveen, S. Mahesh, *Angew. Chem. Int. Ed.* **2006**, *45*, 3261.
9. a) F. Würthner, *Chem. Commun.* **2004**, 1564 and the references cited therein; b) K. Sugiyasu, N. Fujita, S. Shinkai, *Angew. Chem. Int. Ed.* **2004**, *43*, 1229; c) K. Balakrishnan, A. Datar, R. Oitker, H. Chen, J. Zuo, L. Zang, *J. Am. Chem. Soc.* **2005**, *127*, 10496; d) Y. Che, A. Datar, K. Balakrishnan, L. Zang, *J. Am. Chem. Soc.* **2007**, *129*, 7234; e) X. Zhang, Z. Chen, F. Würthner, *J. Am. Chem. Soc.* **2007**, *129*, 4886; f) F. Würthner, B. Hanke, M. Lysetska, G. Lambright, G. S. Harms, *Org. Lett.* **2005**, *7*, 967-970; g) X. Zhang, S. Rehm, M. M. Safont-Sempere, F. Würthner, *Nat. Chem.* **2009**, *1*, 623; h) F. Würthner, T. E. Kaiser, C. R. Saha-Möller, *Angew. Chem. Int. Ed.* **2011**, *50*, 3376; i) T. E. Kaiser, V. Stepanenko, F. Würthner, *J. Am. Chem. Soc.* **2009**, *131*, 6719.
10. a) T. Ishi-i, Y. Ono, S. Shinkai, *Chem. Lett.* **2000**, 808; b) T. Homma, K. Harano, H. Isobe, E. Nakamura, *Angew. Chem. Int. Ed.* **2010**, *49*, 1665.
11. a) P. Mukhopadhyay, Y. Iwashita, M. Shirakawa, S.-i. Kawano, N. Fujita, S. Shinkai, *Angew. Chem. Int. Ed.* **2006**, *45*, 1592; b) H. Shao, T. Nguyen, N. C. Romano, D. A.

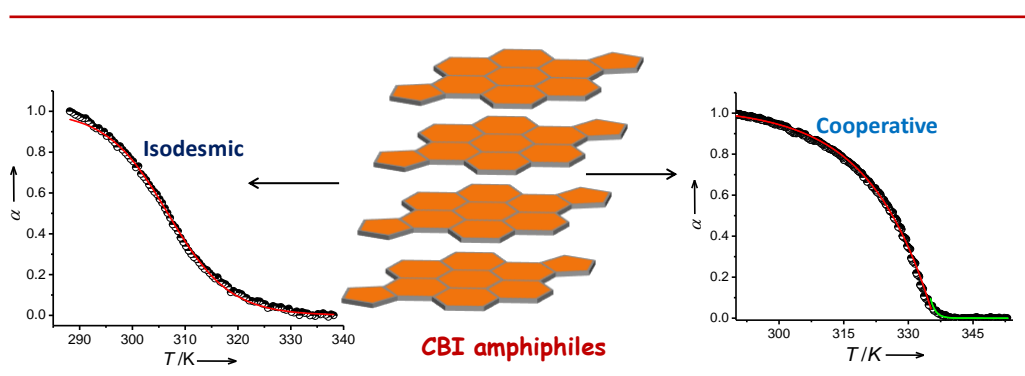
- Modarelli, J. R. Parquette, *J. Am. Chem. Soc.* **2009**, *131*, 16374; c) K. K. McGrath, K. Jang, K. A. Robins, D.-C. Lee, *Chem. Eur. J.* **2009**, *15*, 4070.
12. a) B. Narayan, S. P. Senanayak, A. Jain, K. S. Narayan, S. J. George, *Adv. Funct. Mater.* **2013**, (DOI: 10.1002/adfm.201202298); b) J. Yin, Y. Zhou, T. Lei, J. Pei, *Angew. Chem. Int. Ed.* **2011**, *50*, 6320.
13. a) Y. Yamamoto, T. Fukushima, Y. Suna, N. Ishii, A. Saeki, S. Seki, S. Tagawa, M. Taniguchi, T. Kawai, T. Aida, *Science*, **2006**, *314*, 1761; b) Y. Yamamoto, G. Zhang, W. Jin, T. Fukushima, N. Ishii, A. Saeki, S. Seki, S. Tagawa, T. Minari, K. Tsukagoshi, T. Aida, *Proc. Natl. Acad. Sci. U.S.A.* **2009**, *106*, 21051.
14. a) U. Rohr, P. Schlichting, A. Böhm, M. Gross, K. Meerholz, C. Bräuchle, K. Müllen, *Angew. Chem. Int. Ed.* **1998**, *37*, 1434; b) S. Alibert-Fouet, I. Seguy, J.-F. Bobo, P. Destruel, H. Bock, *Chem. Eur. J.* **2007**, *13*, 1746; c) Z. An, J. Yu, B. Domercq, S. C. Jones, S. Barlow, B. Kippelen, S. R. Marder, *J. Mater. Chem.* **2009**, *19*, 6688.
15. a) G. John, M. Masuda, Y. Okada, K. Yase, T. Shimizu, *Adv. Mater.* **2001**, *13*, 715; b) J. H. Jung, G. John, K. Yoshida, T. Shimizu, *J. Am. Chem. Soc.* **2002**, *124*, 10674.
16. H. Usta, A. Facchetti, T. J. Marks, *Acc. Chem. Res.* **2011**, *44*, 501.
17. a) N. Peng, Q. Zhang, O. K. Tan, N. Marzari, *Nanotechnology* **2008**, *19*, 465201; b) I. Maeng, S. Lim, S. J. Chae, Y. H. Lee, H. Choi, J. H. Son, *Nano Lett.* **2012**, *12*, 551; c) N. Kurra, V. S. Bhadram, C. Narayana, G. U. Kulkarni, *ACS Appl. Mater. Interfaces* **2012**, *4*, 1030.
18. C. Kanimozhi, N. Yaacobi-Gross, K. W. Chou, A. Amassian, T. D. Anthopoulos, S. Patil, *J. Am. Chem. Soc.* **2012**, *134*, 16532.
19. Y.-B. Lim, S. Park, E. Lee, H. Jeong, J.-H. Ryu, M. S. Lee, M. Lee, *Biomacromolecules*, **2007**, *8*, 1404.

PART-2 . 2

Mechanistic Insights into the Self-Assembly Process of Coronene Bisimide Amphiphiles*

Abstract

*In this section, investigations on the self-assembly mechanisms of amphiphilic coronene bisimides (CBIs) using chiroptical properties as a probe are described. Chirality is introduced to the CBI core either via covalent (**cAmph-CBI**) or non-covalent routes (**C-CBI-ATP**). Temperature dependent circular dichroism (CD) studies revealed that covalent and non-covalent chiral CBI amphiphiles follows isodesmic and cooperative mechanisms, respectively during self-assembly. On other hand, co-assembly of **cAmph-CBI** with its achiral analogue, **Amph-CBI** resulted in a cooperative self-assembly process and exhibited remarkable chiral amplification as evident from Sergeant and Soldiers experiments. Although, self-assembly and optoelectronic properties of various amphiphilic π -systems are widely studied, investigation on their self-assembly mechanisms remains elusive.*



*Two manuscripts based on this work are under preparation.

2.2.1 Introduction

Self-assembly of semiconducting π -systems offers an efficient approach to build functional organic nanostructures under thermodynamic control.¹ Supramolecular ordering of π -systems in their self-assembled nanostructures plays a crucial role on their device performance.² Though self-assembled nanostructures of various p-type and n-type semiconducting oligomers are utilized for various optoelectronic functions,³ only few of these studies deal with the mechanisms⁴ of their self-assembly process. Understanding the mechanism of self-assembly process is extremely important for this field, to obtain complex and multicomponent self-assemblies. Amphiphilic π -systems are of particular interest owing to their ability to self-assemble in polar solvents with high association constants to yield well defined nanostructures.⁵ Moreover, self-assembled nanostructures of π -conjugated amphiphiles are shown to have improved optoelectronic functions compared to their lipophilic counter parts.⁶

The process of one dimensional (1D) self-assembly or supramolecular polymerization of π -conjugated oligomers is often described by two mechanisms; isodesmic⁷ and cooperative⁸. In an isodesmic self-assembly, monomer addition to a growing stack is governed by a single equilibrium constant and it is independent of the degree of polymerization. On the other hand, cooperative self-assembly is similar to nucleation-elongation mechanism in which chain growth is preceded by the formation of less favourable nucleus and it is a two step process. In this mechanism, large polymer chains are formed above and below a certain concentration and temperature of monomers, respectively. Chirality is being used as a spectroscopic probe to understand and for the accurate determination of self-assembly mechanisms of π -conjugated oligomers.⁹ In this context, both concentration¹⁰ and temperature⁴ dependent methods have been reported for elucidating the self-assembly mechanisms. However, temperature-dependent studies are shown to be more appropriate because they provide a greater number of data points, which decreases the error in fitting to the desired model. Various electroactive π -conjugated amphiphiles such as oligo(p-phenylenevinylene)s (OPVs),¹¹ perylene bisimides (PBIs),¹² hexabenzocoronenes (HBCs)¹³ made with chiral side chains have been shown to exhibit exciton coupled circular dichroism (CD) signal in the aggregated state, due to the preferential helical assembly governed by chiral side chains. However reports pertaining to the self-assembly mechanism of π -conjugated amphiphiles are rare.¹⁴ Recently we have reported the self-assembly of novel n-type achiral coronene bisimide (CBI) amphiphiles in THF-water mixtures (see Part-2.1).¹⁵ Organic field effect transistor (OFET) made from nanostructures of these amphiphiles showed high electron mobilities in the order of 10^{-2} cm²/V.s. This has motivated us

to further investigate their self-assembly mechanism, which would render control on their functional properties.

In this section, we describe the self-assembly mechanism of CBI amphiphiles using temperature dependent CD measurements. For this purpose chirality is introduced to the CBI molecules via covalent and non-covalent approaches. In the covalent approach, chiral CBI amphiphile (**cAmph-CBI**) in which CBI core is rendered with chiral (S)-(-)-3,7-dimethyloctyl and tetraethylene glycol chains was used (Figure 2.2.1). On the other hand, in case of non-covalent approach, anionic adenosine 5'-triphosphate disodium salt (ATP) was used as a chiral guest to induce chirality to the cationic CBI cores (**C-CBI**) in their co-assembly (Figure 2.2.1). Although, chiral induction and co-assembly of various chromophores with **ATP** have been reported, their self-assembly mechanisms are not yet investigated.¹⁶ Assemblies of both covalent and non-covalent amphiphiles showed strong excitonically coupled CD signal suggesting transfer of side chain or guest chirality to the CBI core during self-assembly. Temperature dependent CD studies provided insight into the mechanisms of self-assembly process of both the amphiphiles. Although, individual **cAmph-CBI** assembly follows sigmoidal pathway, its co-assembly with achiral derivative (**Amph-CBI**) follows a cooperative mechanism. Similarly, co-assembly of **C-CBI** and **ATP** also follows a cooperative mechanism. Interestingly, **cAmph-CBI** forms chiral nanotubes which are formed by coiling of left-handed helical tapes suggesting the expression of molecular chirality at macroscopic level. Moreover, remarkable chiral amplification was observed when small amount of (<10 mol%) of **cAmph-CBI** was co-assembled with **Amph-CBI**.

2.2.2 Design Strategy and Synthesis

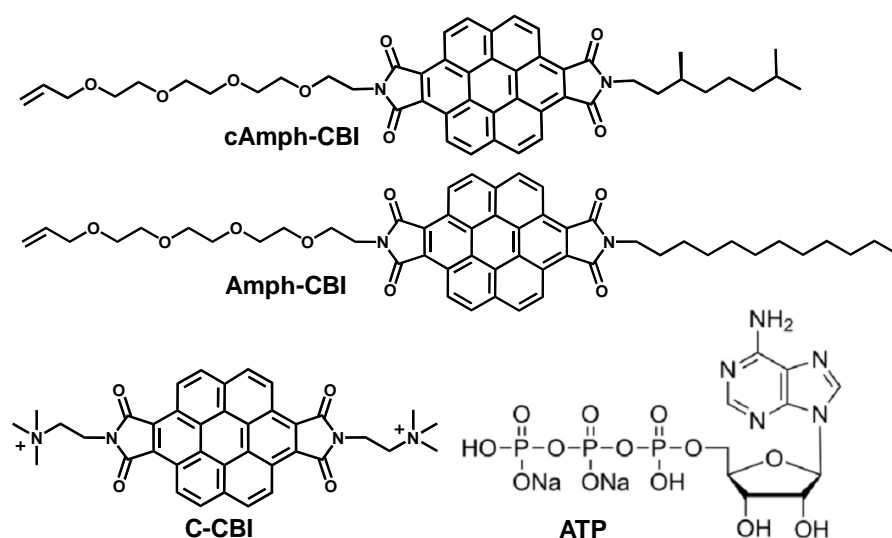


Figure 2.2.1. Molecular structures of CBI amphiphiles and ATP.

cAmph-CBI, **Amph-CBI** and **C-CBI**, were synthesized through imidation of coronene dianhydride (**CDA**) and fully characterized (Figure 2.2.1 and see experimental section). In case of **cAmph-CBI**, we have performed statistical reaction on **CDA** with glycol and chiral (S)-(-)-3,7-dimethyloctyl similar to **Amph-CBI**. All the products were purified by a combination of column chromatography on silica gel and size exclusion chromatography (Bio-beads, SX-3, chloroform). **C-CBI** was synthesized by treating **CDA** with N,N-dimethyl ethylenediamine followed by reacting with methyl iodide. All the CBI derivatives were fully characterized by NMR spectroscopy, matrix-assisted laser-desorption ionization mass spectrometry (MALDI-TOF-MS). Both **cAmph-CBI** and **Amph-CBI** are molecularly soluble in THF and form J-aggregates in THF-water mixtures, whereas **C-CBI** is molecularly soluble in acetonitrile and DMSO and forms H-aggregates in water (Figure 2.2.2). The UV/Vis absorption as well as fluorescence spectra of molecularly dissolved **cAmph-CBI** and **Amph-CBI** in THF (1×10^{-5} M) (see Part-2.1) and **C-CBI** in acetonitrile (1×10^{-5} M) showed all the typical spectral features of substituted coronene bisimides.

2.2.3 Self-Assembly in Solution

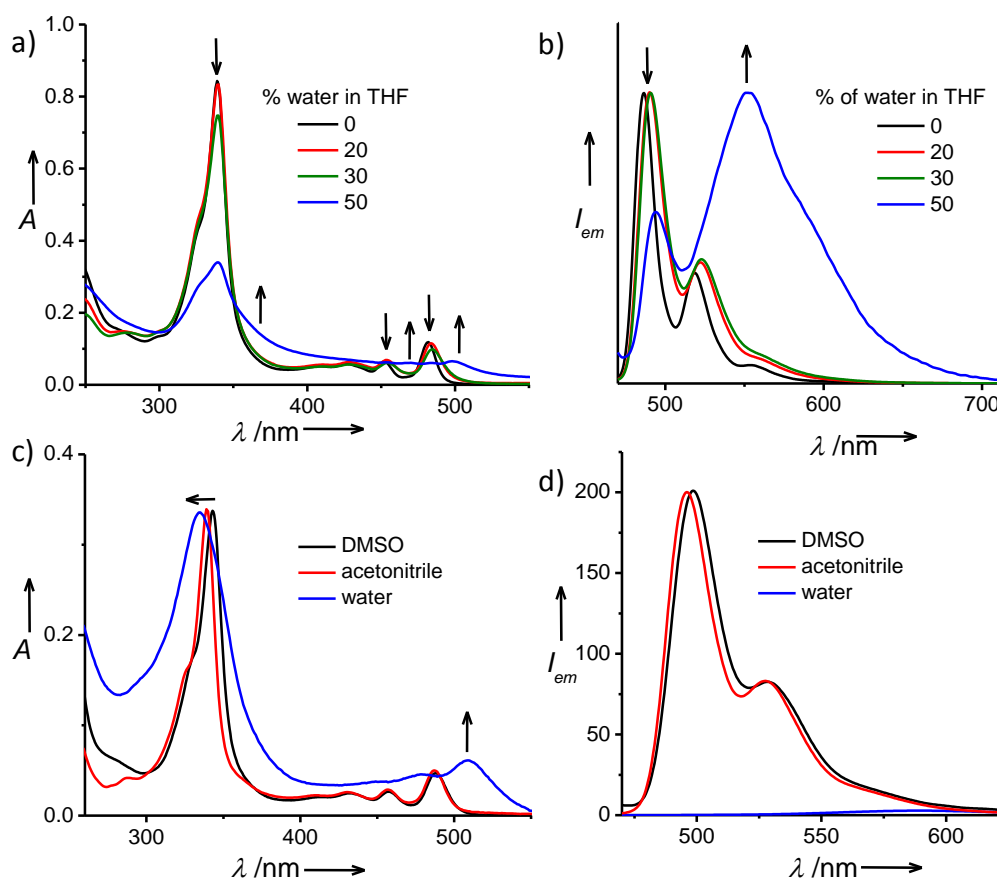


Figure 2.2.2. a) Absorption spectra and b) normalized emission spectra of **cAmph-CBI** in THF-water mixtures ($c = 0.01$ mM, $l = 4$ mm, $\lambda_{ex} = 450$ nm). c) Normalized absorption and d) emission spectra of **C-CBI** in various solvents ($c = 0.01$ mM, $l = 4$ mm, $\lambda_{ex} = 450$ nm).

The self-assembly behavior of all the CBIs in solution was first probed by optical spectroscopic studies (Figure 2.2.2). Similar to **Amph-CBI**, significant changes were observed in the absorption and emission spectra of **cAmph-CBI** with increasing water percentages in THF-water mixtures, characteristic of excitonically coupled J-aggregates. In 1:1 THF-water mixture, the intensities of the characteristic absorption bands of **cAmph-CBI** at 339, 452 and 481 nm decreased with simultaneous increase in the intensity of the red-shifted bands at 360, 475 and 504 nm (Figure 2.2.2a). In addition, gradual decrease in fluorescence intensity of bands at 450-550 nm with the appearance of new red-shifted, broad and structure-less bands at higher wavelengths (555 nm) with increase in water percentages are also consistent with the formation of J-aggregates by **cAmph-CBI** (Figure 2.2.2b). **C-CBI** exists in molecularly dissolved state in acetonitrile and DMSO as evident from the absorption features at 339, 457 and 487 nm in acetonitrile and 343, 457 and 487 nm in DMSO, and shows green emission between 450-600 nm (Figure 2.2.2c and d). However in water, absorption maxima is blue shifted by 5 nm (from 339 to 334 nm) and 9 nm (from 343 to 334 nm) compared to its monomer absorption in acetonitrile and DMSO, respectively. In addition, the emergence of new broad absorption band at 508 nm and significant quenching of monomer emission in presence of water suggest the H-type excitonically coupled aggregates (Figure 2.2.2c and d).^{4a}

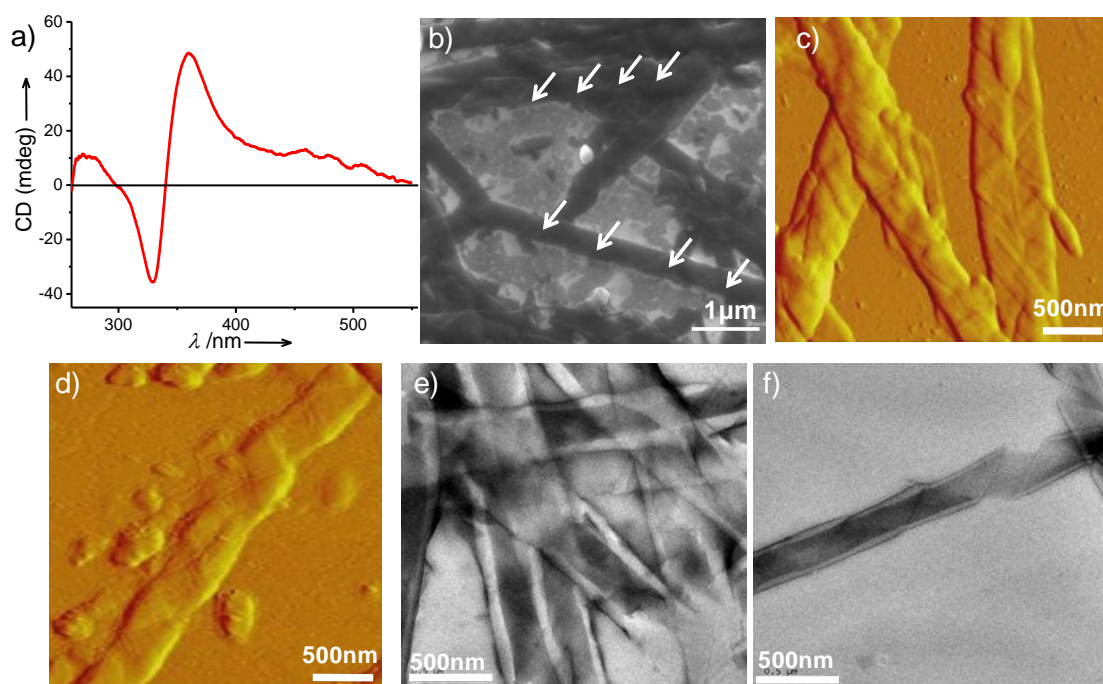


Figure 2.2.3. a) CD spectrum of **cAmph-CBI** in 1:1 THF-water mixture after cooling from 338 K to 293 K ($c = 0.02$ mM, $l = 10$ nm). b) FE-SEM, c), d) AFM, e) and f) TEM images of **cAmph-CBI** aggregates formed in 1:1 THF-water mixture ($c = 0.1$ mM).

The presence of chiral side chain in **cAmph-CBI** further allowed us to characterize its supramolecular aggregates through CD spectroscopy (Figure 2.2.3a). Appearance of strong excitonically coupled CD signal, upon cooling a 1:1 THF-water solution of **cAmph-CBI** from 338 K to 293 K, confirms the transfer of side chain chirality to the CBI core during their self-assembly. In the CD spectrum, positive Cotton effect with monosignation between 450-520 nm (S_0 - S_1 transition) and positive bisignated Cotton effect between 310-420 nm (S_0 - S_n transition) with zero crossing at 339 are observed (Figure 2.2.3a). This further confirms the helical 1D supramolecular polymerization of CBI monomers in 1:1 THF-water mixture with right-handed helical organization of chromophores. Microscopic investigation of these assemblies revealed that, similar to **Amph-CBI**, **cAmph-CBI** also forms nanotapes in which chirality is expressed at the macroscopic level (Figure 2.2.3b-f). Interestingly, they form coiled nanotubes, which are formed by preferential left-handed helical coiling of nanotapes due to the presence of chiral centre in **cAmph-CBI**, which provides a chiral bias during the supramolecular polymerization of **cAmph-CBI** monomers. CD studies indicate that chromophores are in right-handed helical organization which is opposite to the helicity observed in their nanostructures (Figure 2.2.3b-f). It has been shown in literature that, macroscopic helicity of the nanostructures may not have direct correlation with the helical organization of chromophore or molecular chirality.¹⁷ Though most of the nanostructures are nanotubes, partially coiled ones were also observed which provides a clue for the hierarchies involved in the formation of these nanotubes (Figure 2.2.3d and f). Detailed analysis of microscopy images revealed that these nanotubes are 10-15 μm in length (FE-SEM, AFM), 30-40 nm in height (AFM), and 300-350 nm in width (TEM).

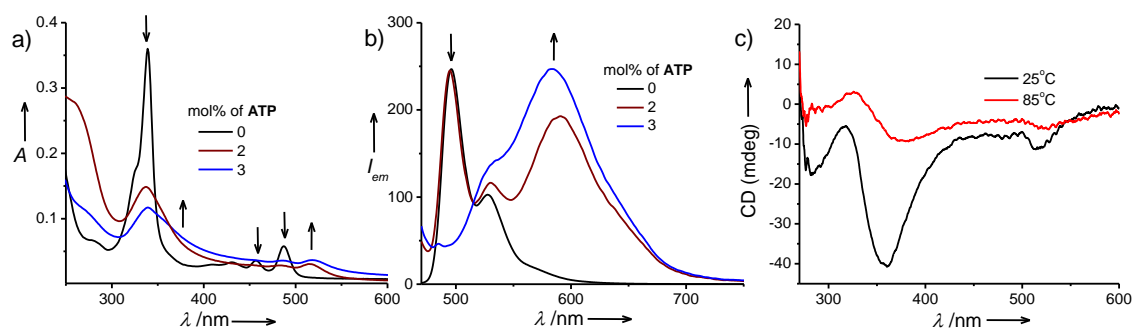


Figure 2.2.4. a) Absorption and b) emission spectra of **C-CBI** with different equivalents of **ATP** in 5% HEPES buffer containing acetonitrile solution ($c = 0.01 \text{ mM}$, $l = 4 \text{ mm}$, $\lambda_{ex} = 450 \text{ nm}$). c) CD spectra of **C-CBI** with two equivalents of **ATP** in 5% HEPES buffer containing acetonitrile solution at 25°C and at 85°C ($c = 0.1 \text{ mM}$, $l = 2 \text{ mm}$).

On the other hand, **C-CBI** is achiral and chirality is induced into the assembly through anionic **ATP** disodium salt via non-covalent ionic interactions (Figure 2.2.4). The co-assembly of **C-CBI** monomers with **ATP** induced aggregation as well as chirality to the otherwise achiral **C-CBI** core. The co-assembly experiments were performed in 5% and 20% HEPES ((4-(2-hydroxyethyl)-1-piperazineethanesulfonic acid) buffer containing acetonitrile and DMSO

respectively, where **C-CBI** is molecularly soluble. When 0.01 mM of **C-CBI** was treated with different equivalents of **ATP** (0-3 equivalents) in 5% HEPES buffer containing acetonitrile, the absorption bands of **C-CBI** at 339, 452 and 481 nm were gradually decreased with the simultaneous appearance of the red-shifted bands at 360, 485 and 515 nm indicating the J-type aggregation of **C-CBI** upon co-assembly with **ATP** (Figure 2.2.4a). In line with absorption changes, the appearance of a new red-shifted, structure-less band at 580-590 nm upon co-assembly with **ATP** is also consistent with the J-aggregation of **C-CBI** (Figure 2.2.4b). These J-aggregates are further studied using CD spectroscopy to understand the chirality induction to **C-CBI** by **ATP** (Figure 2.2.4c). Interestingly, these J-aggregates showed strong CD signal with negative Cotton effects at all transitions (Figure 2.2.4c). However these aggregates are very stable and failed to melt completely even at 85 °C. The morphology of these aggregates was investigated in detail using FE-SEM, TEM, DLS and confocal microscopy (Figure 2.2.5). DLS size distribution profiles showed the formation of aggregates in solution with hydrodynamic radius centered at 100 nm with narrow size distribution (Figure 2.2.5a, inset). This is further evidenced from the FE-SEM images which showed the spherical morphology of these aggregates (nanoparticles), with size of 100-200 nm (Figure 2.2.5a and b). TEM further confirmed that these nanoparticles have vesicular morphology (Figure 2.2.5c). These nanoparticles in solution were further characterized by confocal microscopy which showed the presence of yellow fluorescent nanoparticles (Figure 2.2.5d). The yellow emission of these nanoparticles is in consistent with their J-aggregates emission ($\lambda_{em} = 580-590$ nm).

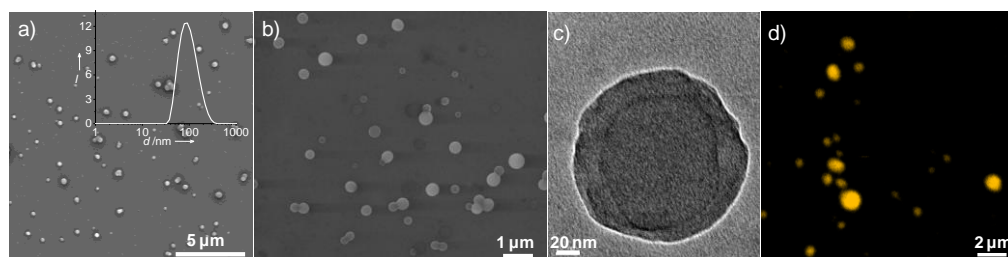


Figure 2.2.5. Microscopy studies of **C-CBI** aggregates upon co-assembly with **ATP** in 5% HEPES buffer containing acetonitrile solution ($c = 0.01$ mM). FE-SEM images upon co-assembly with a) two and b) three equivalents of **ATP**. Inset of 'a' shows the size distribution profile of **C-CBI** co-assembly with two equivalents of **ATP**, probed through DLS. c) TEM and d) confocal fluorescence microscopy images ($\lambda_{ex} = 453$ nm) of **C-CBI** co-assembly with two equivalents of **ATP**.

Similarly, **C-CBI** ($c = 0.1$ mM) monomers in 20% HEPES buffer containing DMSO was titrated with increasing equivalents (0-2) of **ATP**, the absorption maximum at 343 nm showed gradual decrease in absorbance and 10 nm (343-334 nm) blue-shift (Figure 2.2.6a). In addition, the appearance of a new red-shifted absorption band at 520 nm with gradual quenching of **C-CBI** monomer emission with increasing equivalents (0-2) of **ATP** clearly indicates that, **ATP** induce H-type aggregation to the **C-CBI** monomers in this solvent mixture

(Figure 2.2.6a and b). Further increase in the equivalents of **ATP** did not show significant changes in the aggregation of **C-CBI** (Figure 2.2.6c). In contrast to **C-CBI-ATP** J-aggregates formed in acetonitrile-HEPES buffer mixture, these aggregates are thermo-reversible and complete melting of aggregates into monomers could be observed at high temperatures (333-353 K), depending on the ratio between **C-CBI** and **ATP** in the co-assembly. Interestingly, upon cooling the solution of **C-CBI** and **ATP** from 360 K, strong excitonically coupled CD signal was observed which further confirms the successful induction of chirality by non-covalent guest (**ATP**) to the CBI core and their helical organization in the co-assembly (Figure 2.2.6d). In this case, the CD signal showed positive Cotton effects with monosignation between 520-420 nm (S_0 - S_1 transition) and positive bisignated cotton effect between 440-300 nm (S_0 - S_n transition).

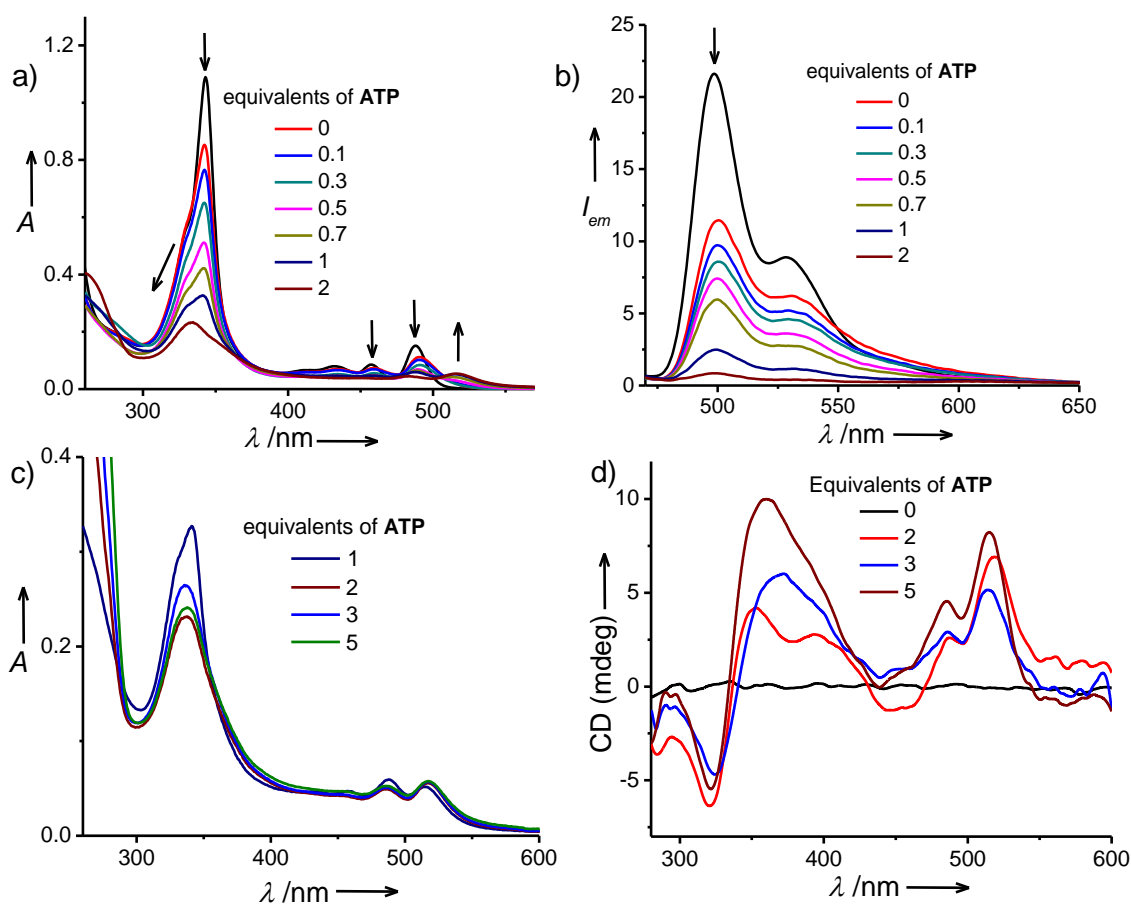


Figure 2.2.6. a) Absorption and b) emission spectra of **C-CBI** co-assembly with different equivalents of **ATP** in 20 % HEPES buffer containing DMSO solution ($c = 0.1$ mM, $l = 1$ mm, $\lambda_{ex} = 450$ nm). c) Absorption spectra of **C-CBI** at higher equivalents of **ATP** in 20% HEPES buffer containing DMSO solution ($c = 0.1$ mM, $l = 1$ mm). d) CD spectra of **C-CBI** with different equivalents of **ATP** in 20 % HEPES buffer containing DMSO solution after cooling from 360 K to 288 K ($c = 0.1$ mM, $l = 2$ mm).

Microscopy investigations on **C-CBI-ATP** co-assembled aggregates showed the formation of nanofibers with different density of bundling depending on the ratio between **C-**

CBI and **ATP** (Figure 2.2.7). In presence of two equivalents of **ATP**, FE-SEM images of the co-assembly showed the formation of short nanofibers of 150-200 nm in length and 30 nm in width with less degree of bundling (Figure 2.2.7a). On the other hand, at five equivalents of **ATP**, nanofibers with high degree of bundling were formed (Figure 2.2.7b-d). This could be due to inter-stack interactions at higher equivalents of **ATP**, probably due to the cross-linking by excess of **ATP** molecules. The supramolecular chirality of these assemblies could not be visualized in their nanostructures using any microscopic techniques.

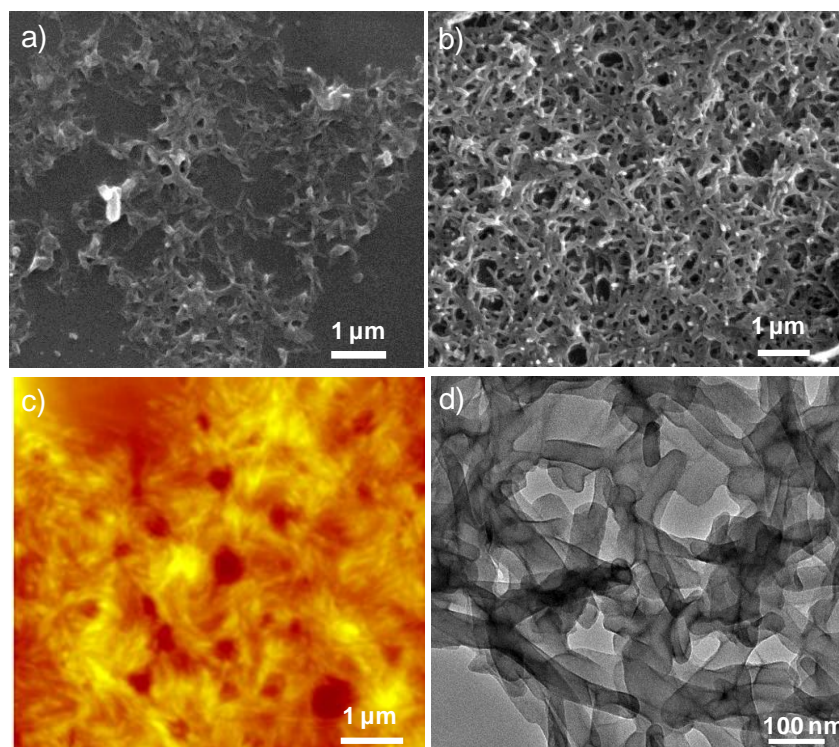


Figure 2.2.7. a) FE-SEM image of **C-CBI** co-assembly with two equivalents of **ATP** in 20% HEPES buffer containing DMSO solution. b) FE-SEM, c) AFM and d) TEM images of **C-CBI** aggregates formed by the co-assembly with five equivalents of **ATP** in 20% HEPES buffer containing DMSO solution ($c = 0.1$ mM).

2.2.4 Mechanisms of Self-Assembly

Self-assembly mechanism of both covalent (**cAmph-CBI**) and non-covalent (**C-CBI-ATP**) chiral CBI amphiphilic derivatives was investigated using temperature dependent CD spectroscopy measurements. Since both **cAmph-CBI** in 1:1 THF-water mixture and **C-CBI-ATP** in 20% HEPES containing DMSO solution show excitonically coupled CD signal upon cooling from their molecularly dissolved state, we have monitored their molar ellipticity at a particular wavelength as a function of temperature to get insights into the mechanism of self-assembly.

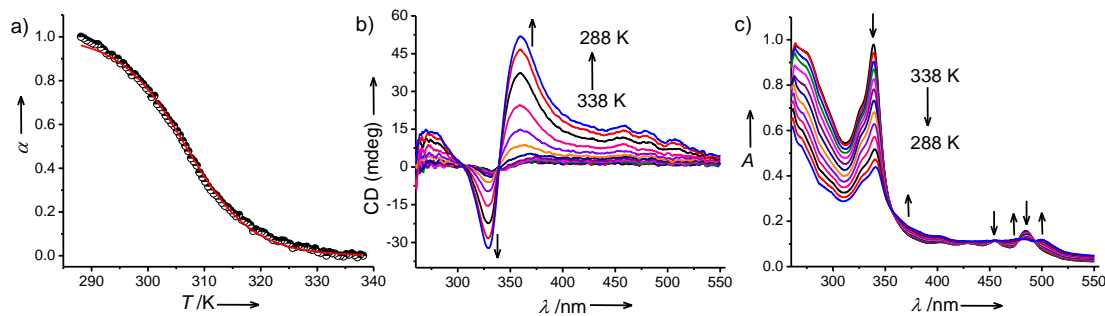


Figure 2.2.8. a) Fraction of aggregation (α) monitored at 329 nm versus temperature of **cAmph-CBI** in 1:1 THF-water mixture with a cooling rate of 2 K/min. The solid line in 'a' shows the fit to the temperature dependent isodesmic model. Corresponding temperature dependent CD and absorption spectra are shown in b) and c), respectively ($c = 0.02$ mM, $l = 10$ mm).

cAmph-CBI (0.02 mM) in 1:1 THF-water solution at 338 K, did not show any molar ellipticity, indicating the absence of any excitonic coupling between chromophores at high temperatures (Figure 2.2.8a and b). This is further supported by the corresponding absorption spectrum at 338 K which showed the monomeric features of **cAmph-CBI** (Figure 2.2.8c). This clearly indicates that, **cAmph-CBI** molecules exist as monomers above 338 K. When the solution was cooled from 338 K at a rate of 2 K/min while monitoring molar ellipticity at 329 nm, the resultant cooling curve clearly shows a sigmoidal behavior which is characteristic of isodesmic self-assembly (Figure 2.2.8a). Moreover, this cooling curve fits well with the temperature-dependent isodesmic model proposed by Smulders et al.¹⁰ Using this model, we have further calculated various thermodynamic parameters governing the supramolecular polymerization. The average enthalpy of polymerization is found to be -147.84 kJ/mol and the estimated melting temperature (T_m) of stacks is 306.7 K.

Further, we investigated the self-assembly mechanism and chiral amplification in the co-assembly of **cAmph-CBI** and achiral **Amph-CBI** using Sergeant and Soldiers experiments¹⁸ and temperature dependent CD experiments (Figure 2.2.9). In a typical experimental procedure, monomeric solutions of both Sergeant (**cAmph-CBI**) and Soldiers (**Amph-CBI**) were mixed together in THF and injected into water to result in a final solution having 1:1 ratio of THF-water mixture. Remarkably, upon cooling these mixtures, strong excitonically coupled CD signal with bisignated Cotton effects at all transitions was observed (Figure 2.2.9a). This unambiguously proves the efficient co-assembly between **cAmph-CBI** and **Amph-CBI**. Moreover, in the co-assembly molar ellipticity of S_0-S_1 transition (440-510 nm) is more prominent and bisignated with opposite sign compared to individual **cAmph-CBI** assembly (Figure 2.2.9a). This clearly indicates that, molecular organization in the co-assembly is mainly governed by **Amph-CBI**. Interestingly, in the co-assembly, CD signal showed sharp rise in intensity with increase in the mol% of **cAmph-CBI** with maximum CD intensity at 7.5 mol%

(Figure 2.2.9b). This indicates remarkable chiral amplification in the present co-assembly system. Though, **cAmph-CBI** self-assembles via isodesmic mechanism, the observed efficient chiral amplification in the co-assembly suggests that, supramolecular polymerization in the co-assembly could be cooperative.

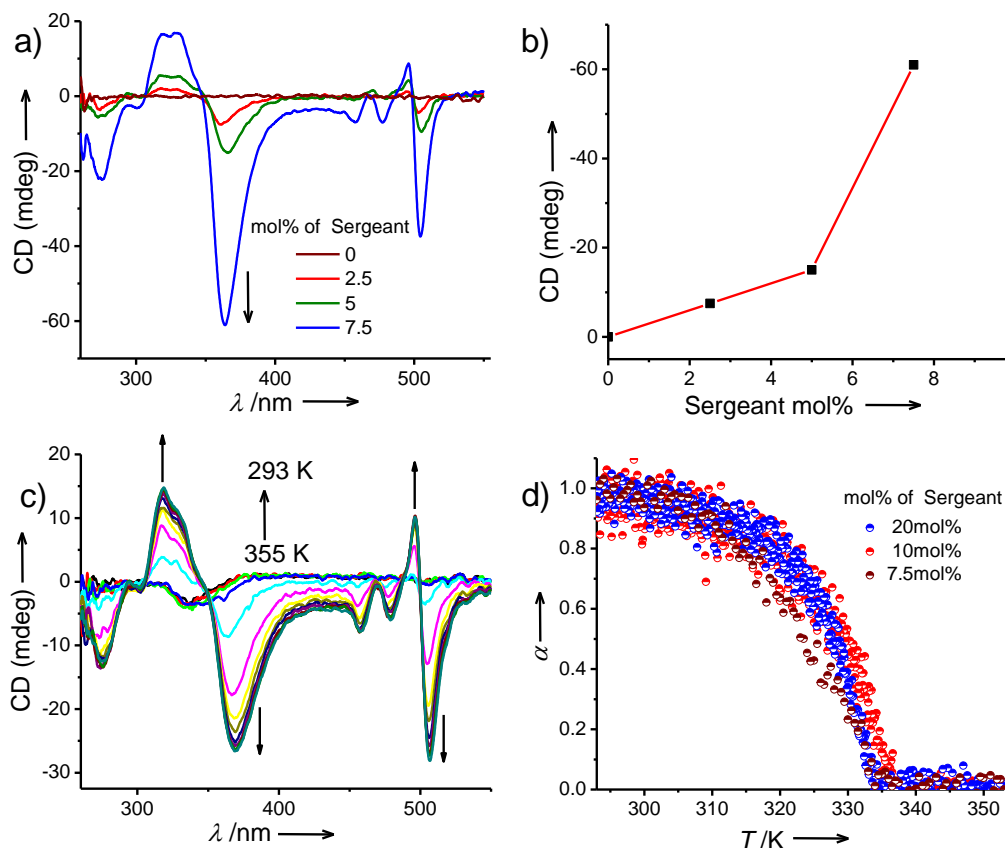


Figure 2.2.9. a) CD spectra of **Amph-CBI** (*Soldier*) co-assembled with different mol% of **cAmph-CBI** (*Sergeant*) in 1:1 THF-water mixture after cooling from 353 K to 293 K and corresponding b) plot of CD (mdeg) versus mol% of **cAmph-CBI** (*Sergeant*). c) Temperature dependent CD spectra of **Amph-CBI** co-assembled with 20 mol% of **cAmph-CBI** in 1:1 THF-water mixture with a cooling rate of 2 K/min. d) Fraction of aggregation (α), monitored at 505 nm versus temperature of **Amph-CBI** co-assembled with different mol% of **cAmph-CBI** (*Sergeant*) in 1:1 THF-water mixture with a cooling rate of 2 K/min ($c = 0.02$ mM, $l = 10$ mm).

Temperature dependent CD measurements provided mechanistic insights into co-assembly process. In a typical experimental procedure, the co-assembled solutions having different mol% (2.5-20) of Sergeants were cooled from their monomeric state (>350 K) at the rate of 2 K/min, while monitoring molar ellipticity at 505 nm. Remarkably, the CD profiles clearly showed a non-sigmoidal behavior, indicating cooperative mechanism of **Amph-CBI** and **cAmph-CBI** co-assembly (Figure 2.2.9c and d). The cooling curve of **Amph-CBI** obtained from temperature dependent absorption spectra monitored at 500 nm also shows non-sigmoidal behavior, indicating cooperative supramolecular polymerization of achiral CBI amphiphile (Figure 2.2.10a and b). This could be the reason for cooperative self-assembly of the co-

assembly as it is mainly controlled by **Amph-CBI** (up to 20 mol% of **cAmph-CBI**). However, this co-assembly process is turned out to be kinetically controlled, because the temperature dependent CD experiments at slower cooling rate (0.5 K/min) showed no chiral induction to **Amph-CBI** from **cAmph-CBI** in the co-assembly (Figure 2.2.10c). This could be because of the significant differences in their self-assembly features and mechanisms of these CBIs which facilitate their phase separation under slow cooling rates. This is further evident from significant differences observed in the aggregate absorption spectra of **Amph-CBI** and **cAmph-CBI** (Figure 2.2.10d). In 1:1 THF-water, **cAmph-CBI** showed absorption maximum at 341 nm and vibronic features corresponding to S_0 - S_1 transition displayed broad features with low intensity. On the other hand, **Amph-CBI** displayed maximum at 342 nm with a shoulder band at 355 nm (which is absent in **cAmph-CBI**) and the vibronic features of S_0 - S_1 transition are more intense than **cAmph-CBI**.

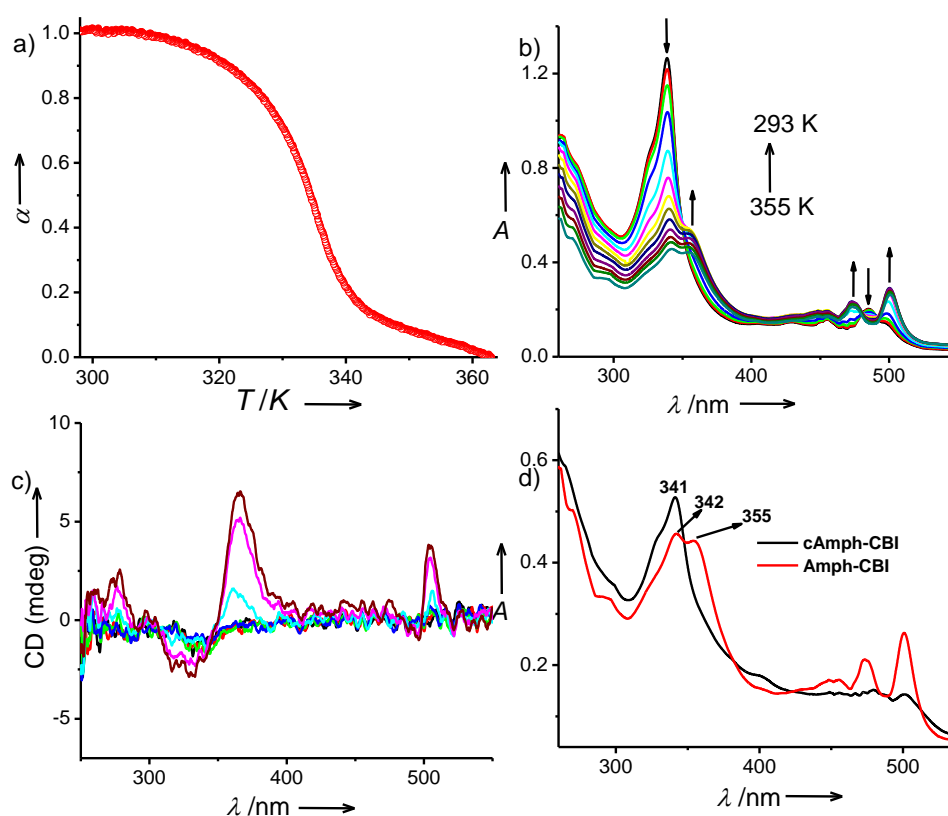


Figure 2.2.10. a) Fraction of aggregation (α) of **Amph-CBI** by monitoring the absorbance at 500 nm versus temperature in 1:1 THF-water mixture with a cooling rate of 2 K/min and corresponding b) absorption spectra. c) Temperature dependent CD spectra of **Amph-CBI** co-assembled with 20 mol% of **cAmph-CBI** in 1:1 THF-water mixture with a cooling rate of 0.5 K/min. d) Absorption spectra of **Amph-CBI** and **cAmph-CBI** in 1:1 THF-water mixture after cooling from 353 K to 253 K with a cooling rate of 2 K/min ($c = 0.02$ mM, $l = 10$ mm).

We have also investigated the self-assembly mechanism of non-covalent chiral CBI amphiphile, **C-CBI-ATP** using temperature dependent CD measurements (Figure 2.2.11). In a typical experimental procedure, **C-CBI** co-assembled with different equivalents of **ATP** (2-5

equivalents) in 20% water containing DMSO were heated up to 360 K and then cooled to 288 K at a rate of 2 K/min while monitoring molar ellipticity at 520 nm. Remarkably, all cooling curves displayed non-sigmoidal behaviour, indicating cooperative supramolecular polymerization of **C-CBI** and **ATP** co-assembly (Figure 2.2.11a). Thermodynamic parameters governing the supramolecular polymerization of **C-CBI** and **ATP** co-assembly were calculated for 1:2 co-assembly of **C-CBI-ATP**. To fit the temperature dependent CD data, we have normalized the data to extract degree of aggregation (α) and fitted to simplified nucleation elongation model, developed by Jonkheijm et al. (Figure 2.2.11b).^{4b} The estimated α is 1.02919 and corresponding elongation temperature (T_e) and enthalpy of polymerization are 335.889 K and 65.147 kJ/mol, respectively. In the cooling curve around T_e sharp transition in the molar ellipticity was observed indicating highly cooperative supramolecular polymerization (Figure 2.2.11b and c). This is further reflected in the value of cooperativity parameter (σ), 1.21×10^{-4} . This is also evident from temperature dependent absorption data which also showed non-sigmoidal behaviour with sharp transition in the absorbance around 337 K which is close to the T_e , observed in the corresponding CD measurements (Figure 2.2.11d).

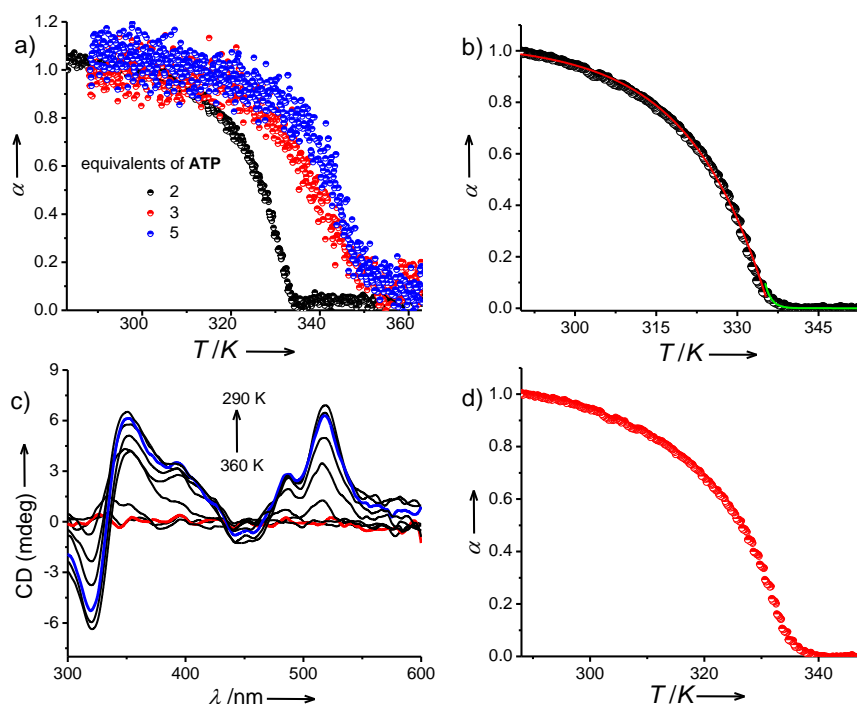


Figure 2.2.11. a) Fraction of aggregation (α) monitored at 520 nm versus temperature of **C-CBI** co-assembled with different equivalents of **ATP** in 20% HEPES buffer containing DMSO with a cooling rate of 2 K/min. b) Fraction of aggregation (α) monitored at 520 nm versus temperature of **C-CBI** co-assembled with two equivalents of **ATP** in 20% HEPES buffer containing DMSO with a cooling rate of 2 K/min and c) corresponding CD spectra. The solid lines in 'b' show the fit to the temperature dependent nucleation-elongation model. d) Fraction of aggregation (α) obtained by monitoring the absorbance at 520 nm versus temperature of **C-CBI** co-assembled with two equivalents of **ATP** in 20% HEPES buffer containing DMSO with a cooling rate of 2 K/min ($c = 0.1$ mM, $l = 2$ mm).

2.2.5 Conclusions

In conclusion, we have investigated the self-assembly mechanisms of CBI amphiphiles using chirality as a probe. Temperature dependent CD experiments revealed that **cAmph-CBI** self-assembles in an isodesmic fashion. On the other hand, achiral CBI amphiphile (**Amph-CBI**), its co-assembly with **cAmph-CBI**, and non-covalent chiral (**C-CBI-ATP**) amphiphiles follow nucleation growth mechanism during self-assembly. These observations clearly indicate that, amphiphilic design of π -systems can also drive their supramolecular polymerization in a cooperative fashion. However, further investigations on various amphiphilic π -systems are required to understand the molecular features governing the supramolecular polymerization.¹⁹ Since self-assembled nanostructures of amphiphilic π -conjugated oligomers and polymers are one of the promising candidates for optoelectronic applications, detailed understanding of their self-assembly mechanisms would help in improving their optoelectronic functions.

2.2.6 Experimental Section

General Methods: Field Emission Scanning Electron Microscopy (FE-SEM) measurements were performed on a NOVA NANO SEM 600 (FEI) by drop casting the aggregate solutions on glass substrate followed by drying in vacuum and were operated with an accelerating voltage of 30 kV. Transmission Electron Microscopy (TEM) measurements were performed on a JEOL, JEM 3010 operated at 300 kV. Samples were prepared by placing a drop of the aggregate solution on carbon coated copper grids followed by drying at room temperature. The images were recorded with an operating voltage of 300 kV. In order to get a better contrast, some samples were stained with uranyl acetate (1 wt% in water) before the measurements. Atomic Force Microscopy (AFM) measurements were performed on a Veeco diInnova SPM operating in tapping mode regime. Micro-fabricated silicon cantilever tips doped with phosphorus and with a frequency between 235 and 278 kHz and a spring constant of 20-40 Nm^{-1} were used. The samples were prepared by drop casting aggregate solutions on glass substrate and dried in air followed by vacuum. Electronic absorption spectra were recorded on a Perkin Elmer Lambda 900 UV-VIS-NIR Spectrometer and emission spectra were recorded on Perkin Elmer Ls 55 Luminescence Spectrometer. CD spectra was recorded in Jasco J-815 spectrometer with a standard sensitivity (100 mdeg), scan rate of 100 nm/second, bandwidth value of 1 and single accumulation for each spectra. NMR spectra were obtained with a Bruker AVANCE 400 (400 MHz) Fourier transform NMR spectrometer with chemical shifts reported in parts per million (ppm) with respect to TMS. Matrix-assisted laser-desorption ionization time-of-flight (MALDI-TOF) spectra were obtained on a Bruker ultraflex 2 MALDI-TOF mass spectrometer with α -cyano-4-hydroxycinnamic acid matrix. Confocal Microscopy imaging was done at room temperature using a Zeiss LSM 510 META laser scanning confocal microscope. The

microscope objective of 63X (NA 1.4) and 20X (NA 0.5) were employed. Sample was prepared by sealing the solution between two glass plates.

2.2.6a Synthesis

Synthesis of **Amph-CBI** and **C-CBI** are described in Part-2.1 and Part-4.2 of this thesis, respectively. 3,6,9,12-tetraoxapentadec-14-en-1-amine²⁰ and (S)-(-)-3,7-dimethyloctyl amine²¹ were synthesized according to literature methods. ATP disodium salt was purchased from Sisco Research Laboratories.

cAmph-CBI: CDA (500 mg, 1.14 mmol), (S)-(-)-3,7-dimethyloctyl amine (0.28 g, 1.91 mmol), 3,6,9,12-tetraoxapentadec-14-en-1-amine (450 mg, 1.91 mmol), imidazole (20 g) and zinc acetate (350 mg, 1.91 mmol) were thoroughly mixed and heated with stirring at 140 °C for overnight. Then the reaction mixture was transferred under hot conditions to 1M HCl and it was extracted with chloroform. The organic layer was repeatedly washed with 1M HCl. Then the organic layer was washed with saturated NaCl solution, dried using anhydrous Na₂SO₄ and then filtered. After evaporating the solvent the crude product, was purified by column chromatography (silica gel, from 100% chloroform to 15% MeOH in chloroform) and Bio-Beads (S-X3, chloroform) to yield, 18% of **cAmph-CBI** (150 mg) as yellowish orange powder; ¹H-NMR (400 MHz, CDCl₃): δ = 8.53 (d, *J* = 8 Hz, 2H), 8.44 (d, *J* = 8 Hz, 2H), 7.52-7.58 (m, 4H), 5.85-5.92 (m, 1H), 5.14-5.26 (m, 2H), 4.1 (t, 2H), 3.97-3.99 (m, 4H), 3.89-3.88 (m, 4H), 3.73-3.55 (m, 10H), 1.9 (t, 2H), 1.42-1.3 (m, 18H), 0.91 (t, *J* = 7 Hz, 3H) ppm. MALDI-TOF MS *m/z* 817.41 [M + Na]⁺, 833.099 [M + K]⁺.

2.2.7 Analysis of the cooling curves

The obtained CD data (mdeg) is normalized between 0 and 1 using the below mentioned formula.

$$\alpha(T) = (CD_T - CD_M)/(CD_{Agg} - CD_M)$$

Where, CD_T is the CD effect (mdeg) at a given temperature T, CD_M is the CD effect (mdeg) at high temperature corresponding to the monomer, CD_{Agg} is the CD effect (mdeg) at low temperatures corresponding to the aggregated state.

2.2.7a Isodesmic Model

The obtained fraction of aggregates (α) versus temperature (K) was fitted to the temperature dependent isodesmic model using the Levenberg-Marquardt algorithm as implemented in Xmgrace software. The regression for each of the fits was between 0.99 and 1.00.

The fraction of aggregation $\alpha(T)$ was fitted using the below given equation in which T_m is the melting temperature or temperature at which the fraction of aggregates (α) is 0.5.

$$\alpha(T) = 1/(1 + \exp[(T - T_m)/T^*])$$

T^* value was obtained by fitting above equation to experimental data; this was further used to calculate the enthalpy of polymerization using below equation.

$$\Delta H = -RT_m^2/(0.908 \times T^*)$$

2.2.7b Nucleation-Elongation Model

The obtained fraction of aggregates (α) versus temperature (K) was fitted to the temperature dependent nucleation-elongation model.

In the elongation regime the fraction of aggregated molecules (α), is given by the following equation

$$\alpha = \alpha_{\text{SAT}} (1 - \exp[-h_e/RT_e^2 (T - T_e)])$$

where

h_e is the molecular enthalpy release due to non-covalent interactions during elongation,

T the absolute temperature

T_e is the elongation temperature

R is the gas constant

α_{SAT} is introduced as a parameter to ensure that $\alpha/\alpha_{\text{SAT}}$ does not exceed unity

At temperatures above the elongation temperature T_e (i.e., the nucleation regime) the fraction of aggregated molecules (α) is described by

$$\alpha = K_a^{1/3} \exp[(2/3K_a^{-1/3} - 1)h_e/RT_e^2 (T - T_e)]$$

where K_a is the dimensionless equilibrium constant of the activation step at T_e

2.2.8 References

-
- a) A. P. H. J. Schenning, E. W. Meijer, *Chem. Commun.* **2005**, 3245; b) A. Ajayaghosh, S. J. George, A. P. H. J. Schenning, *Top. Curr. Chem.* **2005**, 258, 83; c) T. Ishi-i, S. Shinkai, *Top. Curr. Chem.* **2005**, 258, 119; d) J. Wu, W. Pisula, K. Müllen, *Chem. Rev.* **2007**, 107, 718; e) A. Ajayaghosh, V. K. Praveen, *Acc. Chem. Res.* **2007**, 40, 644; f) A. Mishra, C.-

- Q. Ma, P. Bäuerle, *Chem. Rev.* **2009**, *109*, 1141; g) Z. Chen, A. Lohr, C. R.Saha-Möller, F. Würthner, *Chem. Soc. Rev.* **2009**, *38*, 564.
2. a) F. Würthner, *Angew. Chem. Int. Ed.* **2001**, *40*, 1037; b) F. J. M. Hoeben, P. Jonkheijm, E.W. Meijer, A. P. H. J. Schenning, *Chem. Rev.* **2005**, *105*, 1491.
3. a) A. Ajayaghosh, S. J. George, *J. Am. Chem. Soc.* **2001**, *123*, 5148; b) A. P. H. J. Schenning, P. Jonkheijm, E. Peeters, E. W. Meijer, *J. Am. Chem. Soc.* **2001**, *123*, 409; c) K. Balakrishnan, A. Datar, R. Oitker, H. Chen, J. Zuo, L. Zang, *J. Am. Chem. Soc.* **2005**, *127*, 10496; d) Y. Che, A. Datar, K. Balakrishnan, L. Zang, *J. Am. Chem. Soc.* **2007**, *129*, 7234; e) X. Zhang, Z. Chen, F. Würthner, *J. Am. Chem. Soc.* **2007**, *129*, 4886.
4. a) C. Kulkarni, R. Munirathinam S. J. George, *Chem. Eur. J.* **2013** (in press); b) P. Jonkheijm, P. van der Schoot, A. P. H. J. Schenning, E. W. Meijer, *Science* **2006**, *313*, 80; c) T. Hirose, F. Helmich, E. W. Meijer, *Angew. Chem. Int. Ed.* **2013**, *52*, 304; d) A. Lohr, F. Würthner, *Angew. Chem. Int. Ed.* **2008**, *47*, 1232; e) C. C. Lee, C. Grenier, E. W. Meijer, A. P. H. J. Schenning, *Chem. Soc. Rev.* **2009**, *38*, 671-683; f) T. E. Kaiser, V. Stepanenko, F. Würthner, *J. Am. Chem. Soc.* **2009**, *131*, 6719.
5. a) D. Görl, X. Zhang, F. Würthner, *Angew. Chem. Int. Ed.* **2012**, *51*, 6328; b) B. Narayan, S. P. Senanayak, A. Jain, K. S. Narayan, S. J. George, *Adv. Funct. Mater.* **2013**, (DOI: 10.1002/adfm.201202298); c) A. Jain, K. V. Rao, U. Mogera, A. A. Sagade, S. J. George, *Chem. Eur. J.* **2011**, *17*, 12355.
6. a) W.-S. Li, Y. Yamamoto, T. Fukushima, A. Saeki, S. Seki, S. Tagawa, H. Masunaga, S. Sasaki, M. Takata, T. Aida, *J. Am. Chem. Soc.* **2008**, *130*, 8886; b) Y. Hizume, K. Tashiro, R. Charvet, Y. Yamamoto, A. Saeki, S. Seki, T. Aida, *J. Am. Chem. Soc.* **2010**, *132*, 6628; c) R. Charvet, Y. Yamamoto, T. Sasaki, J. Kim, K. Kato, M. Takata, A. Saeki, S. Seki, T. Aida, *J. Am. Chem. Soc.* **2012**, *134*, 2524; d) W.-S. Li, A. Saeki, Y. Yamamoto, T. Fukushima, S. Seki, N. Ishii, K. Kato, M. Takata, T. Aida, *Chem. Asian J.* **2010**, *5*, 1566.
7. R. B. Martin, *Chem. Rev.* **1996**, *96*, 3043.
8. a) P. van der Schoot in *Theory of Supramolecular Polymerization*, Vol. 2 (Ed. : A. Ciferri), Taylor & Francis, London, **2005**, pp. 77; b) D. Zhao, J. S. Moore, *Org. Biomol. Chem.* **2003**, *1*, 3471; c) M. M. J. Smulders, A. P. H. J. Schenning, E. W. Meijer, *J. Am. Chem. Soc.* **2008**, *130*, 606.
9. M. M. J. Smulders, M. M. L. Nieuwenhuizen, T. F. A. de Greef, P. I. van der Schoot, A. P. H. J. Schenning, E. W. Meijer, *Chem. Eur. J.* **2010**, *16*, 362.
10. a) A. P. H. J. Schenning, P. Jonkheijm, E. Peeters, E. W. Meijer, *J. Am. Chem. Soc.* **2001**, *123*, 409; b) G. Fernández, M. Stolte, V. Stepanenko, F. Würthner, *Chem. Eur. J.* **2013**, *19*, 206.

11. a) F. J. M. Hoeben, I. O. Shklyarevskiy, M. J. Pouderoijen, H. Engelkamp, A. P. H. J. Schenning, P. C. M. Christianen, J. C. Maan, E.W. Meijer, *Angew. Chem. Int. Ed.* **2006**, *45*, 1232; b) S. J. George, T. F. A. de Greef, R. Bovee, van J. L. J. Dongen, A. P. H. J. Schenning, E. W. Meijer, *Chem. Asian J.* **2009**, *4*, 910.
12. a) P. K. Sukul, D. Asthana, P. Mukhopadhyay, D. Summa, L. Muccioli, C. Zannoni, D. Beljonne, A. E. Rowan, S. Malik, *Chem. Commun.* **2011**, *47*, 11858; b) P. K. Sukul, P. K. Singh, S. K. Maji, S. Malik, *J. Mater. Chem. B*, **2013**, *1*, 153; c) G. S. Vadehra, B. D. Wall, S. R. Diegelmann, J. D. Tovar, *Chem. Commun.* **2010**, *46*, 3947.
13. a) T. Yamamoto, T. Fukushima, A. Kosaka, W. Jin, Y. Yamamoto, N. Ishii, T. Aida, *Angew. Chem. Int. Ed.* **2008**, *47*, 1672; b) W. Jin, T. Fukushima, M. Niki, A. Kosaka, N. Ishii, T. Aida, *Proc. Natl. Acad. Sci. USA* **2005**, *102*, 10801.
14. M. J. Mayoral, C. Rest, J. Schellheimer, V. Stepanenko, G. Fernández, *Chem. Eur. J.* **2012**, *18*, 15607.
15. K. V. Rao, S. J. George, *Org. Lett.* **2010**, *12*, 2656.
16. a) T. Ma, C. Li, G. Shi, *Langmuir* **2008**, *24*, 43; b) M. Morikawa, M. Yoshihara, T. Endo, N. Kimizuka, *J. Am. Chem. Soc.* **2005**, *127*, 1358.
17. H. Engelkamp, S. Middelbeek, R. J. M. Nolte, *Science* **1999**, *284*, 785
18. A.R. A. Palmans, E. W. Meijer, *Angew. Chem. Int. Ed.* **2007**, *46*, 8948.
19. C. Kulkarni, S. Balasubramanian, S. J. George, *ChemPhysChem* **2013**, *14*, 661.
20. Y.-B. Lim, S. Park, E. Lee, H. Jeong, J.-H. Ryu, M. S. Lee, M. Lee, *Biomacromolecules*, **2007**, *8*, 1404.
21. E. Gößnitzer, R. Malli, S. Schuster, B. Favre, N. S. Ryder, *Arch. Pharm. Pharm. Med. Chem.* **2002**, *11*, 535.

PART-3**Charge-Transfer Nanostructures**

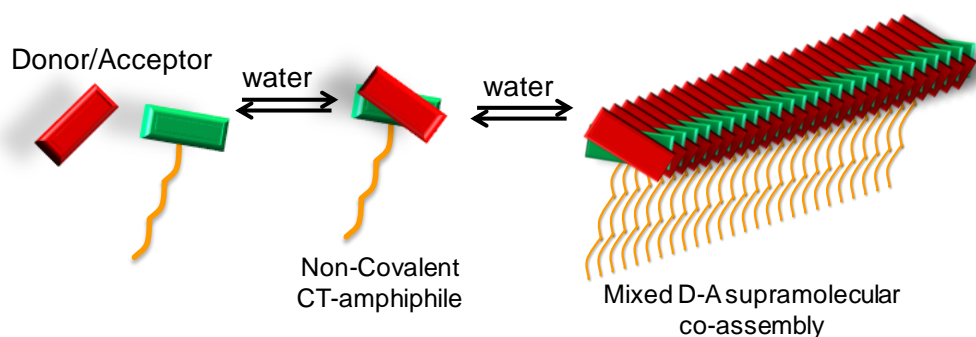
- PART-3.1** Charge-Transfer Nanofibers with Mixed Donor-Acceptor Organization via Non-Covalent Amphiphilic Strategy
- PART-3.2** Autonomous Alignment of Charge-Transfer Fibers via Two-Dimensional Donor-Acceptor Self-Assembly
- PART-3.3** High Charge Carrier Mobility in Non-Covalently Tailored D-A Heterojunction Nanostructures

PART-3.1

Charge-Transfer Nanofibers with Mixed Donor-Acceptor Organization via Non-Covalent Amphiphilic Strategy*

Abstract

In this section, we describe the supramolecular alternate co-assembly of aromatic donor (D) and acceptor (A) molecules as a novel, bottom-up strategy for the design of conducting one dimensional (1D) organic nanostructures. We have used a simple and efficient 'non-covalent amphiphilic strategy' to achieve this alternate, co-facial supramolecular co-polymerization of appropriately designed monomers. We demonstrate that this amphiphilic design is a very powerful tool to promote efficient co-facial assembly of various D-A molecules with structurally different extended π -conjugated backbones. The resultant one-dimensional assemblies, with mixed D-A molecular structure showed high mobility/conductivity without any external doping.



* Papers based on this work have appeared in *Angew. Chem. Int. Ed.* 2010, 49, 4218 –4222; *Chem. Eur. J.* 2012, 18, 14286 –14291.

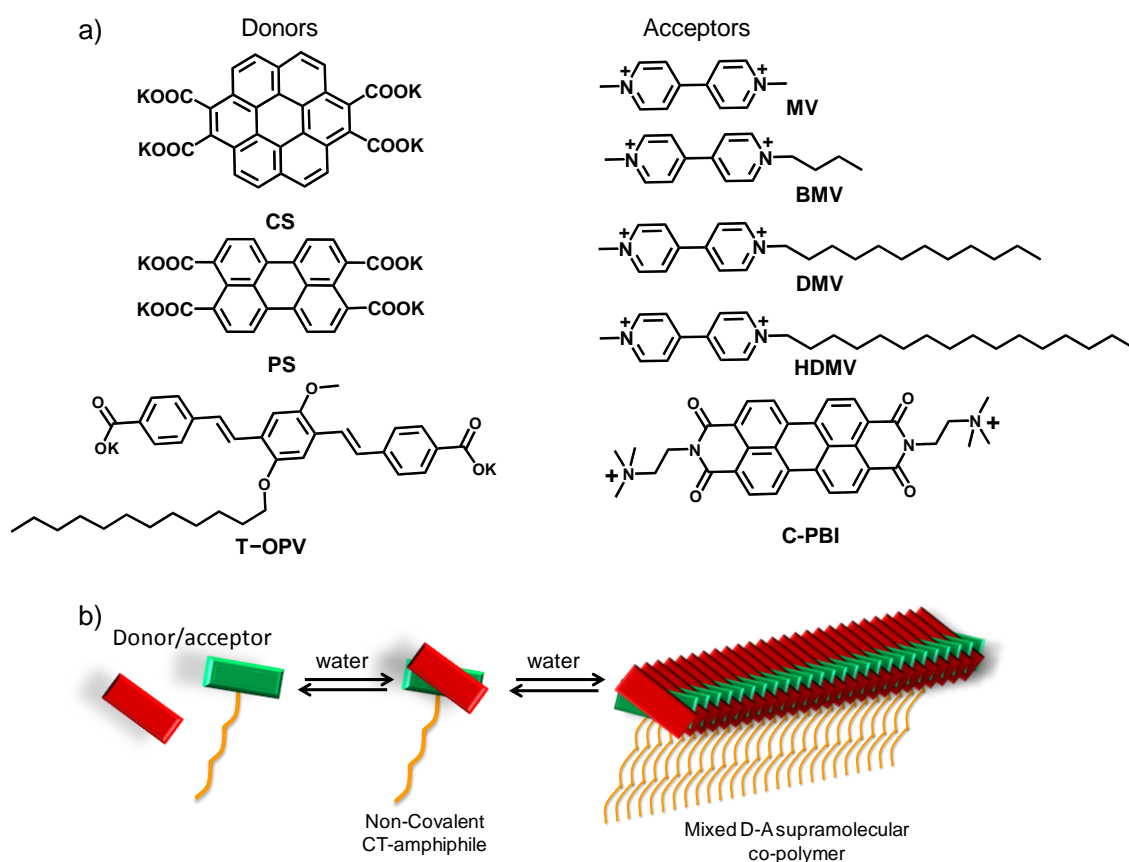
3.1.1 Introduction

Supramolecular polymerization of organic π -conjugated monomers, having optoelectronic functionality, to form one-dimensional (1-D) chains has been the topic of meticulous research, as this provides an efficient bottom up strategy for the design of nanostructures for nano-sized electronics.¹ 1-D assemblies of various π -conjugated molecules have thus been constructed and the non-covalent synthetic design of these systems often utilizes the characteristic π - π stacking interactions of the extended aromatics, supported by directional H-bonding² or amphiphilic interactions.³ However, the use of these 1-D nanostructures as conducting components in nanoelectronic devices definitely requires further control over its function and structure. Thus the current research is targeted to improve their conductivity as well as the design of monodisperse⁴ and multi-component assemblies.⁵ In recent years, the conductivity of these self-assembled 1-D nanostructures has been improved by either the modification of the molecular structure⁶ or by external doping.⁷ However, the former strategy often requires tedious synthetic efforts and in the later approach, uniform doping of the assemblies while preserving their morphology is difficult. On the other hand, charge-transfer (CT) crystals formed from D and A molecules, which are organized either in a segregated (orthogonal, ..D-D-D.. and ..A-A-A..) or mixed (alternate, ...D-A-D...) fashion have gathered immense attention because of their excellent conducting properties.⁸ In this context, we envisage that the supramolecular one-dimensional analogues of these binary CT complexes would provide novel conducting nanostructures through inherent doping and hence can provide new opportunities for nano-sized electronics.⁹

Although segregated D-A organization has been achieved in 1-D assemblies for photo-conductivity studies,¹⁰ the supramolecular alternate co-assemblies with mixed D-A organization of the monomers is rarely studied.¹¹ Intriguingly, extended assemblies having alternate D-A organization has been recently predicted to have ambipolar CT properties^{8b,12} and also shown to have interesting ferroelectric properties.¹³ Extended assemblies of D and A monomers having mixed stack organization were attained by covalent polymerization¹⁴ and liquid-crystalline mesophase co-assembly.¹⁵ However, attempts to co-assemble these molecules in solution to extended stacks, often resulted in phase-separation¹⁶ and hence a smart design principle is essential for the supramolecular analogue of the mixed D-A structure.¹⁷ Extended assemblies of aromatic donors and methyl-viologen acceptors were constructed recently using ‘non-covalent amphiphilic design’, where the co-facial D-A pair formed due to CT interactions resembles a surfactant in their structure to facilitate the 1-D self-assembly in water through amphiphilic interactions.^{11a,b}

In this section, we discuss about the non-covalent amphiphilic design principle to construct the supramolecular alternate co-assembly of various extended π -conjugated D and A molecules in water to form 1-D nanostructures with an unprecedented mixed stack D-A molecular structure exhibiting high mobility/conductivity (Scheme 3.1.1). At higher concentrations, these CT-assemblies form hydrogels which are different from single component peptide¹⁸ and rod-coil¹⁹ amphiphiles as well as sugar derivatives²⁰ reported so far to form hydrogels.²¹

3.1.2 Non-Covalent Amphiphilic Design



Scheme 3.1.1. Non-covalent amphiphilic design strategy. a) Molecular structures of various D and A molecules used in this section. b) Schematic representation of the non-covalent CT-amphiphile and its self-assembly into 1-D supramolecular structures.

Our molecular design consists of hydrophilic aromatic D and A monomers with one of them (D/A) having flexible alkyl chain (Scheme 3.1.1a). Co-assemblies of some of these D-A derivatives, with segregated ‘D-A’ architecture, have been achieved in literature by synergistic hydrogen bonding and π - π interactions.^{10a-c} In the present case, D and A molecules are elegantly designed to form a non-covalent amphiphile in their CT-state through synergistic π - π stacking, charge-transfer and electrostatic interactions and hence would promote the co-assembly in water with mixed stack organization as shown in Scheme 3.1.1b.¹¹ Furthermore, the ionic

nature of both these molecules would impart solubility to the monomers and dynamic nature to the resulting co-assembly in water. We have discussed three different CT-pairs of D and A molecules in this section, which are summarized in the following sessions.

3.1.3 CS-viologen D-A System

3.1.3a Design Strategy

In the first design, we have selected coronene tetracarboxylate (**CS**) as the aromatic D molecule, since it is highly soluble in water and shows blue emission ($\lambda_{\text{max}} = 435 \text{ nm}$, *vide infra*). On the other hand we have selected viologen derivatives as the electron acceptor counterpart for the design of D-A pair. Viologen derivatives are well known electron acceptors and have been extensively used for the design of stimuli responsive supramolecular systems.²² Hence, we have designed the dodecyl methyl-viologen (**DMV**) derivative, an unsymmetric amphiphile, as the acceptor molecule, that would not only allow CT interactions with coronene, but also trigger the self-assembly of the resultant D-A pair through hydrophobic interactions. In addition, we have used both butyl methyl-viologen (**BMV**) derivative and methyl-viologen (**MV**) as the model compounds for single-crystal and NMR studies, which would give a deep insight into the molecular arrangement of the chromophores in the D-A pair.

3.1.3b Synthesis and Optical Studies

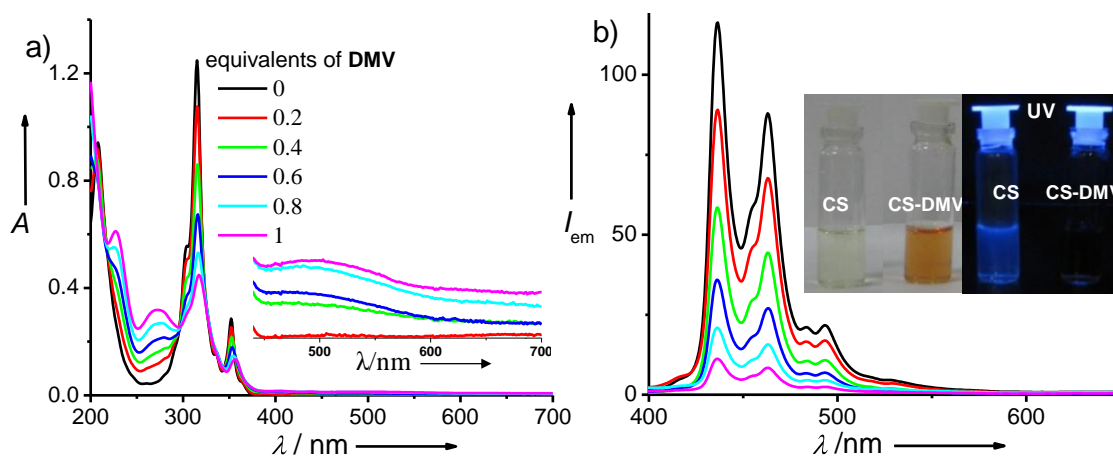


Figure 3.1.1. Spectroscopic titration of **CS** with **DMV** (10% v/v methanol in water). Corresponding a) absorption and b) emission changes ($1 \times 10^{-4} \text{ M}$, $l = 1 \text{ mm}$). Inset of Figure 3.1.1a shows the gradual appearance of the CT band at 500 nm on increasing amounts of **DMV**. Inset of Figure 3.1.1b shows the ground state color and fluorescence (on illumination with 365 nm UV light) changes of **CS** on interaction with **DMV**.

CS was synthesized by a two-fold oxidative benzogenic Diels-Alder reaction of perylene with *N*-ethyl maleimide and the subsequent hydrolysis with KOH in methanol.²³ **DMV**, **HDMV** and **BMV** were synthesized according to the literature procedures.²⁴ CT-

interactions of **CS** with viologens have been studied by optical spectroscopy, NMR and single crystal X-ray crystallography. Self-assembly of D-A pairs were characterized with Atomic force microscopy (AFM), Field emission scanning electron microscopy (FE-SEM) and Transmission electron microscopy (TEM). Since the acceptor amphiphile **DMV** self-assembles in water (as evident from dynamic light scattering studies, *vide infra*), all the D-A mixtures have been prepared by the injection of a methanol solution of **DMV**, in which the viologens are molecularly dissolved, to the aqueous solution containing free **CS** molecules (10 % v/v methanol in water). Although this sample preparation method has been followed to ensure the efficient formation of D-A complexes, further optical spectroscopy studies showed that the **DMV** self-assembly is dynamic enough to reorganize to form D-A CT complexes upon the addition of **CS** molecules. The absorption spectrum of **CS** exhibits strong absorption at 314 nm and a weak band at 351 nm in methanol-water solvent mixture (10% v/v methanol, 1×10^{-4} M), characteristic of molecularly dissolved anionic coronene molecules (Figure 3.1.1).²³ A noticeable red shift of the **CS** absorption maxima (~ 5 nm with 1 equivalent of **DMV**) with concomitant decrease in the absorbance and a broadening of the absorption band was observed with increasing **DMV** concentration, which indicates a strong ground-state intermolecular interactions between these D and A molecules (Figure 3.1.1a). Moreover, the absorption changes are accompanied by the appearance of a new weak, broad band centered around 500 nm, which unambiguously proves the CT interactions between the **CS** and the **DMV**. Remarkably, the intensity of this red-shifted absorption is more prominent after the addition of one equivalent of the **DMV**, suggesting a 1:1 stoichiometry for the D-A complexes.²² Further evidence for CT interactions is provided by fluorescence measurements which showed significant quenching of coronene emission in the **CS-DMV** mixtures. While **CS** shows intense blue fluorescence with emission maxima at 435 nm and 462 nm, the emission intensity of the mixture containing 1 equivalent of **DMV** is reduced by a factor of 10 (Figure 3.1.1b). The changes in the absorption and emission properties on CT complex formation could also be easily visualized with naked eye (inset of Figure 3.1.1b). Spectroscopic studies in buffer solutions (pH = 9) have also shown similar changes as described above.

3.1.3c Gelation Studies

Since the 1:1 **CS-DMV** CT complex structurally resembles a non-covalent amphiphile, polar ionic groups on one end and the hydrophobic dodecyl chain on the other end, a typical surfactant-like higher order self-assembly between the CT complexes can be envisaged in water. Remarkably, a gradual increase in the concentration of 1:1 CT complex of **CS** and **DMV** makes the solution visibly viscous and finally resulting in transparent, dark red colored hydrogel (Figure 3.1.2a). In a typical gelation experimental procedure aqueous solution of **CS-DMV** complex was heated to molecularly dissolved state and cooled at room temperature and

the gel was formed within few minutes as confirmed by inverted vial method. The critical gelator concentration of the **CS-DMV** hydrogel is found to be 7.96 mM. AFM analysis of the **CS-DMV** hydrogel showed the formation of entangled network of very long fibers of several micrometers length and 100-300 nm in diameter (Figure 3.1.2b). Hydrogels thus formed were stable for several months and showed the characteristic CT absorption at 500 nm with a completely quenched fluorescence (Figure 3.1.2c), indicating that the gel fibers are indeed formed by the 1-D assembly of CT complexes.

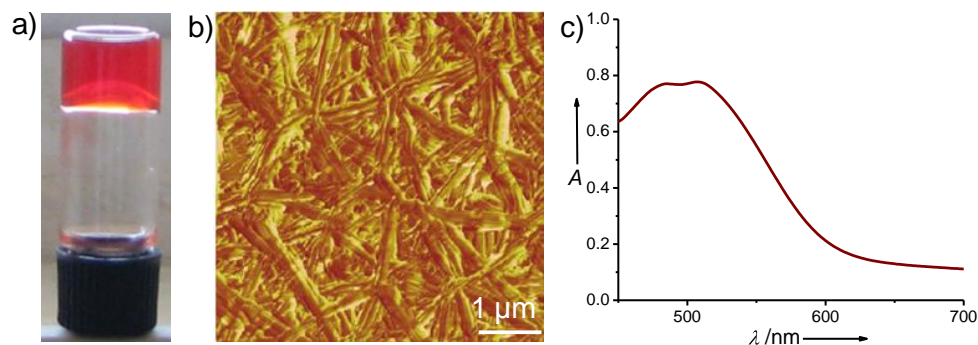


Figure 3.1.2. Physical appearance and characterization of **CS-DMV** hydrogels ($c = 7.9 \text{ mM}$). a) Photograph of the hydrogel, b) AFM phase image of the gel on a glass substrate and c) absorption spectrum of the gel measured in a 1 mm cuvette, showing strong CT band.

3.1.3d Face-to-Face D-A Organization

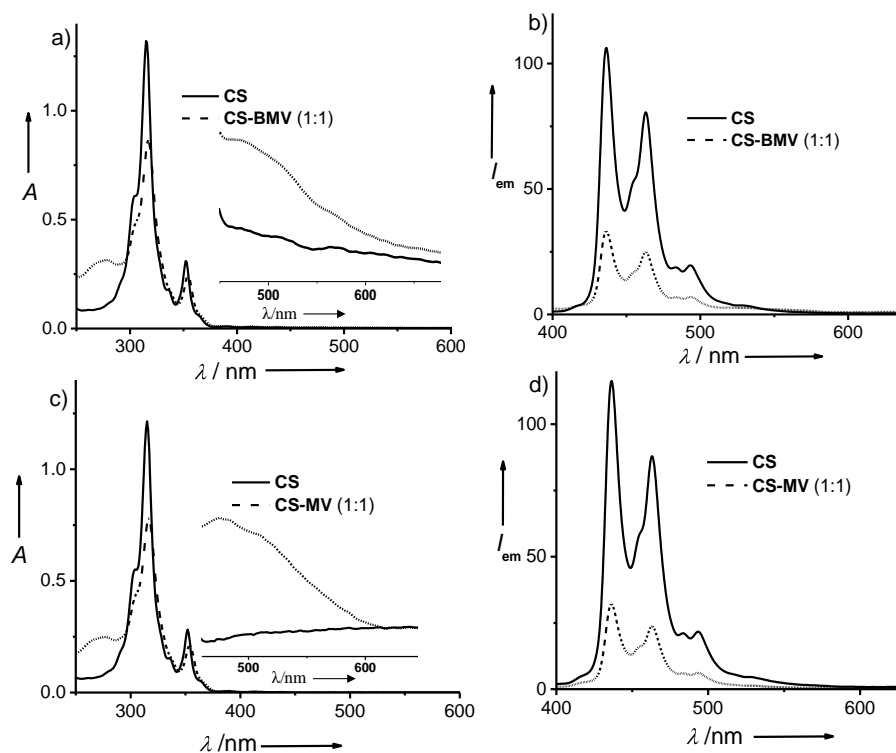


Figure 3.1.3. Absorption and emission spectra of **CS** and its 1:1 complex with **BMV** (a and b), and **MV** (c and d) in water containing 10% methanol ($c = 0.1 \text{ mM}$, $l = 1 \text{ mm}$).

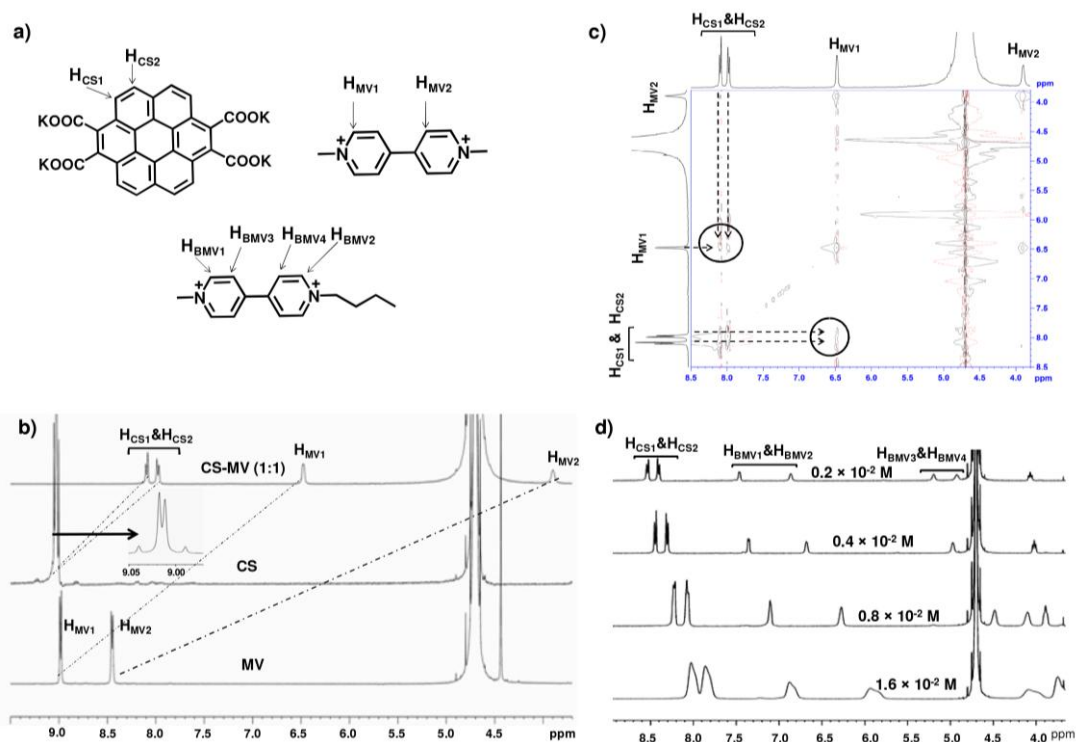


Figure 3.1.4. a) Molecular structures of **CS**, **MV** and **BMV** with chemically different protons marked. b) Aromatic region of the ^1H NMR spectra of **CS**, **MV** and **CS-MV** (D_2O , $c = 1.6 \times 10^{-2}$ M). c) Partial NOESY NMR spectrum of 1:1 **CS-MV** CT complex, showing the through space interactions between the protons of **CS** and **MV** (D_2O , $c = 1.6 \times 10^{-2}$ M). d) Concentration dependent ^1H NMR spectra of 1:1 **CS-BMV** complex in D_2O .

In order to prove the face-to-face organization of D and A molecules in the complexed state, detailed NMR and single crystal XRD studies are required. However, NMR measurements on **CS-DMV** complex were not successful due to its aggregation and gel formation even at low concentrations (*vide infra*). Moreover these systems failed to crystallize due to the presence of long alkyl chain. Hence, we have used two model compounds, **MV** and **BMV** to study their interaction with **CS** by both NMR spectroscopy and single crystal X-ray diffraction. Strong CT interactions of both **MV** and **BMV** with **CS** is evident from optical spectroscopic studies, which showed similar absorption and fluorescence changes as that of **DMV** (Figure 3.1.3 and *vide supra*). Decisive proof for the face-to-face organization is provided by the ^1H NMR studies of the model viologen (**MV**) compound with the **CS** in D_2O . As shown in Figure 3.1.4b, it is observed that all the aromatic proton signals of acceptor **MV** (H_{MV1} and H_{MV2}) undergo a significant up-field shift upon the formation of the CT complex (1.6×10^{-2} M). Interestingly, the central protons of **MV** (H_{MV2}) are significantly shifted up-field (from $\delta = 8.45$ to 3.89 ppm) relative to the terminal protons (H_{MV1}) (from $\delta = 8.98$ to 6.47 ppm), suggesting a face-to-face stacking for the D and A molecules, thus the aromatic π -electrons of **CS** induces a pronounced shielding in the case of former (Figure 3.1.4a and b). At the same time closely associated doublets of coronene aromatic protons (H_{CS1} and H_{CS2}) also

undergo a similar but a small up-field shift (around 1 ppm) with well separated doublets ($\delta = 8.18$ and 7.97 ppm) on interaction with **MV**. Face-to-face stacking in CT complexes could be further supported by the Nuclear Overhauser Effect Spectroscopy (NOESY) experiments which showed through space interaction between the H_{MV1} terminal protons and the H_{CS1} and H_{CS2} protons of **CS** (Figure 3.1.4c). At the same time, no NOE interaction was found for H_{MV2} middle protons, suggesting a diagonal face-to-face arrangement for the D and A molecules (see below). NMR studies of the **BMV** (0.2×10^{-2} M), which is an ideal model amphiphile for the **DMV**, showed similar observation as that for **MV** on interaction with **CS**, suggesting a face-to-face stacking arrangement for the chromophores even in a bilayer type packing (Figure 3.1.4d). Interestingly, as the concentration of the **BMV-CS** CT complex increases, the aromatic resonance signals shifts further up-field with simultaneous broadening of signals characteristic of strong intermolecular association leading to a higher order self-assembly of the CT complexes (Figure 3.1.4d).

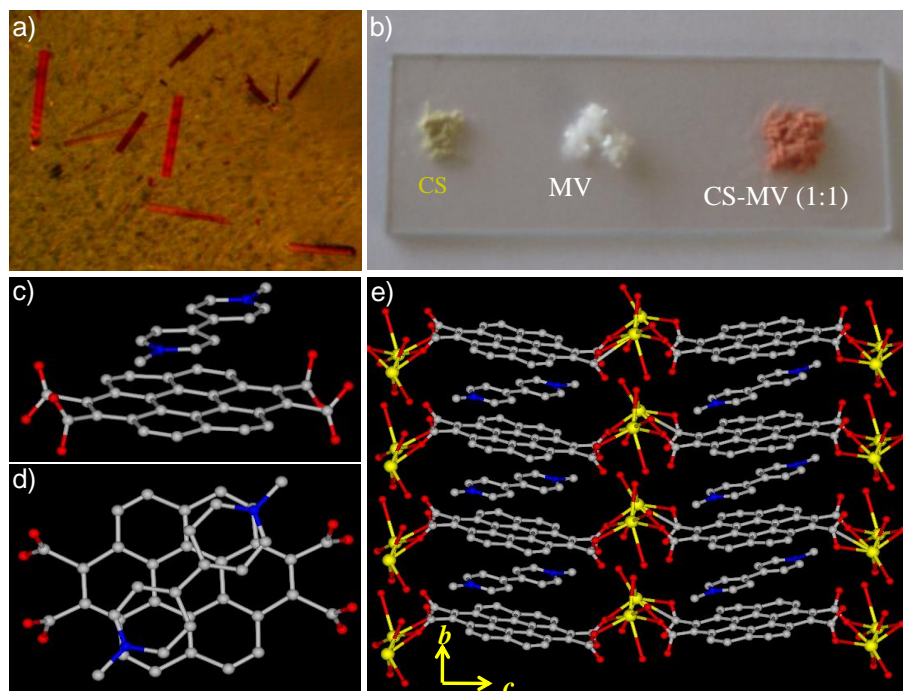


Figure 3.1.5. Photographs of a) 1:1 co-crystals of **CS** and **MV** and b) 1:1 solid-state mixing of **CS** and **MV** powders. Molecular orientation of **CS** and **MV** in the crystal structure, viewing along the crystallographic c) a axis and d) b axis. e) Side view of the extended π -columnar stacks of **CS-MV** co-crystals bridged by potassium ions. Potassium ions are colored in yellow, N atoms in blue and oxygen atoms are shown in red. Hydrogen atoms are omitted for clarity.

Single crystal X-ray diffraction studies of the co-crystals of **CS** and **MV** provided further unequivocal evidence for the formation of D-A CT complex. Single crystals were grown by dissolving the 1:1 mixture of **CS** and **MV** in a water-DMSO mixture (1:1 v/v) and kept at 60°C . Dark red colored crystals (Figure 3.1.5a) were formed slowly which was shown to contain

CS and **MV** in a 1:1 ratio by ^1H NMR spectroscopy indicating strong CT interactions similar to that in solution and the gels of **DMV**. Remarkably, simple mechanical grinding of a 1:1 mixture of **CS** and **DMV** also quickly resulted in a red-color powder consistent with the D-A CT interactions (Figure 3.1.5b). Single crystal X-ray analysis of the **CS-MV** co-crystals revealed an alternate face-to-face co-assembly of **CS** with **MV** (Figure 3.1.5c-e). The **MV** molecules are positioned between the **CS** chromophores in a diagonal orientation as evident from Figures 3.1.5c and d. π -Stacking columns formed by the alternate co-assembly of face-stacked D and A aromatic units, are arranged along the crystallographic *b*-axis with a face-to-face distance around 3.4 Å (Figure 3.1.5e). Detailed analysis of the co-crystals showed an overall formula of $\{(\text{MV})[\text{K}_2(\text{CS})(\mu\text{-OH}_2)(\text{H}_2\text{O})_4].2\text{H}_2\text{O}\}$, and can also be viewed as a one-dimensional chain of **CS** bridged by potassium ions, into which the **MV** dications are intercalated through ionic and charge-transfer interactions. Furthermore, the co-crystals grown from solution containing **CS** and 2 equivalents of **MV** also showed similar arrangement, suggesting the preference for a 1:1 stoichiometry. Unfortunately, the attempts to co-crystallize **CS** and **BMV**, which would have given a better insight into the orientation of chromophores in a bilayer-like assembly, were not successful.

3.1.3e Morphology Studies

Detailed microscopic studies have provided insights into the hierarchical self-assembly of **DMV-CS** CT complexes to 1-D nanofibers and hydrogels (Figure 3.1.6). Dynamic light scattering and FE-SEM studies showed that the **DMV** molecule self-assembles in aqueous solution due to their amphiphilic character into spherical objects with an average diameter of 250 nm as shown in Figure 3.1.6a. Remarkably, detailed TEM and AFM studies of 1 : 1 **DMV-CS** complexes in water (1×10^{-4} M) showed long nanofibers of 50-150 nm width and several micrometers length indicating a highly directional 1-D self-assembly process (Figure 3.1.6b-f). The self-assembly can be envisaged to involve a one-dimensional bilayer type packing of the supramolecular CT amphiphile along the π - π stacking direction of the chromophore assisted by the hydrophobic interactions. Interestingly, TEM analysis of the fibers that are negatively stained with uranyl acetate, revealed the presence of thinner, micrometer long fibres with a uniform diameter of 6 nm (Figure 3.1.6b and c). The diameters of 6 nm of the fibers are in close agreement with twice the length of the CT amphiphile, including the aromatic segments and the dodecyl chains (CPK modelling showed 2.8 nm, Figure 3.1.6g), thus confirming a bilayer packing. Furthermore, AFM cross-sectional analysis of the isolated fibers showed a height of 6-7 nm, which suggests that the CT-amphiphile in the bilayer are arranged in a radial fashion resulting in 1-D cylindrical micelles (Figure 3.1.6e and f). The surface charges on these individual cylindrical micelles might be acting as a glue for their lateral association through columbic interactions to give nanofibers with several nanometres width (50 to 150 nm) as

visible in the AFM images. The laterally associated nanofibers could further coil with each other to give fiber bundles as indicated by the height of 13-14 nm of twin fiber bundles as shown in Figure 3.1.6f, which is twice the diameter of a cylindrical micelle. Thus the microscopic studies demonstrate that the CT amphiphiles first self-assemble into high aspect ratio cylindrical micelles that subsequently form laterally associated fiber bundles and the resulting fibrous structures further coil and entangle at higher concentrations to result in hydrogelation. The hierarchical self assembly of **CS-DMV** amphiphiles into cylindrical micelles and 1-D nanofibers is schematically shown in Figure 3.1.6g. Remarkably, temperature dependent spectroscopic studies have shown that the self-assembly of **CS-DMV** CT complexes in water are completely thermo-reversible, unlike many of the reported aqueous self-assembled π -conjugated systems that are not dynamic due to the strong hydrophobic interactions.

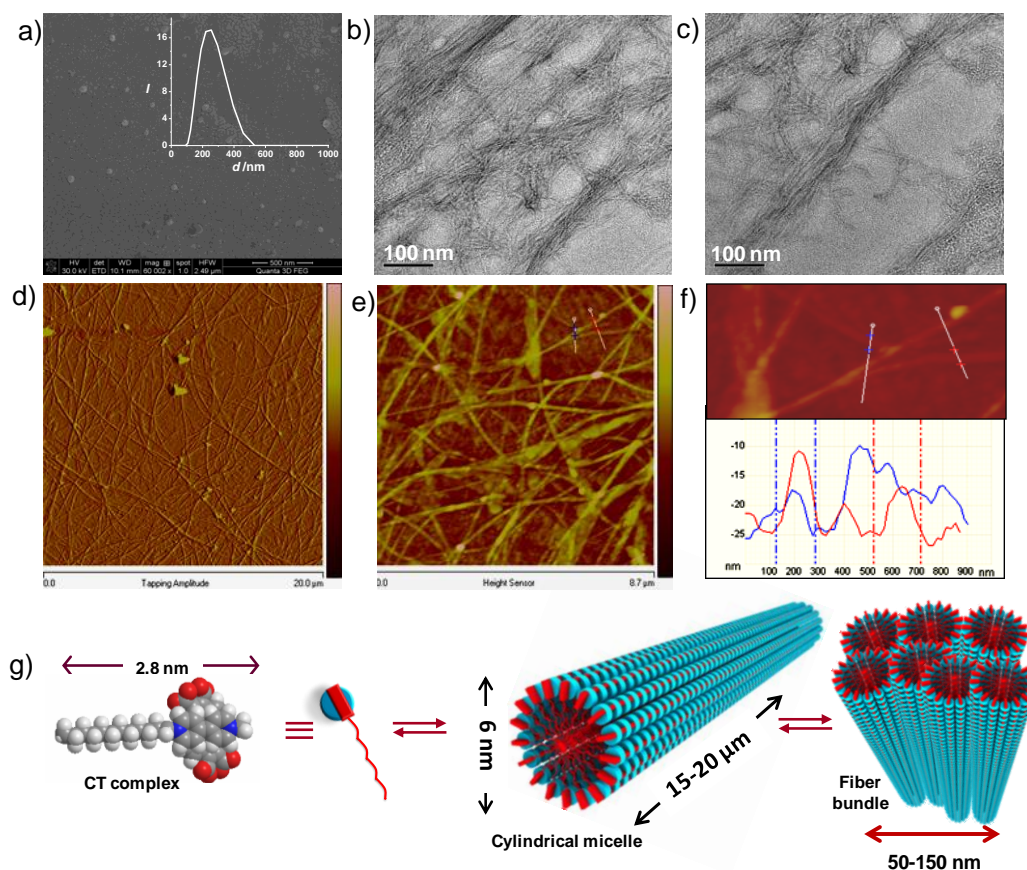


Figure 3.1.6. Microscopic studies of the **CS-DMV** ($1 \times 10^{-4} M$) self-assembly in water. a) FE-SEM image of the spherical objects of **DMV** formed in water ($c = 1 \times 10^{-4} M$) on glass substrate. DLS size distribution profile of **DMV** is shown in the inset. b) and c) are TEM images of **CS-DMV** (1:1) complex on carbon coated copper grids and sample was stained with uranyl acetate (1 wt % in water). AFM d) amplitude and e) height images of **CS-DMV** (1:1) co-assembly on glass substrate. f) AFM height analysis of the isolated fibers and g) schematic representation of the hierarchical self-assembly of the **CS-DMV** CT-amphiphile to cylindrical micelles and fiber bundles.

We have fabricated OFETs, using these CT-nanofibers as active channel elements to realize their device performance and charge transport properties.²⁵ Remarkably, these devices exhibited high hole mobilities up to $4.4 \text{ cm}^2/\text{V}\cdot\text{s}$ while operating at low voltages in ambient conditions, consistent with the design.

3.1.4 PS-Viologen D-A System

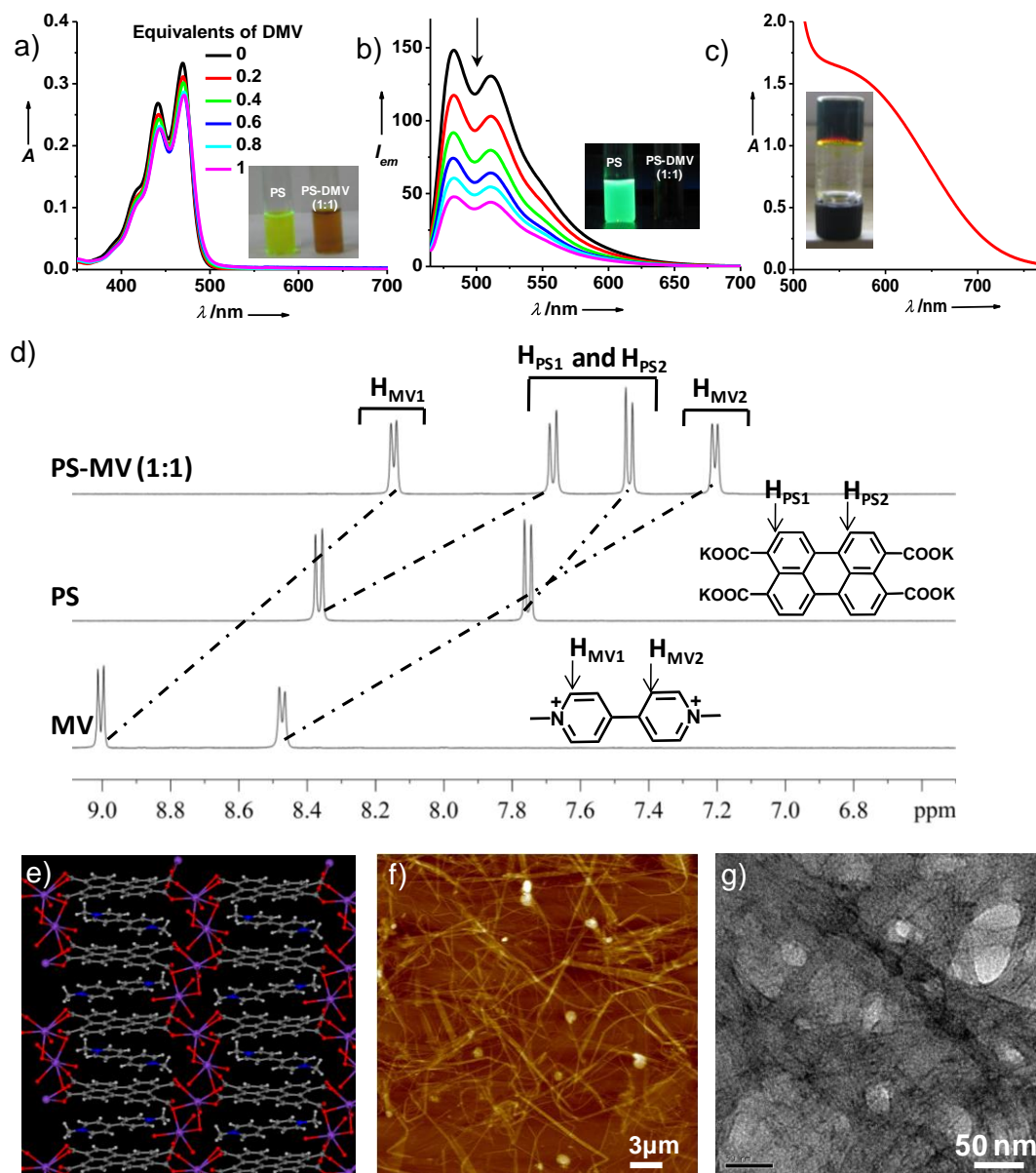


Figure 3.1.7. a) Absorption and b) emission spectra of PS with different equivalents of DMV in 10 % methanol containing water (PS = 0.1 mM, $l = 1 \text{ mm}$). c) Absorption spectra of PS-HDMV hydrogel. Photograph of the hydrogel is shown in the inset. d) Aromatic region of the ^1H NMR spectra of PS, MV and PS-MV in D_2O ($c = 10 \text{ mM}$). e) Side view of the extended π -columnar stacks of PS-MV co-crystals bridged by potassium ions. Potassium ions are colored in purple, N atoms in blue, oxygen atoms in red and hydrogen atoms are shown in white. f) AFM image of PS-HDMV CT-nanofibers formed in water ($c = 0.1 \text{ mM}$). g) TEM image of PS-DMV CT-nanofibers formed in water ($c = 0.1 \text{ mM}$).

Similar to **CS**, perylene tetracarboxylate (**PS**) also showed the formation of face-to-face CT-complexes with all viologen derivatives. **PS** was synthesized by the hydrolysis of perylene tetracarboxylic dianhydride in ethanol-aqueous KOH mixture.²⁶ Titration of **PS** with **DMV** showed significant changes in its absorption features, as a result of ground state CT-interactions (Figure 3.1.7a). This was further supported by gradual quenching in the **PS** emission with increasing equivalents of **DMV** (Figure 3.1.7b). However **PS-DMV** failed to form hydrogel even at 25 mM, probably due to more solubility of this CT-complex in water. To decrease the solubility, we have made CT-complex with **HDMV** which formed hydrogel at 14 mM and showed strong CT absorption band centred at 600 nm (Figure 3.1.7c). The face-to-face organization of this D-A pair in CT-complex was proved with solution state ¹H-NMR and single crystal XRD studies using **MV** as model compound instead of **DMV/HDMV**. The strong up-field shifts in the ¹H-NMR signals of both **PS** and **MV** in their mixed state revealed the formation of CT-complex with face-to-face D-A organization (Figure 3.1.7d). Single crystal analysis on **PS-MV** co-crystals also showed the face-to-face orientation of D-A molecules with 1:1 composition (Figure 3.1.7e). Due to face-to-face organization of D-A molecules, the CT-complex of **PS** with **DMV/HDMV** also resembles like a non-covalent CT-amphiphile. Similar to **CS-DMV**, microscopy investigations on this CT-amphiphiles showed the formation of high aspect ratio nanofibers with cylindrical micellar organization (Figure 3.1.7f and g).

3.1.5 OPV-PBI CT-System

3.1.5a Design Strategy

We have extended this non-covalent amphiphilic design to even larger D-A π -systems such as Oligo(p-phenylenevinylene) (OPV) and perylene bisimide (PBI) (**T-OPV**, **C-PBI**, Scheme 3.1.1a). Co-assemblies of OPV and PBI derivatives, with segregated ‘p-n’ architecture, have been achieved in literature by synergic hydrogen bonding and π - π interactions.^{10a-c} However, the mixed OPV-PBI architecture in extended assemblies is hitherto unknown, due to their self-association through π - π interactions favoring an orthogonal assembly.^{16a} In the present case, the **T-OPV** is elegantly designed with a T-shaped amphiphilic structure, which can form a non-covalent amphiphilic pair with **C-PBI**, possibly through synergistic solvophobic, CT and electrostatic interactions and hence would promote the co-assembly in water as shown in Scheme 3.1.1b.¹¹

3.1.5b Gelation and Rheology Experiments

Interestingly, when the concentration of the equimolar mixture of **T-OPV** and **C-PBI** monomers in water is increased, the resulting solution gradually becomes viscous (0.1 to 3.0

mM) and finally a dark wine colored gel is formed at a concentration of 3.3 mM, suggesting the formation of one-dimensional assembly (Figure 3.1.8a, inset). The very intense absorption band at 700 nm and the non-fluorescent nature of the hydrogels, are characteristic features of the CT interactions and thus provides a proof for the mixed stack organization of the monomers in the co-assembly (Figure 3.1.8a).^{10a} FE-SEM image of the gels shows typical highly interconnected network of fibers, which was further analyzed in detail using atomic force microscopy (AFM) and transmission electron microscopy (TEM) (*vide infra*) (Figure 3.1.8b). Interestingly, this gel exhibits excellent elastic behavior, which prompted us to investigate their mechanical properties (Figure 3.1.8c and d). The storage modulus (G') of the **T-OPV:C-PBI** hydrogels (3.3 mM) measured as a function of angular frequency (ω) (1% strain) showed a significant elastic response and was always greater than the corresponding loss modulus (G''). The value of G' (~ 1000 Pa) and the ratio of G' to G'' (~ 8) remain unaffected up to an angular frequency of 70 rad s^{-1} suggesting the good mechanical stability and the elastic nature of these gels. More importantly, the gel did not collapse when a stress up to 100 Pa (13.5 % strain, $G'/G'' = 2.99$) is applied at a constant frequency of 1 Hz, which is evident from the $G'/G'' > 1$ values.²⁷ This is quite remarkable, as most of the organogels and hydrogels made up of small molecules have a much lower critical strain/stress region where they collapse.

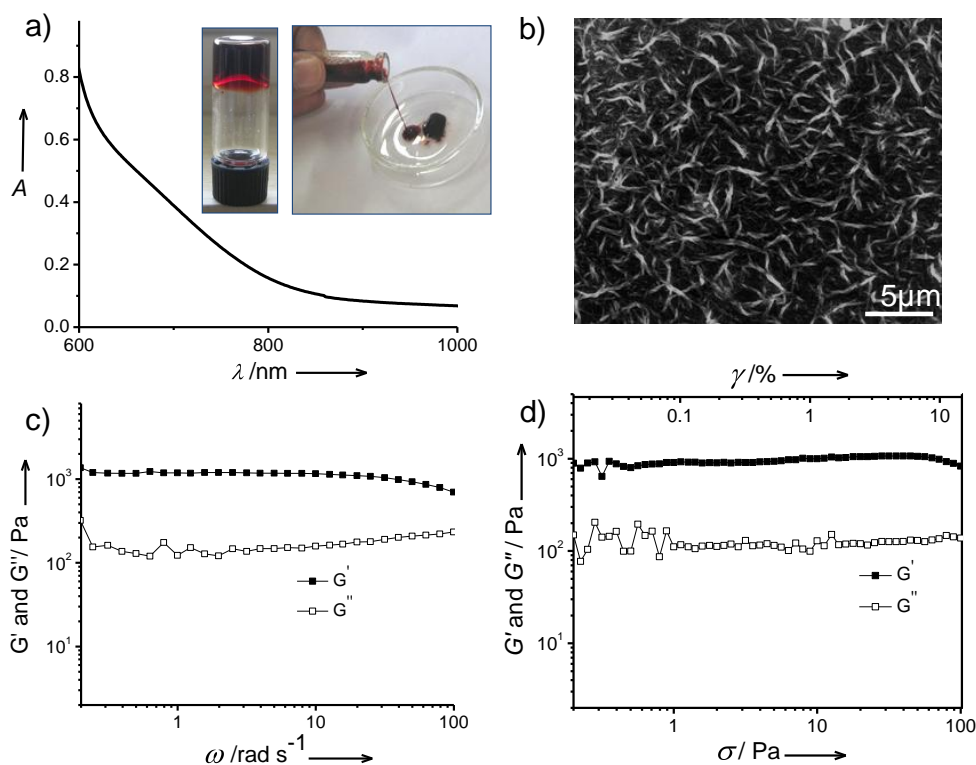


Figure 3.1.8. Characterization of **T-OPV:C-PBI** CT hydrogels. a) Absorption spectrum of CT-gel (3.3 mM, $l = 1$ mm); inset shows the photographs of the gel exhibiting the self-standing and viscous behaviour. b) FE-SEM image of the hydrogel on a glass substrate. Storage (G') and loss (G'') modulus of the gel measured as functions of c) angular frequency (ω) at a constant strain of 1 % and d) stress (σ) or strain (γ) % at a constant frequency of 1 Hz.

3.1.5c Optical Studies

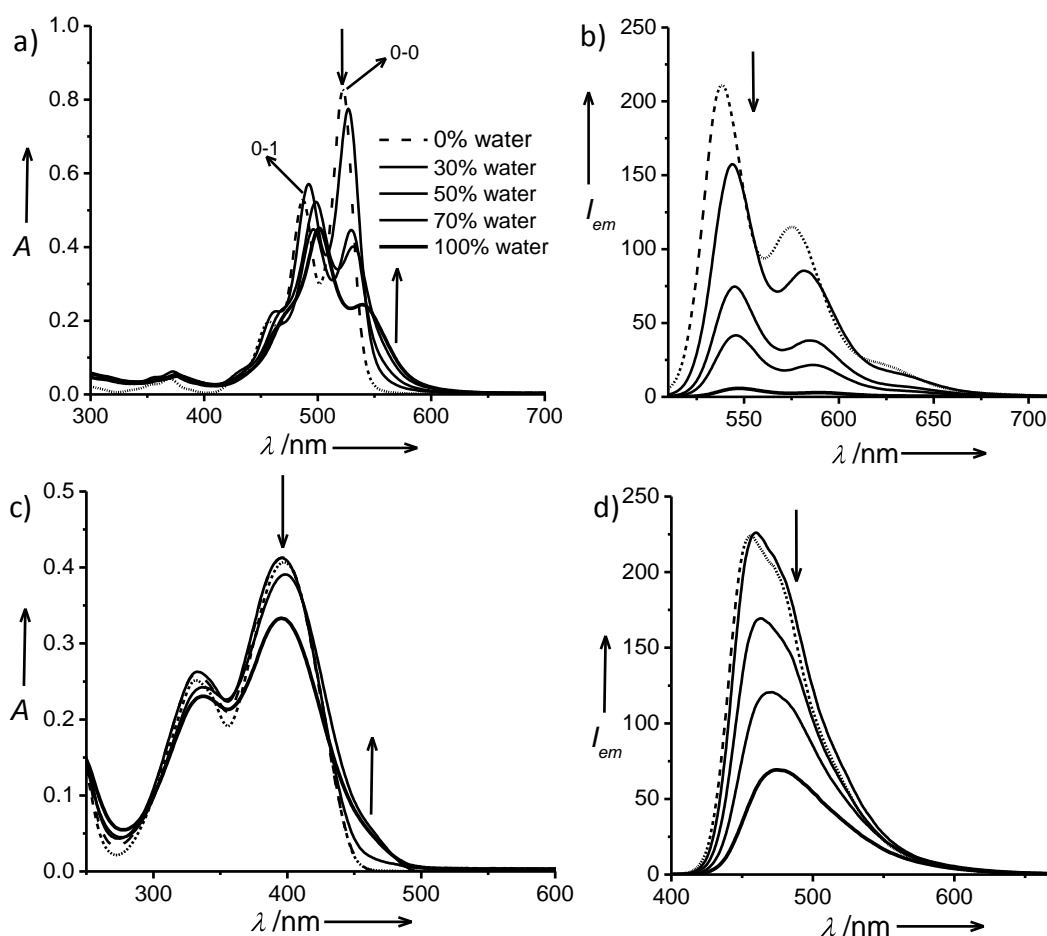


Figure 3.1.9. Aggregation studies of **C-PBI** and **T-OPV** in methanol-water mixtures. a) Absorption and b) emission spectra of **C-PBI** in methanol water mixtures. c) Absorption and d) emission spectra of **T-OPV** in methanol water mixtures ($c = 0.1 \text{ mM}$, $l = 1 \text{ mm}$, $\lambda_{exc} = 380 \text{ nm}$ for **T-OPV** and 500 nm for **C-PBI**). The line symbols signifying the % of water in methanol in Figure 3.1.9a are also same for the rest of the spectra.

Since both **T-OPV** and **C-PBI** molecules have extended π -conjugated backbone with an amphiphilic structure, they individually self-assemble in water to J- and H- type assemblies respectively which were probed in detail by spectroscopic and microscopic techniques. Both **T-OPV** and **C-PBI** monomers do not associate in methanol and showed their characteristic cyan ($\lambda_{exc} = 380 \text{ nm}$, $\lambda_{max} = 456 \text{ nm}$) and orange ($\lambda_{exc} = 500 \text{ nm}$, $\lambda_{max} = 522 \text{ nm}$) colored fluorescence, respectively (Figure 3.1.9). However, **C-PBI**, which is a typical bolaamphiphile, exhibited a reversal in the intensity of 0-1 and 0-0 absorption bands ($I_{0-1}/I_{0-0} > 1$) and quenching of fluorescence with increasing percentages of water in methanol, indicating its self-assembly (Figure 3.1.9a and b). The non-fluorescent nature of PBI self-assembly is characteristic of H-Type face-to-face associated PBI-monomers.²⁸ On the other hand, **T-OPV** showed characteristic spectral changes of OPV chromophoric association, with increasing percentages of water in methanol. The appearance of a shoulder absorption band at 465 nm and the broad

red-shifted emission (~ 19 nm red-shift, $\lambda_{\max} = 475$ nm) in 70% v/v water in methanol are indicative of J-type organization of the OPV molecules (Figure 3.1.9c and d).²⁹

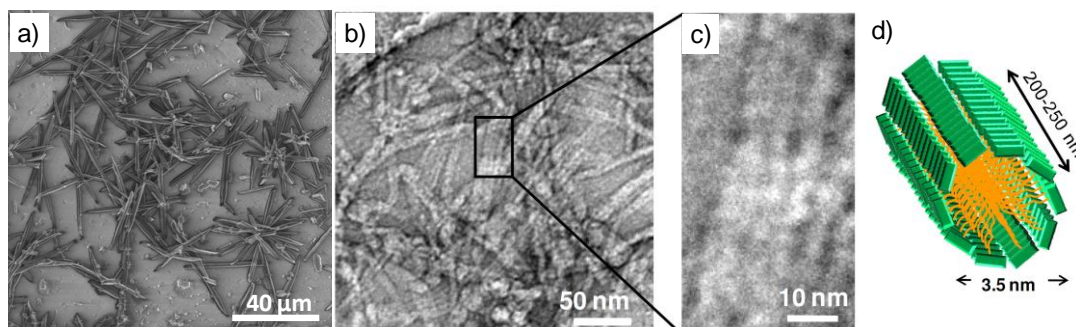


Figure 3.1.10. a) FE-SEM image of **C-PBI** in water at 0.1 mM concentration. b) and c) TEM images and d) schematic representation of **T-OPV** (0.1 mM) cylindrical micelles in water.

FE-SEM images of 0.1 mM of **C-PBI** in water on glass substrates, showed the formation of microrods of 50-70 μm length with widths of 2-3 μm (Figure 3.1.10a).³⁰ TEM of the **T-OPV** self-assembly (0.1 mM) in water showed the formation of 1-D nanostructures of 200-250 nm length with widths in the range of 10-15 nm (Figure 3.1.10b and c). Interestingly, a careful examination of these nanostructures that are negatively stained with uranyl acetate (1 wt % in water) showed that they consist of 3-4 laterally organized primary fibers having a uniform diameter of 3.5 nm. **T-OPV** amphiphile in its fully stretched T-shaped conformation has a molecular length of 1.8 nm along the alky chain direction, which suggests that the fibers might have a cylindrical micellar organization of the OPV bilayers as already reported in various rod-coil shaped amphiphiles (Figure 3.1.10d).^{3d,e}

Since the absorption and fluorescence properties of π -conjugated molecules are very sensitive to the intermolecular and D-A CT interactions, we have performed detailed spectroscopic studies of the diluted solutions of **T-OPV:C-PBI** co-assembly in water, to obtain further insight into their co-assembled microscopic structure. Titration of **C-PBI** with **T-OPV** (1×10^{-4} M) resulted in a gradual red-shift (up to 14 nm) in the absorption maximum of the later, with the concomitant appearance of the CT band at 700 nm, which is very intense at 1:1 stoichiometry of the monomers, suggesting the co-facial organization of monomers (Figure 3.1.11a and b).^{10a} PBI absorption spectral features, particularly the intensity ratio of 0-0 and 0-1 absorption maxima which is very sensitive to inter-chromophoric interactions,²⁹ also provided insight into the mixed organization of the D and A monomers. At the initial stages of titration, the higher intensity of 0-1 peak than the 0-0 peak ($I_{0-1}/I_{0-0} > 1$) in PBI absorption is characteristic of intermolecular PBI interactions, as observed in the homo-assembly of **C-PBI** (*vide supra*). However, upon co-assembly with **T-OPV**, I_{0-1}/I_{0-0} ratio reverses, and the 0-0 peak gets intense compared to the 0-1 peak at 1:1 stoichiometry of the monomers, supporting the mixed-stack D-A organization (Figure 3.1.11a). In addition, complete quenching of the fluorescence is observed for both OPV and PBI monomers, in the 1:1 co-assembly

characteristic of the non-fluorescent nature of the mixed CT D-A complexes (Figure 3.1.11c). The decrease in I_{0-1}/I_{0-0} of PBI absorption (characteristic of alternate co-assembly), the appearance of charge-transfer band at 700 nm and quenching in the **T-OPV** emission was further evident from the reverse titration of **T-OPV** with **C-PBI** (Figure 3.1.11d and e).

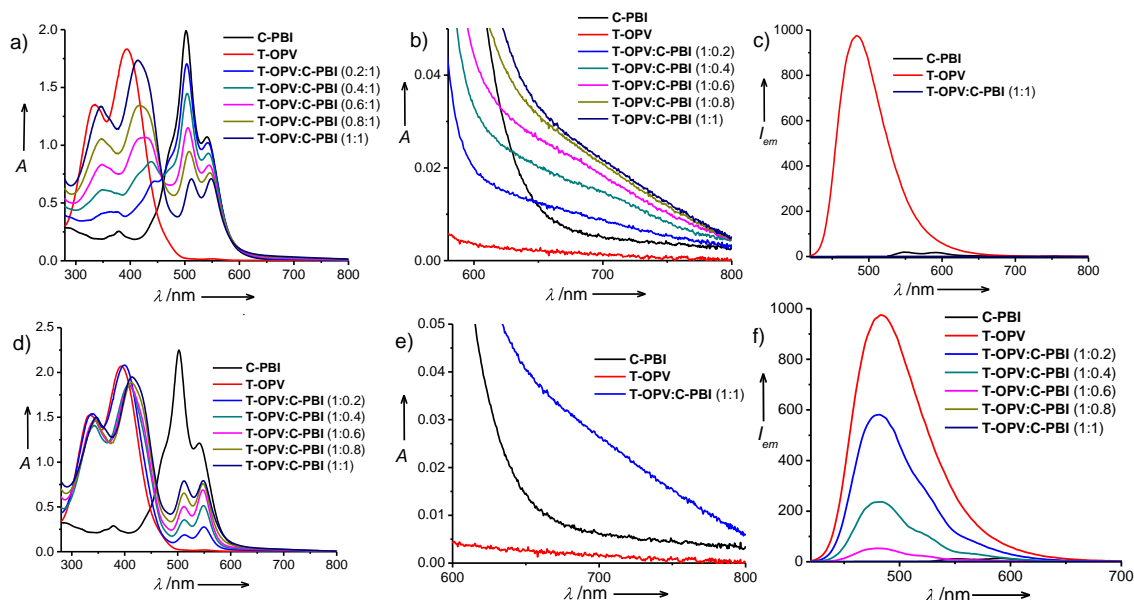


Figure 3.1.11. a) Absorption spectra for the titration of **C-PBI** with **T-OPV** in water. b) Magnified spectra of 'a' between 600-800 nm to show the CT-band clearly ($c = 0.1$ mM, $l = 5$ mm). c) Emission spectra of **T-OPV**, **C-PBI** and their 1:1 CT co-assembly in water ($c = 0.1$ mM, $l = 5$ mm, $\lambda_{exc} = 380$ nm). d) Changes in the absorption spectra for the titration of **T-OPV** with **C-PBI** in water and e) magnified spectra of **C-PBI**, **T-OPV** and **T-OPV:C-PBI (1:1)** from 'd' between 600-800 nm to show the CT-band clearly. f) Changes in the emission spectra for the titration of **T-OPV** with **C-PBI** in water ($\lambda_{exc} = 380$ nm, $c = 0.1$ mM, $l = 5$ mm).

Interestingly, the excitation at 380 nm of the co-assembly showed a non-linear quenching in the fluorescence of **T-OPV** on titration with increasing equivalents of **C-PBI** (Figure 3.1.11f). In addition, this amplification effect in the D quenching also suggest that, the D-A hetero-dimer pairs are incorporated in the **T-OPV** self-assembled chains and act as an energy trap for more number of co-assembled OPV molecules (schematic in the inset of Figure 3.1.12a). Similar amplified fluorescence quenching through Förster resonance energy transfer (FRET) has been observed in D helical and organogel assemblies where the energy acceptors are co-assembled through π - π interactions.³¹ We envisage similar energy transfer from OPV to the non-fluorescent CT state in our system as the transient absorption studies ruled out the possibilities of any photoinduced electron transfer. Time-resolved pico-second fluorescence decay measurements of the co-assembled **T-OPV:C-PBI** and the corresponding monomers further supported the possibility of energy transfer (Figure 3.1.12b). The decay of the **T-OPV** emission (1.8 ns in the monomer self-assembly) is significantly shortened in the co-assembly. The presence of very short **T-OPV** lifetime of < 50 ps (monitored at 475 nm), which almost

follows the instrument lamp profile, at all stages of co-assembly process confirmed the presence of a very fast exciton migration and non-radiative energy transfer in the co-assembly. On the other hand, monitoring the PBI emission in the homo- and co-assembled states (600 nm) showed a mono-exponential decay with a lifetime of around ~ 4.3 ns, characteristic of the PBI monomer, which is in consistent with the non-fluorescent nature of these PBI assemblies. The presence of energy transfer in the co-assembly is further evident from the reverse titration of **T-OPV** with **C-PBI**, which showed only a linear quenching of PBI fluorescence with increasing equivalents of OPV, suggesting that OPV monomers are co-assembled in an isolated way in the PBI stacks, forming ground-state CT interactions with the neighbouring PBI molecules (Figure 3.1.12a). The 1:1 stoichiometry and alternate D-A sequence of the **T-OPV:C-PBI** co-assembly was further confirmed by using Job plot (Figure 3.1.12c). The formation of mixed stacks from the pre-assembled D and A molecules in water further indicates that the individual aggregation of D and A molecules is dynamic enough to reorganize to form more stable alternate D-A co-assembly.

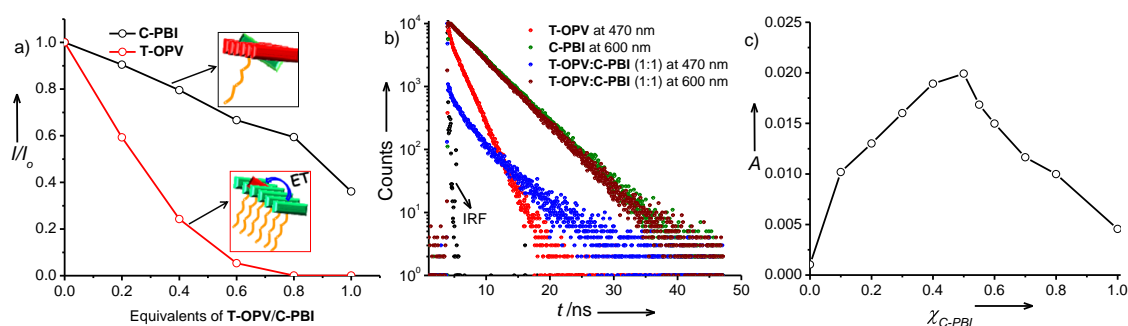


Figure 3.1.12. a) Fluorescence quenching during titration experiments. Red curve show the fluorescence quenching of **T-OPV** ($\lambda_{mon} = 485$ nm) on titration with **C-PBI** and black curve shows the changes in the emission of **C-PBI** ($\lambda_{mon} = 550$ nm) on reverse titration with **T-OPV**. Insets show the schematic representations of the molecular structure of corresponding co-assembly. b) Fluorescence lifetime decay profiles for individual **T-OPV**, **C-PBI** and their 1:1 complex ($\lambda_{exc} = 390$ nm, $c = 0.1$ mM, solvent = 20% methanol in water, $l = 10$ mm, wavelengths mentioned in the inset represents where the decay was monitored and IRF is the instrument response function). c) Job plot by probing the CT absorbance at 700 nm for **T-OPV:C-PBI** co-assembly (Total concentration = 0.2 mM, solvent = water, $l = 5$ mm).

3.1.5d Morphology Studies

Detailed TEM and AFM studies were performed to get insight into the microstructure of the one-dimensional nanostructures formed by the self-assembly of wedge-shaped **T-OPV:C-PBI** non-covalent amphiphile in water. AFM images of a dilute, aqueous solution of these assemblies (0.1 mM) showed dense fiber networks, with extensive cross-linking (Figure 3.1.13a). The dimensions of these nanofibers are about 200-300 nm in width and with a length of more than 15 μm (Figure 3.1.13a and b). Interestingly, TEM images of these 1-D structures negatively stained with uranyl acetate showed the presence of the tubular

morphologies with 35-50 nm diameters, in agreement with the reported nanotube formation of similar wedge-shaped amphiphiles (Figure 3.1.13c and d).³² AFM cross-sectional analysis of these fibers showed a height of 30-40 nm, which is very close to the diameter of the nanotubes, revealing the rigidity of these tubular structures. This further suggests that the fibrous morphology visualized through AFM were bundles of nanotubes, which could have formed by the lateral association of these nanotubes through ionic interactions between their charged surfaces. Detailed TEM analysis of the tubes further revealed a uniform wall thickness of 7 nm, which is two times to the calculated bilayer thickness (3.5 nm) of the CT-amphiphile (Figure 3.1.13e and f). This indicates that the tube walls are constructed by two coats of bilayers, as previously reported for many amphiphilic self-assemblies.³¹ Hence it can be proposed that, the aromatic surfaces of the CT amphiphilic pairs are organized perpendicular to the length of the tubes promoting the 1-D self-assembly through synergic π - π and hydrophobic interactions.

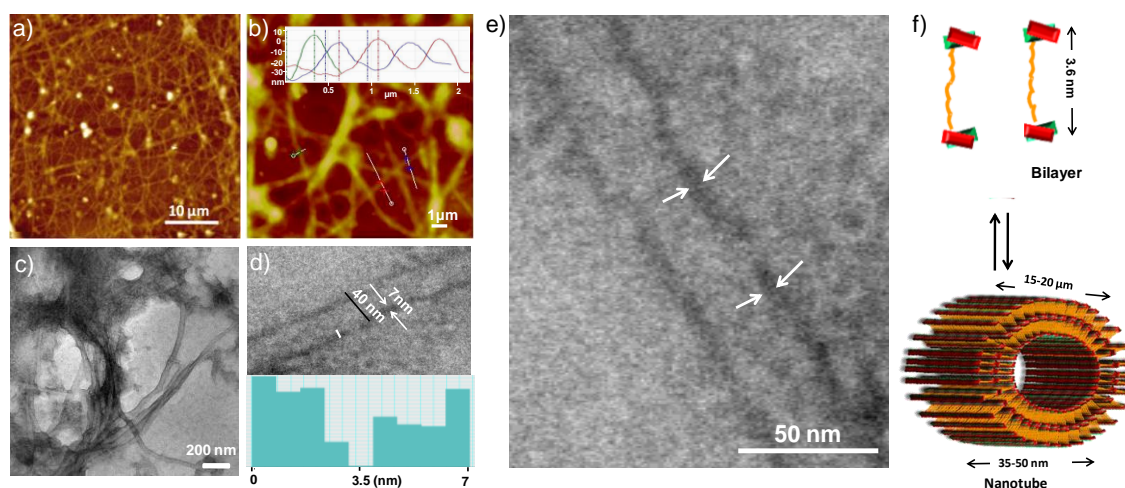


Figure 3.1.13. Microscopic studies of *T-OPV:C-PBI* co-assembly: a) and b) AFM height images of the fibers and the inset of 'b' shows the corresponding cross-sectional analyses. c) and d) TEM images of the nanotubes. Electron density profile of the nanotube wall (marked as white bar in the image) is also shown in Figure 3.1.13d. The dip in the profile could be an indication of the existence of two bilayers in the nanotube wall of 7 nm and e) zoomed picture of 'd'. f) Schematic representation of the bilayers and nanotube formed from the *T-OPV:C-PBI* non-covalent amphiphile.

3.1.5e Conductive AFM Studies

In order to validate our mixed stack CT design for conducting nanostructures, conductive atomic force microscopy (C-AFM) experiments were carried out on the *T-OPV:C-PBI* nanotubes (Figure 3.1.14). The samples were prepared by drop-casting the aqueous solution of the nanotubes onto a gold coated glass substrate followed by vacuum-drying to remove the solvent and AFM images of these substrates showed dense network of CT nanotubes. Interestingly, *I-V* responses of these nanotubes showed non-linear behaviour and the

resistance near voltage (V) = 0 obtained by analyzing the slope of I - V curve was 0.2 M Ω . The conductivity of the fibers having an average height of ~ 35 nm is found out to be 0.02 Scm $^{-1}$, which is one of the highest values reported for a supramolecular nanostructure without any external doping.^{7c} These measurements were further supported by two probe I - V measurements on the nanotubes across the gold electrodes (Figure 3.1.14c). The resistance found in this case is one order higher than C-AFM measurements probably due to the more contact resistance.

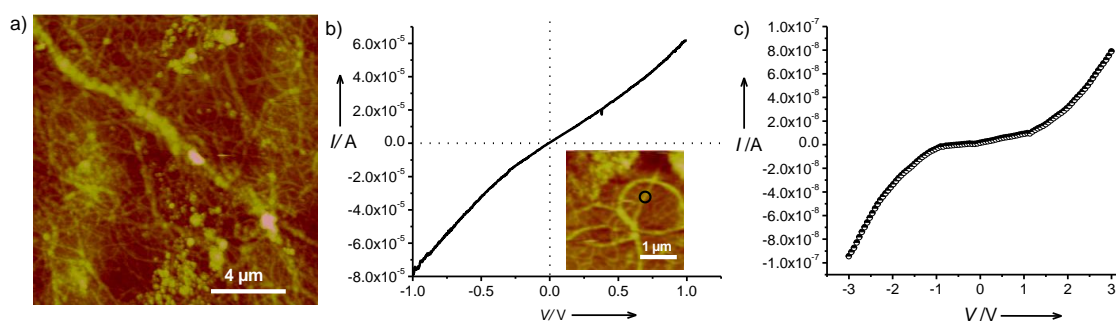


Figure 3.1.14. a) Tapping mode AFM image of the **T-OPV:C-PBI** nano-tubes (0.1 mM) drop casted on gold coated glass substrate and b) the corresponding C-AFM I - V curves. The black circle in the inset image of 'b' shows the fiber where the I - V measurements were performed. c) I - V profile of 0.1 mM solution of **T-OPV:C-PBI** (1:1) nano tubes drop casted on two gold electrodes having a gap of 6 μ m.

3.1.6 Conclusions

In summary, we have presented a novel strategy for the conducting organic nanostructures by the supramolecular alternate, mixed self-assembly of D and A molecules, using a non-covalent amphiphilic design. We demonstrate that this amphiphilic design is a very powerful tool to promote efficient co-facial assembly of even large molecules with structurally different extended π -conjugated backbones, which are otherwise known to phase-segregate. The CT nanostructures presented here, with an unprecedented co-facial organization of D and A chromophores, exhibit high mobility/conductivity even without external doping and hence hold great promise in the emerging area of supramolecular electronics.

3.1.7 Experimental Section

General Methods: Field Emission Scanning Electron Microscopy (FE-SEM) measurements were performed on a NOVANO SEM 600 (FEI) in low vacuum mode by drop casting the solutions on glass substrate followed by drying in vacuum and operated with an accelerating voltage of 5 kV. Transmission Electron Microscopy (TEM) measurements were performed on a JEOL, JEM 3010 operated at 300 kV. Samples were prepared by placing a drop of the solution on carbon coated copper grids followed by drying at room temperature. The images were recorded with an operating voltage 300 kV. In order to get a better contrast samples were stained with uranyl acetate (1 wt% in water) before the measurements. Atomic Force

Microscopy (AFM) measurements were performed on a Veeco diInnova SPM operating in tapping mode regime. Micro-fabricated silicon cantilever tips doped with phosphorus and with a frequency between 235 and 278 kHz and a spring constant of 20-40 Nm^{-1} were used. The samples were prepared by drop casting aqueous solutions on glass substrate and dried in air followed by vacuum drying. Electronic absorption spectra were recorded on a Perkin Elmer Lambda 900 UV-VIS-NIR Spectrometer and emission spectra were recorded on Perkin Elmer Ls 55 Luminescence Spectrometer. UV-Vis and emission spectra were recorded in either 1 mm, or 5 mm path length cuvettes with 350 nm, 380 nm and 500 nm excitation wavelengths. Fluorescence life time decay was recorded in a time-correlated single-photon-counting spectrometer of Horiba-Jobin Yvon. NMR spectra were obtained with a Bruker AVANCE 400 (400 MHz) Fourier transform NMR spectrometer with chemical shifts reported in parts per million (ppm). Rheological measurements were performed on Anton Paar MCR 301, stress controlled rheometer with a cone and plate geometry. The cone diameter is 25 mm and angle is 2°. The experiments were carried out with a plate gap of 49 μm at 26 °C.

Conductive AFM (C-AFM): Conducting-atomic force microscopy (C-AFM) measurements were performed using Pt/Ir coated Si tips operated in contact mode on a diInnova SPM (Veeco, USA). The conducting tip is brought into contact with the substrate until a preset loading force is reached. The bias voltage on the sample is then varied while the resulting current is measured. The conductivity of the CT-nanotubes were calculated using following formula^{7c}

$$\text{Conductivity} = d/(A_t R) \text{ Scm}^{-1}$$

Where d = Height of the nanotube

A_t = Area of the C-AFM probe in contact with the surface

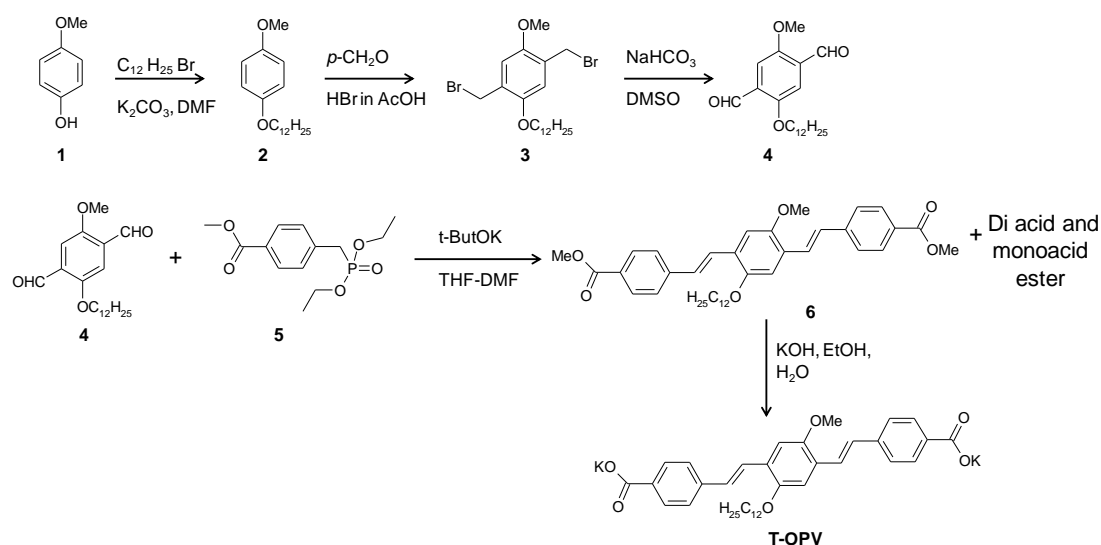
R = Resistance

Hydrogel preparation: In a typical experimental procedure, 1:1 molar ratio of D and A were taken in water at required concentration and the resultant mixture was heated up to 90 °C and left at room temperature. Hydrogel was formed within minutes, which was confirmed by inverted vial method.

3.1.7a Synthesis

Compounds **DMV**,²⁴ **BMV**,²⁴ **CS**,²³ **PS**,²⁶ **C-PBI**,³³ and compounds **2-5**³⁴ were synthesized according to the literature methods. Methyl viologen (**MV**) was purchased from Acros-Organics and compound **1** was purchased from Sigma Aldrich.

Scheme for the synthesis of T-OPV:



Synthesis of T-OPV: A mixture of potassium tertiary butoxide (600 mg) and dry DMF (18 mL) was taken in a R. B. flask and stirred for 10 min. To this, a mixture of **4** (600 mg, 1.72 mmol) and **5** (1.48 g, 5.18 mmol) in dry THF (25 mL) was added and stirred at room temperature for 2 h. Then the temperature was raised to 50 °C and stirring was continued at this temperature for another 12 h. After this, the resulting mixture was added to 100 mL of 3N HCl and then stirred for additional 15 minutes. The yellow precipitate formed was then filtered, washed with water and dried. MALDI-TOF spectra indicated the presence of compound **6** along with fully hydrolyzed diacid and partially hydrolyzed monoacid ester. This crude mixture was then added to ethanol and refluxed at 90 °C. 3% KOH (150 mL) solution was added drop by drop to the reaction mixture over a period of 2 h and continued the reaction for additional 12 h. The yellow precipitate formed was filtered and washed with small amounts of ethanol (10 mL) and dried in vacuum to give the product **T-OPV** in 70 % yield (800 mg). 1H NMR (DMSO- D_6 , 400 MHz) δ (ppm) = 7.81 (d, J = 6.2 Hz, 4H), 7.25-7.43 (m, 10H), 4.09 (t, J = 6.4 Hz, 3H), 3.89 (s, 3H), 1.81 (m, 2H), 1.52 (m, 2H), 1.23 (m, 16H), 0.85 (t, J = 6.7 Hz, 3H); ^{13}C NMR (DMSO- D_6 , 100 MHz) δ (ppm) = 168.4, 151.0, 150.5, 129.4, 129.1, 126.4, 125.8, 125.0, 124.9, 122.4, 109.5, 79.1, 56.0, 31.2, 29.0, 28.9, 28.8, 28.7, 28.6, 25.7, 22.0, 18.5, 13.9.

3.1.8 References

- T. Aida, E. W. Meijer, S. I. Stupp, *Science* **2012**, 335, 813;
 - S. S. Babu, S. Prasanthkumar, A. Ajayaghosh, *Angew. Chem. Int. Ed.* **2012**, 51, 1766;
 - F. J. M. Hoeben, P. Jonkheijm, E. W. Meijer, A. P. H. J. Schenning, *Chem. Rev.* **2005**, 105, 1491;
 - F. Würthner, *Angew. Chem. Int. Ed.* **2001**, 40, 1037;
 - A. Ajayaghosh, S. J. George, A.

-
- P. H. J. Schenning, *Top. Curr. Chem.* **2005**, 258, 83; f) L. Zang, Y. Che, J. S. Moore, *Acc. Chem. Res.* **2008**, 41, 1596; g) P. Terech, R. G. Weiss, *Chem. Rev.* **1997**, 97, 3133.
2. a) A. Ajayaghosh, S. J. George, *J. Am. Chem. Soc.* **2001**, 123, 5148; b) T. F. A. De Greef, M. M. J. Smulders, M. Wolffs, A. P. H. J. Schenning, R.P. Sijbesma, E. W. Meijer, *Chem. Rev.* **2009**, 109, 5687; c) X.-Q. Li, V. Stepanenko, Z. Chen, P. Prins, L. D. A. Siebbeles, F. Würthner, *Chem. Commun.* **2006**, 3871; d) P. Jonkheijm, P. van der Schoot, A. P. H. J. Schenning, E. W. Meijer, *Science* **2006**, 313, 80; e) A. Ajayaghosh, V. K. Praveen, *Acc. Chem. Res.* **2007**, 40, 644.
 3. a) J. P. Hill, W. Jin, A. Kosaka, T. Fukushima, H. Ichihara, T. Shimomura, K. Ito, T. Hashizume, N. Ishii, T. Aida, *Science* **2004**, 304, 1481; b) K. V. Rao, S. J. George, *Org. Lett.* **2010**, 12, 2656; c) W. Jin, Y. Yamamoto, T. Fukushima, N. Ishii, J. Kim, K. Kato, M. Takata, T. Aida, *J. Am. Chem. Soc.* **2008**, 130, 9434; d) K.-S. Moon, H.-J. Kim, E. Lee, M. Lee, *Angew. Chem. Int. Ed.* **2007**, 46, 6807; e) H.-J. Kim, T. Kom, M. Lee, *Acc. Chem. Res.* **2011**, 44, 72; f) X. Zhang, Z. Chen, F. Würthner, *J. Am. Chem. Soc.* **2007**, 129, 4886.
 4. a) M. Numata, D. Kinoshita, N. Taniguchi, H. Tamiaki, A. Ohta, *Angew. Chem. Int. Ed.* **2012**, 51, 1844; b) P. G. A. Janssen, A. Ruiz-Carretero, D. González-Rodríguez, E. W. Meijer, A. P. H. J. Schenning, *Angew. Chem. Int. Ed.* **2009**, 48, 8103.
 5. W. Zhang, W. Jin, T. Fukushima, A. Saeki, S. Seki, T. Aida, *Science* **2011**, 334, 340.
 6. a) M. Hasegawaa, M. Iyoda, *Chem. Soc. Rev.* **2010**, 39, 2420; b) S. Prasanthkumar, A. Saeki, S. Seki, A. Ajayaghosh, *J. Am. Chem. Soc.* **2010** 132, 8866; c) C.-Q. Ma, E. Mena-Osteritz, T. Debaerdemaeker, M. M. Wienk, R. A. J. Janssen, P. Bäuerle, *Angew. Chem. Int. Ed.* **2007**, 46, 1679–1683; d) S. Sengupta, D. Ebeling, S. Patwardhan, X. Zhang, H. von Berlepsch, C. Böttcher, V. Stepanenko, S. Uemura, C. Hentschel, H. Fuchs, F. C. Grozema, L. D. A. Siebbeles, A. R. Holzwarth, L. Chi, F. Würthner, *Angew. Chem. Int. Ed.* **2012**, 51, 6378.
 7. a) J. Puigmartí-Luis, V. Laukhin, Á. P. del Pino, J. Vidal-Gancedo, C. Rovira, E. Laukhina, D. B. Amabilino, *Angew. Chem. Int. Ed.* **2007**, 46, 238; b) Y. Che, A. Datar, K. Balakrishnan, L. Zang, *J. Am. Chem. Soc.* **2007**, 129, 7234; c) S. Prasanthkumar, A. Gopal, A. Ajayaghosh, *J. Am. Chem. Soc.* **2010**, 132, 13206.
 8. a) J. Ferraris, D. O. Cowan, V. Walatka, J. H. Perlstein, *J. Am. Chem. Soc.* **1973**, 95, 948; b) V. Coropceanu, J. Cornil, D. A. da S. Filho, Y. Olivier, R. Silbey, J.-L. Brédas, *Chem. Rev.* **2007**, 107, 926; c) A. Girlando, A. Painelli, C. Pecile, G. Calestani, C. Rizzoli, R. M. Metzger, *J. Chem. Phys.* **1993**, 98, 7692.
 9. A. P. H. J. Schenning, E. W. Meijer, *Chem. Commun.* **2005**, 3245.
 10. a) E. H. A. Beckers, S. C. J. Meskers, A. P. H. J. Schenning, Z. Chen, F. Würthner, P. Marsal, D. Beljonne, J. Cornil, R. A. J. Janssen, *J. Am. Chem. Soc.* **2006**, 128, 649; b) A.
-

- P. H. J. Schenning, J. van Herrikhuyzen, P. Jonkheijm, Z. Chen, F. Würthner, E. W. Meijer, *J. Am. Chem. Soc.* **2002**, *124*, 10252; c) P. Jonkheijm, N. Stutzmann, Z. Chen, D. M. de Leeuw, E. W. Meijer, A. P. H. J. Schenning, F. Würthner, *J. Am. Chem. Soc.* **2006**, *128*, 9535; d) M. Lista, J. Areephong, N. Sakai, S. Matile, *J. Am. Chem. Soc.* **2011**, *133*, 15228; e) R. Charvet, Y. Yamamoto, T. Sasaki, J. Kim, K. Kato, M. Takata, A. Saeki, S. Seki, T. Aida, *J. Am. Chem. Soc.* **2012**, *134*, 2524; f) S. Bhosale, A. L. Sisson, P. Talukdar, A. Fürstenberg, N. Banerji, E. Vauthey, G. Bollot, J. Mareda, C. Röger, F. Würthner, N. Sakai, S. Matile, *Science*, **2006**, *313*, 84; g) Y. Yamamoto, T. Fukushima, Y. Suna, N. Ishii, A. Saeki, S. Seki, S. Tagawa, M. Taniguchi, T. Kawai, T. Aida; *Science* **2006**, *314*, 1761; h) K. Sugiyasu, S.-i. Kawano, N. Fujita, S. Shinkai, *Chem. Mater.* **2008**, *20*, 2863.
11. a) C. Wang, Y. Guo, Y. Wang, H. Xu, R. Wang, X. Zhang, *Angew. Chem. Int. Ed.* **2009**, *48*, 8962; b) C. Wang, S. Yin, S. Chen, H. Xu, Z. Wang, X. Zhang, *Angew. Chem. Int. Ed.* **2008**, *47*, 9049; c) K. Liu, C. Wang, Z. Li, X. Zhang, *Angew. Chem. Int. Ed.* **2011**, *50*, 4952–4956; d) X. Zhang, C. Wang, *Chem. Soc. Rev.* **2011**, *40*, 94; e) F. Biedermann, O. A. Scherman, *J. Phys. Chem. B* **2012**, *116*, 2842.
12. L. Zhu, Y. Yi, Y. Li, E.-G. Kim, V. Coropceanu, J.-L. Brédas, *J. Am. Chem. Soc.* **2012**, *134*, 2340.
13. a) G. Giovannetti, S. Kumar, A. Stroppa, J. van den Brink, S. Picozzi, *Phys. Rev. Lett.* **2009**, *103*, 266401; b) M. Masino, A. Girlando, *Phys. Rev. B* **2007**, *76*, 064114; c) P. Ranzieri, M. Masino, A. Girlando, M.-H. Lemée-Cailleau, *Phys. Rev. B* **2007**, *76*, 134115; d) S. Horiuchi, Y. Tokura, *Nat. Mater.* **2008**, *7*, 357.
14. a) U. Rauwald, O. A. Scherman, *Angew. Chem. Int. Ed.* **2008**, *47*, 3950; b) E. A. Appel, F. Biedermann, U. Rauwald, S. T. Jones, J. M. Zayed, O. A. Scherman, *J. Am. Chem. Soc.* **2010**, *132*, 14251; c) S. Ghosh, S. Ramakrishnan, *Angew. Chem. Int. Ed.* **2004**, *43*, 3264; d) R. S. Lokey, B. L. Iverson, *Nature* **1995**, *375*, 303.
15. a) L. Schmidt-Mende, A. Fechtenkötter, K. Müllen, E. Moons, R. H. Friend, J. D. MacKenzie, *Science* **2001**, *293*, 1119; b) W. Pisula, M. Kastler, D. Wasserfallen, J. W. F. Robertson, F. Nolde, C. Kohl, K. Müllen, *Angew. Chem. Int. Ed.* **2006**, *45*, 819; c) D. Adam, P. Schuhmacher, J. Simmerer, L. Häußling, W. Paulus, K. Siemensmeyer, K.-H. Eitzbach, H. Ringsdorf, D. Haarer, *Adv. Mater.* **1995**, *7*, 276.
16. a) J. V. van Herrikhuyzen, A. Syamakumari, A. P. H. J. Schenning, E. W. Meijer, *J. Am. Chem. Soc.* **2004**, *126*, 10021; b) G. De Luca, A. Liscio, M. Melucci, T. Schnitzler, W. Pisula, C. G. Clark Jr, L. M. Scolaro, V. Palermo, K. Müllen, P. Samorì, *J. Mater. Chem.* **2010**, *20*, 71; c) A. Das, M. R. Molla, A. Banerjee, A. Paul, S. Ghosh, *Chem. Eur. J.* **2011**, *17*, 6061; d) Y. Guan, S.-H. Yu, M. Antonietti, C. Bçttcher, C. F. J. Faul, *Chem. Eur. J.*

- 2005**, *11*, 1305; e) A. Jain, K. V. Rao, U. Mogera, A. A. Sagade, S. J. George, *Chem. Eur. J.* **2011**, *17*, 12355.
17. L. F. Dössel, V. Kamm, I. A. Howard, F. Laquai, W. Pisula, X. Feng, C. Li, M. Takase, T. Kudernac, S. De Feyter, K. Müllen, *J. Am. Chem. Soc.* **2012**, *134*, 5876.
18. a) J. D. Hartgerink, E. Beniash, S. I. Stupp, *Science* **2001**, *294*, 1684; b) H. Cui, T. Muraoka, A. G. Cheetham, S. I. Stupp, *Nano Lett.* **2009**, *9*, 945; c) B. Adhikari, J. Nanda, A. Banerjee, *Soft Matter* **2011**, *7*, 9259; d) J. Naskar, S. Roy, A. Joardar, S. Das, *Org. Biomol. Chem.* **2011**, *9*, 6610.
19. a) E. Lee, J.-K. Kim, M. Lee, *Angew. Chem. Int. Ed.* **2008**, *47*, 6375; b) J.-H. Ryu, M. Lee, *J. Am. Chem. Soc.* **2005**, *127*, 14170.
20. a) S. Kiyonaka, K. Sugiyasu, S. Shinkai, I. Hamachi, *J. Am. Chem. Soc.* **2002**, *124*, 10954; b) J. H. Jung, G. John, M. Masuda, K. Yoshida, S. Shinkai, T. Shimizu, *Langmuir* **2001**, *17*, 7229; c) N. Kameta, K. Yoshida, M. Masuda, T. Shimizu, *Chem. Mater.* **2009**, *21*, 5892.
21. a) U. Maitra, S. Mukhopadhyay, A. Sarkar, P. Rao, S. S. Indi, *Angew. Chem. Int. Ed.* **2001**, *40*, 2281-2283; b) J. C. Tiller, *Angew. Chem. Int. Ed.* **2003**, *42*, 3072; c) L. A. Estroff, A. D. Hamilton, *Chem. Rev.* **2004**, *104*, 1201; d) J. F. Hulvat, M. Sofos, K. Tajima, S. I. Stupp, *J. Am. Chem. Soc.* **2005**, *127*, 366; e) P. K. Vemula, G. John, *Chem. Commun.* **2006**, 2218; f) K. M. Anderson, G. M. Day, M. J. Paterson, P. Byrne, N. Clarke, J. W. Steed, *Angew. Chem. Int. Ed.* **2008**, *47*, 1058; g) Y. Chen, X.-H. Pang, C.-M. Dong, *Adv. Funct. Mater.* **2010**, *20*, 579.
22. a) H. D. Nguyen, D. T. Dang, J. L. J. van Dongen, L. Brunsveld, *Angew. Chem. Int. Ed.* **2010**, *49*, 895; b) F. Wang, J. Zhang, X. Ding, S. Dong, M. Liu, B. Zheng, S. Li, L. Wu, Y. Yu, H. W. Gibson, F. Huang, *Angew. Chem. Int. Ed.* **2010**, *49*, 1090.
23. a) S. A-Fouet, I. Seguy, J.-F. Bobo, P. Destruel, H. Bock, *Chem. Eur. J.* **2007**, *13*, 1746; b) A. Ghosh, K. V. Rao, S. J. George, C. N. R. Rao, *Chem. Eur. J.* **2010**, *16*, 2700.
24. M. F. Pepitone, G. G. Jernigan, J. S. Melinger, O.-K. Kim, *Org. Lett.* **2007**, *9*, 801.
25. A.A. Sagade, K. V. Rao, U. Mogera, S. J. George, A. Datta, G. U. Kulkarni, *Adv. Mater.* **2013**, *25*, 559.
26. W. Wang, Y. Bando, C. Zhi, W. Fu, E. Wang, D. Golberg, *J. Am. Chem. Soc.* **2008**, *130*, 8144.
27. a) Q. Wang, J. L. Mynar, M. Yoshida, E. Lee, M. Lee, K. Okuro, K. Kinbara, T. Aida, *Nature* **2010**, *463*, 339; b) S. Samai, K. Biradha, *Chem. Mater.* **2012**, *24*, 1165.
28. a) B. Wang, C. Yu, *Angew. Chem. Int. Ed.* **2010**, *49*, 1485; b) W. Wang, L.-S. Li, G. Helms, H.-H. Zhou, A. D. Q. Li, *J. Am. Chem. Soc.* **2003**, *125*, 1120.

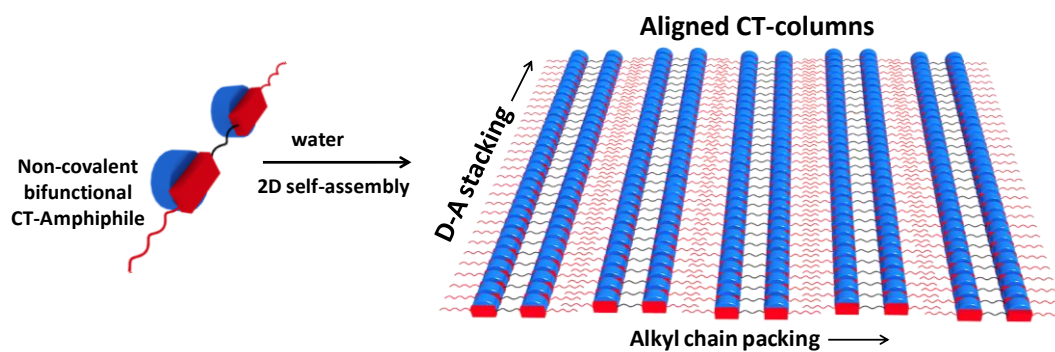
-
29. a) A. Ajayaghosh, S. J. George, *J. Am. Chem. Soc.* **2001**, *123*, 5148; d) A. P. H. J. Schenning, P. Jonkheijm, E. Peeters, E. W. Meijer, *J. Am. Chem. Soc.* **2001**, *123*, 409.
30. Y. Huang, B. Quan, Z. Wei, G. Liu, L. Sun, *J. Phys. Chem. C* **2009**, *113*, 3929.
31. a) F. J. M. Hoeben, L. M. Herz, C. Daniel, P. Jonkheijm, A. P. H. J. Schenning, C. Silva, S. C. J. Meskers, D. Beljonne, R. T. Phillips, R. H. Friend, E. W. Meijer, *Angew. Chem. Int. Ed.* **2004**, *43*, 1976; b) A. Ajayaghosh, V. K. Praveen, C. Vijayakumar, S. J. George, *Angew. Chem. Int. Ed.* **2007**, *46*, 6260; c) S. S. Babu, K. K. Kartha, A. Ajayaghosh, *J. Phys. Chem. Lett.* **2010**, *1*, 3413.
32. T. Shimizu, M. Masuda, H. Minamikawa, *Chem. Rev.* **2005**, *105*, 1401.
33. a) T. Deligeorgiev, D. Zaneva, I. Petkov, *Dyes Pigments* **1994**, *24*, 75; b) T. Ma, C. Li, G. Shi, *Langmuir* **2008**, *24*, 43.
34. a) B. Wang, M. R. Wasielewski, *J. Am. Chem. Soc.* **1997**, *119*, 12; b) P. Shao, Z. Li, J. Luo, H. Wang, J. Qin, *Synth. Commun.* **2005**, *35*, 49.

PART-3 . 2

Autonomous Alignment of Charge-Transfer Fibers via Two-Dimensional Donor-Acceptor Self-Assembly*

Abstract

In this section, we describe a supramolecular cross-linking design to construct aligned charge-transfer (CT) columns of donor (D)-acceptor (A) molecules in solution and on surface. This has been realized via two dimensional (2D) self-assembly of a non-covalent mixed-stack CT-complex, formed between coronene tetracarboxylate (CS) donor and a bi-functional viologen (CV) acceptor in water through a combination of CT and hydrophobic interactions between. Detailed microscopy, linear dichroism (LD) studies and powder XRD measurements revealed the autonomous formation of aligned nanostructures in solution via 2D self-assembly. Furthermore, we have demonstrated the use of CV as a supramolecular cross-linker to induce alignment to the otherwise random CT nanostructures.



**Manuscript based on this work is under preparation*

3.2.1 Introduction

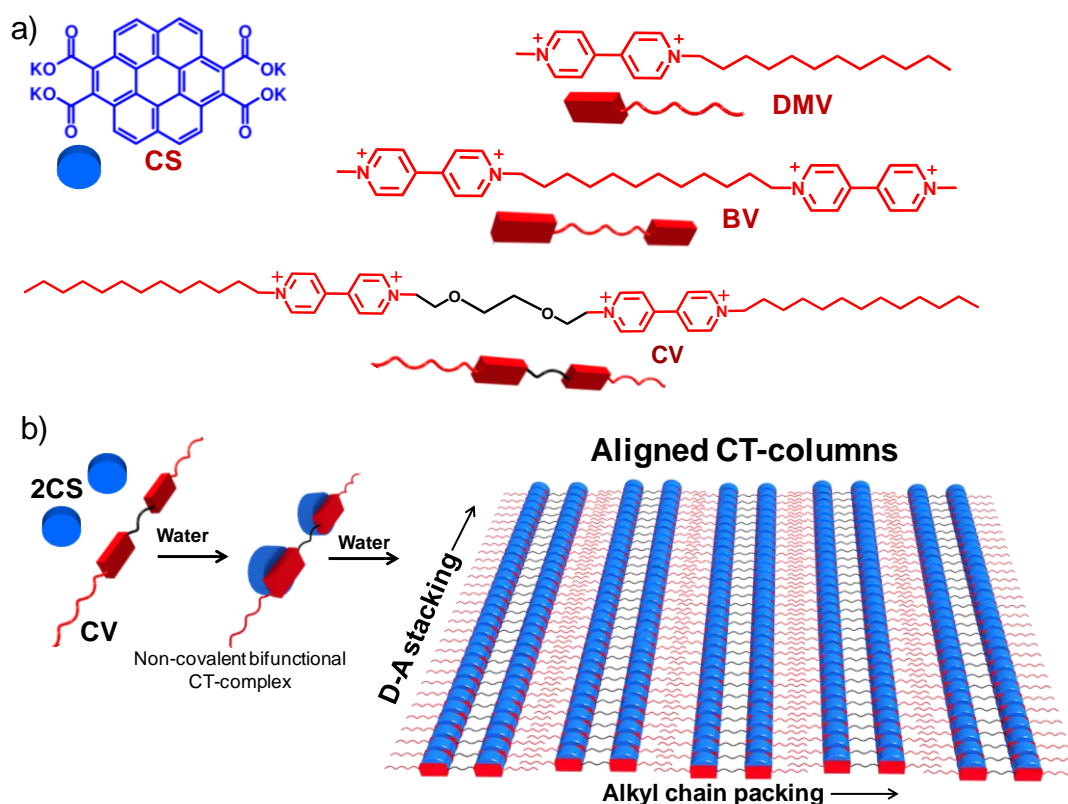
Mixed-stack charge-transfer (CT) assemblies¹ formed via face-to-face organization of electron donor (D) and acceptor (A) molecules have attracted significant attention owing to their effective utilization in the synthesis of new functional materials with tailored properties.² Recently, fascinating optoelectronic³ and ferroelectric⁴ properties are predicted and reported for various D-A mixed stack CT-crystals. The supramolecular D-A organization is shown to be very crucial for the ambipolar charge transport and interesting luminescent properties of CT crystals obtained from various D-A π -conjugated pairs.⁵ Moreover, mixed stack CT-assemblies are the potential candidates for achieving room temperature ferroelectricity with high polarization and they hold great promise in the fabrication of non-volatile memory devices.⁶ We have recently reported the supramolecular synthesis of CT-nanowires using a non-covalent amphiphilic design, for their effective utilization in nanosized electronic devices (see Part-3.1).^{7,8} Field effect transistor (FET) devices made from these nanofibers showed high mobility compared to their CT-crystals with remarkable self-repairing behaviour.⁹ However, similar to other 1D self-assembled nanowires, these CT-nanofibers showed random entanglement when transferred from solution to the surface. In order to improve the performance of these 1D nanofibers on devices, further control over their hierarchical organization is indeed necessary. Anisotropic orientation of nanowires is important for efficient charge transport across their length to minimize the scattering of charge carriers due to local defects.¹⁰

Precise and unidirectional positioning of supramolecular nanowires on device structure is challenging, similar to inorganic nanowires and carbon nanotubes. Alignment of nanostructures is one of the strategies adopted in order to get better organization.¹¹ In this context, several physical methods such as electricfield,¹² magneticfield¹³ and lithography¹⁴ based approaches were successfully demonstrated for aligning conjugated polymers and supramolecular nanofibers of small π -conjugated molecules. Apart from these general methods, Müllen et al. developed a zone-casting technique for generating long range oriented nanowire films from several polyaromatic hydrocarbons.¹⁵ Kato and others demonstrated the use of liquid crystal medium to induce alignment of supramolecular aggregates of π -conjugated molecules.¹⁶ A combination of self-assembly and dewetting were utilized for generation of long range 1D patterns of various electro active π -systems.¹⁷ Surface guided self-assembly,¹⁸ filtration-and-transfer,¹⁹ sound induced alignment²⁰ and physical dragging of fibrous gels²¹ are some other techniques demonstrated for inducing long range alignment to the self-assembled nanowires.

More recently, non-covalent cross-linking of 1D supramolecular stacks and polymer chains has been demonstrated for the construction of aligned and stimuli responsive supramolecular materials.²² Moreover, non-covalent cross-linking is made reversible in some

cases by using stimuli responsive cross-linker.²³ For example, Shinkai et al. utilized specially designed molecular entities for the alignment of conjugated polymers through co-ordination chemistry.²⁴ Scherman et al. have synthesized multistimuli responsive cross-linked polymer hydrogels via host induced CT-interactions.²⁵ However, less attention has been paid on the design of molecules that would give autonomous alignment to the 1D stacks during the process of self-assembly in solution.²⁶ This design would be useful for large area device fabrication in a cost effective manner as it is tedious and expensive to attain the alignment under the influence of physical forces such as electric or magnetic field. Although host-guest interactions have been exploited to align the conjugated polymers in solution, functional aspects of these polymers can be affected by the ground or excited state interactions between host and guest molecules.²⁴ Some of these issues can be addressed by the targeted molecular design of a self-assembling monomer which would give autonomously aligned π -stacks in solution without affecting their electronic functionality.

3.2.2 Design Strategy



Scheme 3.2.1. a) Molecular structures and schematic representation of various donor (CS) and acceptor (DMV, CV, BV) molecules used in the present study. b) Proposed schematic representation of the autonomous alignment of CS-CV CT-columns into crystalline layers in water via 2D self-assembly.

We have used a judicious molecular design of D and A molecules to construct autonomously aligned 1D CT-columns in water. This was achieved by co-assembly between

electron rich coronene tetracarboxylate (**CS**) and electron deficient bi-functional viologen (**CV**) acceptor through a combination of CT interactions and crystallization of paraffinic chains, operating in orthogonal directions (two dimensional (2D) self-assembly, Scheme 3.2.1). The use of **CV** terminating with long alkyl chains at both the ends turned out to be crucial for the alignment of CT-columns, as the CT-complexes formed from mono functional viologen amphiphile (**DMV**) or bisviologen (**BV**) without terminating alkyl chains could only yield randomly aligned 1D nanofibers (Scheme 3.2.1). Transmission electron microscopy (TEM) images revealed the presence of large number of laterally aligned 1D CT-columns, whereas AFM images displayed aligned nanofibers over $15 \times 15 \mu\text{m}^2$ area. These observations are in consistent with the remarkable 1D and 2D lattice correlation lengths observed from powder X-ray diffraction (PXRD) studies. Remarkably, the observed strong linear dichroism of **CS-CV** complex in solution indicated the formation of autonomously aligned assembly in solution. The alignment of the present system in solution would be advantageous for large area device fabrication which is mainly possible by solution processing. Moreover, at higher concentrations, **CS-CV** complex forms hydrogels with ultrahigh content of water (>99.5). Furthermore, we have successfully demonstrated the alignment and cross-linking of unaligned **CS-DMV** cylindrical micelles by co-assembling with small mole fractions of bi-functional **CV**, which further improved their stability and gelation properties.

3.2.3 Optical Studies and Gelation Experiments

The donor (**CS**) and acceptor molecules (**DMV**, **BV** and **CV**) were synthesized according to the literature methods and were fully characterized (see experimental section). All optical and microscopy measurements were performed in water, where **CS** is molecularly soluble. On the other hand, all the viologen derivatives under investigation are weakly assembled in water into spherical aggregates. Titration experiments were performed on dilute solutions (0.1 mM) of **CS** with different equivalents of **CV** to understand the nature and composition of the resultant CT-complex (Figure 3.2.1). Similar to **CS-DMV** CT complex (see Part-3.1), the increase in **CV** concentrations up to 0.05 mM in 0.1 mM solution of **CS** caused ground state spectroscopic changes such as broadening and decrease in the absorbance of **CS** with concomitant appearance of new broad band centred at 500 nm (Figure 3.2.1a and b). This clearly indicates the efficient CT-complex formation between **CS** and **CV** at 1:0.5 (**CS:CV**) molar ratio, in consistent with design. Further increase in the **CV** equivalents (> 0.5) resulted in scattering. Gradual quenching in the **CS** emission was observed with increasing concentration of **CV** which reached saturation at 0.5 equivalents in line with the absorption changes (Figure 3.2.1c and d). Interestingly, at higher concentration (**CS** = 4.0 mM and **CV** = 2 mM) of **CS-CV** complex in 1:0.5 molar ratio, the solutions became viscous and bright red and transparent

hydrogels were formed (Figure 3.2.1d, inset). The observed low critical gelator concentration (CGC) of **CS-CV** complex compared to **CS-DMV** (~8.0 mM), indicates the high water content for these gels. The **CS-CV** network is capable of holding more than 99.5 wt% of water which is one of the highest values reported so far for hydrogels formed from small molecules.²⁷

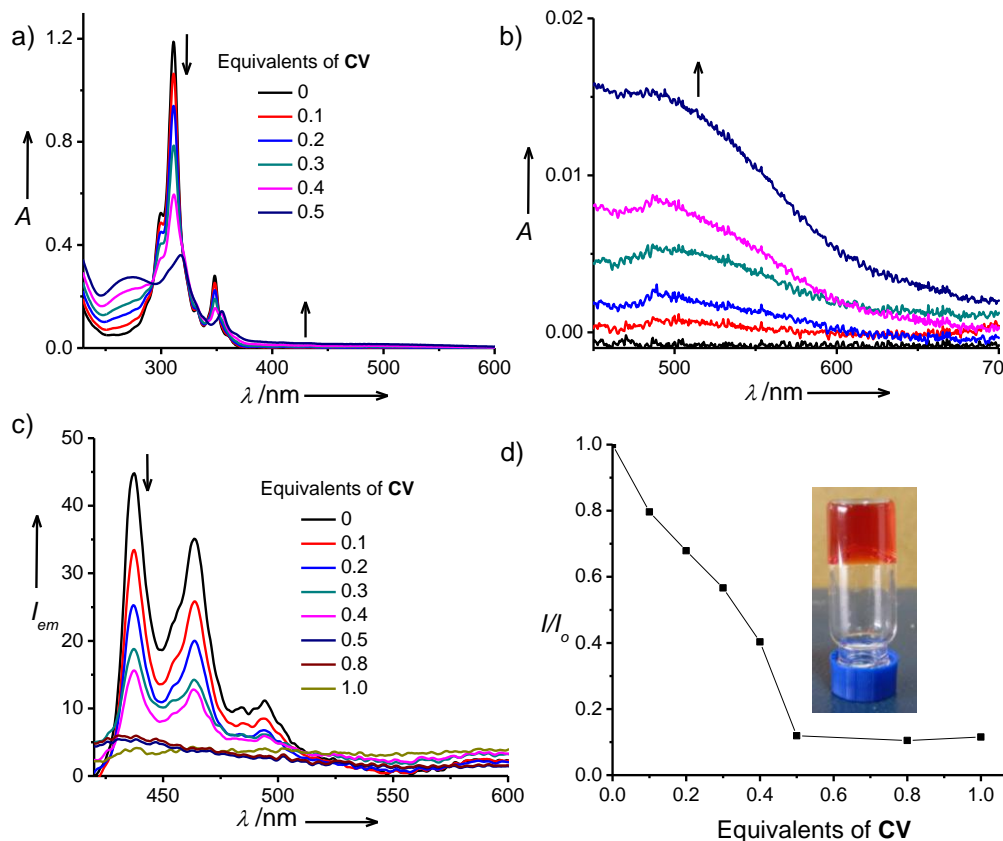


Figure 3.2.1. a) Absorption spectra of CS (0.1mM) with different equivalents of CV in water ($l = 1$ mm). b) Magnified spectra of Figure 3.2.1a between 450-700 nm. c) Corresponding emission spectra of CS with different equivalents of CV in water. d) Plot of emission quenching of CS versus equivalents of CV and inset shows the photograph of the CS-CV hydrogel.

3.2.4 Morphology Studies

Morphological features of these CT-hydrogel networks and their dilute solutions were investigated in detail using transmission electron microscopy (TEM) and atomic force microscopy (AFM). For TEM measurements, the samples were drop casted from their dilute aqueous solutions (0.1 mM) followed by negative staining with uranyl acetate. **CV** alone in water showed the formation of spherical aggregates of 50-100 nm (Figure 3.2.2a). Whereas the TEM images of **CS-CV** (1:0.5) complex showed the presence of aligned structures of few microns in length and few nanometres in width with periodically spaced alternate bright and dark regions (Figure 3.2.2b-d). Since TEM imaging was done in the bright field mode, the dark regions correspond to the hydrophilic segments where staining agent is present and bright regions correspond to the hydrophobic alkyl chains. The widths of the individual dark and

bright regions are ~ 3.0 nm and ~ 2.5 nm respectively, whereas the calculated lengths of hydrophilic and hydrophobic segments of **CS-CV** CT-complex are ~ 2.2 nm and ~ 3 nm, respectively. The observed shorter distances of hydrophobic segments in TEM images suggest that, alkyls chains in the nanostructures are partially interdigitated. The interdigitation of alkyl chains is further evident from PXRD measurements (*vide infra*). On the other hand the width of hydrophilic aromatic segment is more than the calculated values, which might be due to the presence of staining agent. AFM image of the drop casted **CS-CV** dilute solutions (0.1 mM) and hydrogels on glass substrate showed bundles of aligned nanowires even over large areas ($15 \times 15 \mu\text{m}^2$, Figure 3.2.2e and f). Our previous results on **CS-DMV** complex showed that, it can only form randomly entangled 1D nanofibers from water as there are no specific group interactions to induce lateral association of these cylindrical micelles (Figure 3.2.2g).

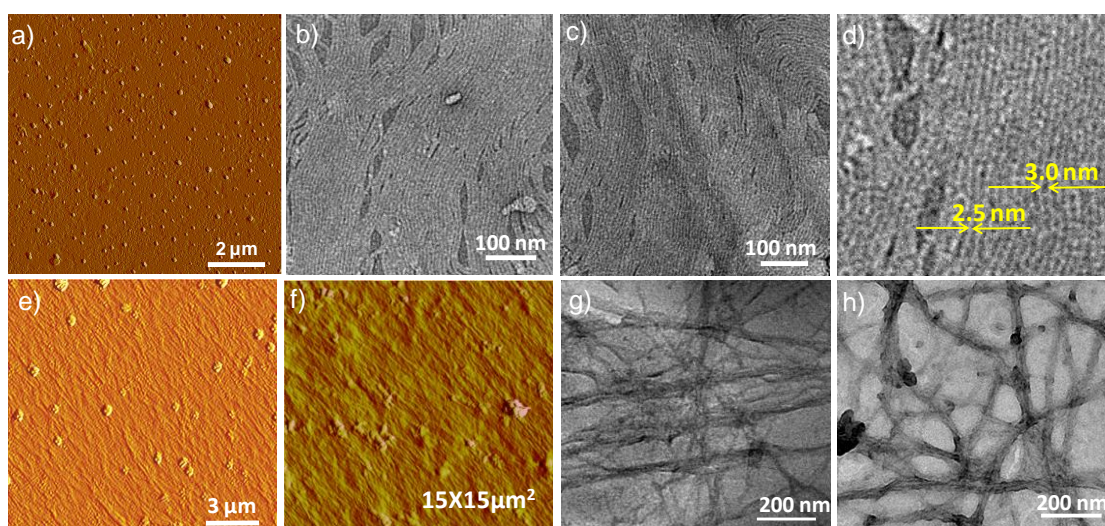


Figure 3.2.2. a) AFM image of **CV** (0.05 mM) formed in water. b), c) and d) TEM images, and e) corresponding AFM image of **CS-CV** co-assembly formed in water. f) AFM image of the **CS-CV** hydrogel. TEM images of g) **CS-DMV** and h) **CS-BV** co-assembly formed in water (**CS** and **DMV** = 0.1 mM, **BV** and **CV** = 0.05 mM).

In contrast to the **CS-DMV** CT-amphiphile, the appearance of aligned CT-columns (dark regions in the aligned structure) in the **CS-CV** assembly can be attributed to the presence of terminating hydrophobic alkyl chains in the bifunctional **CV**. To minimize the repulsive interactions with water, these long alkyl chains interact with each other which further serves as a glue to align the CT-columns of **CS** and viologen in lateral directions. This was further proved by controlled experiments with bifunctional viologen (**BV**) having alkyl chain in the middle instead of at terminal positions as in **CV**. Under similar conditions, TEM images of 0.1 mM water solutions of **CS-BV** (1:0.5) complex showed only 1D nanofibers without any alignment (Figure 3.2.2h). These observations clearly indicate the crucial role of two terminal alkyl chains of **CV** in inducing lateral association of the CT-columns of **CS** and viologen. Since aligned nanostructures were observed only for **CS-CV** CT-complex and not for **CS-DMV** and

CS-BV, under identical conditions and concentrations, we anticipate that this aligned nanostructures are indeed formed in the solution via 2D self-assembly (*vide supra*) and not on the surface due to drying effects. This proposal was further proved using linear dichroism studies in solution.

3.2.5 Linear Dichroism and Powder XRD Studies

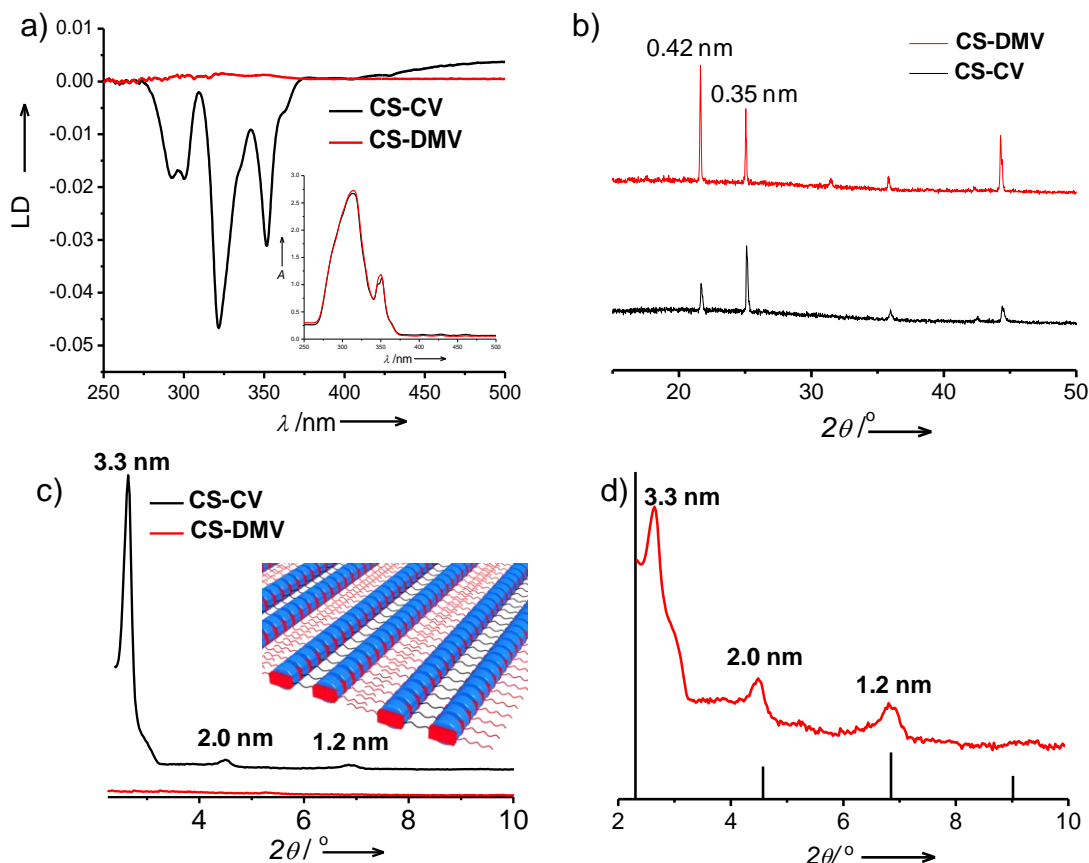


Figure 3.2.3. a) LD spectra of **CS-CV** and **CS-DMV** CT-nanofibers in water (**CS** and **DMV** = 0.5 mM, **CV** = 0.25 mM, $l = 2$ mm) and corresponding absorption spectra is shown in the inset. PXRD patterns of **CS-CV** and **CS-DMV** xerogels on glass substrate; b) in the wide angle region and c) in the small angle region. Schematic representation of aligned CT-columns via 2D self-assembly is shown in the inset of 'c'. d) Comparison of PXRD pattern of **CS-CV** (red curve) with CDB (black lines) crystal pattern.

Since linear dichroism (LD) is a powerful tool to study the alignment of nanowires in solution,^{20,28} we have measured the LD of dilute aqueous solutions (0.5 mM) of **CS-DMV** and **CS-CV** complexes under identical conditions (Figure 3.2.3a). This would provide evidence for the existence of aligned nanostructures in solution. Remarkably, under identical conditions, the aqueous solution of **CS-CV** complex showed strong LD signal, whereas **CS-DMV** did not show any signal. This unambiguously proves that, the aligned structures of **CS-CV** complex are indeed formed in solution via self-assembly, rather than any dewetting process on surfaces. Interestingly all the absorption features of viologen (260-300 nm) and **CS** (290-360 nm)

including their CT-band (440-500 nm) appeared in the corresponding LD spectrum due to the existence of highly oriented anisotropic CT nanostructures in solution.

Small and wide angle PXRD measurements of both **CS-DMV** and **CS-CV** xerogels were performed on glass substrate to get insight into their degree of ordering and crystallinity (Figure 3.2.3b-d). Although both the samples displayed several sharp diffraction peaks between $15-50^\circ$ (2θ), low angle ($2\theta = 2-10^\circ$) peaks are observed only for **CS-CV** hydrogel. This clearly suggests that, only **CS-CV** complex exhibits higher order self-assembled structures. In the wide angle region of PXRD pattern, sharp diffraction peak at $\sim 25^\circ$ (2θ) are observed for both the xerogels which corresponds to the π - π distance between D-A molecules. The observed D-A stacking distances for **CS-DMV** and **CS-CV** complexes are 3.55 \AA and 3.54 \AA , respectively. Moreover, the sharpness of these reflections indicates the existence of long range order in the D-A stacking direction which is along the length of the nanostructures. This motivated us to further evaluate the correlation lengths corresponding to these reflections using Scherrer formula which would provide a quantitative measure of long range order along the D-A stacking direction.²⁹ The observed correlation lengths are 90 nm and 85 nm for **CS-DMV** and **CS-CV** CT-nanofibers, respectively. These values are quite remarkable, as this kind of sharp diffraction peaks with high correlation lengths along the π - π stacking distances in self-assembled π -systems are seldom observed and have been only reported in crystalline and liquid crystalline assemblies.²⁹ In addition, sharp diffraction peaks at $\sim 21^\circ$ (2θ) for both the xerogels indicate that alkyl chains are self-assembled in these nano structures with long range order. However, in sharp contrast to **CS-DMV** xerogel, **CS-CV** xerogel displayed three sharp diffraction peaks in the low angle region ($2\theta = 2-10^\circ$). The first sharp peak was observed at $2\theta = 2.63^\circ$ followed by two other small peaks at $2\theta = 4.5^\circ$ and 6.84° . Moreover, this powder XRD pattern is similar to the patterns of 4-cyano-4'-dodecyloxybiphenyl (CDB)³⁰ and polypyromelliticimides bearing (n-alkyloxy)biphenyloxy groups (PDIB)³¹ (Figure 3.2.3d). It has been shown that, both these molecules have 2D order in their solid-state which is stabilized by a combination of π - π stacking between biphenyl groups and van der Waal's interactions between alkyl chains. The 2D self-assembly of **CS-CV** in the present case is supported by CT-interactions between **CS** and viologen as well as interaction between dodecyl chains due to hydrophobic effects (Figure 3.2.3c, inset). The approximate total length of the **CS-CV** complex in its fully stretched conformation is 52 \AA . However the first sharp peak in PXRD pattern of **CS-CV** corresponds to the d-spacing of 33.5 \AA ($2\theta = 2.63^\circ$) which is less than the length of CT-complex. This might be due to the interdigitation of alkyl chains (*vide supra*) and tilted orientation of molecules in the nanostructures similar to PDIB polymers.³¹ We further investigated the crystallite size of these 2D layers. The quantification of the sharpness of first diffraction peak ($2\theta = 2.63^\circ$) using Scherrer formula resulted in a reasonably good correlation

length of ~ 45 nm for this 2D lattice. All these observations indicate that **CS-CV** complex self-assembles in water to form aligned nanostructures with long range mixed stack organization. We propose that this approach can be further extended to align the π -stacked columns of either single or multichromophoric systems.

3.2.6 Cross-linking Experiments

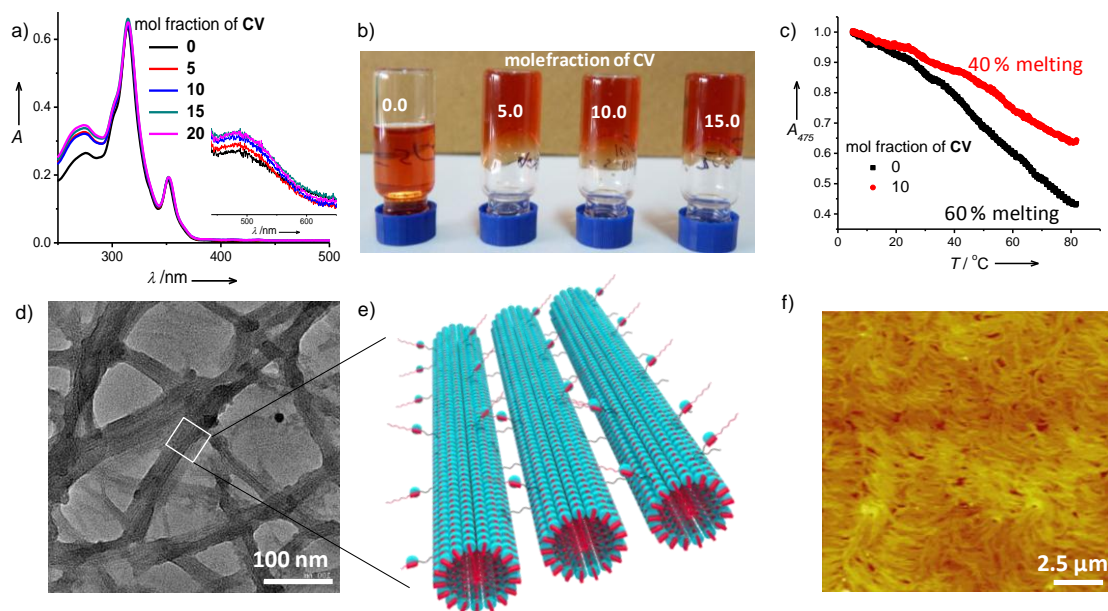


Figure 3.2.4. a) Absorption spectra of **CS-DMV** complex with different mole fractions of **CV** and corresponding CT-band absorption is shown the inset (**CS** and **DMV** = 0.1 mM, $l = 1$ mm). b) Photographs of **CS-DMV** complex at 5.5 mM in water with different mole fractions of **CV**. c) Melting curves of **CS-DMV** nanofibers with and without **CV** (**CS** and **DMV** = 0.5 mM, $l = 2$ mm) monitored at 475 nm. d) TEM image of **CS-DMV** complex co-assembled with $\chi_{cv} = 10$ of **CV** in water. e) Schematic representation of cross-linked **CS-DMV** micelles by **CV**. f) AFM image of **CS-DMV** complex co-assembled with $\chi_{cv} = 10$ of **CV** in water.

The 2D self-assembly of **CS-CV** complex further encouraged us to use **CV** as a supramolecular cross-linker to align the randomly oriented cylindrical micelles of **CS-DMV**, as the molecular structure of **CV** is composed of two **DMV** molecules linked by oligo ethylene oxide spacer. The bifunctional **CV** is expected to glue together **CS-DMV** cylindrical micelles by acting as cross-linker when co-assembled. In a typical experimental procedure, aqueous solution of **CS** was added to the mixture containing different ratios of **DMV** and **CV**, to result in a final composition having one **CS** molecule per viologen moiety. The presence of different mole fractions of **CV** did not alter the CT-interactions which, suggest the efficient co-assembly of **CV** with **CS-DMV** micelle, as evident from the absorption spectra (Figure 3.2.4a). Co-assembly was further probed using gelation, melting point, and microscopy experiments (Figure 3.2.4b-e). Since **CV** can form gel together with **CS** at much lower concentrations than **DMV**, we envisage that the co-assembly of **CV** should induce the gelation to **CS-DMV** with

lower CGC due to cross-linking (Figure 3.2.4b). For gelation experiments, we have used 5.5 mM **CS-DMV** complex in water which is in sol state (CGC is 8 mM). Interestingly, small mole fraction of **CV** ($\chi_{cv} = 5$) in **CS-DMV** complex resulted in a weak gel, which strengthens with the increase in the mole fraction of **CV** ($\chi_{cv} = 15$). This not only gives a decisive proof for the efficient co-assembly of **CV** with **CS-DMV** micelle, but also indicates the enhanced cross-linking in fibrous network of **CS-DMV** owing to the bifunctional nature of **CV**. In addition, temperature dependent experiments on **CS-DMV** CT-fibers upon co-assembly with **CV** were carried out to understand the effect of **CV** on their thermal stability by probing CT-band absorbance. In case of pure **CS-DMV** (0.5 mM) in solution, CT-band absorbance (at 475 nm) decreased gradually with the increase in the temperature (10-80 °C) and a total decrease of 60% was observed at 80 °C (Figure 3.2.4c). Whereas in case of mixed nanofibers of **CS-DMV** having $\chi_{cv} = 10$ of **CV**, the decrease was only 40%. This increased thermal stability of **CS-DMV** CT-fibres with small mole fraction of **CV** further indicates their efficient solution state co-assembly without any phase segregation. This was further supported by TEM and AFM analysis of **CS-DMV** CT-fibers with and without **CV**. **CS-DMV** alone showed high aspect ratio nanofibers with less degree of cross-linking due to the lack of cross-linker (*vide supra*). On the other hand, TEM image of **CS-DMV** assembly having $\chi_{cv} = 10$ of **CV** (Figure 3.2.4e) showed densely cross-linked and aligned nanofibers via inter micelle bridging by **CV** as shown in the schematic of Figure 3.2.4e. This was further evident in the corresponding AFM images, which showed densely aligned nanofibers over large areas (Figure 3.2.4f).

3.2.7 Conclusions

In conclusion, we have demonstrated the use of 2D self-assembly process for the non-covalent synthesis of aligned CT-columns in solution and on surface. LD studies provided insights into their anisotropic bundling even in solution. Microscopic analyses on their dilute solutions and xerogels showed aligned nanostructures on substrates even up to $15 \times 15 \mu\text{m}^2$ areas. Interestingly, PXRD analyses of these xerogels revealed the existence of 2D self-assembly with aligned CT-columns. Moreover the aligned assembly exhibited 2D lattice correlation length up to 45 nm with a remarkable crystalline order (~ 85 nm) along the D-A stacking direction. Furthermore, docking with small amounts of bifunctional **CV** to 1D micelle induced alignment to the unaligned nanostructures while improving their gelation properties and thermal stability. We propose that this strategy can be extended to various other functional π -systems for achieving aligned π -stacked columns in solution and on substrate, which would be useful for improving their performance on devices.

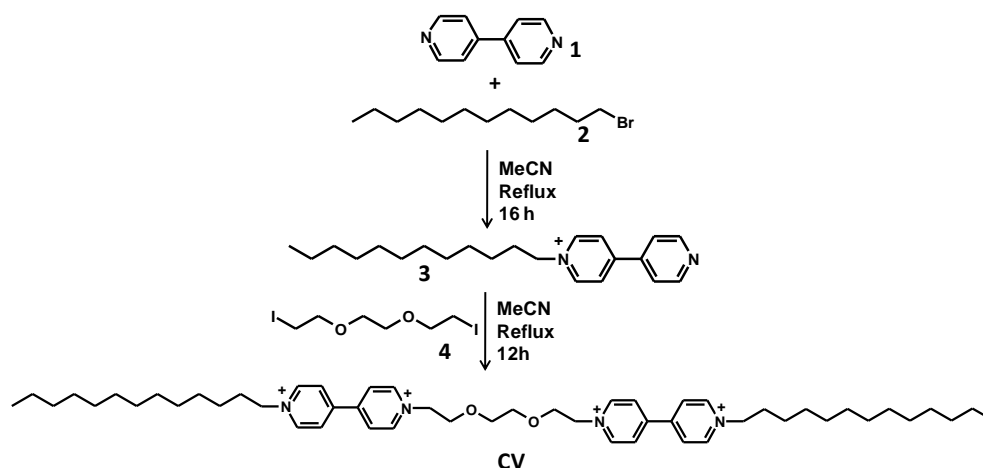
3.2.8 Experimental Section

General Methods: Transmission Electron Microscopy (TEM) TEM measurements were performed on a JEOL, JEM 3010 operated at 300 kV. Samples were prepared by placing a drop of the solution on carbon coated copper grids followed by drying at room temperature. The images were recorded with an operating voltage 300 kV. In order to get a better contrast, samples were stained with uranyl acetate (1 wt % in water) before the measurements. Atomic Force Microscopy (AFM) measurements were performed on a Veeco diInnova SPM operating in tapping mode regime. Micro-fabricated silicon cantilever tips doped with phosphorus and with a frequency between 235 and 278 kHz and a spring constant of 20-40 Nm⁻¹ were used. The samples were prepared by drop casting aqueous solutions on glass substrate and dried in air followed by vacuum drying. Electronic absorption spectra were recorded on a Perkin Elmer Lambda 900 UV-VIS-NIR Spectrometer and emission spectra were recorded on Perkin Elmer Ls 55 Luminescence Spectrometer. UV-Vis and emission spectra were recorded in 1 mm cuvette. NMR spectra were obtained with a Bruker AVANCE 400 (400 MHz) Fourier transform NMR spectrometer with chemical shifts reported in parts per million (ppm). Linear dichroism (LD) spectra of samples were recorded in Jasco, J-815 CD spectrometer.

3.2.8a Synthesis

Compounds **CS**,³² **DMV**,³³ **BV**^{34,3} and **3**² were synthesized according to the literature methods. Compounds **1**, **2** and **4** were purchased from Aldrich.

Scheme for the synthesis of CV



Synthesis of CV: Compound **3** (520 mg, 1.3 mmol) and Bis 2-iodoethoxy ethane (**4**, 240 mg, 0.65 mmol) were taken in a 50 mL round bottomed flask having 20 mL of acetonitrile. The reaction mixture was stirred at 90 °C for 24 hrs under inert conditions. The solution was cooled to room temperature and the orange precipitate formed was filtered and washed with diethyl

ether to yield pure product (227 mg, 30%). ^1H NMR (400 MHz, DMSO- D_6): δ (ppm) 9.38 (d, $J = 6.8$ Hz, 4H), 9.33 (d, $J = 6.8$ Hz, 4H), 8.80 (dd, $J = 6.8$ Hz, 8H), 4.89 (t, $J = 4.4$ Hz, 4H), 4.69 (t, $J = 7.2$ Hz, 4H), 3.96 (t, $J = 4.8$ Hz, 4H), 3.55 (s, 4H), 1.978 (s, 4H), 1.31-1.24 (36H), 0.853 (t, $J = 6.8$ Hz, 6H); ^{13}C NMR (100 MHz, DMSO- D_6): δ (ppm) 148.8, 148.4, 146.1, 145.7, 126.7, 126.3, 69.5, 68.6, 60.8, 60.3, 31.2, 30.7, 29.0, 28.9, 28.7, 28.6, 28.3, 25.4, 22.1, 13.9; HRMS (ESI) calculated for $\text{C}_{50}\text{H}_{78}\text{N}_4\text{O}_2 = 383.3051$ [M^{+2} /2] and found 383.3022.

3.2.9 References

1. R. S. Lokey, B. L. Iverson, *Nature* **1995**, *375*, 303.
2. V. Percec, M. Glodde, T. K. Bera, Y. Miura, I. Shiyonovskaya, K. D. Singer, V. S. K. Balagurusamy, P. A. Heiney, I. Schne, A. Rapp, H.-W. Spiess, S. D. Hudsonk, H. Duank, *Nature* **2002**, *419*, 384.
3. L. Zhu, Y. Yi, Y. Li, E.-G. Kim, V. Coropceanu, J.-L. Brédas, *J. Am. Chem. Soc.* **2012**, *134*, 2340.
4. S. Horiuchi, Y. Tokura, *Nature Mater.* **2008**, *7*, 357.
5. a) T. Wakahara, P. D' Angelo, K. Miyazawa, Y. Nemoto, O. Ito, N. Tanigaki, D. D. C. Bradley, T. D. Anthopoulos, *J. Am. Chem. Soc.* **2012**, *134*, 7204; b) J. Zhang, J. Tan, Z. Ma, W. Xu, G. Zhao, H. Geng, C. Di, W. Hu, Z. Shuai, K. Singh, D. Zhu, *J. Am. Chem. Soc.* **2013**, *135*, 558; c) S. K. Park, S. Varghese, J. H. Kim, S.-J. Yoon, O. K. Kwon, B.-K. An, J. Gierschner, S. Y. Park, *J. Am. Chem. Soc.* **2013**, *135*, 4757.
6. A. S. Tayi, A. K. Shveyd, A. C.-H. Sue, J. M. Szarko, B. S. Rolczynski, D. Cao, T. J. Kennedy, A. A. Sarjeant, C. L. Stern, W. F. Paxton, W. Wu, S. K. Dey, A. C. Fahrenbach, J. R. Guest, H. Mohseni, L. X. Chen, K. L. Wang, J. F. Stoddart, S. I. Stupp, *Nature* **2012**, *488*, 485.
7. a) A. P. H. J. Schenning, E. W. Meijer, *Chem. Commun.* **2005**, 3245; b) F. J. M. Hoeben, P. Jonkheijm, E. W. Meijer, A. P. H. J. Schenning, *Chem. Rev.* **2005**, *105*, 1491; c) S. S. Babu, S. Prasanthkumar, A. Ajayaghosh, *Angew. Chem. Int. Ed.* **2012**, *51*, 1766.
8. a) C. Wang, Y. Guo, Y. Wang, H. Xu, R. Wang, X. Zhang, *Angew. Chem. Int. Ed.* **2009**, *48*, 8962; b) K. V. Rao, K. Jayaramulu, T. K. Maji, S. J. George, *Angew. Chem. Int. Ed.* **2010**, *49*, 4218; c) K. V. Rao, S. J. George, *Chem. Eur. J.* **2012**, *18*, 14286.
9. A. A. Sagade, K. V. Rao, U. Mogera, S. J. George, A. Datta, G. U. Kulkarni, *Adv. Mater.* **2013**, *25*, 559.
10. a) Y.-Y. Noh, J.-J. Kim, Y. Yoshida, K. Yase, *Adv. Mater.* **2003**, *15*, 699-702; b) X. L. Chen, A. J. Lovinger, Z. Bao, J. Sapjeta, *Chem. Mater.* **2001**, *13*, 1341.
11. B. Su, Y. Wu, L. Jiang, *Chem. Soc. Rev.* **2012**, *41*, 7832.

-
12. a) V. Duzhko, J. Du, C. A. Zorman, K. D. Singer, *J. Phys. Chem. C* **2008**, *112*, 12081; b) L. Sardone, V. Palermo, E. Devaux, D. Credgington, M. de Loos, G. Marletta, F. Cacialli, J. van Esch, P. Samorì, *Adv. Mater.* **2006**, *18*, 1276; c) M. Yoshio, Y. Shoji, Y. Tochigi, Y. Nishikawa, T. Kato, *J. Am. Chem. Soc.* **2009**, *131*, 6763; d) M. Mas-Torrent, D. den Boer, M. Durkut, P. Hadley, A. P. H. J. Schenning, *Nanotechnology* **2004**, *15*, S265; e) D. Miyajima, F. Araoka, H. Takezoe, J. Kim, K. Kato, M. Takata, T. Aida, *Angew. Chem., Int. Ed.* **2011**, *50*, 7865; f) K. Sato, Y. Itoh, T. Aida, *J. Am. Chem. Soc.* **2011**, *133*, 13767; g) B. W. Messmore, J. F. Hulvat, E. D. Sone, S. I. Stupp, *J. Am. Chem. Soc.*, **2004**, *126*, 14452.
13. a) I. O. Shklyarevskiy, P. Jonkheijm, P. C. M. Christianen, A. P. H. J. Schenning, A. Del Guerzo, J.-P. Desvergne, E. W. Meijer, J. C. Maan, *Langmuir* **2005**, *21*, 2108; b) I. O. Shklyarevskiy, P. Jonkheijm, N. Stutzmann, D. Wasserberg, H. J. Wondergem, P. C. M. Christianen, A. P. H. J. Schenning, D. M. de Leeuw, Ž. Tomović, J. Wu, K. Müllen, J. C. Maan, *J. Am. Chem. Soc.* **2005**, *127*, 16233; c) J. C. Gielen, M. Wolffs, G. Portale, W. Bras, O. Henze, A. F. M. Kilbinger, W. J. Feast, J. C. Maan, A. P. H. J. Schenning, P. C. M. Christianen, *Langmuir* **2009**, *25*, 1272; d) D. Y. Yang, B. Lu, Y. Zhao, X. Y. Jiang, *Adv. Mater.* **2007**, *19*, 3702; e) Y. Q. Liu, X. P. Zhang, Y. N. Xia, H. Yang, *Adv. Mater.* **2010**, *22*, 2454.
14. a) S. Y. Chou, P. R. Krauss and P. J. Renstrom, *Science* **1996**, *272*, 85; b) N. E. Voicu, S. Ludwigs, E. J. W. Crossland, P. Andrew, U. Steiner, *Adv. Mater.* **2007**, *19*, 757; c) Z. J. Hu, B. Muls, L. Gence, D. A. Serban, J. Hofkens, S. Melinte, B. Nysten, S. Demoustier-Champagne, A. M. Jonas, *Nano Lett.* **2007**, *7*, 3639; d) M. Aryal, K. Trivedi, W. C. Hu, *ACS Nano*, **2009**, *3*, 3085; e) N. Hosono, T. Kajitani, T. Fukushima, K. Ito, S. Sasaki, M. Takata, T. Aida, *Science* **2010**, *330*, 808.
15. a) W. Pisula, A. Menon, M. Stepputat, I. Lieberwirth, U. Kolb, A. Tracz, H. Sirringhaus, T. Pakula and K. Müllen, *Adv. Mater.* **2005**, *17*, 684; b) W. Pisula, Z. Tomović, M. Stepputat, U. Kolb, T. Pakula, K. Müllen, *Chem. Mater.* **2005**, *17*, 2641; c) A. Tracz, J. K. Jeszka, M. D. Watson, W. Pisula, K. Müllen, T. Pakula, *J. Am. Chem. Soc.* **2003**, *125*, 1682.
16. a) T. Kitamura, S. Nakaso, N. Mizoshita, Y. Tochigi, T. Shimomura, M. Moriyama, K. Ito, T. Kato, *J. Am. Chem. Soc.* **2005**, *127*, 14769; b) Y. Hirai, S. S. Babu, V. K. Praveen, T. Yasuda, A. Ajayaghosh, T. Kato, *Adv. Mater.* **2009**, *21*, 4029; c) A. M. Kendhale, A. P. H. J. Schenning, M. G. Debije, *J. Mater. Chem. A* **2013**, *1*, 229.
17. a) R. van Hameren, P. Schon, A. M. van Buul, J. Hoogboom, S. V. Lazarenko, J. W. Gerritsen, H. Engelkamp, P. C. M. Christianen, H. A. Heus, J. C. Maan, T. Rasing, S. Speller, A. E. Rowan, J. Elemans, R. J. M. Nolte, *Science* **2006**, *314*, 1433; b) W. H. Lee, D. H. Kim, Y. Jang, J. H. Cho, M. Hwang, Y. D. Park, Y. H. Kim, J. I. Han, K. Cho, *Appl.*

- Phys. Lett.* **2007**, *90*, 132106; c) N. L. Liu, Y. Zhou, L. Wang, J. B. Peng, J. A. Wang, J. A. Pei, Y. Cao, *Langmuir* **2009**, *25*, 665; d) Y. H. Tong, Q. X. Tang, H. T. Lemke, K. Moth-Poulsen, F. Westerlund, P. Hammershoj, K. Bechgaard, W. P. Hu, T. Bjornholm, *Langmuir* **2010**, *26*, 1130; e) C. Y. Zhang, X. J. Zhang, X. H. Zhang, X. Fan, J. S. Jie, J. C. Chang, C. S. Lee, W. J. Zhang, S. T. Lee, *Adv. Mater.* **2008**, *20*, 1716; f) Z. Wang, R. Bao, X. Zhang, X. Ou, C.-S. Lee, J. C. Chang, X. Zhang, *Angew. Chem. Int. Ed.* **2011**, *50*, 2811.
18. a) B. Su, S. T. Wang, Y. C. Wu, X. Chen, Y. L. Song, L. Jiang, *Adv. Mater.* **2012**, *24*, 2780; b) S. Prasanthkumar, A. Saeki, S. Seki, A. Ajayaghosh, *J. Am. Chem. Soc.* **2010**, *132*, 8866; c) G. De Luca, A. Liscio, P. Maccagnani, F. Nolde, V. Palermo, K. Müllen, P. Samori, *Adv. Funct. Mater.* **2007**, *17*, 3791.
19. J. H. Oh, H. W. Lee, S. Mannsfeld, R. M. Stoltenberg, E. Jung, Y. W. Jin, J. M. Kim, J. B. Yoo, Z. N. Bao, *Proc. Natl. Acad. Sci. U. S. A.* **2009**, *106*, 6065.
20. A. Tsuda, Y. Nagamine, R. Watanabe, Y. Nagatani, N. Ishii, T. Aida, *Nat. Chem.* **2010**, *2*, 977.
21. B. D. Wall, S. R. Diegelmann, S. Zhang, T. J. Dawidczyk, W. L. Wilson, H. E. Katz, H.-Q. Mao, J. D. Tovar, *Adv. Mater.* **2011**, *23*, 5009.
22. a) L. Chen, Y.-K. Tian, Y. Ding, Y.-J. Tian, F. Wang, *Macromolecules* **2012**, *45*, 8412; b) T. Haino, E. Hirai, Y. Fujiwara, K. Kashiwara, *Angew. Chem. Int. Ed.* **2010**, *49*, 7899; c) T. Suzuki, S. Shinkai, K. Sada, *Adv. Mater.* **2006**, *18*, 1043; d) T. Mes, M. M. E. Koenigs, V. F. Scalfani, T. S. Bailey, E. W. Meijer, A. R. A. Palmans, *ACS Macro Lett.* **2012**, *1*, 105; e) J.-H. Ryu, M. Lee, *J. Am. Chem. Soc.* **2005**, *127*, 14170.
23. a) O. Kretschmann, S. W. Choi, M. Miyauchi, I. Tomatsu, A. Harada, H. Ritter, *Angew. Chem. Int. Ed.* **2006**, *45*, 4361; b) T. Haino, Y. Hirai, T. Ikeda, H. Saito, *Org. Biomol. Chem.* **2013**, *11*, 4164; c) K. Imato, M. Nishihara, T. Kanehara, Y. Amamoto, A. Takahara, H. Otsuka, *Angew. Chem. Int. Ed.* **2012**, *51*, 1138; d) M. Nakahata, Y. Takashima, A. Hashidzume, A. Harada, *Angew. Chem. Int. Ed.* **2013**, *52*, 5731.
24. a) Y. Kubo, Y. Kitada, R. Wakabayashi, T. Kishida, M. Ayabe, K. Kaneko, M. Takeuchi, S. Shinkai, *Angew. Chem. Int. Ed.* **2006**, *45*, 1548; b) T. Kaseyama, S. Takebayashi, R. Wakabayashi, S. Shinkai, K. Kaneko, M. Takeuchi, *Chem. Eur. J.* **2009**, *15*, 12627.
25. E. A. Appel, F. Biedermann, U. Rauwald, S. T. Jones, J. M. Zayed, O. A. Scherman, *J. Am. Chem. Soc.* **2010**, *132*, 14251.
26. a) E. Moulin, F. Niess, M. Maaloum, E. Buhler, I. Nyrkova, N. Giuseppone, *Angew. Chem. Int. Ed.* **2010**, *49*, 6974; b) V. Faramarzi, F. Niess, E. Moulin, M. Maaloum, J.-F. Dayen, J.-B. Beaufrand, S. Zanettini, B. Doudin, N. Giuseppone, *Nat. Chem.* **2012**, *4*, 485; c) E. Lee, J.-K. Kim, M. Lee, *Angew. Chem. Int. Ed.* **2008**, *47*, 6375.

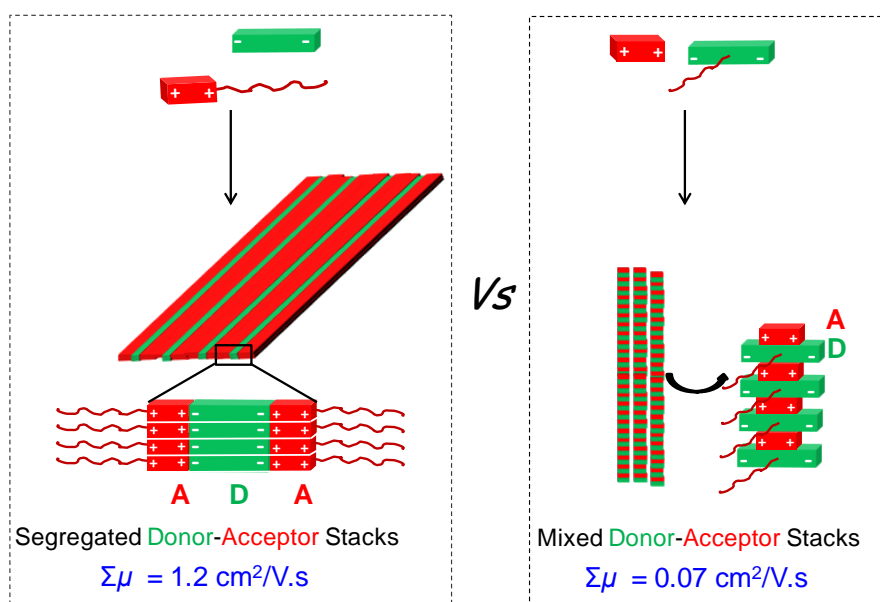
-
27. a) E. A. Appel, X. J. Loh, S. T. Jones, F. Biedermann, C. A. Dreiss, O. A. Scherman, *J. Am. Chem. Soc.* **2012**, *134*, 11767; b) Q. Wang, J. L. Mynar, M. Yoshida, E. Lee, M. Lee, K. Okuro, K. Kinbara, T. Aida, *Nature* **2010**, *463*, 339; c) P. H. J. Kouwer, M. Koepf, V. A. A. Le Sage, M. Jaspers, A. M. van Buul, Z. H. Eksteen-Akeroyd, T. Woltinge, E. Schwartz, H. J. Kitto, R. Hoogenboom, S. J. Picken, Roeland J. M. Nolte, E. Mendes, A. E. Rowan, *Nature* **2013** (doi:10.1038/nature11839); d) H. Wang, C. Yang, M. Tan, L. Wang, D. Konga, Z. Yang, *Soft Matter* **2011**, *7*, 3897.
28. a) M. Wolffs, S. J. George, Z. Tomovic, A. P. H. J. Schenning and E. W. Meijer, *Angew. Chem. Int. Ed.* **2007**, *46*, 8203.
29. T. Osawa, T. Kajitani, D. Hashizume, H. Ohsumi, S. Sasaki, M. Takata, Y. Koizumi, A. Saeki, S. Seki, T. Fukushima, T. Aida, *Angew. Chem. Int. Ed.* **2012**, *51*, 7990.
30. L. G. Kuz'mina, N. S. Kucherepa, A. V. Churakov, *Crystallography Reports* **2012**, *57*, 213.
31. S. B. Lee, G. J. Shin, J. H. Chi, W.-C. Zin, J. C. Jung, S. G. Hahm, M. Ree, T. Chang, *Polymer* **2006**, *47*, 6606.
32. a) S. A-Fouet, I. Seguy, J.-F. Bobo, P. Destruel, H. Bock, *Chem. Eur. J.* **2007**, *13*, 1746; b) A. Ghosh, K. V. Rao, S. J. George, C. N. R. Rao, *Chem. Eur. J.* **2010**, *16*, 2700.
33. M. F. Pepitone, G. G. Jernigan, J. S. Melinger, O.-K. Kim, *Org. Lett.* **2007**, *9*, 801.
34. a) Y. Kawaguchi, A. Harada, *Org. Lett.* **2000**, *2*, 1353; b) H. Yamaguchi, A. Harada, *Chem. Lett.* **2002**, *31*, 382.

PART-3.3

High Charge Carrier Mobility in Non-Covalently Tailored D-A Heterojunction Nanostructures*

Abstract

In this section, we describe a simple non-covalent approach to control the co-assembly of electron rich oligo(*p*-phenylenevinylene) and electron deficient viologen derivatives into mixed stack and segregated donor (D)-acceptor (A) heterojunction nanostructures. This was achieved by tailoring the alkyl chain position in D and A molecules. Self-assembly of these non-covalent D-A complexes resulted in the formation of nanostructures with controlled D-A organization. The segregated D-A nanostructures exhibited well defined nanoscale heterojunctions with wide D-A interface. Transient photocurrent measurements showed high mobility of photogenerated charges in segregated D-A nanostructures ($1.2 \text{ cm}^2/\text{Vs}$) than mixed stack ($0.07 \text{ cm}^2/\text{Vs}$) nanostructures due to efficient charge separation and migration which is not possible in latter case because of unfavourable orientation of D-A molecules.



* Manuscript based on this work is under preparation.

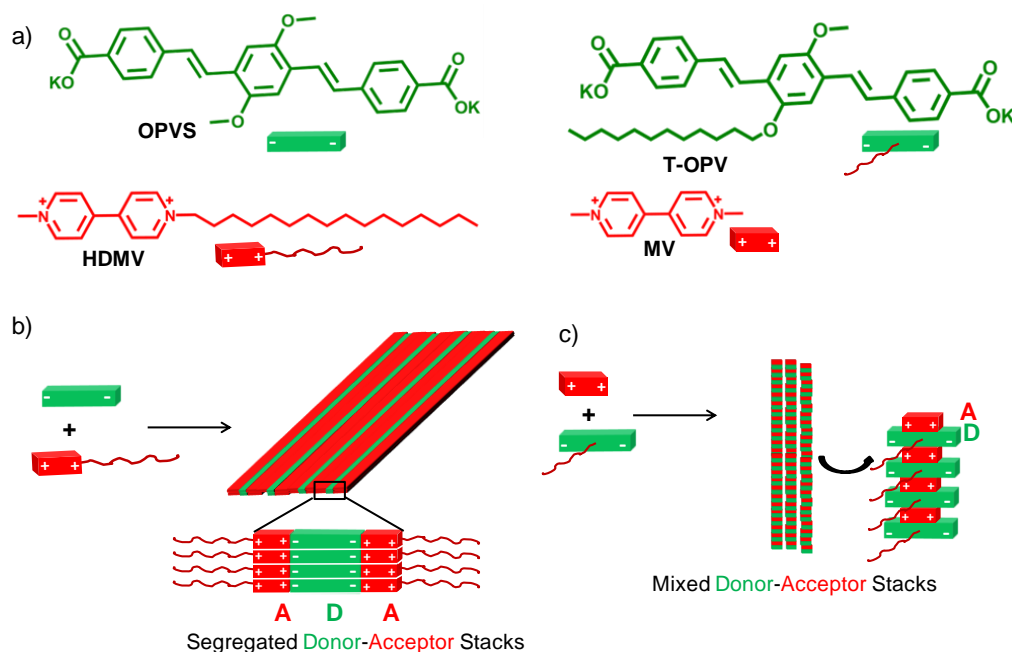
3.3.1 Introduction

Nanoscale tailoring of the molecular organization of electron rich donors (D) and electron deficient acceptors (A) in p-n heterojunction nanostructures, is a meticulous area of research as it plays a pivotal role in the performance of organic electronic devices.¹ Though mixed stack D-A assemblies are known to have interesting optoelectronic properties,² segregated D-A stacks are important for organic electronic devices owing to their ability to provide efficient transport pathways for the photogenerated charges in the bulk state.³ Despite having high efficiencies, bulk heterojunctions solar cells (BHJSC) obtained from randomly blended D-A molecules have draw backs in terms of active layer material and fabrication process.⁴ Moreover, morphology of the active layer in BHJSC is kinetically formed which reduces the device efficiency over time. In this regard, organization of D-A molecules via supramolecular self-assembly has shown to be an efficient approach for the construction of stable bicontinuous D-A heterojunctions.⁵ However, devices made from the self-assembled structures of covalently linked fullerene with π -conjugated polymers/oligomers exhibited poor mobilities due to symmetry mismatch between D-A molecules.⁶ This clearly indicates that, in addition to the morphology, the mobility of photogenerated charges along the D and A components is also crucial for achieving high photo conversion efficiency (PCE). In this context, segregated D-A heterojunction nanostructures developed by Aida et al. through the self-assembly of covalently linked D-A amphiphiles are striking examples.⁷ In these examples, the self-assembled heterojunction nanostructures of HBC amphiphile covalently linked with trinitrofluorenone/ C_{60} showed high charge carrier mobilities up to $3/2 \text{ cm}^2/\text{Vs}$ when probed via time-resolved microwave conductivity measurements. Recently, segregated D-A stacks have also been made through the self-assembly of non-amphiphilic, covalently linked D-A molecules.⁸ However, the resultant heterojunctions suffer from low charge carrier mobility and interference of energy-transfer process. In this context, a simple non-covalent strategy for nanoscale tailoring of heterojunctions would be more attractive to avoid the synthetic complexity in covalent D-A systems.⁹ Since self-assembled nanostructures of amphiphilic π -conjugated molecules are known to exhibit high mobilities¹⁰ due to enhanced π -ordering, we focus on non-covalent D-A amphiphilic design to construct heterojunction nanostructures with wide interface and high charge carrier mobility.

3.3.2 Design Strategy

In this section we describe a simple and novel non-covalent approach for the nanoscale tailoring of D and A heterojunctions of oligo(*p*-phenylenevinylene) and viologen chromophores in water (Scheme 3.3.1). The position of alkyl chain at D or A site plays a crucial role in controlling the organization (segregated/mixed stack) of D-A molecules in the resultant non-

covalent D-A complex. Detailed analyses of these non-covalent complexes revealed that in this D-A pair, D and A molecules prefer segregated orientation when alkyl chain is linked with viologen (**HDMV**), whereas they form face-to-face ground state CT-complex if the alkyl chain is at D site to form T-shaped oligo(*p*-phenylenevinylene) donor (**T-OPV**). Interestingly, the self-assembly of these segregated non-covalent D-A complexes resulted in high aspect ratio nanotapes with lamellar packing and wide D-A interface, whereas the mixed stack complexes showed only the formation of micelles. Transient photocurrent measurements on both these nanostructures showed high mobility of photogenerated charges in segregated D-A nanostructures ($1.2 \text{ cm}^2/\text{Vs}$), which is two orders of magnitude higher than the corresponding mixed stack nanostructures ($0.07 \text{ cm}^2/\text{Vs}$), reiterating the importance of molecular organization in multicomponent D-A assemblies.



Scheme 3.3.1. Molecular structures of a) D (**OPVS** and **T-OPVS**) and A (**MV** and **HDMV**) molecules. Schematic representation for the formation of b) segregated nanostructures of **OPVS-HDMV** and c) mixed stack nanostructures of **T-OPV-MV** non-covalent amphiphilic complexes.

3.3.3 Characterization of D and A Co-Assembly

D (**OPVS** and **T-OPV**) and A molecules (**MV** and **HDMV**) were synthesized according to the literature methods and were fully characterized (see experimental section). **OPVS** and **MV** are molecularly dissolved in water, whereas **T-OPV** and **HDMV** form supramolecular aggregates due to their amphiphilic nature (*vide infra*). When **OPVS** (1 mM) was titrated with increasing equivalents of **MV** in water, the observed red-shifts (up to 3-4 nm) in its absorption spectra with concomitant appearance of new broad CT-band between 500-700

nm and visible color changes in the solution, clearly indicated the formation of ground state CT-complex between **OPVS** and **MV** (Figure 3.3.1a-c).¹¹ The formation of CT-band was more evident from the absorption spectra at high concentration (1.65 mM, Figure 3.3.1d). This was further supported by gradual quenching in the **OPVS** emission with the increase in equivalents of **MV** and a fluorescence quenching of 40% was observed at 1 equivalent of **MV** (Figure 3.3.1e). The significant residual emission of **OPVS** even at one equivalent of **MV** might be due to the weak association of **OPVS-MV** CT-complex. The composition of D-A molecules in this ground state CT-complex was investigated using Job's method by probing CT-band absorbance at 550 nm (Figure 3.3.1f). In this case, studies were done at high concentration (3.3 mM) due to weak association between **OPVS** and **MV** at lower concentrations (1 mM). The appearance of maximum at 0.5 in the Job plot confirms the formation of 1:1 CT-complex between **OPVS** and **MV**.

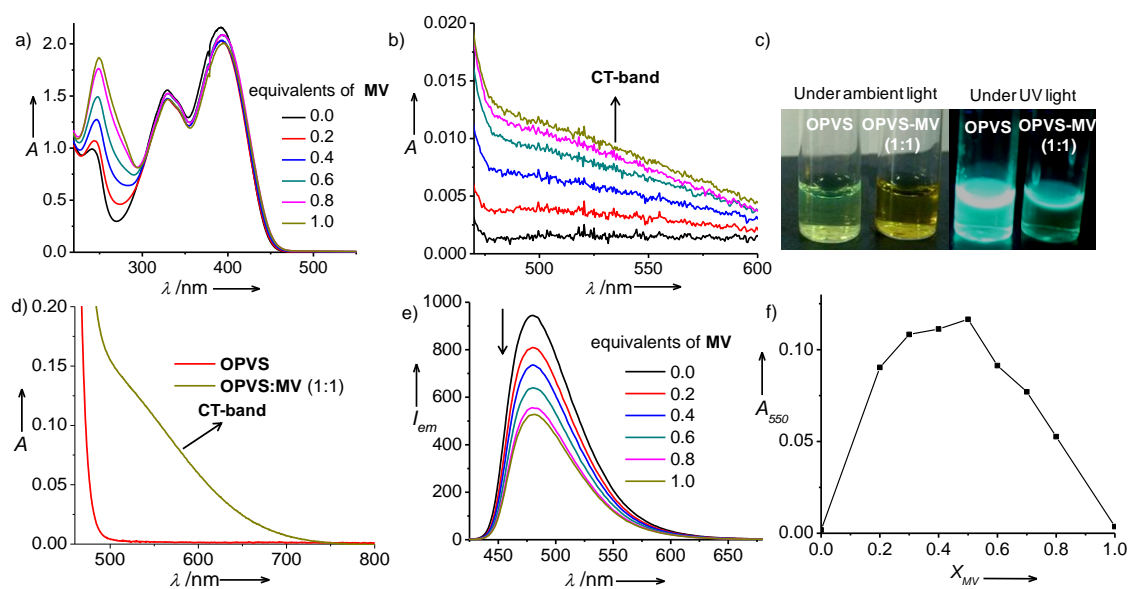


Figure 3.3.1. a) Absorption spectra of **OPVS** (1 mM) with different equivalents of **MV** in water ($l = 1$ mm). b) Magnified spectra of Figure 3.3.1a between 450-600 nm showing the CT-band. c) Photographs of aqueous solution of **OPVS** (1 mM) with and without one equivalent of **MV** in water under ambient and 365 nm UV light. d) Absorption spectra of **OPVS** (1.65 mM) with and without **MV** ($l = 5$ mm). e) Emission spectra of **OPVS** (1 mM) with different equivalents of **MV** in water ($l = 1$ mm and $\lambda_{exc} = 380$ nm). f) Job plot by probing the CT band absorbance at 550 nm for **OPVS-MV** co-assembly in water (Total concentration = 3.3 mM, $l = 5$ mm).

The face-to-face orientation of D-A molecules in **OPVS-MV** CT-complex was confirmed using solution state $^1\text{H-NMR}$ in D_2O at 10 mM concentration. The strong up-field shifts in both **OPVS** and **MV** protons in the CT-complex state compared to their individual spectra, clearly indicate the face-to-face orientation of D-A molecules in the CT-complex (Figure 3.3.2). In case of **MV**, all the protons (H_{MV1} and H_{MV2}) experienced an up-field shift of 0.35 ppm due to the shielding from facially organized **OPVS** aromatic clouds. However, in

case of **OPVS** protons, the up-field shifts were not uniform for all the signals. Among all **OPVS** protons, up-field shifts were less for terminal protons (H_{opvs1} , ~ 0.1 ppm) and increased gradually up to 0.65 ppm when approaching the middle protons of **OPVS** (H_{opvs5}) core. This clearly indicates that, in the face-to-face CT-complex, **MV** is oriented at the centre of **OPVS** which results in more shielding of the middle protons (H_{opvs3} - H_{opvs5}) than the terminal ones (H_{opvs1}) (schematic in Figure 3.3.2). Even though both **MV** and **OPVS** are linear π -systems, the differences in the shielding experienced by **OPVS** protons by **MV** is mainly due to the differences in their molecular dimensions.

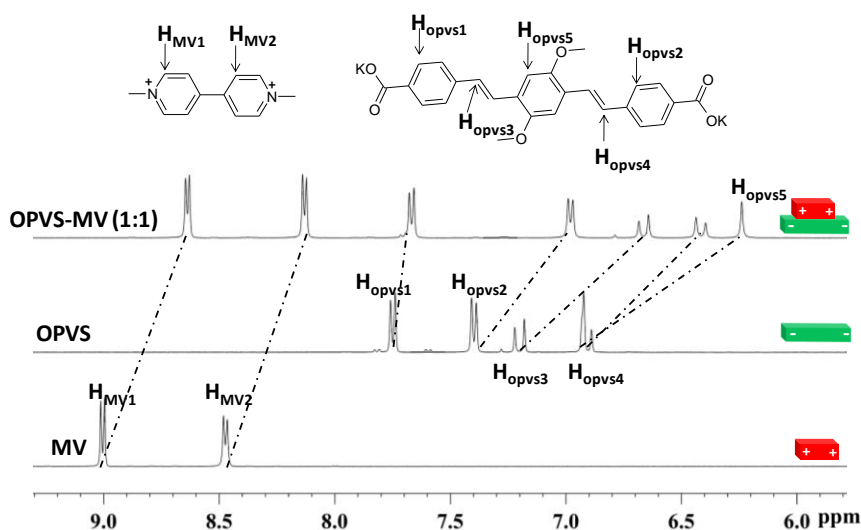


Figure 3.3.2. Aromatic region of the ^1H NMR spectra of **OPVS**, **MV** and **OPVS-MV (1:1)** co-assembly in D_2O ($c = 10$ mM).

On the other hand, when **OPVS** was mixed with two equivalents of hexadecyl triethyl ammonium bromide (**HTAB**), a cationic surfactant, in water both the absorption bands of **OPVS** showed blue shifts (392-378 nm and 330-326 nm) with significant quenching in its monomer emission (Figure 3.3.3a). These observations clearly indicate that, **HTAB** induced H-aggregation of **OPVS** chromophores by forming an 1:2 (**OPVS:HTAB**) complex through ionic interactions with terminal carboxylate groups of **OPVS** (Figure 3.3.3a, inset). This observation encouraged us to make 1:2 **OPVS:HDMV** co-assembly having segregated D-A organization by utilizing the ionic interactions between **OPVS** and **HDMV**. Remarkably, the absorption spectra of 1:2 co-assembly of **OPVS-HDMV** is similar to that of 1:2 **OPVS:HTAB** ionic complex, which indicates the segregated orientation of D-A molecules (Figure 3.3.3b).¹² This further suggests that the donor **OPVS** molecules are organized in a face-to-face manner (H-type). Moreover, absence of any CT-band in the absorption spectra of **OPVS:HDMV** co-assembly between 500-700 nm further confirms that, no ground state face-to-face CT-complexation exists between **OPVS** and **HDMV**. Furthermore, the complete quenching of **OPVS** monomer emission in **OPVS-HDMV** complex can be either due to H-type aggregation or due to an

excited state interaction between **OPVS** and **HDMV** (Figure 3.3.3c). Though the difference between **MV** and **HDMV** is only in the length of alkyl chains, the former one forms face-to-face CT-complex whereas the latter forms segregated D-A complex with **OPVS**. NMR studies showed that, in **OPVS-MV** CT-complex, **MV** prefers to stay at the centre of **OPVS** molecule (*vide supra*). Similar ground state face-to-face CT-complex between **HDMV** and **OPVS** is not favored probably because of repulsion between the hydrophobic alkyl chain of **HDMV** with that of hydrophilic carboxylate groups of **OPVS**. We anticipate that, in order to minimize these repulsive interactions, **HDMV** prefers to form segregated D-A complex with **OPVS** through ionic interactions rather than face-to-face CT-complex (Figure 3.3.3b, inset).

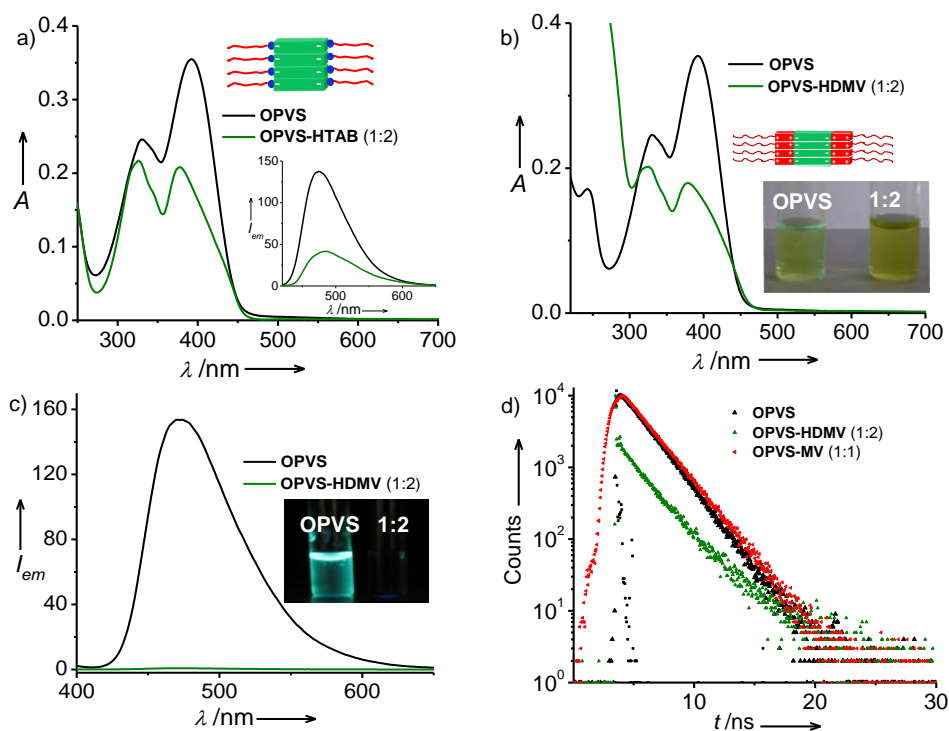


Figure 3.3.3. a) Absorption spectra of **OPVS** (0.1 mM) and its 1:2 ionic complex with **HTAB** in water ($l = 1$ mm). Inset shows the corresponding emission spectra and schematic representation of **OPVS-HTAB** ionic complex aggregates. b) Absorption spectra of **OPVS** (0.1 mM) and its 1:2 ionic complex with **HDMV** in 10% methanol containing water ($l = 1$ mm). Inset shows the schematic representation of **OPVS-HDMV** ionic complex aggregates and photographs of corresponding solutions. c) Emission spectra of **OPVS** (0.1 mM) and its 1:2 ionic complex with **HDMV** in 10% methanol containing water ($l = 1$ mm, and $\lambda_{exc} = 380$ nm) and inset shows the photographs of corresponding solutions under 365 nm UV light. d) Fluorescence lifetime decay profiles of **OPVS** and its complexes with **MV** and **HDMV** monitored at 480 nm ($c = 0.1$ mM (**OPVS-HDMV**) and 1 mM (**OPVS-MV**), $l = 10$ mm, and $\lambda_{exc} = 370$ nm).

The segregated orientation of **OPVS** and **HDMV** in the co-assembly was further supported by fluorescence lifetime (Figure 3.3.3d) and $^1\text{H-NMR}$ measurements (Figure 3.3.4). **OPVS** alone in 10% methanol containing water showed a single exponential decay with a lifetime of 1.95 ns and did not show much change (2.0 ns) in its CT-complex state with **MV**,

consistent with the ground CT-complex formation between **OPVS** and **MV**. Interestingly, **OPVS** displayed an additional short lifetime (<50 ps) component in its decay profile upon co-assembly with 2 equivalents of **HDMV**. These observations suggest that the excited state interactions between **OPVS** and viologen exist only in the case of **OPVS-HDMV** co-assembly and not in **OPV-MV** ground state CT-complex. The segregated D-A organization was further supported by $^1\text{H-NMR}$ measurements of **OPVS** with **BMV** (Figure 3.3.4, model compound for **HDMV**). In **OPVS-BMV** (1:2) co-assembly, no significant up-field shifts were observed for both **OPVS** and **BMV** protons compared to their individual spectra and signals of the co-assembly were broad due to aggregation (Figure 3.3.4). This unambiguously proves that the preferred orientation between **OPVS** and viologen amphiphiles (**HDMV/BMV**) in the co-assembly is segregated similar to **OPVS-HTAB** co-assembly rather than face-to-face orientation.

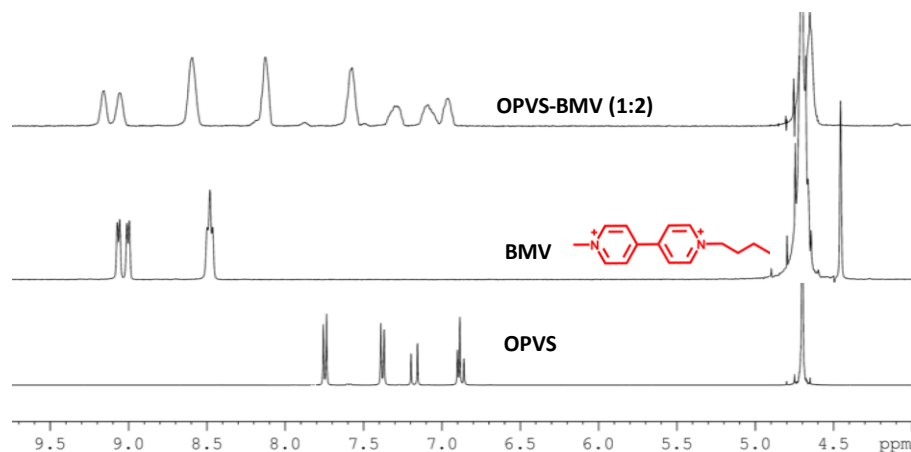


Figure 3.3.4. Aromatic region of the ^1H NMR spectra of **OPVS**, **BMV** and **OPVS-BMV** (1:2) co-assembly in D_2O ($c = 10$ mM)

3.3.4 Transient Absorption Measurements

The segregated orientation of D-A molecules in the present **OPVS-HDMV** ionic co-assembly is suitable for efficient photoinduced electron transfer from **OPVS** to **MV** and in fact it is signaled by decrease in the **OPVS** fluorescence lifetime in the **OPVS-HDMV** co-assembly when **OPVS** was selectively (370 nm) excited. In order to probe this, we have performed transient absorption measurements on **OPVS-HDMV** co-assembly using laser flash photolysis (Figure 3.3.5). When **OPVS** was selectively excited at 355 nm, the obtained transient absorption spectrum between 500-800 nm with maximum at 600 nm clearly indicates the formation of viologen radical cation ($\text{MV}^{\bullet+}$) (Figure 3.3.5a).¹³ This further gave a decisive proof for the photoinduced electron transfer from **OPVS** to **HDMV** in the **OPVS-HDMV** co-assembly. Analysis of decay profile of transient species ($\text{MV}^{\bullet+}$) at 600 nm showed a lifetime of 420 ns for the transient species (Figure 3.3.5b).

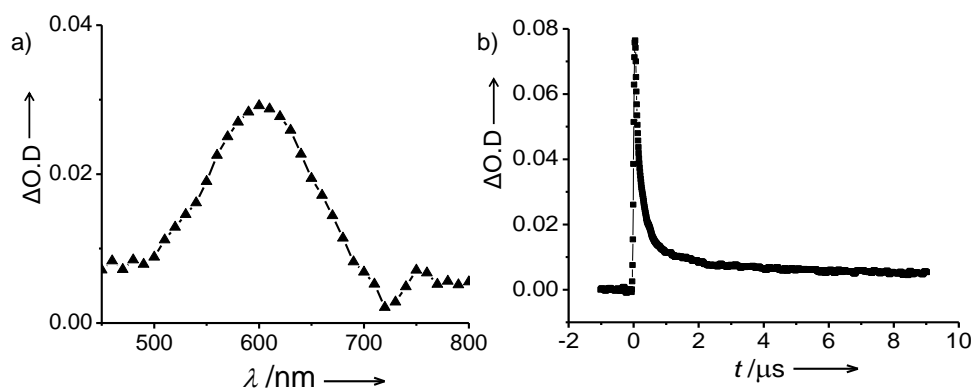


Figure 3.3.5. a) Transient absorption spectrum of **OPVS-HDMV** (1:2) ionic co-assembly ($c = 0.1 \text{ mM}$, $l = 10 \text{ mm}$, $\lambda_{exc} = 355 \text{ nm}$) recorded at 500 ns after excitation. b) Corresponding lifetime decay profile of transient species (MV^+) monitored at 600 nm .

3.3.5 Morphology

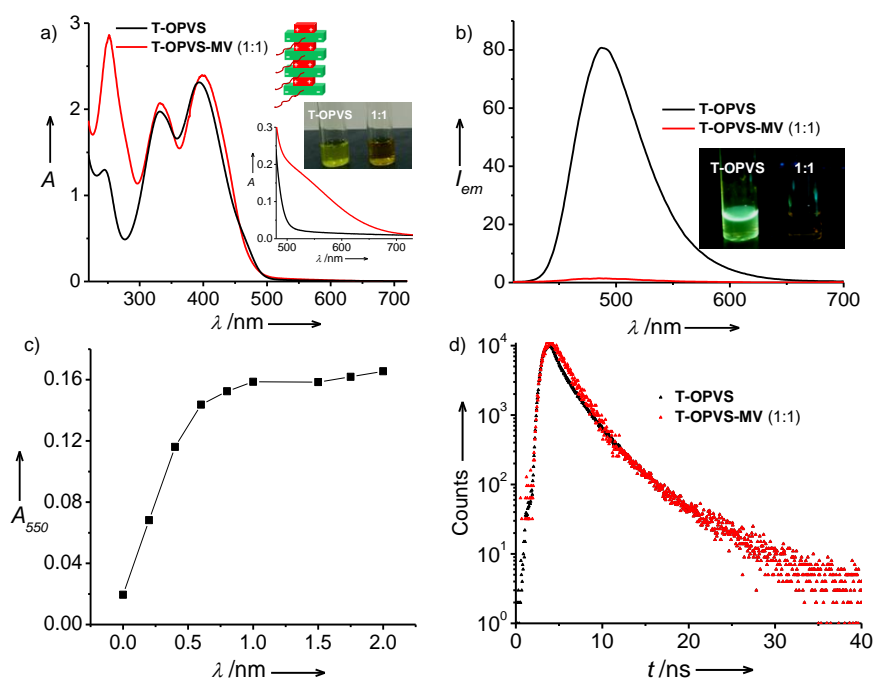


Figure 3.3.6. a) Absorption spectra of **T-OPVS** (0.15 mM) and its 1:1 co-assembly with **MV** ($l = 5 \text{ mm}$) in water. Inset shows the photographs of corresponding solutions, schematic representation of **T-OPV-MV** ionic co-assembly, and magnified spectra between $450\text{-}600 \text{ nm}$. b) Emission spectra of **T-OPVS** (0.15 mM) and its 1:1 co-assembly with **MV** and inset shows the photographs of corresponding solutions under 365 nm UV light ($l = 1 \text{ mm}$ and $\lambda_{exc} = 380 \text{ nm}$). c) Plot of CT-band absorbance at 550 nm versus equivalents of **MV** in **T-OPVS** (0.15 mM) solution showing saturation with 1 equivalent of **MV** ($l = 5 \text{ mm}$). d) Fluorescence lifetime decay profiles of **T-OPVS** (0.15 mM) and its co-assembly with one equivalent of **MV** in water ($l = 10 \text{ mm}$ and $\lambda_{exc} = 370 \text{ nm}$).

The structure of **OPVS-HDMV** non-covalent amphiphile indicates that it can self-assemble in water to form nanostructures due to the amphiphilic interactions. However, face-to-face **OPVS-MV** exists as molecular complex, due to the absence of any flexible alkyl chains.

Since we are interested to investigate the differences in their respective nanostructures with distinct orientation of D-A molecules, we designed T-shaped amphiphile, **T-OPVS** for the face-to-face extended co-assembly with **MV**. The resultant **T-OPVS-MV** CT-complex is ideal for forming self-assembled nanostructures because of its non-covalent CT-amphiphilic molecular structure. Similar to **OPVS**, **T-OPVS** also forms 1:1 face-to-face CT-complex with **MV** as evidenced from the red-shift in its absorption spectra with concomitant appearance of CT-band at 550 nm and fluorescence quenching in the presence of **MV**. Probing CT-band as function of **MV** equivalents, showed the 1:1 composition of D and A molecules in the co-assembly (Figure 3.3.6a-c).¹⁴ This was further supported by fluorescence lifetime measurements which did not show any significant change in the lifetime of **T-OPV** in the presence of **MV** (Figure 3.3.6d).

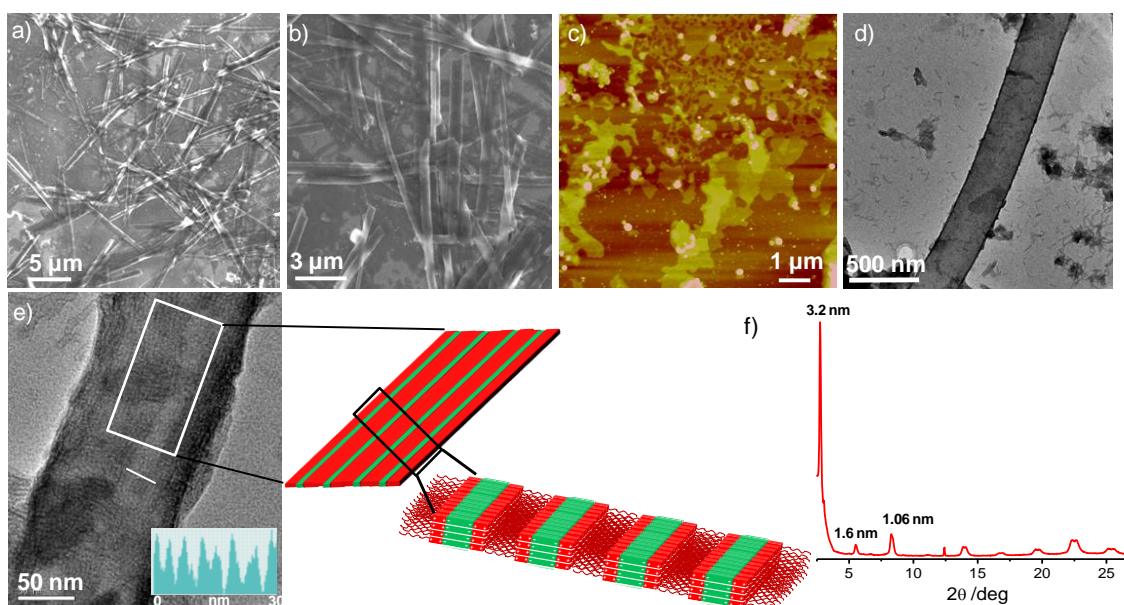


Figure 3.3.7. *a) and b) SEM images of OPVS-HDMV (1:2) ionic co-assembly formed in 10% methanol containing water ($c = 0.1$ mM) showing nanotape morphology. c) AFM image showing the sheet like of aggregates HDMV formed in 10% methanol containing water ($c = 0.1$ mM). d) TEM image of a single nanotape of OPVS-HDMV. e) TEM image of a single nanotape showing the nanoscale striations (see the intensity profile in the inset) on its surface and schematic representation for the lamellar packing of OPVS-HDMV (1:2) ionic complex in nanotapes. f) PXRD pattern OPVS-HDMV (1:2) nanotapes showing the lamellar packing.*

Interestingly, scanning electron microscopy (SEM) images of **OPVS-HDMV** co-assembly showed the formation of nano tapes with 0.5-1 μm in width and lengths up to 15-20 μm , which are completely different from the sheet like aggregates of **HDMV** alone (Figure 3.3.7a-c). Remarkably, transmission electron microscopy (TEM) images of these nanotapes showed ordered nanoscale striations on their surface (Figure 3.3.7d and e). This is further supported by powder XRD (PXRD) measurements which showed the lamellar packing of ionic complexes in the nanotapes as evidenced from the appearance of first sharp diffraction at 3.2 nm followed by two other peaks at 1.6 nm and 0.8 nm (Figure 3.3.7f). The calculated length of

1:2 **OPVS-HDMV** ionic complex with alkyl chains in its fully stretched form is 7.6 nm which is higher than the observed d -spacing from the first reflection. This suggests the tilted orientation and interdigitation of hexadecyl chains in the nanotapes (Figure 3.3.7e, schematic representation). This is supported by the appearance of diffraction peaks corresponding to d -spacing of 0.39 nm and 0.45 nm which arise because of the interaction between alkyl chains due to interdigitation (Figure 3.3.7f). Moreover, the two diffraction peaks observed at $\sim 25^\circ$ (2θ) with d -spacings of 0.35 nm and 0.354 nm could be attributed to the individual π -stacking distances of **OPVS** and **HDMV** chromophores in the segregated stacks. The lamellar packing of **OPVS-HDMV** ionic complex in the present case allowed to create nanoscale heterojunctions of **OPVS** and **HDMV** with wide interface as evidenced from the nanoscale striations observed on the nanotapes. This kind of D-A morphology in the active layers of organic photovoltaic devices is a prerequisite for efficient charge separation and migration of photogenerated charges. However, mixed stack **T-OPV-MV** complex showed entirely different morphology with no diffraction peaks in the corresponding PXRD pattern (Figure 3.3.8a and b). The nanostructures of this complex are very small (< 5 nm) and careful analysis of them reveals the self-assembly of **T-OPVS-MV** complex into bilayers having width ~ 4 nm which are different from the cylindrical micelles formed due to the aggregation of **T-OPVS** alone (Figure 3.3.8c).

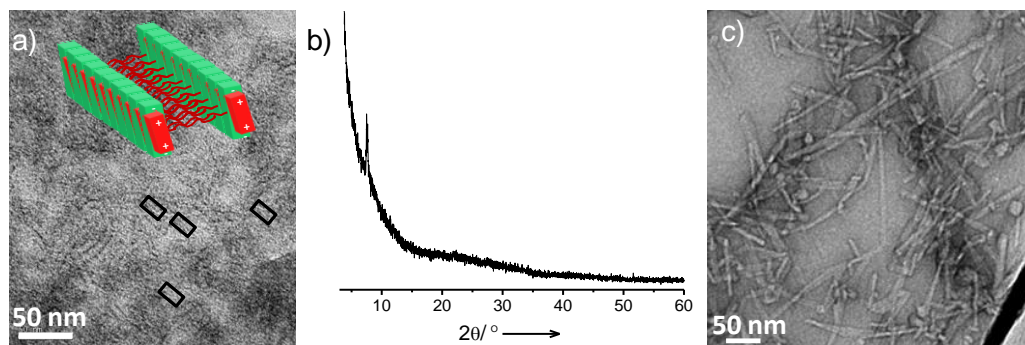


Figure 3.3.8. a) TEM image of **T-OPVS-MV** (1:1) co-assembly formed in water at 0.15 mM. b) PXRD pattern of corresponding nanostructures on glass. c) TEM image of **T-OPVS** alone in water ($c = 0.15$ mM).

3.3.6 Transient Photocurrent Measurements

Since **OPVS-HDMV** co-assembled nanostructures have segregated D-A stacks with wide interface and showed efficient PET, we have evaluated the total charge carrier mobility of photogenerated charges (electrons and holes) using direct-current (DC)-mode transient photocurrent measurements. These measurements were performed using comb-type interdigitated gold electrodes patterned on glass substrates (Figure 3.3.9).¹⁵ For the experimental evaluation of mobility we have used transient absorption of the $\text{MV}^{•+}$, which

would give the direct estimation of the efficiency of photogenerated free charge carriers (ϕ).¹⁶ The solutions of nanostructures were drop casted on gold electrodes and exposed with 355 nm laser pulse from the back side. The photocurrent transients of these nanostructures are scaled with increasing applied bias voltage up to $4 \times 10^4 \text{ V cm}^{-1}$ (Figure 3.3.9). The ϕ of **OPVS-HDMV** co-assembled nanostructures is found to be 6.6×10^{-5} and estimated total charge carrier mobility ($\Sigma\mu$) is as high as $1.2 \text{ cm}^2/\text{V.s}$ (Figure 3.3.9a). This is the highest value reported so far for non-covalently tailored self-assembled D-A heterojunction nanostructures. The importance of segregated bicontinuous nanostructures of **OPVS-HDMV** co-assembly is further evident from the low charge carrier mobility ($\Sigma\mu = 0.07 \text{ cm}^2/\text{V.s}$) of the mixed stack **T-OPV-MV** CT-complex nanostructures (Figure 3.3.9b). Despite having higher ϕ (5.8×10^{-4}), the reason for low $\Sigma\mu$ in **T-OPV-MV** nanostructures is due to more time taken for the photogenerated charges to reach electrodes than **OPVS-HDMV** nanostructures. This clearly indicates that segregated stacks with wide D-A interface are prerequisite for efficient mobility of photogenerated charges than the mixed stack D-A nanostructures.

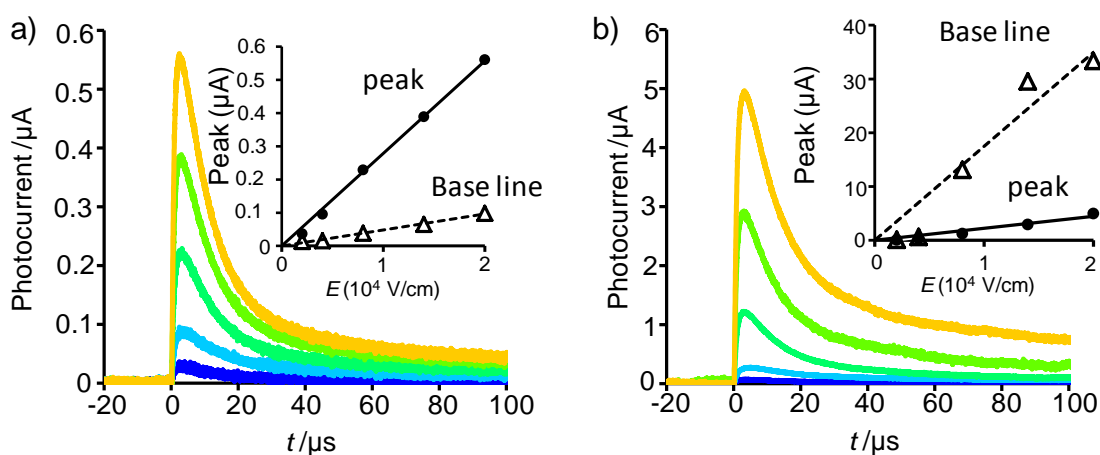


Figure 3.3.9. Photocurrent transients of nanostructures of a) **OPVS-HDMV** (1:2) and b) **T-OPVS-MV** (1:1) co-assembly on comb-type interdigitated gold electrodes fabricated on a glass substrate, upon exposure to 355 nm laser. The applied bias, E , was increased from blue to yellow. The inset shows the peak current (closed circles) and baseline current (open triangles) dependences on the electric field (E).

3.3.7 Conclusions

In conclusion we showed a simple non-covalent strategy to construct both segregated and mixed stack nanostructures from similar D and A chromophores. In the present case, the orientation of D and A molecules in the resultant D-A complex was controlled by appropriate utilization of difference in their molecular length and other non-covalent interactions. Solution phase self-assembly of these non-covalent complexes resulted in the distinct morphologies due to the differences in the orientation of D and A chromophores. Lamellar packing of segregated CT complex resulted in the formation of nanotapes having nanoscale D-A heterojunctions with

wide D-A interface and showed efficient PET from D to A. These features are absent in mixed stack D-A complex nanostructures due to the face-to-face orientation of D and A molecules. This was further reflected in their charge carrier mobility where segregated D-A nanostructures displayed two orders of magnitude higher charge carrier mobility than the mixed stack nanostructures.

3.3.8 Experimental Section

General Methods: Field Emission Scanning Electron Microscopy (FE-SEM) measurements were performed on a NOVANANO SEM 600 (FEI) in low vacuum mode by drop casting the solutions on glass substrate followed by drying in vacuum and operated with an accelerating voltage of 5 kV. Transmission Electron Microscopy (TEM) measurements were conducted on a JEOL, JEM 3010 operated at 300 kV. Samples were prepared by placing a drop of the solution on carbon coated copper grids followed by drying at room temperature. The images were recorded with an operating voltage 300 kV. In order to get a better contrast, samples were stained with uranyl acetate (1 wt % in water) before the measurements. Electronic absorption spectra were recorded on a Perkin Elmer Lambda 900 UV-VIS-NIR Spectrometer and emission spectra were recorded on Perkin Elmer Ls 55 Luminescence Spectrometer. UV-Vis and emission spectra were recorded in either 1 mm, or 5 mm path length cuvettes with 380 nm excitation wavelength. Fluorescence lifetime decay was recorded in a time-correlated single-photon-counting spectrometer of Horiba-Jobin Yvon. NMR spectra were obtained with a Bruker AVANCE 400 (400 MHz) Fourier transform NMR spectrometer with chemical shifts reported in parts per million (ppm). Flash photolysis was carried out using a Nd:YAG laser source producing nanosecond pulses (8 ns) of 355 nm light with the energy of the laser pulse being around 200 mJ. Dichroic mirrors were used to separate the third harmonic from the second harmonic and the fundamental output of the Nd-YAG laser. The monitoring source was a 150 W pulsed xenon lamp, which was focused on the sample at 90° to the incident laser beam. The beam emerging through the sample was focused onto a Czerny-Turner monochromator using a pair of lenses. Detection was carried out using a Hamamatsu R-928 photomultiplier tube. Transient signals were captured with an Agilent infinium digital storage oscilloscope and the data was transferred to the computer for further analysis.

3.3.8a Transient photocurrent measurements

Transient photocurrent measurements were performed using an interdigitated comb-type gold electrode with 5 μm gaps, 50 nm height, and 2 mm width fabricated by lithographic process in the laboratory was used for photocurrent experiments. A 0.5 mm thick glass plate was cleaned in a piranha solution (H_2O_2 : H_2SO_4 =1:2 v/v) for 20 min, washed by distilled water and isopropylalcohol for 10 min each. The dried substrates were exposed to UV/ozone for 5

min. The surface was kept in a toluene solution of n-octyltrichlorosilane (OTS) for 1 h in a glovebox and sequentially washed by toluene, acetone and isopropylalcohol with ultrasonication. Thin lift-off layer (Rohm and Haas Electronic Materials, LOLTM 1000) was spin-coated on the glass and annealed. Positive-tone resist (Rohm and Haas Electronic Materials, S1805G) was spin-coated on the lift-off layer and annealed. The substrate was exposed to a light from a Xe lamp (photolithography) through a mask and immediately developed by a developer (Rohm and Haas Electronic Materials, MFCD26) and rinsed by water. 1 nm Ti and 50 nm Au was deposited in a thermal evaporator. The electrodes were lift-off in DMSO with ultrasonication and rinsed by DMSO and isopropylalcohol. Prior to the experiments, the electrodes were checked by an optical microscope and a circuit tester. After casting the sample, an electrode was placed in a vacuum prober and exposed to THG (355 nm) of a Nd:YAG laser (Spectra Physics Inc. GCR-100, 5-8 ns pulse duration). The applied bias was controlled by an Advantest Corp. model R8252 digital electrometer. The transient photocurrent was measured by a Tektronix model TDS3052B digital oscilloscope equipped with termination resistance (10 k Ω). The experiments were carried out at room temperature.

3.3.8b Synthesis

Compounds HDMV,¹⁷ BMV,¹⁵ OPVS¹⁸ and T-OPVS¹⁸ were synthesized according to the literature methods (see Part-3.1). Methyl viologen (MV) was purchased from Acros-Organics.

3.3.9 References

1. a) X. He, F. Gao, G. Tu, D. G. Hasko, S. Hüttner, N. C. Greenham, U. Steiner, R. H. Friend, W. T. S. Huck, *Adv. Funct. Mater.* **2011**, *21*, 139; b) M. Wang, F. Wudl, *J. Mater. Chem.* **2012**, *22*, 24297; c) L. Dou, J. You, J. Yang, C.-C. Chen, Y. He, S. Murase, T. Moriarty, K. Emery, G. Li and Y. Yang, *Nat. Photonics* **2012**, *6*, 180; d) B. Walker, A. B. Tamayo, X.-D. Dang, P. Zalar, J. H. Seo, A. Garcia, M. Tantiwiwat, T.-Q. Nguyen *Adv. Funct. Mater.* **2009**, *19*, 3063.
2. a) L. Zhu, Y. Yi, Y. Li, E.-G. Kim, V. Coropceanu, J.-L. Brédas, *J. Am. Chem. Soc.* **2012**, *134*, 2340; b) S. K. Park, S. Varghese, J. H. Kim, S.-J. Yoon, O. K. Kwon, B.-K. An, J. Gierschner, S. Y. Park, *J. Am. Chem. Soc.* **2013**, *135*, 4757; c) V. Percec, M. Glodde, T. K. Bera, Y. Miura, I. Shiyonovskaya, K. D. Singer, V. S. K. Balagurusamy, P. A. Heiney, I. Schnell, A. Rapp, H.-W. Spiess, S. D. Hudson, H. Duan, *Nature*, **2002**, *419*, 384; d) A. A. Sagade, K. V. Rao, U. Mogera, S. J. George, A. Datta, G. U. Kulkarni, *Adv. Mater.* **2013**, *25*, 559.

-
3. a) L. Bu, X. Guo, B. Yu, Y. Qu, Z. Xie, D. Yan, Y. Geng, F. Wang, *J. Am. Chem. Soc.* **2009**, *131*, 13242; b) M. Wang, A. J. Heeger, F. Wudl, *Small*, **2011**, *7*, 298.
 4. a) K. M. Coakley and M. D. McGehee, *Chem. Mater.* **2004**, *16*, 4533; b) W. L. Ma, C. Y. Yang, X. Gong, K. Lee and A. J. Heeger, *Adv. Funct. Mater.* **2005**, *15*, 1617; c) J. Peet, M. L. Senatore, A. J. Heeger, G. C. Bazan, *Adv. Mater.* **2009**, *21*, 1521.
 5. a) J. Roncali, *Adv. Energy Mater.* **2011**, *1*, 147; b) Y. Yamamoto, T. Fukushima, Y. Suna, N. Ishii, A. Saeki, S. Seki, S. Tagawa, M. Taniguchi, T. Kawai, T. Aida, *Science*, **2006**, *314*, 1761; c) d) E. H. A. Beckers, S. C. J. Meskers, A. P. H. J. Schenning, Z. Chen, F. Würthner, P. Marsal, D. Beljonne, J. Cornil, R. A. J. Janssen, *J. Am. Chem. Soc.* **2006**, *128*, 649.
 6. a) J. L. Segura, N. Martín, D. M. Guldi, *Chem. Soc. Rev.* **2005**, *34*, 31; b) S. Loser, C. J. Bruns, H. Miyauchi, R. P. Ortiz, A. Facchetti, S. I. Stupp and T. J. Marks, *J. Am. Chem. Soc.* **2011**, *133*, 8142; c) Y. Matsuo, Y. Sato, T. Niinomi, I. Soga, H. Tanaka, E. Nakamura, *J. Am. Chem. Soc.* **2009**, *131*, 16048; d) J. C. Hummelen, B. W. Knight, F. Lepeq, F. Wudl, J. Yao, C. L. Wilkins, *J. Org. Chem.* **1995**, *60*, 532; e) G. Zhao, Y. He and Y. Li, *Adv. Mater.* **2010**, *22*, 4355; f) X. Zhan, Z. Tan, B. Domercq, Z. An, X. Zhang, S. Barlow, Y. Li, D. Zhu, B. Kippelen, S. R. Marder, *J. Am. Chem. Soc.* **2007**, *129*, 7246.
 7. a) Y. Yamamoto, G. Zhang, W. Jin, T. Fukushima, N. Ishii, A. Saeki, S. Seki, S. Tagawa, T. Minari, K. Tsukagoshi, T. Aida, *Proc. Natl. Acad. Sci. U.S.A.* **2009**, *106*, 21051; b) Y. Hizume, K. Tashiro, R. Charvet, Y. Yamamoto, A. Saeki, S. Seki, T. Aida, *J. Am. Chem. Soc.* **2010**, *132*, 6628; c) W.-S. Li, Y. Yamamoto, T. Fukushima, A. Saeki, S. Seki, S. Tagawa, H. Masunaga, S. Sasaki, M. Takata, T. Aida; *J. Am. Chem. Soc.* **2008**, *130*, 8886; d) W.-S. Li, A. Saeki, Y. Yamamoto, T. Fukushima, S. Seki, N. Ishii, K. Kato, M. Takata, T. Aida, *Chem. Asian J.* **2010**, *5*, 1566; e) M.-C. Yeh, Y.-L. Su, M.-C. Tzeng, C. W. Ong, T. Kajitani, H. Enozawa, M. Takata, Y. Koizumi, A. Saeki, S. Seki, T. Fukushima, *Angew. Chem. Int. Ed.* **2013**, *52*, 1031; f) Y. Yamamoto, T. Fukushima, A. Saeki, S. Seki, S. Tagawa, N. Ishii, T. Aida, *J. Am. Chem. Soc.* **2007**, *129*, 9276.
 8. L. F. Doessel, V. Kamm, I. A. Howard, F. Laquai, W. Pisula, X. Feng, C. Li, M. Takase, T. Kudernac, S. De Feyter K. Müllen, *J. Am. Chem. Soc.* **2012**, *134*, 5876.
 9. a) F. Würthner, Z. Chen, F. J. M. Hoeben, P. Osswald, C.-C. You, P. Jonkheijm, J. van Herrikhuyzen, A. P. H. J. Schenning, P. P. A. M. van der Schoot, E. W. Meijer, E. H. A. Beckers, S. C. J. Meskers, R. A. J. Janssen, *J. Am. Chem. Soc.* **2004**, *126*, 10611; b) P. Jonkheijm, N. Stutzmann, Z. Chen, D. M. de Leeuw, E. W. Meijer, A. P. H. J. Schenning, F. Würthner, *J. Am. Chem. Soc.* **2006**, *128*, 9535.
 10. a) B. Narayan, S. P. Senanayak, A. Jain, K. S. Narayan, S. J. George, *Adv. Funct. Mater.* **2013** (DOI: 10.1002/adfm.201202298); b) Y. Che, A. Datar, K. Balakrishnan, L. Zang, *J.*
-

-
- Am. Chem. Soc.* **2007**, *129*, 7234; c) J. P. Hill, W. Jin, A. Kosaka, T. Fukushima, H. Ichihara, T. Shimomura, K. Ito, T. Hashizume, N. Ishii, T. Aida, *Science* **2004**, *304*, 1481.
11. a) C. Wang, Y. Guo, Y. Wang, H. Xu, R. Wang, X. Zhang, *Angew. Chem. Int. Ed.* **2009**, *48*, 8962; b) K. V. Rao, K. Jayaramulu, T. K. Maji, S. J. George, *Angew. Chem. Int. Ed.* **2010**, *49*, 4218; c) C. Wang, S. Yin, S. Chen, H. Xu, Z. Wang, X. Zhang, *Angew. Chem. Int. Ed.* **2008**, *47*, 9049; d) K. Liu, C. Wang, Z. Li, X. Zhang, *Angew. Chem. Int. Ed.* **2011**, *50*, 4952; e) X. Zhang, C. Wang, *Chem. Soc. Rev.* **2011**, *40*, 94; f) F. Biedermann, O. A. Scherman, *J. Phys. Chem. B* **2012**, *116*, 2842.
12. **OPVS-HDMV** (1:2) complex was prepared by adding two equivalents of **HDMV** in methanol to one equivalent of **OPVS** in water and the resultant solution (10 % methanol in water) was heated up to 60 °C and cooled to room temperature. The resultant solution was used for all the measurements. Heat treatment was employed to make thermodynamically stable assemblies, because as prepared **OPVS-HDMV** (1:2) complex failed to show consistent absorption spectra.
13. a) C. Kong, L. Qin, J. Liu, X. Zhong, L. Zhu, Y.-T. Long, *Anal. Methods* **2010**, *2*, 1056; b) T. Tachikawa, S. Tojo, M. Fujitsuka, T. Majima, *Langmuir* **2004**, *20*, 9441.
14. We have used high concentrations of **OPVS/T-OPVS-MV** complexes for optical studies than **OPVS-HDMV** complex because of their weak association.
15. Y. Yasutani, A. Saeki, T. Fukumatsu, Y. Koizumi, S. Seki, *Chem. Lett.* **2013**, *42*, 19.
16. A. Saeki, Y. Koizumi, T. Aida, S. Seki, *Acc. Chem. Res.* **2012**, *45*, 1193.
17. M. F. Pepitone, G. G. Jernigan, J. S. Melinger, O.-K. Kim, *Org. Lett.* **2007**, *9*, 801.
18. K. V. Rao, S. J. George, *Chem. Eur. J.* **2012**, *18*, 14286.

PART-4**Luminescent Soft-Hybrids**

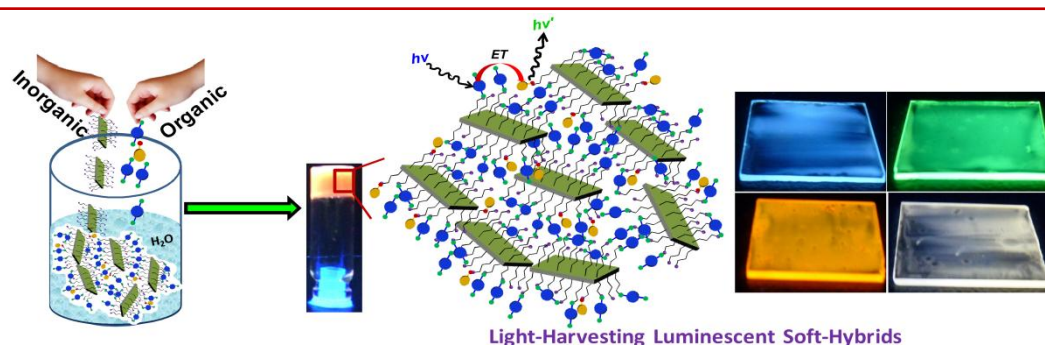
- PART-4.1** Light-Harvesting Organic-Inorganic Soft-Hybrids: Energy Transfer Induced Amplified Fluorescence and Highly Pure Solid-State White-Light Emission
- PART-4.2** Controlling the Molecular Organization of π - Systems via Hybrid Co-Assembly: A Non-Covalent Strategy towards Solution Processable Luminescent Hybrids

PART-4 . 1

Light-Harvesting Organic-Inorganic Soft-Hybrids: Energy Transfer Induced Amplified Fluorescence and Highly Pure Solid-State White-Light Emission*

Abstract

In this section, design of novel class of light-harvesting soft-hybrids formed by the non-covalent assembly of highly fluorescent donor and acceptor chromophores with organoclay is described. The aminopropyl functionalized clay layers template the supramolecular organization of chromophores and thereby facilitates an efficient Förster Resonance Energy Transfer (FRET) between donor and acceptor molecules. In mixed chromophoric hydrogels and films, an efficient light-harvesting results in enhancement of acceptor emission leading to amplified fluorescence. We further extended this strategy to achieve white-light emitting, soft-hybrid materials having excellent solution processability and high color purity. The unique solution processability of these organic-inorganic hybrids has been displayed by painting and writing on large glass and flexible plastic surfaces. These demonstrations unambiguously proves the simplicity and potential of these so-called 'soft-hybrids' as water processable, high transmittance materials for environmental friendly, large area display fabrication. Moreover, the dynamics of the dye molecules in these soft-hybrids are probed by energy transfer in solution. These non-covalent soft and dynamic hybrid networks may be useful for the design of light-emitting devices, sensors and other stimuli-responsive supramolecular systems.



*Papers based on this work have appeared in *Angew. Chem. Int. Ed.* 2011, 50, 1179; *Chem. Eur. J.* 2012, 18, 2184; *Adv. Mater.* 2013, 25, 1713.

4.1.1 Introduction

Light-harvesting and energy transfer between fluorescent donor and acceptor molecules have received increased attention in recent years because of their crucial role in photosynthesis and optoelectronic devices.¹ Since the supramolecular organization of donor and acceptor molecules is an important parameter in these photophysical processes, there has been an increasing interest in the design of various multichromophoric scaffolds.² Non-covalent and energy transfer design principles have been elegantly combined to achieve tunable emission in organic assemblies,² including white light.³ Nevertheless, the multistep synthesis and fluorescence quenching due to aggregation of chromophores are the major challenges in organic assemblies to realize their applications in devices. The hybridization of organic chromophores with inorganic systems either covalently or non-covalently have emerged recently as an alternative, efficient design for luminescent materials.⁴ The structural versatility and nanoscopic periodicity/space present in the inorganic component help to spatially organize the chromophores in these hybrids, which minimizes the inter-chromophoric interactions. As a result, these hybrid assemblies are expected to show high quantum yield, with added advantages of synthetic simplicity and transparent nature compared to the organic assemblies. In this context, silicate based materials with their versatile structural chemistry and nanoscale periodicity could be a natural choice to host the chromophores for efficient light-harvesting. Several luminescent hybrid materials of organic chromophores with inorganic scaffolds like zeolites,^{3c,5} periodic mesoporous organosilica (PMO),⁶ metal–organic frameworks (MOFs)⁷ and inorganic nanosheets⁸ have been reported, where the emission color has been tuned by the inter-chromophoric energy transfer. Although efficient light emission have been achieved in these hybrids,^{4,7} their substrate transferability remains elusive because of their limited solution processability. This further restricts the dynamics of donor-acceptor molecules in the final hybrid assembly. Since most of the organic chromophores are soluble in various solvents, the important thing to achieve solution processable hybrids depends on the selection of crystalline inorganic material. It would be advantageous if the inorganic component participates in the self-assembly process as a molecular entity along with the organic molecules, instead of acting as a rigid host or platform. In this respect, we envisage that the design of soft-hybrids as emissive materials would endow them with both solution processability and finer hybrid properties.^{3a} Nanoscale MOF⁹ based light-harvesting hybrids, reported recently are striking designs towards these soft-hybrids.

Out of many inorganic materials, clays have special importance owing to their ability to host and organize various organic dyes between their inter layer galleries.^{7,10} However, similar to other inorganic materials, most of the clays have poor solubility in water. This has been solved in layered magnesium silicates by covalent functionalization with organo amines (Figure

4.1.1a).¹¹ The resultant amino functionalized clays, amino clay (**AC**) are soluble in water via protonation of their amine groups and exfoliate into single layers due to charge repulsion (Figure 4.1.1b). These exfoliated **AC** sheets resemble like multivalent 2D cationic macromolecules and can be co-assembled with anionically charged,¹² photo-functional organic dyes. We envisaged that the ionic co-assembly between **AC** and anionic dye molecules would result solution processable light-harvesting organic-inorganic soft-hybrids with tailored luminescent properties (Figure 4.1.1b). Furthermore the non-covalent nature of these hybrids would impart dynamic property to the system.

4.1.2 Design Strategy

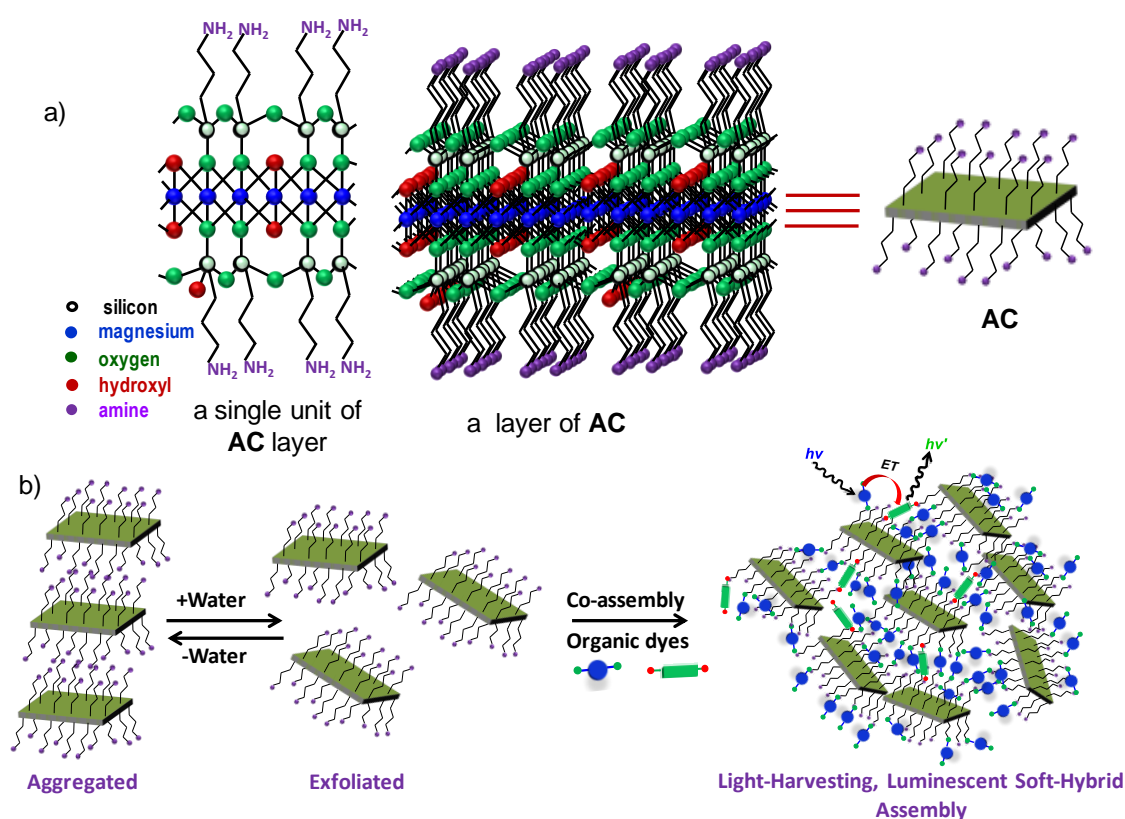


Figure 4.1.1. a) Molecular structure and schematic representation of the inorganic aminoclay (**AC**). b) Scheme for the synthesis of light-harvesting soft-hybrids via ionic co-assembly between **AC** and organic dye molecules.

In this section, we discuss on the multicomponent self-assembly of novel clay–chromophore hybrids that form hydrogels by controlling the spatial distribution of the chromophores to result in fluorescence. While clay–polymer hydrogels are known in literature¹³ this is the first report of the non-covalent interactions between clay layers¹⁴ and fluorescent dye molecules being exploited for the design of hydrogels. This multi-component self-assembly in water results in transparent, tractable hybrid hydrogels. We have also exploited **AC** as a template for the supramolecular organization of donor and acceptor molecules, which facilitates

fluorescence resonant energy transfer (Figure 4.1.1b). The efficient light-harvesting between the chromophores anchored to the **AC** was further exploited for enhanced fluorescence and tunable emission. Solution processability of these hybrids is demonstrated by painting and writing on large surface area lamps and flexible substrates. We have further extended this organic-inorganic hybrid approach to address the challenges in white light emissive materials. Through partial energy transfer between blue and yellow emitting dye molecules mediated by **AC** sheets, highly pure solid-state white-light was achieved with nearly ideal Commission Internationale de L'Eclairage (CIE) coordinates of (0.33, 0.32).

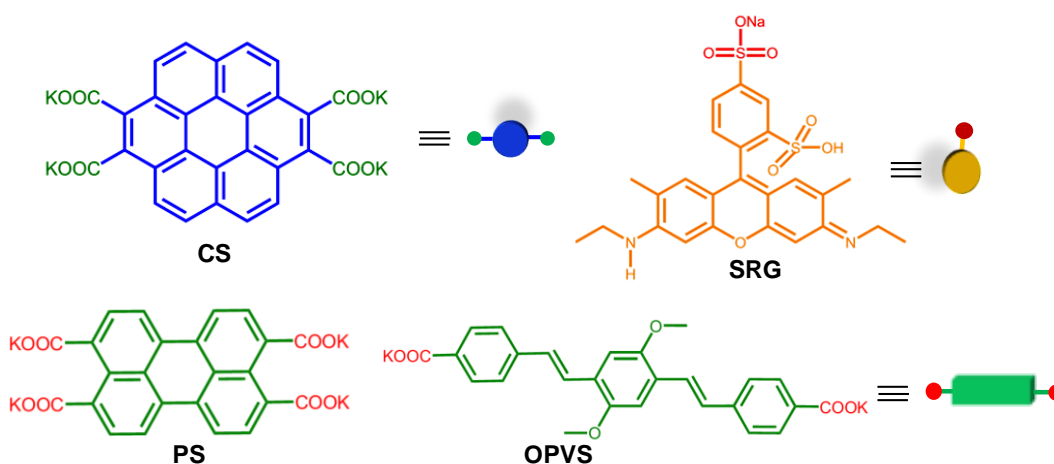


Figure 4.1.2. Molecular structures and schematic representation of the anionic organic components (**CS**, **PS**, **OPVS**, and **SRG**).

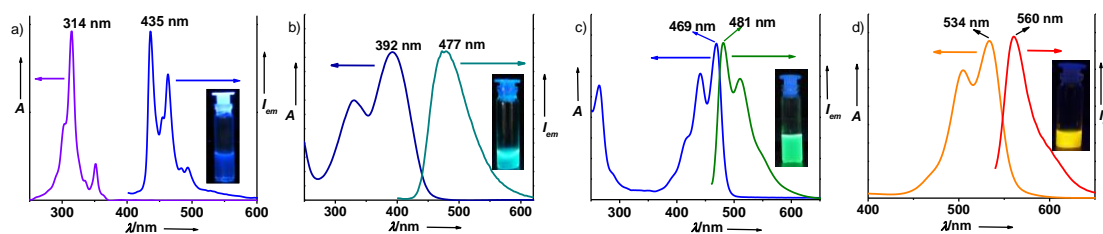


Figure 4.1.3. Normalized absorption and emission spectra of a) **CS**, b) **OPVS**, c) **PS** and d) **SRG** in water. Insets show the corresponding photographs of solutions under 365 nm UV-light.

We have chosen amino group functionalized organoclay (**AC**) for the design of hybrid clay materials, since the functional amino groups can be exploited for the non-covalent attachment of the chromophore molecules. The clay (**AC**) used herein is a layered magnesium organosilicate having the structure analogous to 2:1 trioctahedral smectites with an approximate composition of $R_8Si_8Mg_6O_{16}(OH)_4$, where R is covalently linked aminopropyl substituents (Figure 4.1.1a). For the non-covalent functionalization of **AC** we have used anionically charged molecules, coronene salt (**CS**, $\lambda_{\text{abs}} = 314$ nm, $\lambda_{\text{em}} = 435$ nm), oligo(p-phenylenevinylene) salt (**OPVS**, $\lambda_{\text{abs}} = 392$ nm, $\lambda_{\text{em}} = 477$ nm), perylene salt (**PS**, $\lambda_{\text{abs}} = 469$ nm, $\lambda_{\text{em}} = 481$ nm), and sulfurhodamine G (**SRG**, $\lambda_{\text{abs}} = 534$ nm, $\lambda_{\text{em}} = 560$ nm) as they have high fluorescence

quantum yields and excellent solubility in water (Figure 4.1.2 and 4.1.3). The negatively charged groups of these dyes are expected to interact electrostatically with the positively charged AC in water, thus resulting in non-covalent hybrid materials. Among all these anionic dye molecules CS becomes the key organic ingredient in the design of soft light-harvesting hybrids owing to its pure blue emission (0.15, 0.12) and high fluorescence lifetime (10.87 ns) (*vide infra*). These features make CS-AC hybrid as novel donor scaffold for excited state energy transfer with wide range of luminescent guest molecules.

4.1.3 Organic-Inorganic Co-Assembly

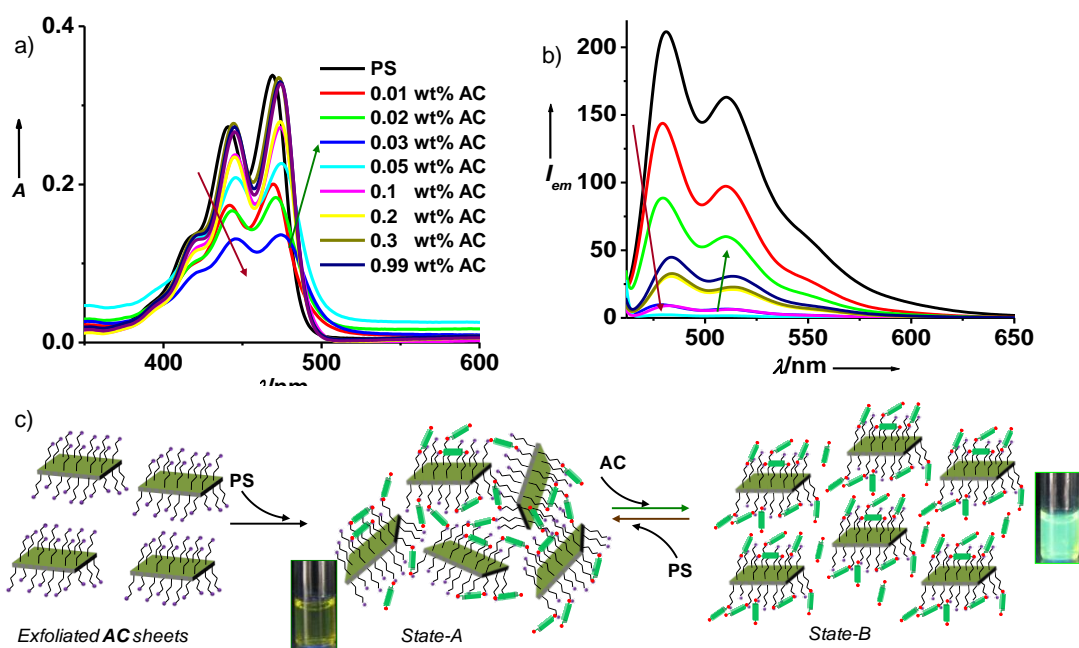


Figure 4.1.4. Changes in a) absorption and b) emission spectra of PS on titration with different wt% of AC ($c = 0.1$ mM, $l = 1$ mm, $\lambda_{exc} = 450$ nm). The red and green arrows show the gradual formation of State-A and State-B respectively. c) Schematic representation of different states of AC-PS hybrids in solution and the photographs of corresponding solutions of hybrids under UV-light.

First we investigated the individual interaction of the PS, CS and OPVS with clay in water. Spectroscopic titration experiments of the PS ($c = 0.1$ mM, 1 mL) with a stock solution of AC in water (1.0 wt%) initially showed a decreasing trend in the absorbance accompanied by concomitant scattering, broadening and a red-shift in the absorption maxima (469 nm to 474 nm, up to 0.03 wt% of AC in the final solution) owing to the interaction between the clay and dye molecules (Figure 4.1.4a). Further addition of AC (≥ 0.05 wt%) however, reversed this trend without any further changes in the red-shifted absorption maxima at 474 nm. A complete recovery of the absorption intensity equivalent to the pure PS was observed when the AC content in the final solution reached 0.3 wt%. A similar trend was observed in the fluorescence behavior of PS, although to a different extent upon addition of AC. For example, PS solution

containing 0.03-0.1 wt % of the clay was almost non-fluorescent and only 25% of the original emission intensity was regained even at the higher concentration of clay (> 0.3 wt %, corrected emission spectra for optical density, Figure 4.1.4b). Furthermore, the recovered dye emission maxima at higher clay concentrations (> 0.3 wt %) are red-shifted by an additional 3 nm (481 nm to 484 nm), when compared to the emission maxima of pure dye molecules or dye with lesser amount of **AC**. These optical changes suggest the presence of two different states for clay-dye hybrids in which the molecular organization of the individual components could be different. At the initial stages, when the amount of **AC** is less, the aggregation and cross-linking of large number of **PS** molecules interacting with each layer of clay would lead to the clustering of clay hybrids (we designate it as *State-A*, Figure 4.1.4c) and hence results in the decrease of absorption and emission intensity. The clustering of the clay hybrids in *State-A* is further supported by the observation of precipitate of clay-dye hybrid flakes with time as well as by the scattering observed in the UV-Vis spectra. However, when the amount of clay is increased for the same concentration of **PS** (1×10^{-4} M), the density of dye molecules sticking to each layer of **AC** will be reduced (designated as *State-B*, Figure 4.1.4c) mimicking more or less the condition of exfoliated **AC** layers with dangling dye molecules and hence the absorption and fluorescence are increased in intensity. The titration of coronene dye, **CS** with **AC** also showed a similar trend in optical properties. The particle size measurements carried out using dynamic light scattering (DLS) over these two sets of clay-**PS** hybrid solutions further proved the difference in their sizes (Figure 4.1.5a). The very broad and larger size distribution obtained for the low **AC** amount is consistent with the presence of large aggregated structures. On the other hand, solution with higher clay amount showed a narrow distribution and smaller size, which closely matches with the size distribution observed for the exfoliated clay sheets.

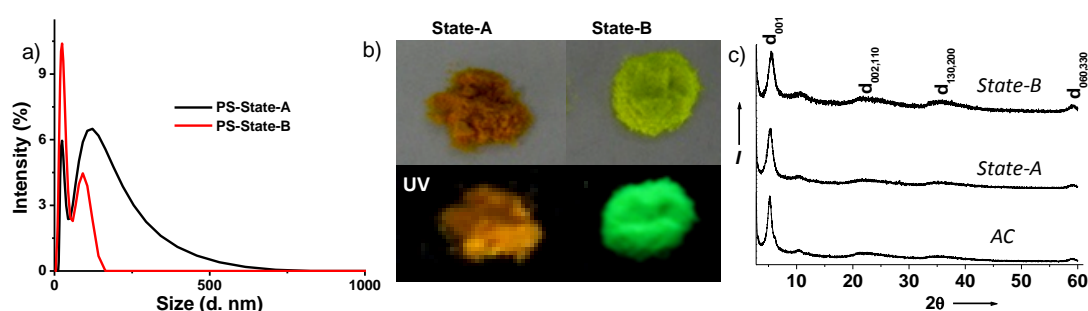


Figure 4.1.5. a) Particle size distribution of **PS** at *State-A* ($c = 0.1$ mM and **AC** = 0.1 wt%) and *State-B* ($c = 0.1$ mM and **AC** = 0.8 wt%) measured by DLS. b) Photographs of the **AC-PS** hybrid powders under ambient and 365 nm UV light. c) Powder XRD patterns of **AC** and **AC-PS** hybrids.

The molecular organization and the spectral properties of the **AC-PS** hybrids in solution was also retained in the solid-state as evident from the changes in color and fluorescence of the powders obtained by precipitation from different states, by the addition of

ethanol (Figure 4.1.5b). The solids formed from *State-B* are green in color and are highly fluorescent whereas, the powder from *State-A* is non fluorescent like the solid powders of **PS** alone and is light-brown in color suggesting the intermolecular interaction between the chromophores. However, powder X-Ray diffraction (PXRD) studies for the dye incorporated clay samples from both states did not show any significant changes in the basal d_{001} spacing as compared to the parent clay within the concentration range we have studied (Figure 4.1.5c). The d_{001} values for **AC-PS** both in *State-A* and *State-B* are found to be 1.68 nm and 1.60 nm, respectively which are more or less equal to the d_{001} spacing (1.68 nm) obtained for the as synthesized **AC**. This could be due to a parallel orientation of the dye molecules between the clay layers as a result of the stacking of **AC** sheets in the solid-state.

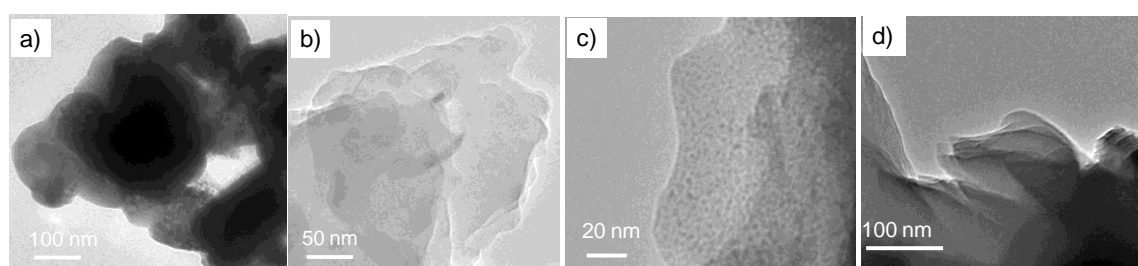


Figure 4.1.6. TEM images of a) **PS** alone, b) **AC**, c) **PS-AC** in *State-A* ($c = 0.1$ mM and **AC** = 0.1 wt%) and d) **PS-AC** in *State-B* ($c = 0.1$ mM and **AC** = 0.8 wt%).

TEM studies provided evidence for the role of **AC** in preventing aggregation of dye molecules at higher concentrations, due to its efficient capping functionality which helps to anchor and uniformly distribute the chromophores (Figure 4.1.6). Although, **PS** is molecularly dissolved in water to result in green fluorescent solution, **PS** in powder form or in the film state showed very weak fluorescence characteristic of the aggregation between molecules. This is further evident from the electron microscopy which clearly showed aggregated rod like nanostructures (Figure 4.1.6a). On the other hand, **AC** showed crystalline lamellar structure (plate like morphology) wherein, the lateral dimensions are in micron regime and thickness is of the order of few nanometers (Figure 4.1.6b). TEM studies of the drop-casted **AC-PS** hybrid solution from *State-A* shows regions where 5 nm sized spherical aggregates of **PS** molecules distributed over the surface of **AC** matrix (Figure 4.1.6c). It is to be noted that the **PS** molecules, in addition to forming large aggregates on the clay surface can also be distributed at the molecular level in the clay interlayer spacings which would be difficult to differentiate in TEM. Interestingly, sample prepared by drop-casting the solution from *State-B* shows no such aggregates on the clay surface suggesting the homogenous molecular level dispersion of **PS** dyes over **AC** matrix (Figure 4.1.6d).

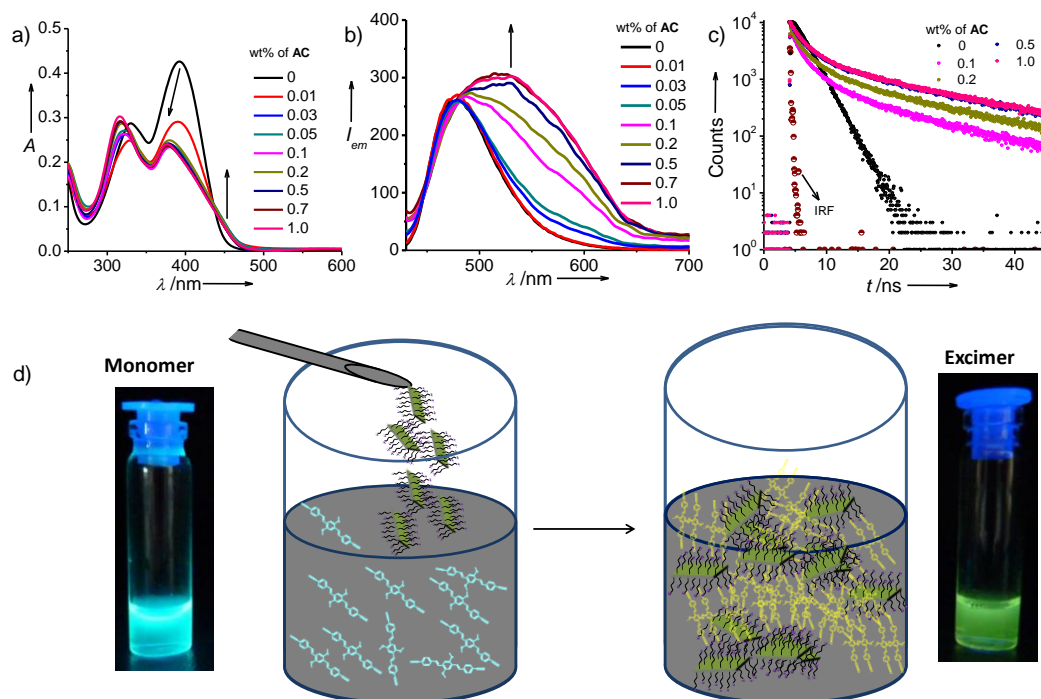


Figure 4.1.7. a) Absorption spectra, b) normalized emission spectra and c) lifetime decay profiles of **OPVS** with different wt% of **AC** in water. Where *IRF* is the instruments response function. d) Schematic representation and solution photographs under 365 nm UV-light showing the conversion of **OPVS** monomers in water into preassociated excimers after treating with **AC** sheets ($c = 0.1$ mM, $l = 1$ mm, $\lambda_{exc} = 370$ nm, $\lambda_{monitored} = 520$ nm).

On the other hand, in case of **OPVS** co-assembly with **AC**, we have not observed two different states. In water, **OPVS** behaves as molecularly dissolved species with its characteristic absorption peaks at 392 and 330 nm and shows cyan emission ($\lambda_{max} = 477$ nm). With increasing amounts of **AC** (0.01 wt% to 1.0 wt%), the absorption bands of **OPVS** are blue shifted and with 1.0 wt% of **AC** they showed maxima at 377 and 315 nm (Figure 4.1.7a). The blue shift in absorption revealed the H-type aggregation of **OPVS** in presence of **AC**. Interestingly, with increase of **AC** wt% the monomer emission at 478 nm is quenched significantly with concomitant appearance of new broad band centred at 528 nm (Figure 4.1.7b). Lifetime measurements suggest that this new red shifted emission is due to the formation excimer by **OPVS** in presence of **AC** (Figure 4.1.7c). **OPVS** alone in water showed single decay profile corresponding to a lifetime of 2.23 ns consistent with its monomeric behaviour. Remarkably, as the **AC** wt% increases the decay profiles showed multi exponential decay with the appearance of new long lived components. **OPVS-AC** decay profiles were fitted to triexponential equation and with increase of **AC** wt% the contribution from first two components in the decay profile decreases with significant increase (52 % to 85 %) in contribution from long lived components. The lifetime of third component is increased from 11 ns to 17 ns with the increase in the amount of **AC** from 0.1 to 1.0 wt% in 0.1 mM solution of **OPVS**. The observed high lifetime and blue shifted absorption spectra of **OPVS** in presence of **AC** unambiguously proves the

existence of H-type **OPVS** excimer. This kind of excimer formation with similar lifetime was previously observed in some chromophores with AIE behaviour.¹⁵ In the present case, excimer formation by **OPVS** is accompanied by its H-type aggregation in the ground state, suggesting that they are preassociated or static excimer (Figure 4.1.7d).¹⁶

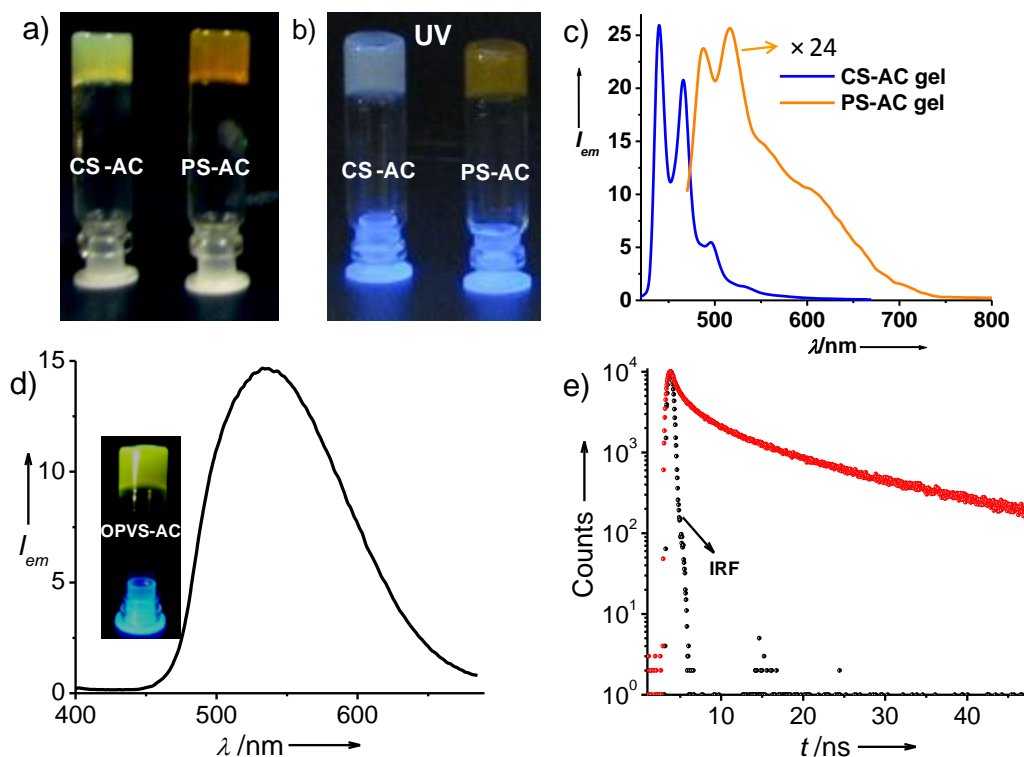


Figure 4.1.8. a) and b) are the photographs of **CS**, **PS** hydrogels with **AC** under visible and UV-light, respectively. c) Emission spectra of the **CS-AC** ($\lambda_{exc} = 350$ nm) and **PS-AC** ($\lambda_{exc} = 450$ nm) gels recorded in a 1 mm cuvette with front-face geometry. d) Emission spectra of **OPVS-AC** hydrogel and the photograph of the gel is shown in the inset. e) Nanosecond lifetime decay profile of **OPVS-AC** hydrogel ($c = 5.0$ mM, **AC** = 8 wt%, $l = 1$ mm, $\lambda_{exc} = 370$ nm, $\lambda_{monitored} = 520$ nm and **IRF** is the instrument response function).

Interestingly, when the concentration of dyes (**CS**, **PS**) and **AC** is increased (~ 100 times) by keeping the ratio between them similar to *State-A* (10^{-4} M dye: 0.1 wt% **AC**) in water, highly stable transparent hydrogels were formed, which is confirmed by an inverted vial method (Figure 4.1.8a). In a typical experimental procedure, the precipitate formed by mixing the aqueous solutions of dye (**CS/PS**) and the clay was sonicated until the solution becomes clear and then left at room temperature. Stable, self-standing hydrogels were formed within 20 minutes, which is consistent with the cross-linking nature of the dyes in *State-A*. The critical gelator concentrations were found to be 7.5×10^{-3} M (**AC** = 7.5 wt%) for **CS** and 5.0×10^{-3} M (**AC** = 5.0 wt%) for **PS**, which suggested a stronger cross-linking interaction of **PS** with **AC**. The total wt% of hybrid components in case of **CS-AC** and **PS-AC** gel is nearly 12.0 and 8.0 respectively, suggesting the high water content in the hydrogels. Although hydrogels were

formed with high efficiency, they are weakly fluorescent due to the intermolecular interactions between the chromophores in *State-A* (Figure 4.1.8b). **CS-AC** and **PS-AC** hybrid hydrogels shows weak blue ($\lambda_{\text{max}} = 440 \text{ nm}$, $\lambda_{\text{exc}} = 350 \text{ nm}$) and greenish-yellow ($\lambda_{\text{max}} = 516 \text{ nm}$, $\lambda_{\text{exc}} = 450 \text{ nm}$) fluorescence, respectively. The decrease in fluorescence intensity along with the red shift in emission maxima (2-3 nm) of the dyes in hybrid gels compared to that of *State-A* solution suggests the strong intermolecular interaction between the dyes. Moreover, in **PS-AC** hybrid gel, the higher intensity of the emission band at 516 nm compared to the high energy band at 487 nm along with the appearance of the new broad band around 600 nm are characteristic of the J-aggregation of perylene chromophores.¹⁷ The clay to dye ratio in *State-A* is also found to be very crucial for the formation of the gels, as higher clay to dye ratio (*State-B*) failed to produce gels at any concentration. However, in case of **OPVS-AC** hybrids, the optimum concentrations of **AC** and **OPVS** to form hydrogel were found to be 8 wt% and 2 mM, respectively (Figure 4.1.8c). The average lifetime of this hybrid hydrogel was found to be 9.6 ns with 67% contribution from long lived component (13.1 ns). This indicates that **AC-OPVS** hybrid hydrogel contains the mixture of both monomeric and excimeric form of **OPVS** molecules (Figure 4.1.8d). These finding clearly suggest that molecular organization of **OPVS** in the co-assembled **AC-OPVS** hybrids is significantly different from tetracarboxylates (**CS/PS**). The shape and net charge on the molecules might have significant effect on the extent of interaction with **AC** which might be the reason for the differences observed between **OPVS-AC** and **CS/PS-AC** hybrids.

4.1.4 Energy Transfer in Solution

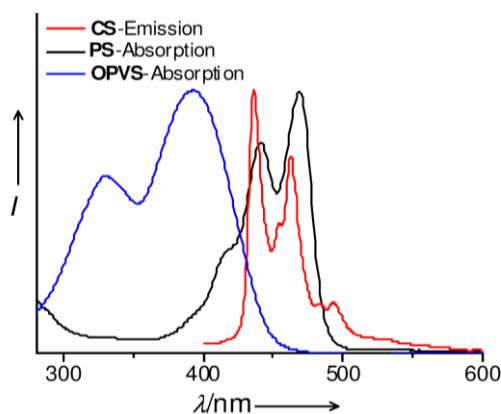


Figure 4.1.9. Normalized absorption spectra of acceptors (**PS** and **OPVS**) with the emission spectrum of donor (**CS**).

We explored the efficiency of **AC**, as novel class of supramolecular templates to facilitate photo-induced Förster Resonance Energy Transfer (FRET) between donor and acceptor chromophores that are non-covalently anchored onto the clay surface. Since FRET process involves a through-space dipole-dipole interaction, the presence of ordered

aminopropyl groups on the **AC** nanosheets are expected to provide an efficient scaffold to orient the donor and acceptor molecules in the mixed chromophore clay hybrids to facilitate energy transfer. Furthermore, an efficient energy transfer to fluorescent acceptor molecules in mixed chromophoric clay hybrids would also help the design of luminescent hybrids even in the gel/solid phases, compared to the quenched fluorescence of individual dye-clay gels. The emission spectrum of **CS** (donor, 425-500 nm) has a very good spectral overlap with the absorption bands of the **PS** (acceptor, 380-500 nm) and partial overlap with **OPVS** (acceptor, 300-470 nm), and hence an efficient Förster type energy-transfer between from **CS** to **PS** and **OPVS** can be envisaged, if there is a proper spatial orientation between the chromophores (Figure 4.1.9). Furthermore, in case of **CS-PS** pair, the well-separated absorption bands of the donor and acceptor molecules (Figure 4.1.3) ensures that both the **CS** and **PS** molecules can be selectively excited at 350 and 450 nm, respectively in mixed chromophore hybrids which would help to analyze the energy transfer efficiencies.

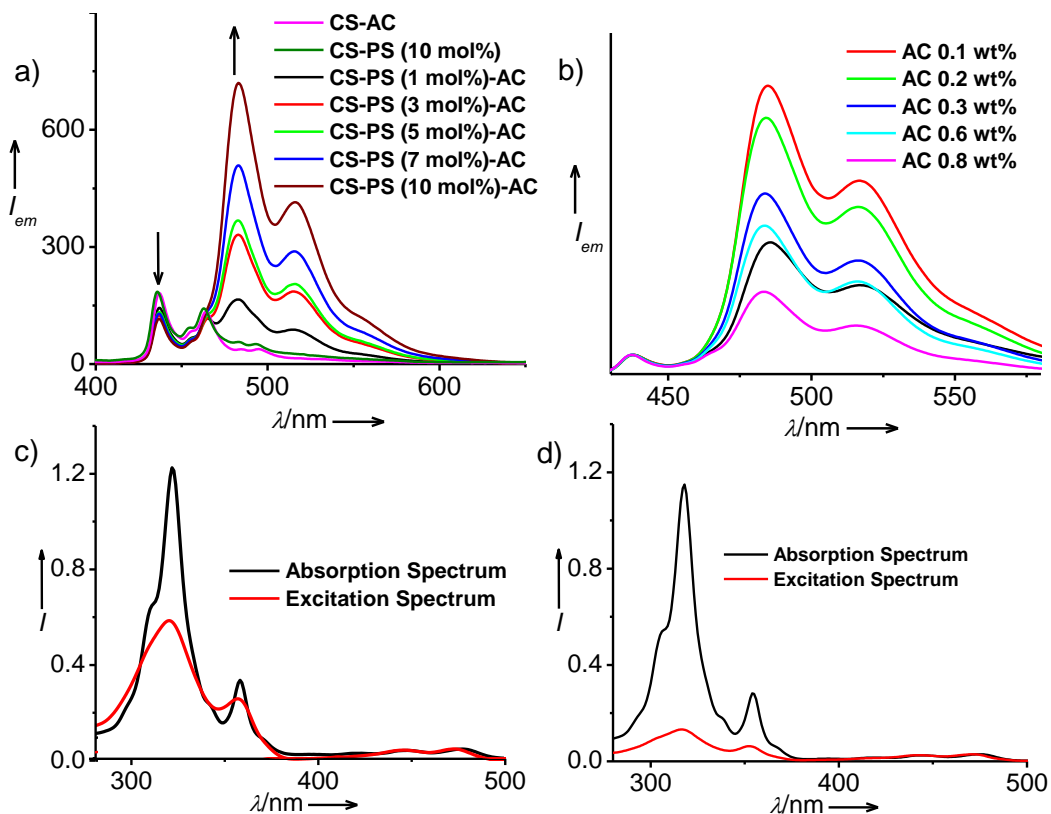


Figure 4.1.10. a) Fluorescence titration spectra of **CS-AC** hybrids in State-B ($CS = 0.1$ mM, $AC = 0.8$ wt%, $\lambda_{exc} = 350$ nm, $l = 1$ mm) with different mol % of **PS** and b) normalized emission spectra at donor emission for different amounts of **AC** ($CS = 1 \times 10^{-4}$ M, $PS = 10$ mol%, $\lambda_{exc} = 350$ nm, $l = 1$ mm) in water. Normalized absorption and excitation spectra of **CS-PS-AC** hybrids in c) State-A and d) State-B ($\lambda_{normalized} = 445$ nm, $\lambda_{emission} = 515$ nm).

Despite having a good overlap of emission of **CS** with the absorption of **PS**, no energy transfer was observed from **CS** (0.1 mM) to **PS** (0.01 mM, 10 mol% relative to **CS**) in the

absence of clay sheets suggesting the molecularly dissolved nature of the dye molecules in water (Figure 4.1.10a). We first investigated the feasibility of energy transfer of mixed **CS-PS**-clay hybrids in aqueous solution. Hence, mixed chromophore-clay hybrids were prepared with various donor-acceptor compositions, by keeping the clay to **CS** (donor) dye ratio similar as that in *State-B* (10^{-4} M dye, 0.8 wt% **AC**) where the clay sheets are completely exfoliated and are highly fluorescent. When the mixed chromophore-clay hybrid sheets are excited at 350 nm (the donor, **CS** absorption), quenching of the donor emission between 450-500 nm could be seen, with the concomitant increase in the **PS** emission at 500-600 nm, indicating the excitation energy transfer from the **CS** to **PS** (Figure 4.1.10a). However, significant amount of **CS** emission remains even upto 10 mol% loading of the acceptor **PS** dyes indicating a less efficient energy-transfer. In order to get further understanding about the mechanism of energy transfer we have carried out a titration experiment with increasing amounts of **AC** keeping the concentration and composition of the donor and acceptor chromophores constant (**CS** containing 10 mol % of **PS** at 0.1 mM, Figure 4.1.10b). Energy transfer was monitored by the normalization of the emission spectra at the donor emission, and then plotting the increase in acceptor emission between 475-600 nm as a function of clay concentration. More efficient energy transfer was observed when the dyes are anchored to 0.1 wt% of **AC** which corresponds to *State-A* (Figure 4.1.10b). Further increase in clay concentration above 0.1 wt% led to a gradual decrease in the energy transfer and became less efficient in *State-B* (0.8 wt% **AC**). Hence it is evident that the low energy-transfer efficiency in *State-B* could be either due to the absence of any inter-clay excitation energy transfer as the clay sheets are fully exfoliated or the donor chromophores in the clay sheets are too sparsely dispersed. Furthermore, excitation spectra collected at the **PS** emission ($\lambda_{em}=515$ nm) in the mixed chromophore-clay hybrids matches with the absorption spectra of **CS**, which provides an unambiguous proof of the energy transfer process (Figure 4.1.10c and d).

Energy-transfer efficiencies at different states were calculated by comparing the excitation spectra ($\lambda_{em} = 515$ nm) with corresponding absorption spectra normalized at the λ_{max} of the acceptor perylene dye and the efficiencies in *State-A* and *State-B* are found to be 50% and 10% respectively (Figure 4.1.10c and d). Remarkably, in *State-A* of the mixed hybrids (10 mol% of **PS**), excitation of the donor, **CS** at 350 nm gives 11 times higher **PS** emission due to energy transfer compared to the direct excitation of the acceptor **PS** alone at 450 nm whereas it is only 3 times in *State-B* (Figure 4.1.11a and b). This amplified emission is a definitive proof of a Förster type energy transfer mechanism and an antenna effect in light-harvesting. Efficient energy transfer in *State-A* is further evidenced from fluorescence lifetime measurements. **CS** in *State-A* displayed an average lifetime of 10.87 ns which was decreased to 8.2 ns with the addition of 10 mol% of **PS** (Figure 4.1.11c). Probing the **PS** emission while exciting **CS** at 335

nm showed increase in its lifetime (6.57 ns) compared to the characteristic lifetime (5.14 ns) of **PS** in the clay scaffold, which is obtained by the direct excitation of the mixed hybrid (**CS-PS-AC**) at 440 nm (Figure 4.1.11d). The decay profile of the acceptor in mixed hybrids is also marked by the rising component at shorter time scales, indicating the growth of the acceptor excited states via energy transfer. These changes in decay profiles are characteristic of an efficient FRET process and any trivial mechanisms for energy transfer can thus be ruled out.

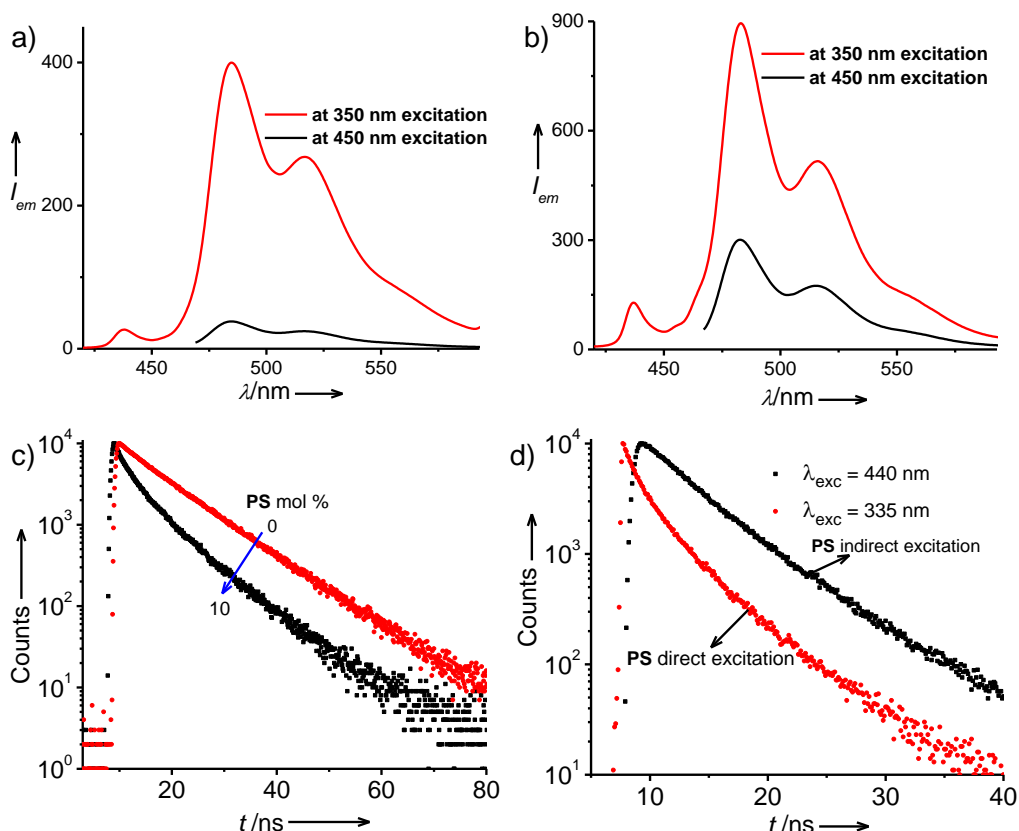


Figure 4.1.11. Emission spectra of solutions at a) State-A ($[CS] = 0.1$ mM and AC = 0.1 wt%) and b) State-B ($[CS] = 0.1$ mM and AC = 0.8 wt%) containing 10 mol% **PS**. Selective excitation of the donor and acceptor are done at 350 nm and 450 nm, respectively. Lifetime decay profiles of c) **CS-AC** hybrids with and without **PS** ($\lambda_{exc} = 335$ nm) monitored at **CS** emission (435 nm) and d) **CS-AC** hybrids having 10 mol% of **PS**, monitored at **PS** emission (485 nm).

Similarly, in **CS-OPVS-AC** mixed hybrids also energy transfer is more efficient in *State-A* than *State-B*. Despite having partial spectral overlap, efficient quenching in the **CS** emission with concomitant enhancement in the **OPVS** emission intensity was observed as the concentration **OPVS** in **CS-AC** hybrid increases from 0 to 50 mol%. This further suggests the perfect alignment of donor-acceptor dipoles in presence of **AC**. The observed emission intensity when **OPVS** was directly excited at 400 nm (where **CS** does not absorb) is 4 times less in *State-A* and 2 times less in *State-B* than the intensity observed when **CS** was excited at 320 nm, indicating the involvement antenna effect and direct energy transfer without radiation

reabsorption process (Figure 4.1.12b and c). Excited state lifetime measurements gave further insights into the energy transfer process. The decay profiles of hybrids were fitted with multi exponential decay and average lifetimes were considered for the analysis. The average lifetime of **CS** solution in *State-A* is 10.87 ns which decreased to 8.04 ns with 5 mol% of **OPVS** and 5.13 ns with 10 mol% of **OPVS**. The observed decrease in donor lifetime (**CS**) further supports the direct energy transfer without radiation reabsorption process (Figure 4.1.12d). The excitation spectra collected at **OPVS** emission (550 nm, where **CS** does not emit) for **CS-AC** solution having 10 mol% of **OPVS** shows the major contribution from **CS**, which unambiguously proves the FRET from **CS** to **OPVS** (Figure 4.1.12e and f). Similar to **CS-PS-AC** hybrids, maximum FRET efficiency was observed in *State-A* (45 %) than in *State-B* (10 %) at 10 mol% of **OPVS** (Figure 4.1.12e and f). Despite having poor spectral overlap, energy transfer efficiencies of **CS-OPVS** pair are comparable to that of **CS-PS** pair. This further highlights the structural elegance of **AC** in providing good spatial organization between donor-acceptor molecules.

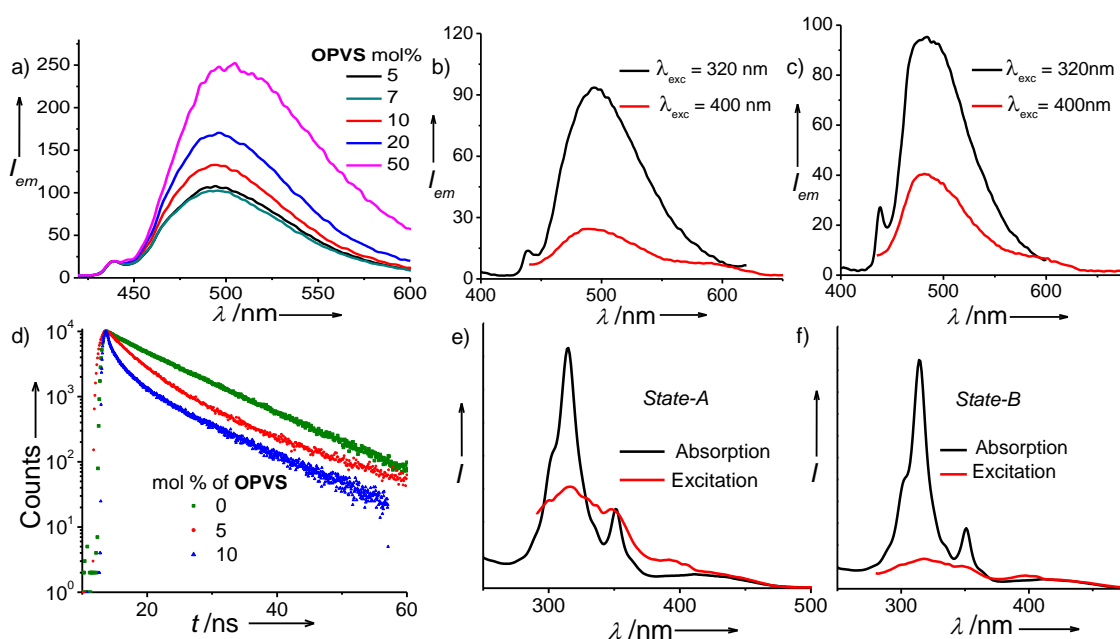


Figure 4.1.12. a) Normalized emission spectra of **CS-AC** solution with different mol% of **OPVS** in *State-A* ($\lambda_{exc} = 320$ nm). Emission spectra of **CS-AC** solutions having 10 mol% of **OPVS** in b) *State-A* and c) in *State-B*. Selective excitation of the donor and acceptor are done at 320 nm and 400 nm, respectively. d) Lifetime decay profiles of **CS-AC** solutions in *State-A* with different mol% of **OPVS** ($\lambda_{exc} = 350$ nm and $\lambda_{monitored} = 435$ nm). Normalized absorption and excitation spectra of **CS-AC** solution containing 10 mol% of **OPVS** e) in *State-A* and f) in *State-B*. All fluorescence measurements were done in 1 mm cuvette in front face geometry to avoid self-absorption at higher concentrations.

4.1.5 Energy Transfer in Gels and Films

Mixed chromophore-clay gels with donor and acceptor molecules were also investigated for energy transfer. These gels were prepared with various donor-acceptor (0-50

mol% of **PS** or **OPVS** relative to **CS**) compositions, by the incorporation of required amounts of acceptors into the aqueous solution of **AC** containing **CS** at its critical gelator concentration. The mixture was further sonicated and kept at room temperature to form corresponding hybrid gels. In case of **CS-PS** pair, upon excitation of the hybrid gels at 350 nm, the emission intensity at 440 nm showed a gradual decrease, with the concomitant formation of a green emission at 485 nm, as the **PS** loading increases, suggesting the energy transfer (Figure 4.1.13a). This green emission via energy transfer is remarkable, as the corresponding pure **PS-AC** gels are virtually non-fluorescent. However, at lower percentages of acceptor, **PS** (1 to 5 mol %), the acceptor emission at 475-600 nm was greater when **PS** was directly excited at 450 nm, indicating the absence of antenna effect. Further loading of the (**PS** > 7%) results in amplified green emission from the gels due to energy transfer and the fluorescence reaching a maximum. However, increase of **PS** concentration above 10% results in decrease of fluorescence at 485 nm with a simultaneous bathochromic shift indicating the interaction between the perylene chromophores. Interaction between the chromophores in hybrid hydrogels at higher percentages of **PS** is further evident from the normalized emission spectra at 485 nm, which showed a gradual increase in the intensity and red-shift of the emission band at 515 nm and the appearance of a broad emission around 600 nm, characteristic of the perylene chromophore stacking (Figure 4.1.13a and c). This indicates that at low **PS** loadings, the acceptor molecules exist as isolated energy traps resulting in highly intense green emission from individual perylene chromophores. On the other hand, at higher **PS** loadings the acceptor molecules are able to interact with each other resulting in aggregate energy traps with lower energy to give red-shifted emission with low quantum yield. Similarly, as the mol% of **OPVS** increases in the **CS-AC** gel, there is a continuous quenching in the **CS** emission associated with the enhanced **OPVS** emission (Figure 4.1.13b). In case of solution state at 20 mol% of **OPVS** *ca.* 3 times quenching in the **CS** emission was observed, whereas in gel state it reached up to 8 times indicate the enhanced energy transfer efficiency due to decreased donor-acceptor distances in the gel state.

Since efficient energy transfer in the solid films is a prerequisite for the device applications, we have extended the studies to the films made from the gels (xerogels) which showed the same fluorescence trend as the gels (Figure 4.1.13d and e). Remarkably, the films with even 1 mol% of **PS**, showed a significant quenching of the donor emission and an enhanced fluorescence intensity due to energy transfer compared to the direct excitation of the acceptor, suggesting a very efficient light-harvesting (Figure 4.1.13d). In case of xerogels of **CS-OPVS-AC** hybrids, with 10 mol% of **OPVS** complete quenching of **CS** emission was observed indicating 100% energy transfer with enhanced acceptor emission (Figure 4.1.13e). The photographs of these light-harvesting hybrid gels and films under 365 nm UV light are shown in Figure 4.1.13f and g. These show the bright emission in the mixed dye hybrids than

their individuals as a consequence of energy transfer. This significant amplified emission through energy transfer in the film state is unprecedented and shows the remarkable efficiency of clay-dye hybrids as novel supramolecular scaffolds for energy-transfer.

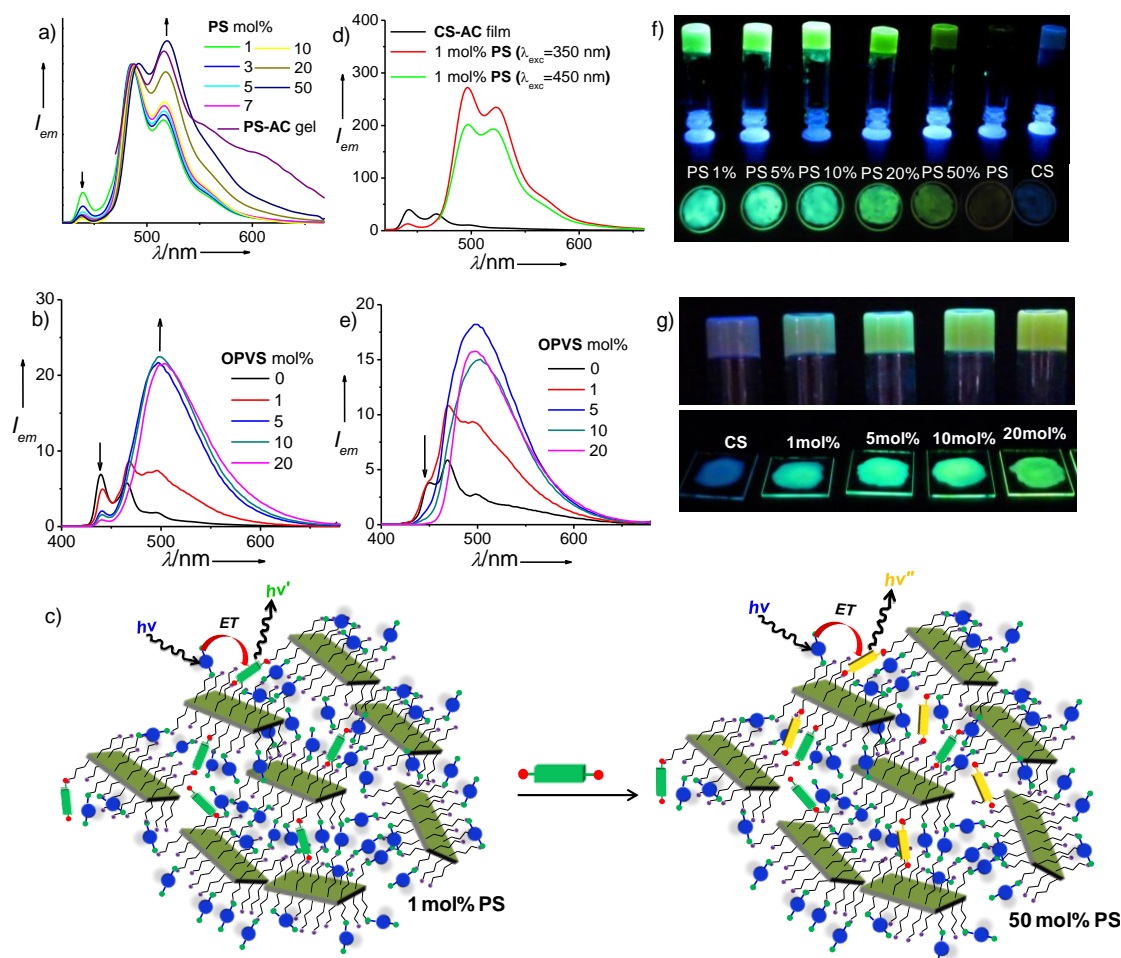


Figure 4.1.13. a) Normalized emission spectra of hybrid CS-AC gels with different mol% of PS ($\lambda_{exc} = 350$ nm, $l = 1$ mm, $\lambda_{normalized} = 487$ nm). b) Emission spectra of CS-AC hybrids containing different mol% of OPVS in gel state ($\lambda_{exc} = 350$ nm, $l = 1$ mm). c) Schematic representation of the self-assembly and energy transfer to isolated and aggregated traps in clay-dye hybrid gels. d) Normalized emission spectra of CS-AC hybrid xerogels with and without 1 mol% of PS dried on quartz plates ($\lambda_{exc} = 350$ nm). e) Emission spectra of CS-AC hybrid xerogels with different mol% of OPVS on glass plates ($\lambda_{exc} = 320$ nm). f) Photographs of CS-AC hydrogels and xerogels containing different mol% of f) PS and g) OPVS under 365 nm UV-light.

4.1.6 White-Light Emission

We have further extended the above described light-harvesting design for the construction of processable white luminescent materials. In order to achieve white-light emission, we have used yellow emitting SRG as the acceptor in the pure blue fluorescent CS-AC donor scaffold (Figure 4.1.2). Their spectral overlap further suggests that they can act as donor-acceptor couple for excitation energy transfer (Figure 4.1.14). The bi-functional nature of the donor ensures an extended co-assembly with the AC nanolayers containing protonated

amino groups on both sides. The acceptor, on the other hand with its mono functional group electrostatically docks on to the clay sheets in required amounts, without affecting the hybrid co-assembly. **CS-AC** hybrid hydrogel exhibits pure blue emission ($\lambda_{\max} = 435$ nm) with CIE-coordinates of (0.15, 0.12) and therefore, used as a donor-scaffold for the design of white light emission via partial excitation energy transfer to the co-assembled acceptor dye molecules. The mixed **CS-SRG-AC** hybrids can be conveniently prepared either by the co-assembly of all three components in water (pre-synthetic pathway) or by encapsulation of **SRG** acceptors to the pre-assembled **CS-AC** hybrids (post-synthetic), as the components in the assembly are very dynamic (*vide infra*). This procedure is very simple and is characteristic of our soft-hybrids in contrast to the tedious and time-consuming procedures often required for the loading of acceptors in hybrid materials.^{5,6,8}

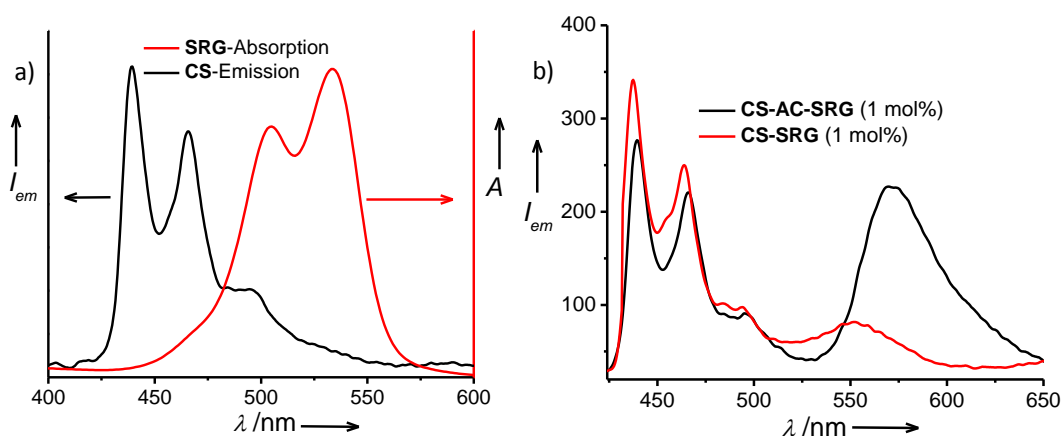


Figure 4.1.14. a) Normalized absorption spectrum of acceptor (**SRG**) with the emission spectrum of donor (**CS**) in water. b) Emission spectra of **CS** (0.1 mM) with 1 mol% of **SRG** in water with and without **AC** (0.1 wt%).

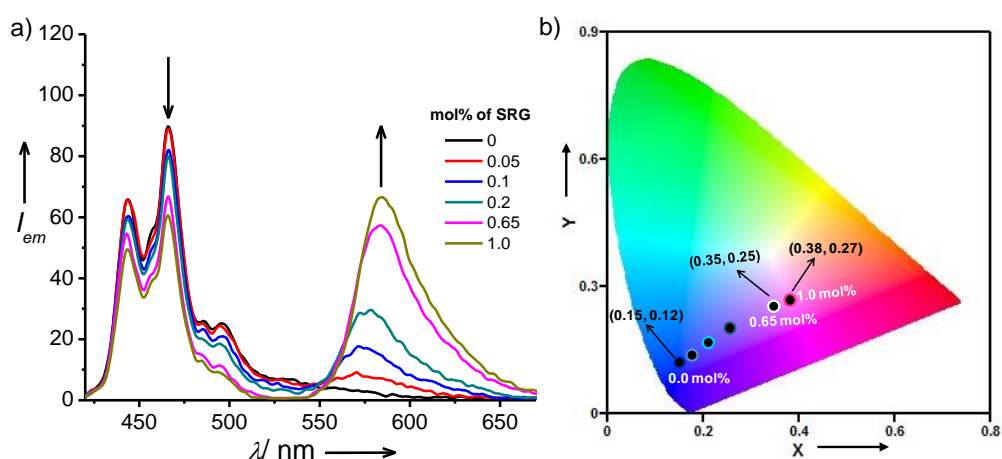


Figure 4.1.15. a) Emission spectra of mixed **CS-AC** hydrogels with different mol% of **SRG** ($\lambda_{exc} = 350$ nm, $l = 1$ mm) and spectra were recorded in front face geometry to avoid the contribution from self-absorption) and b) the corresponding 1931 CIE coordinate diagram.

In the absence of **AC**, no energy-transfer from **CS** to **SRG** (**CS** = 0.1 mM, **SRG** = 0.001 mM) occurred, when excited at 350 nm (Figure 4.1.14b). The weak emission at 550 nm might be due to direct excitation of **SRG** chromophores at 350 nm. Significant energy transfer from **CS** to **SRG** was observed in presence of 0.1 wt% of **AC** as evidenced from the decrease in **CS** emission with concomitant enhancement in **SRG** emission at 570 nm (Figure 4.1.14b). In the corresponding gel state, decrease in **CS** emission with increasing amounts of **SRG**, suggests the energy transfer between this particular donor-acceptor couple (Figure 4.1.15a). Incorporation of 0.65 mol% of **SRG** (with respect to **CS**) to **CS-AC** hydrogels result in pink-white gels with a CIE co-ordinates of (0.35, 0.25) (Figure 4.1.15b, 4.1.16a-c). Further, co-assembly of 1 mol% of **SRG** results in 32% quenching of the **CS** emission to yield purplish-yellow gels with a CIE coordinates of (0.38, 0.27). This clearly suggests that emission color of these hybrids can be easily tuned by doping the required amounts of acceptor molecules, by a remarkably simple co-assembly process. Furthermore, the weak spectral overlap of donor and acceptor components is advantageous here as it allows partial energy transfer through controlled funnelling of donor excitation energy towards acceptor (Figure 4.1.14). This results in the persistence of significant blue emission even in the co-assembled donor-acceptor hybrids, which is a prerequisite for achieving white light emission (Figure 4.1.15).

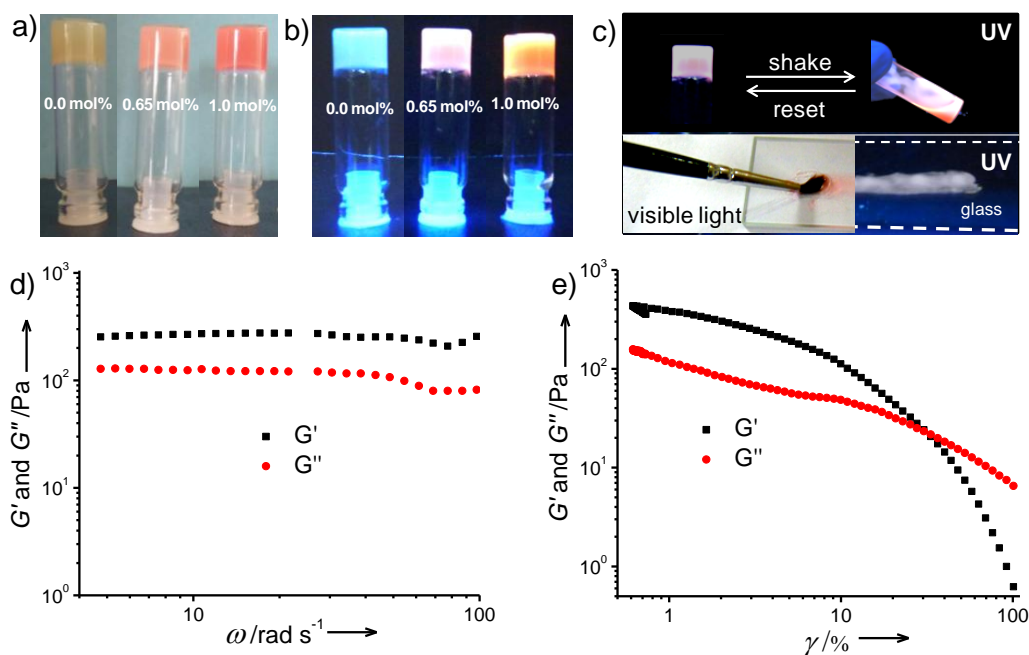


Figure 4.1.16. Photograph of **CS-AC** hybrid hydrogels having different mol% of **SRG** under a) visible and b) 365 nm UV-light. c) Photographs showing the thixotropic and processable nature of mixed **CS-SRG-AC** hybrid hydrogel loaded with 0.65 mol% of **SRG**, viewed under 365 nm UV light. The soft-nature of the hybrid gels allows its painting onto a glass substrate, using a brush, as shown under visible (left) and UV-light (right) in the bottom panel of Figure 4.1.16c. Storage (G') and loss (G'') modulus of the **CS-AC** hybrid gel measured as functions of d) angular frequency (ω) at a constant strain of 1 % and e) strain (γ) % at a constant frequency of 10 Hz.

Rheological measurements on these hydrogels showed a significant elastic response (Figure 4.1.16d and e). The display of storage modulus values well above the loss modulus over the measured angular frequency range ($\omega = 3$ to 100 rad s^{-1}), confirms the gel-like character of these hybrids. However, the low values of G' (270 Pa) and $\tan \delta$ (G''/G' , 0.45), indicate the poor mechanical properties for these gels. This is further evident from the collapse of these gels even at low strain values of $\gamma = 9.0\%$, as indicated by the decrease of G' values and crossing of the G' and G'' curves. The thixotropic and soft-character of these hybrid gels are indeed advantageous, as they can be easily transferred to solid substrates by spin/drop casting processes, thereby rendering these hybrids an unprecedented processability feature (Figure 4.1.16c, *vide infra*).

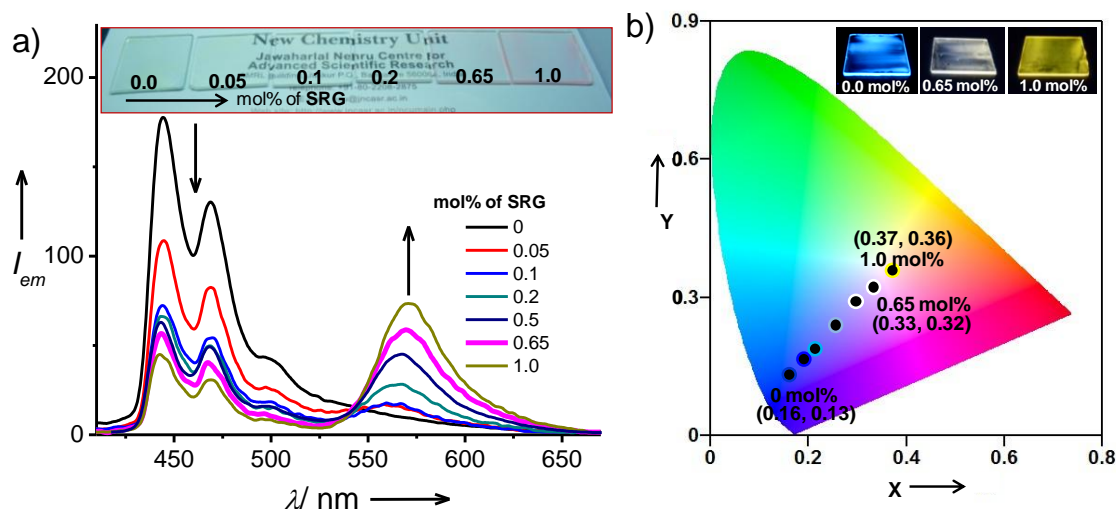


Figure 4.1.17. a) Emission spectra of mixed **CS-SRG-AC** hybrid films obtained by drop-casting corresponding hydrogels on glass substrates ($\lambda_{exc} = 350 \text{ nm}$ and spectra were recorded in front face geometry to avoid the contribution from self-absorption at higher concentrations). Photographs of the hybrid-coated films are shown in the inset, which clearly demonstrates its transparent nature. b) 1931 CIE coordinate diagram of the hybrid-coated films. Inset shows the photographs of the films (for 0 %, 0.65 mol% and 1 mol% loading of the **SRG** with respect to the donor **CS**) upon 365 nm UV irradiation.

Since substrate transferability of luminescent active materials is rudimentary for device fabrication, we have prepared thin films of mixed (**CS-SRG-AC**) hybrids. In order to prepare the hybrid thin films, the corresponding gels with appropriate donor-acceptor ratio were sonicated and the resulting viscous solutions were drop-casted onto glass substrates (Inset, Figure 4.1.17a). While the concentration of the **CS** donor is maintained at 7.5 mM (0.47 wt%) in these hybrids, the amount of the acceptor **SRG** was changed from 0.05 to 1 mol% with respect to the donor. Remarkably, all these hybrid films are highly transparent (inset, Figure 4.1.17a), which is crucial to avoid the loss of incident light via scattering, and thereby to increase the luminescence efficiency. The entire hybrid films pose high light transmittance of *ca.* 90-95 % at 750 nm where both the donor and acceptor do not absorb. Figure 4.1.17a shows the fluorescence spectra of mixed **CS-SRG-AC** hybrid films upon excitation at 350 nm. The

CS-AC hybrid film without having **SRG** acceptor retains the pure blue emission as that of the corresponding gel with CIE co-ordinates of (0.16, 0.13) (Figure 4.1.17b). This suggests that, inorganic clay still holds the molecular organization of organic components in the hybrid assemblies by not allowing them to aggregate even during the casting process. The mixed hybrid films showed a gradual decrease in the donor (**CS**) emission between 430-500 nm and a concomitant increase in the acceptor (**SRG**) emission at 570 nm, with the increase in the acceptor loading (0.05-1 mol%). Since the acceptor has very less absorption at the excitation wavelength of 350 nm, the appearance of **SRG** emission in the mixed hybrids is clearly due to the energy transfer process (*vide infra*). The blue light emission of the mixed hybrids was significantly quenched (77%) even with 1 mol% loading of the **SRG**, as evident from the corresponding yellow fluorescent film with a CIE co-ordinates of (0.37, 0.36). Remarkably, with 0.65 mol% loading of the acceptor (70% quenching of **CS** emission), these hybrid films showed highly pure white light emission as evident from the CIE co-ordinates of (0.33, 0.32) which are very close to the ideal white light (0.33, 0.33) coordinates (Figure 4.1.17b). Similarly pseudo-white light films with (0.29, 0.29) CIE coordinates were obtained upon 0.5 mol% loading of **SRG** (66 % quenching of **CS** emission).

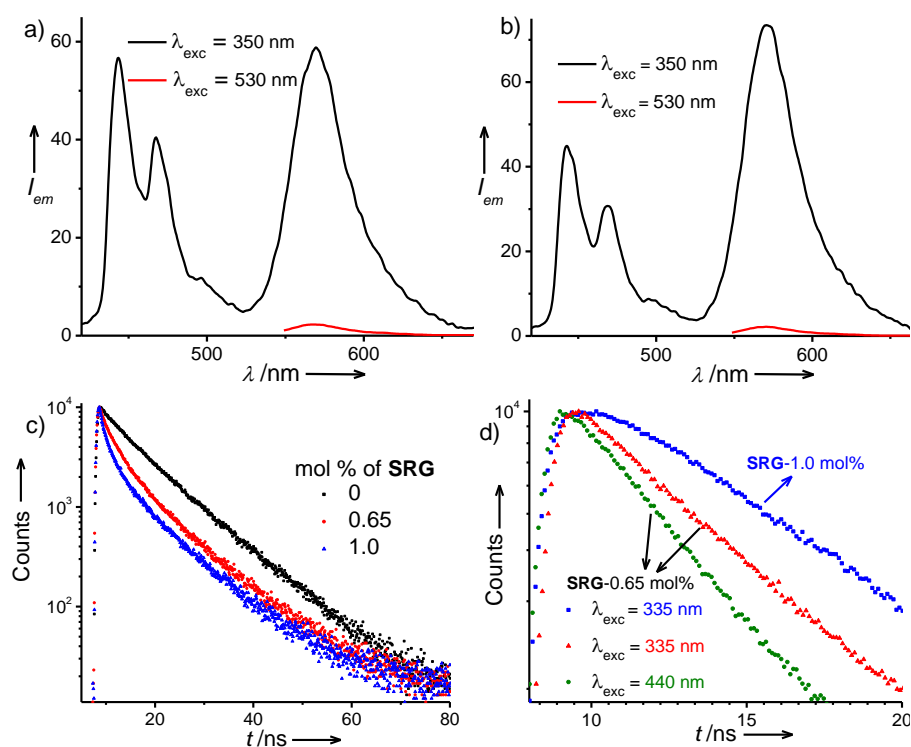


Figure 4.1.18. Emission spectra of **CS-AC** hybrid films loaded with a) 0.65 mol% and b) 1 mol% of **SRG** acceptor obtained by the selective excitation of the donor (**CS**) and acceptor (**SRG**) at 350 nm and 530 nm, respectively. c) Lifetime-decay profiles ($\lambda_{exc} = 335$ nm, $\lambda_{monitored} = 440$ nm) of **CS-AC** hybrid films having different mol% of **SRG**. d) Lifetime decay profiles of **CS-AC** hybrid films loaded with different mol% of **SRG** obtained when monitored at the acceptor emission ($\lambda_{monitored} = 570$ nm) upon direct ($\lambda_{exc} = 440$ nm) and indirect ($\lambda_{exc} = 335$ nm) excitation.

The energy transfer in the hybrid films has been investigated further in detail with steady-state and time resolved emission measurements (Figure 4.1.18). An antenna effect (amplified emission) by energy transfer in the mixed hybrids is evident by the much higher acceptor emission by excitation of the donor (indirect excitation) relative to the direct excitation of the acceptor, **SRG** molecules. For example, in case of white light emitting film with 0.65 mol% of the acceptor, excitation at 350 nm results in 25 times higher **SRG** emission due to energy transfer, compared to its direct excitation at 530 nm (Figure 4.1.18a). The amplified emission in yellow emissive films with 1.0 mol% of **SRG** is 40 times higher, which is a definitive proof of a Förster type energy transfer mechanism (Figure 4.1.18b). Fluorescence lifetime decay profiles of the **CS-AC** hybrid films monitored at the **CS** emission ($\lambda_{\text{exc}} = 335$ nm, $\lambda_{\text{em}} = 440$ nm), showed shortening of the lifetime with increasing loading of **SRG**, clearly indicating the energy transfer (Figure 4.1.18c). The lifetime profiles were fitted to bi or triexponential decay and the weighted average lifetime values were used for further analysis. **CS** showed an average lifetime of 10.87 ns in **CS-AC** hybrids with a bi-exponential decay having lifetimes of 4.82 ns (15.49%) and 11.96 ns (84.51 %). After the addition of 1 mol% **SRG**, the average lifetime of **CS** in the hybrids was reduced to 7.93 ns with a tri-exponential decay and the observed lifetime values are 3.64 ns (29.39%), 11.62 ns (57.94%) and 1.05 ns (12.66%). The appearance of additional short lifetime components in **CS** emission in presence of **SRG** suggests the excited state fluorescence quenching of the former by later. Probing the corresponding acceptor decay profile ($\lambda_{\text{em}} = 570$ nm), while exciting the donor, showed an increase in its lifetime (6.34 ns) compared to the acceptor's characteristic lifetime (4.44 ns) in the clay scaffold, which is obtained by the direct excitation of **SRG** in the mixed hybrid (**CS-SRG-AC**, (Figure 4.1.18d). The decay profile of the acceptor in mixed hybrids is also marked by the rising component at shorter time scales (<1 ns), indicating the growth of the acceptor excited states via energy transfer. These changes in decay profiles are characteristic of an efficient FRET process and any trivial mechanism for energy transfer can thus be ruled out.

Excellent solution processability, high transmittance, color tunability, simple synthetic protocols for bulk quantities and environmentally benign solvent medium of these chromophoric-clay assemblies renders a unique class of 'soft-hybrids', which can be exploited for large area device fabrication. Moreover, the low mechanical stability and thixotropic nature of these hybrid gels, further facilitates the spin-coating or drop casting on various substrates, as typically used for various polymers and organic assemblies. This is demonstrated in Figure 4.1.19 where the gels are painted on glass and flexible substrates. The white light emitting gels could also be used to write or paint directly on any substrate. In order to display it, a commercial 365 nm UV-lamp having a surface area of 125 cm² was coated completely with the soft-hybrids (Figure 4.1.19a-c). No significant differences were observed under visible light for

both coated and uncoated lamps reiterating the high transmittance of the hybrid layer. However, when the lamps were connected to the electrical power, the hybrid coated lamp glowed with bright white color whereas, the uncoated lamp was showing only dull blue emission (Figure 4.1.19d). Similarly, letters written on the lamp with the soft-hybrid are readily readable under UV-lamp, as they emit the white light upon excitation (Figure 4.1.19d). These hybrid materials could also be painted on a transparent, flexible plastic sheet ($5 \times 15 \text{ cm}^2$) as shown in Figure 4.1.19e-g, which emits bright white fluorescence upon illumination with 365 nm radiation. Interestingly, flexing and rolling of these sheets did not show any changes in the white light emission.

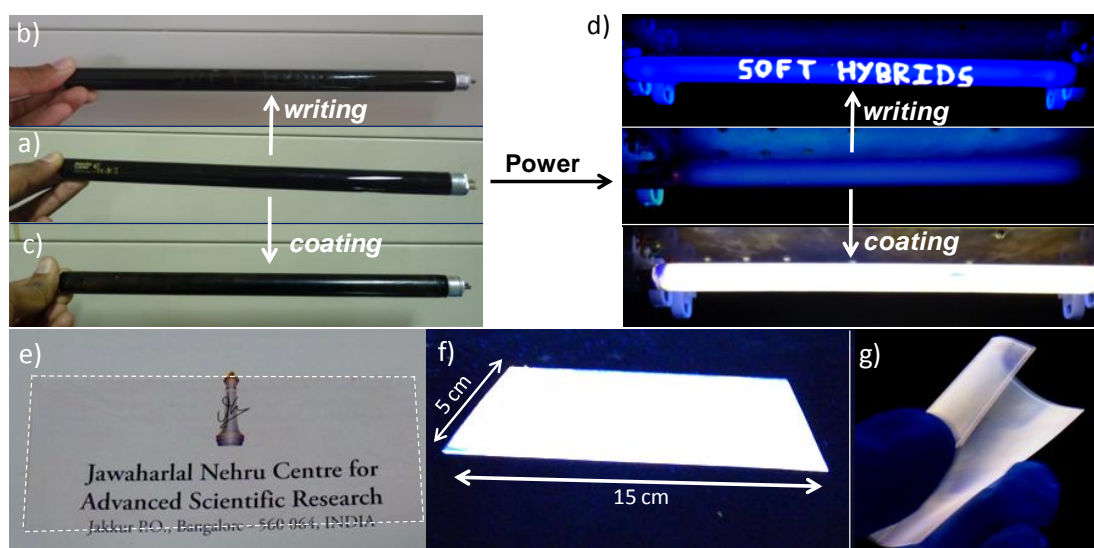


Figure 4.1.19. Demonstrations of the solution processability of white light emitting, CS-AC hybrids containing 0.65 mol% of the acceptor SRG molecule. The soft-hybrid hydrogels were used to paint or write on various substrates: a-c) hybrids were used to paint and write on commercial UV-lamps (365 nm, surface area = 125 cm^2); a) uncoated lamp, b) written as 'SOFT HYBRIDS' on the surface of the lamp and c) fully coated lamp with the soft-hybrids. The hybrid coating is difficult to visualize under the normal light (4.1.19b and c), as they are transparent. d) Hybrid-coated lamps are exposed to the UV irradiation by glowing the lamps, which showed bright white light for both written letters and the fully-coated lamp. e) A flexible transparent sheet ($5 \times 15 \text{ cm}^2$) after painting with the hybrids, which retains its transparency even after coating (dotted line indicates the boundary of the sheet); f) and g) the hybrid coated transparent sheet shows white light emission when exposed to the UV-light. All the images were taken after drying the coated substrates in air for 6 hours.

4.1.7 Dynamics in solution

We have further investigated the dynamic nature of dye molecules in these hybrids. If the ionic interactions between anionic dyes and cationic AC are dynamic, dye molecules should undergo dynamic exchange between the AC sheets. To get insights into this dynamic behaviour, we have made CS-OPVS-AC hybrid solutions in three different ways and the changes were followed using energy transfer from CS to OPVS as a probe (Figure 4.1.20). In the first method, 10 mol% of OPVS containing CS solution was added to exfoliated AC sheets

in water (i in Figure 4.1.20). In this case both **CS** and **OPVS** interact with **AC** and showed efficient FRET from **CS** to **OPVS** when excited at 320 nm. In the second method, 10 mol% of **OPVS** in water was added to preformed **CS-AC** hybrid in water (ii in Figure 4.1.20). In this case when **CS** was excited at 320 nm, the obtained emission is almost overlapped with emission spectrum in the first method. This clearly indicates that the newly added **OPVS** molecules are able to immediately bind to **AC** and both **CS** and **OPVS** organize themselves on **AC** sheets in such a way that energy transfer is feasible from **CS** to **OPVS**. This clearly suggests that **CS** molecules bound on clay surface are dynamic enough to reorganise and facilitate energy transfer to **OPVS**. In the third method, we have mixed 10 mol% of preformed **OPVS-AC** hybrid with **CS-AC** hybrid (iii in Figure 4.1.20). Again, efficient energy transfer was observed from **CS** to **OPVS**, with almost same efficiency as that of two cases. This would be possible only when **CS** and **OPVS** are able to exchange or migrate among the **AC** sheets, reiterating the dynamic nature of dyes. The observed energy transfer from **CS** to **OPVS** in all these samples unambiguously proves the dynamic binding and inter sheet migration of **CS** and **OPVS** in solution.

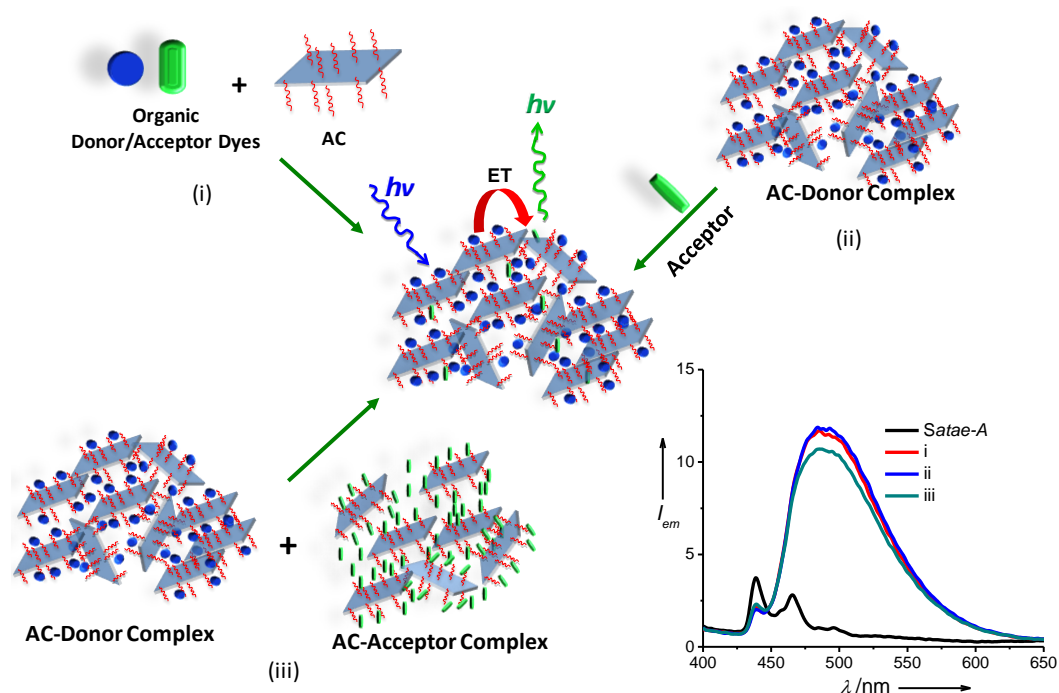


Figure 4.1.20. Schematic representation of **AC**, donor (**CS**) and acceptor (**OPVS**) hybrids made in three different ways and their corresponding emission spectra in water (**CS** = 0.1 mM, **AC** = 0.1 wt%, **OPVS** = 0.01 mM, $l = 1$ mm, $\lambda_{exc} = 350$ nm) in comparison with **CS-AC** emission in State-A.

4.1.8 Conclusions

In conclusion, we have showed that the non-covalently assembled **AC**-dye hybrids are versatile solution processable dynamic scaffolds for light-harvesting and energy transfer.

Control over molecular organizations of dye molecules was achieved by varying the dye-AC composition. Light-harvesting and energy transfer efficiencies are fine tuned by controlling the concentration and dye-AC ratio. Furthermore, we show that the gel state luminescence could be preserved in the film state as well, with enhanced energy transfer efficiency. We have also demonstrated a novel supramolecular strategy for the design of solution processable white luminescent hybrids with good colour purity. The unique solution processability of these organic-inorganic hybrids has been displayed by painting and writing on large glass and flexible plastic surfaces. These demonstrations unambiguously proves the simplicity and potential of these so-called ‘soft-hybrids’ as water processable, high transmittance materials for environmental friendly large area display fabrication. We have also provided insights into the dynamic nature of the AC-dye hybrids in solution using energy transfer as a probe. This indicates the dye molecules are dynamic enough to migrate within and between sheets. The combination of the dynamic nature of the non-covalent hybrid networks with the possibility to incorporate a variety of molecules that can trigger the fluorescence changes in the hydrogels holds great promise for applications as stimuli-responsive supramolecular systems, sensors and hybrid optoelectronics. However, the stability of these materials on devices is yet to be investigated.

4.1.9 Experimental Section

General methods: Transmission Electron Microscopy (TEM) measurements were performed on a JEOL, JEM 3010 operated at 300 kV. Samples were prepared by placing a drop of the solution on carbon coated copper grids followed by drying at room temperature. The images were recorded with an operating voltage of 300 kV. Electronic absorption spectra were recorded on a Perkin Elmer Lambda 900 UV-Vis-NIR Spectrometer and emission spectra were recorded on Perkin Elmer Ls 55 Luminescence Spectrometer. UV-Vis and emission spectra were recorded in 1 mm path length cuvette. Fluorescence spectra of solutions were recorded in front-face geometry. Dynamic Light Scattering experiments (DLS) measurements were carried out using a NanoZS (Malvern UK) employing a 532 nm laser at a back scattering angle of 173°. Fluorescence lifetimes were measured using IBH (FluoroCube) time-correlated picosecond single photon counting (TCSPC) system. Solutions were excited with a pulsed diode laser (<100 ps pulse duration) at a wavelength of 335 and 440 nm (NanoLED-11) with a repetition rate of 1 MHz. The detection system consists of a microchannel plate photomultiplier (5000U-09B, Hamamatsu) with a 38.6 ps response time coupled to a monochromator (5000M) and TCSPC electronics (Data Station Hub including Hub-NL, NanoLED controller and preinstalled Fluorescence Measurement and Analysis Studio (FMAS) software). The fluorescence lifetime values were determined by deconvoluting the instrument response function with biexponential decay using DAS6 decay analysis software. The quality of the fit

has been judged by the fitting parameters such as χ^2 (< 1.2) as well as the visual inspection of the residuals. Rheological measurements were performed at 25 °C on Anton Paar MCR 150, stress controlled rheometer having a cone and plate geometry with a plate gap of 100 μm .

4.1.9a Synthesis

Compounds **CS**,¹⁸ **PS**,¹⁹ **OPVS**²⁰ and **AC**¹⁰ were synthesized according to the literature methods. **SRG** was purchased from Aldrich.

4.1.10 References

1. T. Nguyen, J. Wu, V. Doan, B. J. Schwartz, S. H. Tolbert, *Science* **2000**, 288, 652.
2. a) F. J. M. Hoeben, P. Jonkheijm, E. W. Meijer, A. P. H. J. Schenning, *Chem. Rev.* **2005**, 105, 1491; *Dendrimers for energy transfer, see:* b) C. Devadoss, P. Bharathi, J. S. Moore, *J. Am. Chem. Soc.* **1996**, 118, 9635; c) D.-L. Jiang, T. Aida, *Nature* **1997**, 388, 454; d) A. P. H. J. Schenning, E. Peeters, E. W. Meijer, *J. Am. Chem. Soc.* **2000**, 122, 4489; e) Y. Zeng, Y.-Y. Li, J. Chen, G. Yang, Y. Li, *Chem. Asian J.* **2010**, 5, 992; *H-bonded scaffolds for energy transfer, see:* f) M. D. Ward, *Chem. Soc. Rev.* **1997**, 26, 365; g) F. J. M. Hoeben, L. M. Herz, C. Daniel, P. Jonkheijm, A. P. H. J. Schenning, C. Silva, S. C. J. Meskers, D. Beljonne, R. T. Phillips, R. H. Friend, E. W. Meijer, *Angew. Chem. Int. Ed.* **2004**, 43, 1976; *Organogels for energy transfer, see:* h) A. Ajayaghosh, S. J. George, V. K. Praveen, *Angew. Chem. Int. Ed.* **2003**, 42, 332; i) K. Sugiyasu, N. Fujita, S. Shinkai, *Angew. Chem. Int. Ed.* **2004**, 43, 1229; j) A. D. Guerzo, A. G. L. Olive, J. Reichwagen, H. Hopf, J.-P. Desvergne, *J. Am. Chem. Soc.* **2005**, 127, 17984; k) A. Ajayaghosh, V. K. Praveen, C. Vijayakumar, S. J. George, *Angew. Chem. Int. Ed.* **2007**, 46, 6260; l) A. Ajayaghosh, C. Vijayakumar, V. K. Praveen, S. S. Babu, R. Varghese, *J. Am. Chem. Soc.* **2006**, 128, 7174; m) A. Ajayaghosh, V. K. Praveen, S. Srinivasan, R. Varghese, *Adv. Mater.* **2007**, 19, 411; n) A. Ajayaghosh, V. K. Praveen, C. Vijayakumar, *Chem. Soc. Rev.* **2008**, 37, 109; *Self-assembled monolayer for energy transfer, see:* o) L. A. J. Christoffels, A. Adronov, J. M. J. Fréchet, *Angew. Chem. Int. Ed.* **2000**, 39, 2163; *Vesicles for energy-transfer see:* p) F. J. M. Hoeben, I. O. Shklyarevskiy, M. J. Pouderoijen, H. Engelkamp, A. P. H. J. Schenning, P. C. M. Christianen, J. C. Maan, E. W. Meijer, *Angew. Chem. Int. Ed.* **2006**, 45, 1232.
3. a) X. Zhang, S. Rehm, M. M. Safont-Sempere, F. Würthner, *Nat. Chem.* **2009**, 1, 623; b) M. R. Molla, S. Ghosh, *Chem. Eur. J.* **2012**, 18, 1290; c) R. Varghese, H.-A. Wagenknecht, *Chem. Eur. J.* **2009**, 15, 9307; d) R. Abbel, R. van der Weegen, W. Pisula, M. Surin, P. Leclère, R. Lazzaroni, E. W. Meijer, A. P. H. J. Schenning, *Chem. Eur. J.* **2009**, 15, 9737; e) C. Vijayakumar, V. K. Praveen, A. Ajayaghosh, *Adv. Mater.* **2009**, 21,

- 2059; f) C. Giansante, G. Raffy, C. Schäfer, H. Rahma, M.-T. Kao, A. G. L. Olive, A. Del Guerso, *J. Am. Chem. Soc.* **2011**, *133*, 316; g) X. Yang, R. Lu, P. Xue, B. Li, D. Xu, T. Xu, Y. Zhao, *Langmuir* **2008**, *24*, 13730; h) C. Giansante, C. Schäfer, G. Raffy, A. Del Guerso, *J. Phys. Chem. B* **2012**, *116*, 21706; i) C. Vijayakumar, K. Sugiyasu, M. Takeuchi, *Chem. Sci.* **2011**, *2*, 291; j) K.-P. Tseng, F.-C. Fang, J.-J. Shyue, K.-T. Wong, G. Raffy, A. D. Guerso, D. M. Bassani, *Angew. Chem. Int. Ed.* **2011**, *50*, 7032; k) R. Abbel, R. van der Weegen, E. W. Meijer, A. P. H. J. Schenning, *Chem. Commun.* **2009**, 1697; l) R. Abbel, C. Grenier, M. J. Pouderoijen, J. W. Stouwdam, P. E. L. G. Leclère, R. P. Sijbesma, E. W. Meijer, A. P. H. J. Schenning, *J. Am. Chem. Soc.* **2009**, *131*, 833; m) D. K. Maiti, A. Banerjee, *Chem. Commun.* **2013** (DOI: 10.1039/C3CC43371D).
4. a) K. V. Rao, K. K. R. Datta, M. Eswaramoorthy, S. J. George, *Chem. Eur. J.* **2012**, *18*, 2184; b) N. Mizoshita, T. Taniab, S. Inagaki, *Chem. Soc. Rev.* **2011**, *40*, 789; c) G. Calzaferri, S. Huber, H. Maas, C. Minkowski, *Angew. Chem. Int. Ed.* **2003**, *42*, 3732; d) Y. Cui, Y. Yue, G. Qian, B. Chen, *Chem. Rev.* **2012**, *112*, 1126.
5. a) G. Calzaferri, K. Lutkouskaya, *Photochem. Photobiol. Sci.* **2008**, *7*, 879; b) D. Brühwiler, G. Calzaferri, T. Torres, J. H. Ramm, N. Gartmann, L.-Q. Dieu, I. López-Duarte, M. V. Martínez-Díaz, *J. Mater. Chem.* **2009**, *19*, 8040; c) G. Calzaferri, Marc Pauchard, H. Maas, S. Huber, A. Khatyr, T. Schaafsma, *J. Mater. Chem.* **2002**, *12*, 1; d) C. Minkowski, R. Pansu, M. Takano, G. Calzaferri, *Adv. Funct. Mater.* **2006**, *16*, 273.
6. a) S. Inagaki, O. Ohtani, Y. Goto, K. Okamoto, M. Ikai, K. Yamanaka, T. Tani, T. Okada, *Angew. Chem. Int. Ed.* **2009**, *48*, 4042; b) Y. Maegawa, N. Mizoshita, T. Taniab, S. Inagaki, *J. Mater. Chem.* **2010**, *20*, 4399; c) N. Mizoshita, Y. Goto, T. Tani, S. Inagaki, *Adv. Mater.* **2009**, *21*, 4798; d) N. Mizoshita, Y. Goto, Y. Maegawa, T. Tani, S. Inagaki, *Chem. Mater.* **2010**, *22*, 2548.
7. a) C. Y. Lee, O. K. Farha, B. J. Hong, A. A. Sarjeant, S. T. Nguyen, J. T. Hupp, *J. Am. Chem. Soc.* **2011**, *133*, 15858; b) H.-J. Son, S. Jin, S. Patwardhan, S. J. Wezenberg, N. C. Jeong, M. So, C. E. Wilmer, A. A. Sarjeant, G. C. Schatz, R. Q. Snurr, O. K. Farha, G. P. Wiederrecht, J. T. Hupp, *J. Am. Chem. Soc.* **2013**, *135*, 862; c) S. Jin, H.-J. Son, O. K. Farha, G. P. Wiederrecht, J. T. Hupp, *J. Am. Chem. Soc.* **2013**, *135*, 955.
8. a) S. Takagi, D. A. Tryk, H. Inoue, *J. Phys. Chem. B* **2002**, *106*, 5455; b) C. V. Kumar, A. Chaudhari, *J. Am. Chem. Soc.* **1994**, *116*, 403; c) Y. Ishida, T. Shimada, D. Masui, H. Tachibana, H. Inoue, S. Takagi, *J. Am. Chem. Soc.* **2011**, *133*, 14280.
9. a) X. Zhang, Z.-K. Chen, K. P. Loh, *J. Am. Chem. Soc.* **2009**, *131*, 7210; b) X. Zhang, M. A. Ballem, M. Ahrén, A. Suska, P. Bergman, K. Uvdal, *J. Am. Chem. Soc.* **2010**, *132*, 10391; c) X. Zhang, M. A. Ballem, Z.-J. Hu, P. Bergman, K. Uvdal, *Angew. Chem. Int. Ed.* **2011**, *50*, 5729;

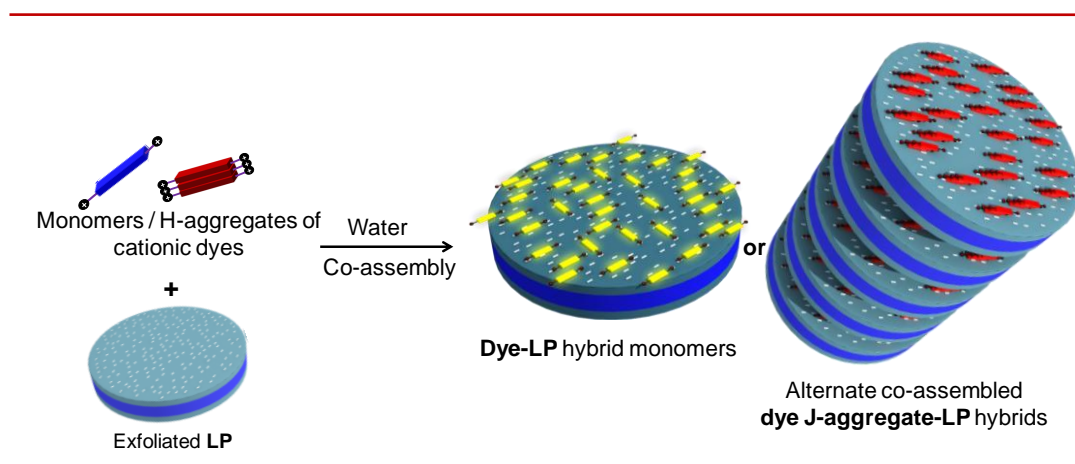
-
10. a) Q. Wang, D. O'Hare, *Chem. Rev.*, **2012**, *112*, 4124; b) D. Yan , J. Lu , M. Wei , S. Qin , L. Chen , S.Zhang, D. G. Evans , X. Duan, *Adv. Funct. Mater.* **2011**, *21*, 2497; c) J. H. Lee, J.Chang, J.-H. Cha, D.-Y. Jung, S. S. Kim, J. M. Kim, *Chem. Eur. J.* **2010**, *16*, 8296.
 11. S. L. Burkett, A. Press, S. Mann, *Chem. Mater.* **1997**, *9*, 1071.
 12. a) E. Muthusamy, D. Walsh, S. Mann, *Adv. Mater.* **2002**, *14*, 969; b) N. T. Whilton, S. L. Burkett, S. Mann, *J. Mater. Chem.* **1998**, *8*, 1927; c) A. J. Patil, E. Muthusamy, S. Mann, *Angew. Chem. Int. Ed.* **2004**, *43*, 4928; d) A. J. Patil, M. Li, E. Dujardin, S. Mann, *Nano Lett.* **2007**, *7*, 2660; e) J. E. Martin, A. J. Patil , M. F. Butler, S. Mann, *Adv. Funct. Mater.* **2011**, *21*, 674.
 13. a) K. Haraguchi, T. Takehisa, *Adv. Mater.* **2002**, *14*, 1120; b) O. Okay, W. Oppermann, *Macromolecules* **2007**, *40*, 3378; c) B. H. Cipriano, T. Kashiwagi, X. Zhang, S. R. Raghavan, *ACS Appl. Mater. Interfaces* **2009**, *1*, 130.
 14. Q. Wang, J. L. Mynar, M. Yoshida, E. Lee, M. Lee, K. Okuro, K. Kinbara, T. Aida, *Nature* **2010**, *463*, 339.
 15. S.-J. Yoon , J. H. Kim , K. S. Kim , J. W. Chung , B. Heinrich , F. Mathevet, P. Kim, B. Donnio , A.-J. Attias, D. Kim , S. Y. Park, *Adv. Funct. Mater.* **2012**, *22*, 61.
 16. a) R. Zhang, D. Tang, P. Lu, X. Yang, D. Liao, Y. Zhang, M. Zhang, C. Yu, V. W. W. Yam, *Org. Lett.* **2009**, *11*, 4302; b) M. Kumar, S. J. George, *Nanoscale* **2011**, *3*, 2130.
 17. Z. Chen, A. Lohr, C. R. Saha-Möller, F. Würthner, *Chem. Soc. Rev.* **2009**, *38*, 564.
 18. a) S. A-Fouet, I. Seguy, J.-F. Bobo, P. Destruel, H. Bock, *Chem. Eur. J.* **2007**, *13*, 1746; b) A. Ghosh, K. V. Rao, S. J. George, C. N. R. Rao, *Chem. Eur. J.* **2010**, *16*, 2700.
 19. W. Wang, Y. Bando, C. Zhi, W. Fu, E. Wang, D. Golberg, *J. Am. Chem. Soc.* **2008**, *130*, 8144.
 20. K. V. Rao, S. J. George, *Chem. Eur. J.* **2012**, *18*, 14286.

PART-4 . 2

Controlling the Molecular Organization of π - Systems via Hybrid Co-Assembly: A Non-Covalent Strategy towards Solution Processable Luminescent Hybrids*

Abstract

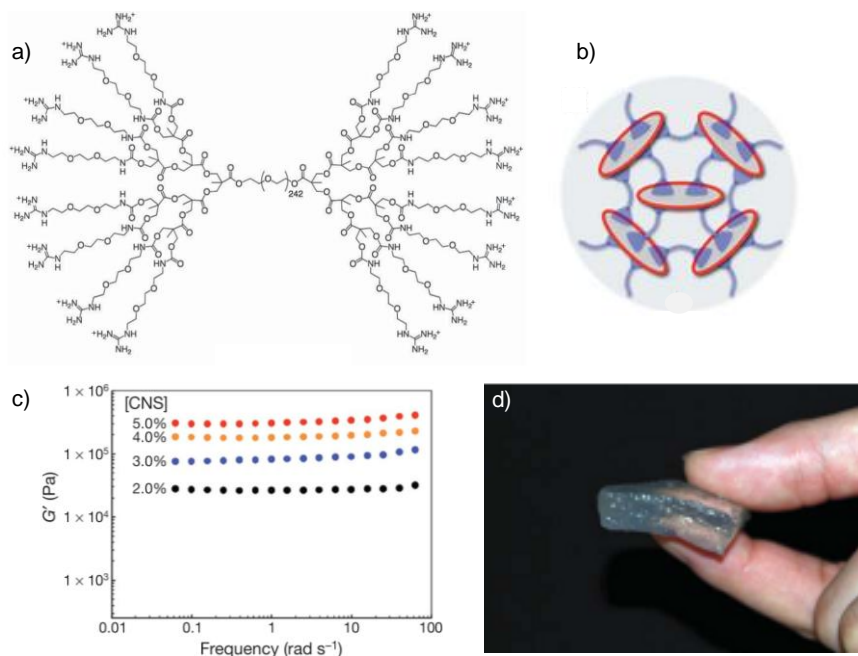
A simple non-covalent strategy to make solution processable luminescent hybrids of three *n*-type cationic organic semiconductors and negatively charged crystalline inorganic laponite (**LP**) nanoparticles via ionic co-assembly is described. This hybrid co-assembly approach further allows controlling the molecular organization of cationic dye molecules. These cationic dyes are weakly/non-fluorescent in water and in solid-state due to the formation of H-aggregates. However, in the hybrid co-assembly, the competitive ionic interactions provided by **LP** particles break the individual dye aggregation and form co-assembled **dye-LP** hybrids. Depending on the ratio between **LP** and cationic dyes, the dye molecules are either monomerically organized on the **LP** surface with high fluorescence quantum yield or aggregate in J-type fashion to result in fluorescent hybrid hydrogels. The films made from these hydrogels showed an unprecedented extended organization between **dye J-aggregates** and **LP** nanoparticles and resembles like an alternate (...ABAB...) organic-inorganic supramolecular co-polymer. Remarkably, the solution and gel state emission of these hybrids were successfully retained in the solid-state due to fencing of dye molecules by **LP** without giving any room for their individual aggregation.



*Manuscripts based on this chapter are under preparation

4.2.1 Introduction

Controlling the molecular organization of semiconducting π -conjugated systems is of paramount importance in the design of multifunctional organic and hybrid materials.^{1,2} In the view of environmental safety, it is important to introduce new functional materials having the components of nature's choice. Since water and clays are being the nature's preference, it is reasonable to make materials integrated with water and clay.³ In this context, aqua materials (high water content hydrogels) synthesized by Aida et al. through non-covalent cross-linking of clay nanosheets with dendritic molecular binder are the striking examples (Scheme 4.2.1).^{3a} These aqua materials have high mechanical strength and excellent self-healing behaviour, and can be potential replacements to conventional plastics. Similarly, non-covalently assembled clay-chromophore hybrids would also be potential candidates for environmental friendly optoelectronic functions (see Part-4.1). These materials would combine the advantages of both organic and inorganic materials with promising applications in LEDs, sensors, paints and flexible electronics.⁴ Although, several organic-inorganic hybrid systems such as periodic mesoporous silica (PMO),⁵ zeolites,⁶ layered double hydroxides⁷ and metal-organic frameworks (MOFs)⁸ hosting various π -conjugated molecules either covalently or non-covalently are explored for various optoelectronic applications, lack of solution processability and excitonic coupling between the chromophores in these hybrid systems can negate their large scale device fabrication. In this context, further softening of chromophore derived organic-inorganic hybrid systems is indispensable for the ease of processing.



Scheme 4.2.1. a) Molecular structure of dendritic molecular binder. b) Schematic representation of cross-linking between clay and dendritic binder in the hydrogel. c) Storage modulus (G') values of hydrogels with different weight ratios of clay nano sheets (CNS). d) Photograph showing the freestanding nature of aqua material (hydrogel) [reproduced from ref. 3a].

Molecular aggregates of n-type organic semiconductors are shown to have significant importance in organic electronics.⁹ On the other hand, clay minerals are important class of materials with diverse industrial and bio-medical applications owing to their structural elegance and nanoscale periodicity.¹⁰ We presumed that, integration of optoelectronic functionality of dye aggregates with nanoscopic inorganic clays would result in novel class of clay-dye hybrid materials with diverse functionalities. J-type aggregation of artificial π -systems is of prime importance than H-type aggregation owing to their ability to have high excitonic mobility and efficient light-harvesting as observed in natural photosynthetic pigments.⁹ Recently Mann et al. achieved enhanced photocatalytic activity by integrating titania into the pre-synthesized porphyrin J-aggregates.¹¹ Many reports have demonstrated improvement in function and property of molecular J-aggregates upon conjugation with inorganic components.¹² However, in all these systems either the inorganic part is incorporated into the pre-synthesized J-aggregates or J-aggregates are grown on an inorganic template, which may not be efficient as they can lead to phase segregation. In this regard, an efficient approach to create organic-inorganic hybrid assemblies is highly desirable to exploit their functional properties. We envisage that, this can be achieved by creating an efficient molecular level co-assembly between organic dyes and inorganic component.¹³ However, use of soluble inorganic part is crucial for this purpose to promote efficient co-assembly with the organic dyes.¹⁴ Since laponite (**LP**) particles are soluble in water and known to interact with dye molecules via ionic interactions, we envisaged that co-assembly of ionic π -systems with **LP** nanoparticles would be advantageous for fine tuning their supramolecular organization without scarifying the solution processability.¹⁵ The resultant clay-dye hybrids would be the potential candidates as environmental friendly optoelectronic materials.

In this section, we describe a simple non-covalent strategy to make solution processable luminescent hybrids through controlled molecular organization of cationic naphthalene, perylene and coronene diimides via ionic co-assembly with laponite (**LP**) nanoparticles in water (Figure 4.2.1). The molecular organization of chromophores was precisely controlled as fluorescent hybrid **dye-LP** monomers or alternate **dye J-aggregate-LP** hybrids, depending on the ratio between **LP** particles and chromophores, by preventing the individual dye aggregation thorough competitive ionic interactions (Figure 4.2.1b and c). In **dye-LP** monomers, the dye molecules are monomerically organized on the **LP** surface and exhibit high fluorescence quantum yield of the dye monomer (Figure 4.2.1b). On the other hand, at high concentration, fluorescent hybrid hydrogels with alternately stacked **dye J-aggregates** and **LP** nanoparticles having strong excitonically coupled chromophores are formed (Figure 4.2.1c). These kinds of strongly coupled molecular J-aggregates of aromatic diimides are so far achieved only by elegant supramolecular design strategies.¹⁶ Moreover in

these hybrids, both the solution state monomer and gel state aggregate emissions were further retained even in the film state upon processing due to fencing of dye molecules by **LP** without giving any room for their individual H-aggregation. Detailed analysis of microscopy images and powder XRD along with the optical data provided insights into the hierarchical organization between cationic dyes and **LP** particles in their co-assembled state.

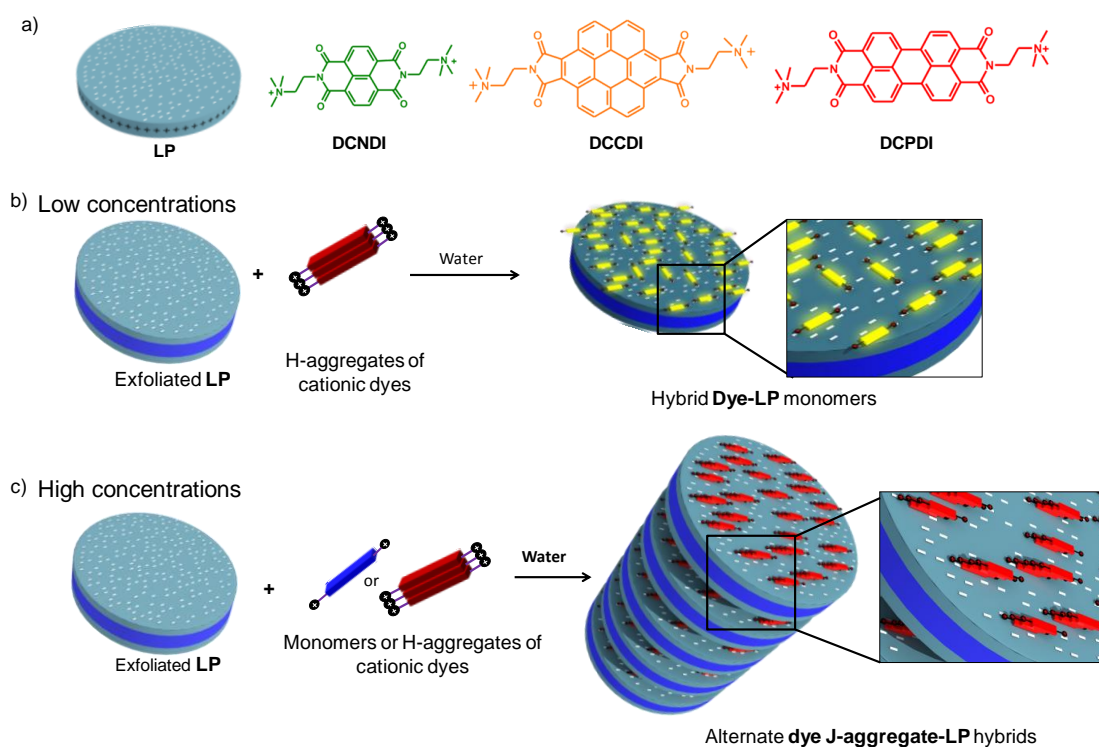


Figure 4.2.1. a) Schematic representation of single **LP** particle and chemical structures of dicationic diimides. Schematic representation for the co-assembly between exfoliated **LP** particles and b) H-aggregates of dyes at low concentrations and c) H-aggregates/monomers of dyes at high concentrations.

4.2.2 Design Strategy and Synthesis

The schematic representation of **LP** nanoparticle and molecular structures of dicationic dyes are shown in Figure 4.2.1. **LP** nanoparticles are of 25 nm in diameter and 0.9 nm thickness with $-ve$ charge on the surface and $+ve$ charge at the edges. These **LP** particles were exfoliated in water by wrapping the positively charged edges with anionic polymer such as sodium polyacrylate (Figure 4.2.1b and c, blue band around the **LP** particle edge) to prevent their “House of Cards” packing in water. These exfoliated particles resemble multivalent anionic macromolecules owing to the presence of dense $-ve$ charges on their surface (Figure 4.2.1b and c). To promote ionic co-assembly with **LP** particles, we have designed and synthesized dicationic naphthalene (**DCNDI**), perylene (**DCPDI**) and coronene (**DCCDI**) diimides (Figure 4.2.1). All cationic dyes were synthesized in two steps from corresponding aromatic dianhydrides (see experimental section) and were fully characterized. **DCNDI** is

molecularly soluble in water whereas **DCCDI** and **DCPDI** are molecularly soluble in acetonitrile, methanol and in ethanol. On the other hand, both **DCCDI** and **DCPDI** form non-fluorescent H-aggregates in water (Figure 4.2.2).

4.2.3 H-Aggregates to Fluorescent Hybrid Dye-LP Monomers

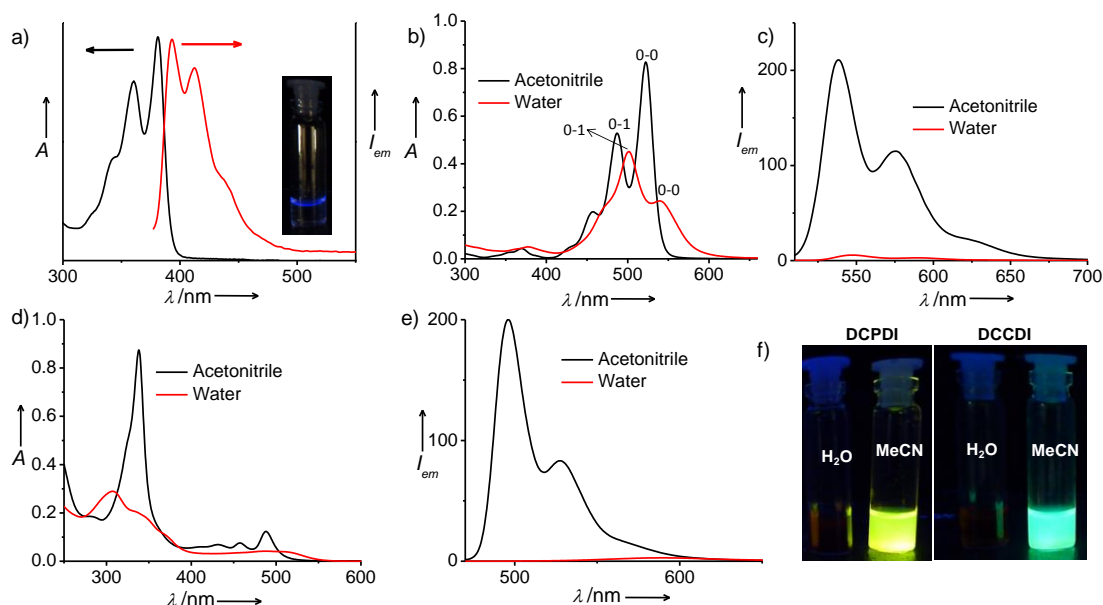


Figure 4.2.2. a) Normalized absorption and emission spectra of **DCNDI** in water ($c = 0.1$ mM, $l = 1$ mm, $\lambda_{exc} = 350$ nm) and inset shows the photograph of corresponding **DCNDI** in water under 365 nm UV light. b) Absorption and c) emission spectra of **DCPDI** in water and in acetonitrile ($c = 0.1$ mM, $l = 1$ mm, $\lambda_{exc} = 500$ nm). d) Absorption and e) emission spectra of **DCCDI** in water and in acetonitrile ($c = 0.1$ mM, $l = 1$ mm, $\lambda_{exc} = 375$ nm). f) Photographs of corresponding **DCPDI** and **DCCDI** solutions in water and acetonitrile under 365 nm UV light.

Since absorption and emission spectra of these π -systems are very sensitive to their intermolecular interactions, optical spectroscopic measurements were carried out to understand the modulations in their molecular organization during co-assembly process with anionic **LP** particles. The blue shifts in the absorption spectra of **DCCDI** and **DCPDI** (0.1 mM) alone in water compared to their monomer (in acetonitrile) absorption spectra, clearly indicate their H-type aggregation in water (Figure 4.2.2b and d). In case of **DCPDI** this can be understood by low intensity of 0-0 peak than that of 0-1 peak due to H-aggregation (Figure 4.2.2b).¹⁷ Further evidence came from the weak fluorescence of these dyes in water compared to acetonitrile (Figure 4.2.2c, e and f).

Interestingly, significant changes in the absorption spectra of H-aggregates of both the diimides upon the addition of different amounts **LP** particles (0-0.25 wt%) clearly indicate their interactions with **LP** particles (Figure 4.2.3). As the amount of **LP** increases, the intensity of 0-0 peak of **DCPDI** increased gradually and dominates the 0-1 peak with concomitant increase of fluorescence quantum yield ($\Phi = 0.01$ to 0.8) (Figure 4.2.3a and b).¹⁸ Similarly, **DCCDI** H-

aggregate absorption spectrum also gradually reached its monomer spectra with the addition of **LP** particles with concomitant increase of fluorescence quantum yield ($\Phi = 0.01$ to 0.7) (Figure 4.2.3d and e). This is a definitive proof for the competitive multivalent ionic interactions offered by the **LP** particle surface which destroys the H-aggregation of these two dye molecules by organizing them monomerically on **LP** surface (inset, Figure 4.2.3b and e). Fluorescence lifetime measurements on these samples provided further insight into this molecular reorganization (Figure 4.2.3c and f). **DCPDI** alone in water showed a single exponential decay of 4.2 ns due to residual free monomers as it forms non-fluorescent H-aggregates. However, in presence of 0.25 wt% **LP** particles, total lifetime was slightly increased to 4.5 ns with biexponential decay due to interaction with **LP** particles. This further supports the existence of **DCPDI** molecules as **LP** bound monomers in presence of 0.25 wt% of **LP**. On the other hand, fluorescence lifetime of **DCCDI** in water is significantly increased from 2.4 ns to 10.9 ns with the addition 0.25 wt% of **LP**. However, this high lifetime is in close agreement with its monomer lifetime (9.24 ns) obtained in acetonitrile and again supports the bound monomeric nature of **DCCDI** in presence of 0.25 wt% of **LP** (Figure 4.2.3f). This phenomenon was not observed for **DCNDI** as it is molecularly soluble in water.

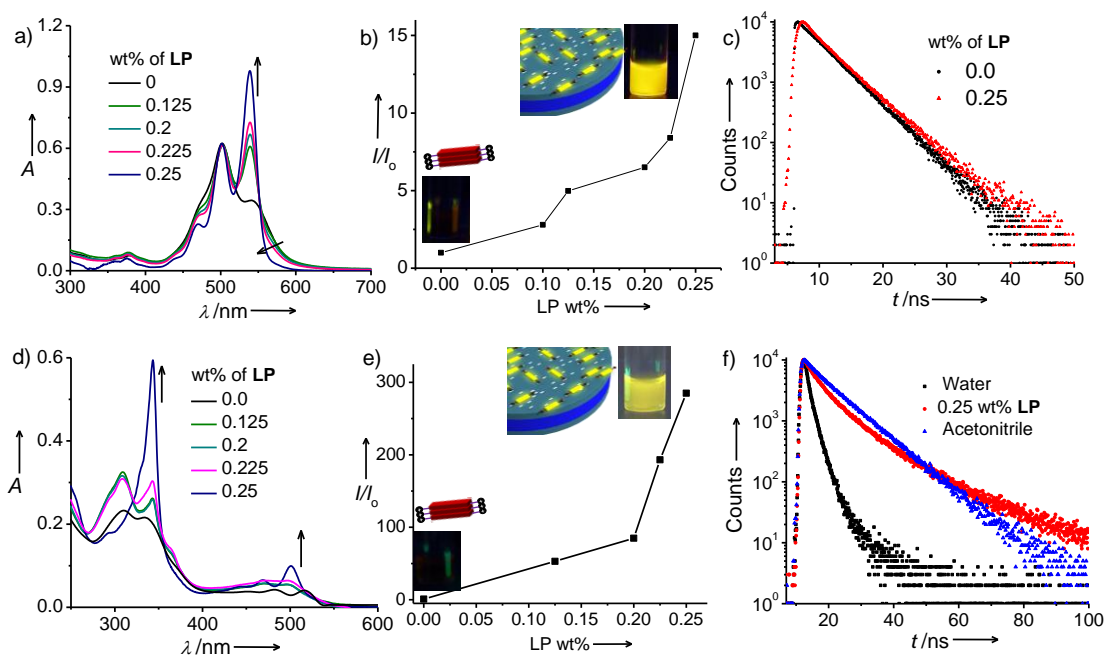


Figure 4.2.3. Spectroscopic probing of the changes in the molecular organization of **DCCDI** and **DCPDI** molecules upon co-assembly with **LP** particles in water. Changes in the a) absorption spectra, b) emission intensity and c) lifetime decay profiles ($\lambda_{exc} = 405$ nm and monitored at 550 nm) of **DCPDI** with different wt% of **LP** particles in water. Changes in the d) absorption spectra and e) emission intensity of **DCCDI** with the addition of different wt% of **LP** particles in water. f) Lifetime decay profiles ($\lambda_{exc} = 405$ nm and monitored at 600 nm) of **DCCDI** in acetonitrile and, with and without **LP** particles in water ($c = 0.1$ mM, $l = 1$ mm, $\lambda_{exc} = 500$ nm (**DCPDI**) and 375 nm (**DCCDI**)). Inset in Figure 4.2.3b and e shows the photographs of corresponding solutions with and without **LP** under 365 nm UV light and schematic representation for the organization of cationic dye molecules in water and on **LP** surface.

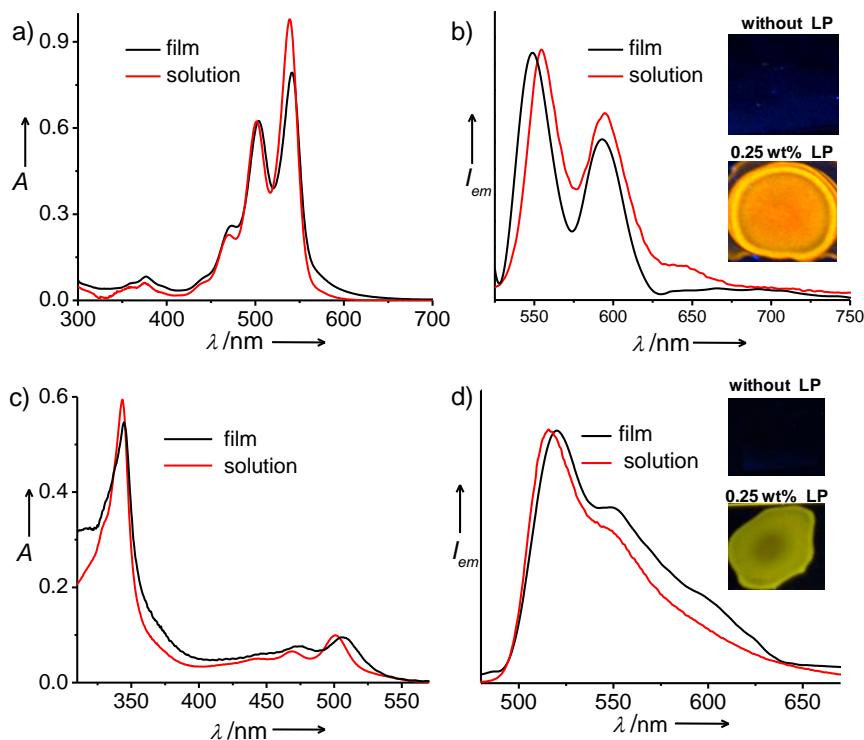


Figure 4.2.4. Normalized a) absorption and b) emission spectra of **DCPDI-LP** hybrids in water and in the film state. Inset of Figure 4.2.4b shows the films of **DCPDI** made from water with and without **LP** under 365 nm UV light. Normalized c) absorption and d) emission spectra of **DCCDI-LP** hybrids in water and in the film state. Inset of Figure 4.2.4d shows the films of **DCCDI** made from water with and without **LP** under 365 nm UV light ($c = 0.1$ mM, **LP** = 0.25 wt%, $\lambda_{exc} = 500$ nm (**DCPDI**) and 375 nm (**DCCDI**)).

Remarkably, the films made from these **LP-DCPDI/DCCDI** hybrid solutions retained the monomeric absorption and emission features of the dye molecules even in the solid-state (Figure 4.2.4), whereas the films made from dyes alone without **LP** particles failed to show any solid-state emission (inset, Figure 4.2.4b and d). This clearly indicates that inorganic **LP** particles are fencing the dye molecules without giving any room for individual dye aggregation even in the solid-state. This highlights the role of nanoscopic inorganic template and the importance of hybrid co-assembly to make highly luminescent solid-state materials.

4.2.4 Fluorescent Dye J-aggregates-LP Hybrids

Since **LP** particles are known to modulate the growth of supramolecular aggregates of dye molecules,¹⁹ we have extended this hybrid co-assembly strategy to make fluorescent hybrid supramolecular assemblies of cationic diimides. Our initial investigations in this direction showed the formation of fluorescent supramolecular aggregates of all cationic diimides on **LP** surface at high concentrations of dye (> 1mM) and **LP** (up to 2.25 wt%) particles in water. We have investigated this process in detail by titrating **LP** particles (concentration fixed at 2.25 wt%) with different concentration of cationic diimides. Optical and dynamic light scattering (DLS) studies on these **LP-dye** hybrids provided insights into the modulations in the molecular

organization of cationic dyes caused by anionic **LP** particles during the co-assembly process. In a typical experimental procedure, different concentrations (0.1-5 mM) of cationic diimides were added to 2.25 wt% of exfoliated **LP** in water and sonicated for few minutes until clear solutions were obtained. Zetapotential measurements in DLS studies showed that, $-ve$ charge on **LP** particles decreases with concomitant increase in the hydrodynamic radius, when the concentration of **DCNDI** is increased from 0.1 mM to 5 mM, (Figure 4.2.5a). This clearly indicates the co-assembly between **LP** and **DCNDI** through ionic interactions. Interestingly, increase in the concentration of **DCNDI** in these hybrids resulted in significant decrease in its monomer emission (380-470 nm) with concomitant appearance of new broad emission band centred at 515 nm (Figure 4.2.5b).

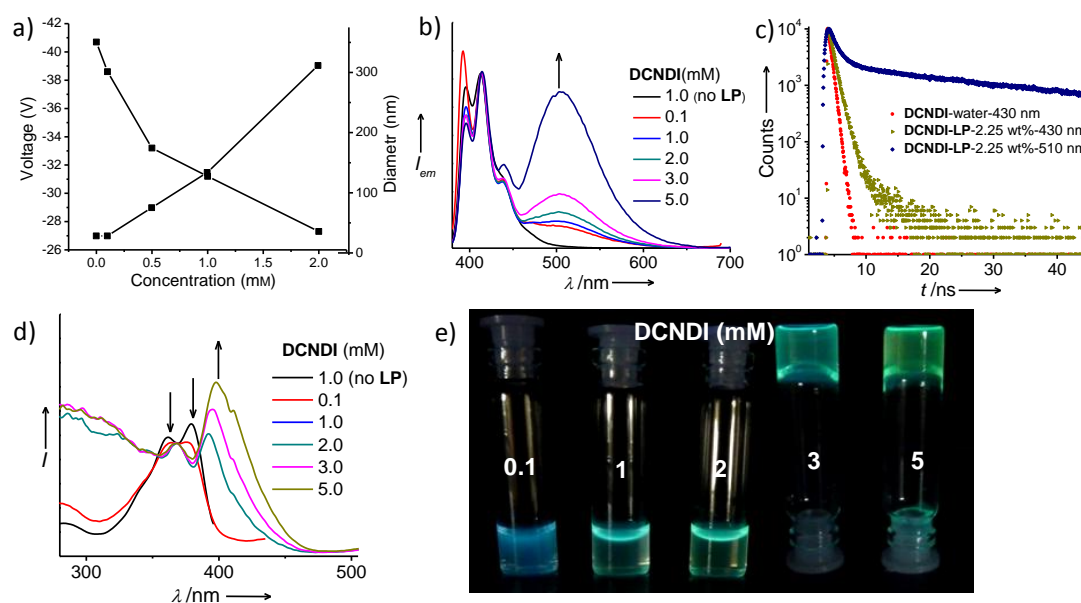


Figure 4.2.5. a) Decrease in net charge and increase in the size of **DCNDI-LP** hybrids with increase in the concentration of **DCNDI**, obtained from DLS measurements. b) Emission spectra of **DCNDI-LP** hybrids with increase in the concentration of **DCNDI** ($\lambda_{exc} = 350$ nm, $l = 1$ mm). c) Fluorescence lifetime decay profiles of **DCNDI** collected at monomer (430 nm) and excimer emission wavelengths in water ($\lambda_{exc} = 370$ nm). d) Excitation spectra of **DCNDI-LP** with increase in the concentration of **DCNDI** monitored at 430 (without **LP**, black line) and 510 nm. e) Photographs of **DCNDI-LP** hybrid aqueous solutions and hydrogels. Unless otherwise mentioned, all these measurements were done with 2.25 wt% of **LP** nanoparticles in water.

Fluorescence lifetime and excitation spectra measurements provided further insights into the nature and origin of this new emission band. Lifetime decay profiles collected at monomer emission (430 nm) followed monoexponential decay and the estimated lifetime is 0.74 ns which is consistent with the monomer emission of **DCNDI** (Figure 4.2.5c). Whereas the decay profile collected at 510 nm was fitted to triexponential equation which showed major contribution from long lifetime of 29.8 ns (85.4 %) along with the two short lifetimes, 0.68 (7.3 %) and 1.58 ns (7.3 %) (Figure 4.2.5c). This gives an indication that the newly formed emission

band in these hybrids is due to the formation of excimer by **DCNDI** chromophores (Figure 4.2.5b). To understand whether the excimer is formed just due to excited state dimerization of monomers or due to ground state preorganization of **DCNDI** upon binding with **LP** nanoparticles, we have collected excitation spectra at both monomer (415 nm) as well as at excimer (515 nm) emission wavelengths (Figure 4.2.5d). The excitation spectra collected at 415 nm resembles like monomer absorption spectrum of **DCNDI**. On the other hand, the excitation spectra collected at excimer emission (515 nm) wavelength showed gradual bathochromic shifts with increase in the concentration of **DCNDI**. Moreover, at 5 mM of **DCNDI**, the excitation spectrum maximum is 18 nm red-shifted than the monomer and displayed sharp vibrational transitions of **DCNDI**. These observations clearly indicate the J-aggregation of **DCNDI** molecules in presence of **LP** with strong excitonic coupling. Moreover, it is evident that the ground state preorganization of **DCNDI** on **LP** is also responsible for the formation of excimer in the excited state. This kind of aggregation driven excimers are known as preassociated/static excimers.²⁰ These changes are also visible when the 2.25 wt% of **LP** solutions having different concentrations of **DCNDIs** were visualized under 365 nm UV light (Figure 4.2.5e). Interestingly, hydrogel formation was observed for the hybrids containing more than 3mM of **DCNDI** (Figure 4.2.5e). This is quite remarkable as **DCNDI** alone is insoluble in water above 3 mM, whereas **DCNDI-LP** hybrids form transparent green emitting hybrid hydrogels even at 5 mM. Moreover, the increase in the size (65 nm to 300 nm) of hybrids (Figure 4.2.5a) and hydrogel formation with increase in the concentration of **DCNDI** suggests that, in addition to the J-aggregation of chromophores, there is indeed the formation of higher order aggregates by **DCNDI-LP** hybrids (see below).

Similar to **DCNDI**, both **DCPDI** and **DCCDI** also showed the formation of J-aggregates upon the co-assembly with **LP** particles (Figure 4.2.6). As the concentration of dyes was increased from 0.1 mM to 5 mM, monomer emission peaks corresponding to **DCPDI** (500-630 nm) and **DCCDI** (520-620 nm) are significantly reduced with concomitant increase in the intensity of aggregate emission at higher wavelengths. This is also clear from the photographs of these hybrids visualized under 365 nm UV irradiation (Figure 4.2.6c). In case of **DCPDI**, the aggregate emission was observed between 620-850 nm where as it is centred at 590 nm for **DCCDI**. Again, excitation spectra provided insights into the ground state organization of emissive **DCPDI** and **DCCDI** species in the hybrid co-assembly (Figure 4.2.6b and e). Interestingly, the excitation spectra monitored at 700 nm for **DCPDI-LP** hybrids (**DCPDI**-5mM and **LP**-2.25 wt%) displayed a new sharp peak at 590 nm whereas the corresponding 0.1 mM solution showed only weak shoulder band at 575 nm (Figure 4.2.6b). This sharp red shifted peak centred at 590 nm unambiguously proves that the emissive species between 620-850 nm corresponds to strong excitonically coupled **DCPDI** J-aggregates.^{9a,16} Similarly, in case of 5

mM **DCCDI-LP** hybrids, excitation spectra collected at 600 nm showed strong red-shifted bands at 375 nm and 510 nm which are weak at lower concentrations of **DCCDI** (0.1 mM). These features are again in consistent with the strongly coupled J-aggregates of **DCCDI**s, which are responsible for the emission in higher wavelength regions (530-750 nm).²¹

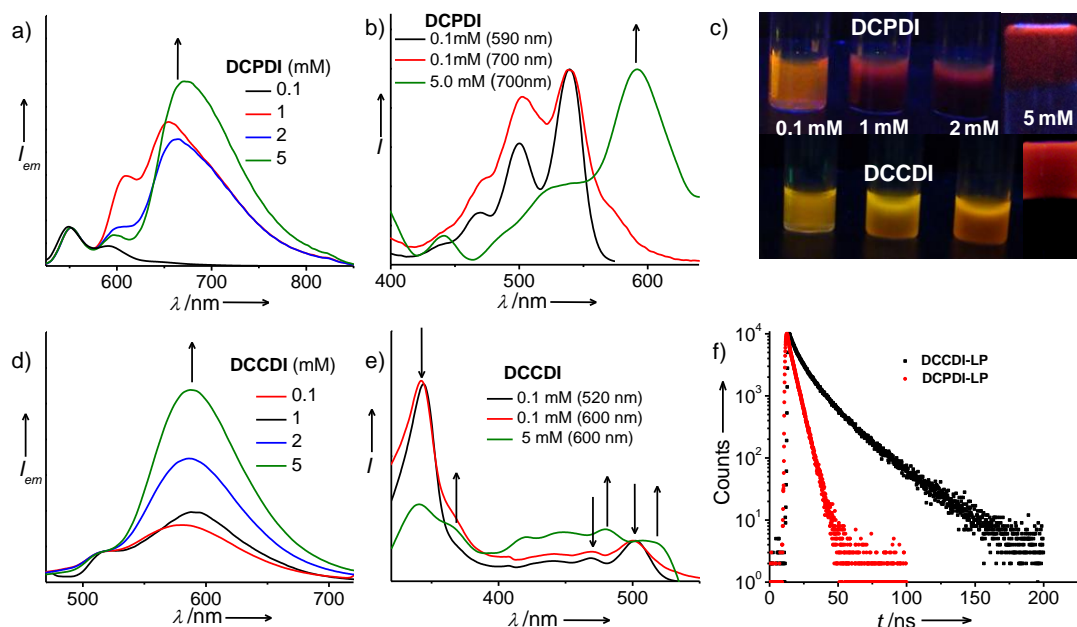


Figure 4.2.6. a) Emission ($\lambda_{exc} = 500$ nm, $l = 1$ mm) and b) excitation spectra (monitored at 700 nm) of **DCPDI-LP** hybrids in water with increasing concentration of **DCPDI**. c) Photographs of **DCPDI-LP** and **DCCDI-LP** hybrids aqueous solutions/gels with increase in the concentration of **DCPDI** and **DCCDI** under 365 nm UV light. d) Emission ($\lambda_{exc} = 375$ nm, $l = 1$ mm) and e) excitation spectra (monitored at 600 nm) of **DCCDI-LP** hybrids in water with increase in the concentration of **DCCDI**. f) Fluorescence lifetime decay profiles of **DCPDI-LP** (monitored at 550 nm) and of **DCCDI-LP** (monitored at 600 nm) hybrid aqueous solutions ($\lambda_{exc} = 405$ nm, $c = 0.1$ mM). All measurements were done with 2.25 wt% of **LP** nanoparticles in water.

Fluorescence lifetime decay profiles of **DCCDI/DCPDI-LP** hybrids at 0.1 mM dye concentration provided further insight into the nature of emission at higher wavelengths (Figure 4.2.6f). In case of **DCCDI-LP** hybrids, the decay profiles monitored at 600 nm (aggregate emission) were fitted to triexponentials and the resultant lifetime values were found to be 3.89 ns (13.83%), 10.94 ns (47.64%) and 25.54 ns (38.53%). The long lived lifetime component (25.54 ns) indicates the formation of excimer by **DCCDI** chromophores in the co-assembly state with **LP** particles. Since the corresponding excitation spectra showed the J-type aggregation by **DCCDI** chromophores, similar to **DCNDI**, **DCCDI** also exists as static/preassociated excimer in **DCCDI-LP** hybrids which is more prominent at higher concentrations (see below). On the other hand, **DCPDI** in **DCPDI-LP** hybrids (**DCPDI**-0.1 mM) did not show appreciable change in the lifetime compared to its monomer due to very less contribution from aggregate emission at this concentration (Figure 4.2.6f). However, significant

lifetime change was observed due to J-aggregation of **DCPDI**s in **DCPDI-LP** hybrids at higher concentrations (see below). Interestingly both **DCCDI-LP** and **DCPDI-LP** hybrids forms high water content (90%) hydrogels at 5 mM concentrations of cationic diimides and 2.25 wt% of **LP**, reiterating the hierarchical organization of organic and inorganic components in these hybrids into higher ordered aggregates (Figure 4.2.6c).²²

4.2.5 Rheology Studies on Hybrid Hydrogels

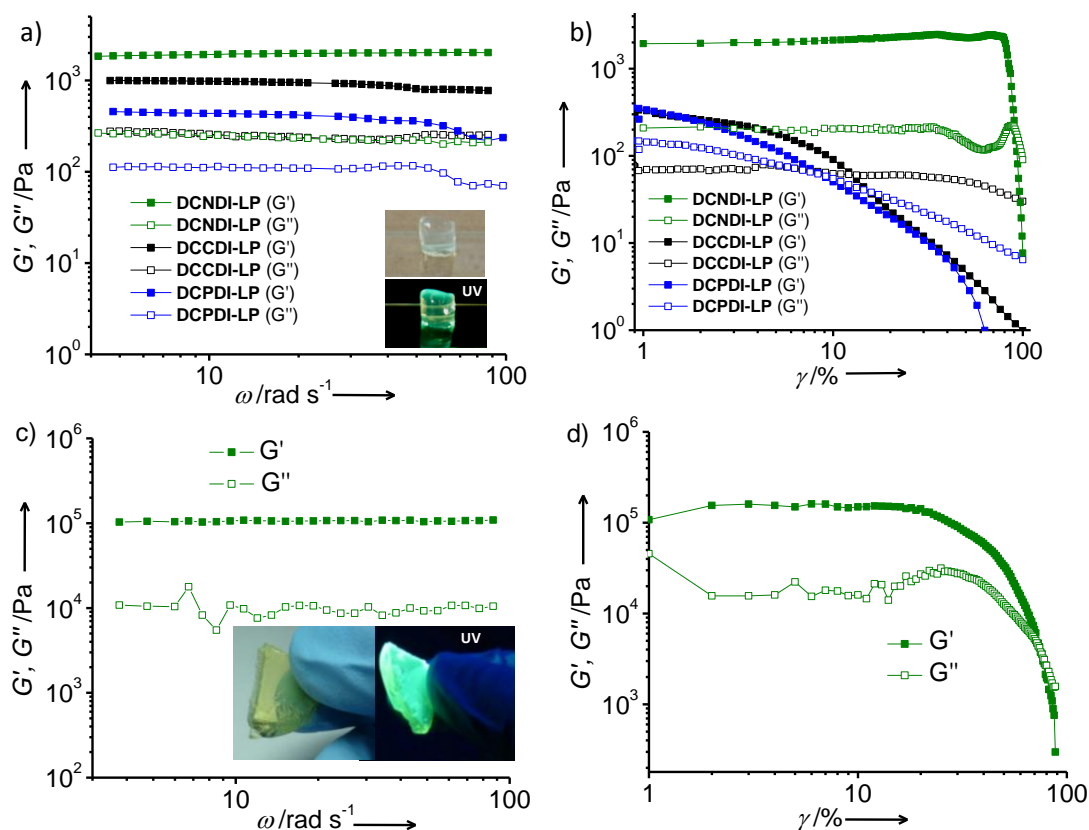


Figure 4.2.7. Storage (G') and loss (G'') modulus of the **dye-LP** hybrid hydrogels measured as functions of a) angular frequency (ω) at a constant strain (γ) of 1 % and b) γ (%) at a constant frequency of 5 Hz. Storage (G') and loss (G'') modulus of the **DCNDI-LP** hybrid hydrogel (after removing 10-15% of water) measured as functions of c) ω at a constant γ of 1% and d) γ (%) at a constant frequency of 5 Hz. Insets in Figure 4.2.7a and 4.2.7c show the photographs of corresponding freestanding **DCNDI-LP** hybrid hydrogels under ambient and 365 nm UV light.

Rheology measurements on these hybrid hydrogels showed highest mechanical strength for **LP-DCNDI** hybrids, followed by **DCCDI-LP** and **DCPDI-LP** hydrogels, respectively (Figure 4.2.7). The storage (G') modulus of the all **dye-LP** hybrid hydrogels measured as a function of angular frequency (ω) at 1% strain (γ) showed significant elastic response and always greater than the corresponding loss (G'') modulus up to 100 rad/s (Figure 4.2.7a). The values of G' for **DCNDI-LP**, **DCCDI-LP** and **DCPDI-LP** hydrogels are 2000 Pa, 1000 Pa and 500 Pa respectively. This is further clear from the (G') and (G'') measured as

function of γ at constant frequency of 5 Hz (Figure 4.2.7b). Both **DCCDI-LP** and **DCPDI-LP** hybrid hydrogels failed to show good linear response and gels were collapsed after 10% of γ . This indicates the moderate mechanical strength and soft-nature of these hybrids and can be easily processed. On the other hand, hybrid hydrogels of **DCNDI-LP** could sustain up to 100% of γ with good linear response between 1-100% of γ . The high mechanical strength **DCNDI-LP** gels helped to mould them into freestanding fluorescent objects (Figure 4.2.7a, inset). We have further improved the mechanical strength of these **DCNDI-LP** hybrid hydrogels by removing 10-15% of water from it. The resultant freestanding hydrogels displayed significant elastic response with G' as high as 10^5 Pa ($G'' = 10^4$ Pa) and they are stable up to 30% of γ (Figure 4.2.7c and d). The resultant **DCNDI-LP** hybrid hydrogel pieces are highly transparent and exhibit bright green emission from preassociated **DCNDI** excimer (Figure 4.2.7c, inset). The high mechanical strength of **DCNDI-LP** hybrid hydrogels compared to **DCPDI-LP/DCCDI-LP** hybrids could be due to the high solubility of **DCNDI** and its hybrids with **LP** in water. As a result, **DCNDI-LP** hybrids are more uniformly dispersed in water than other hybrids thereby improving the mechanical strength. This is further evident from the high transmittance of **DCNDI-LP** xerogels compared to **DCPDI-LP** and **DCCDI-LP** hybrids (*vide infra*).

4.2.6 Transparent and Luminescent Films of Dye J-Aggregate-LP Hybrids

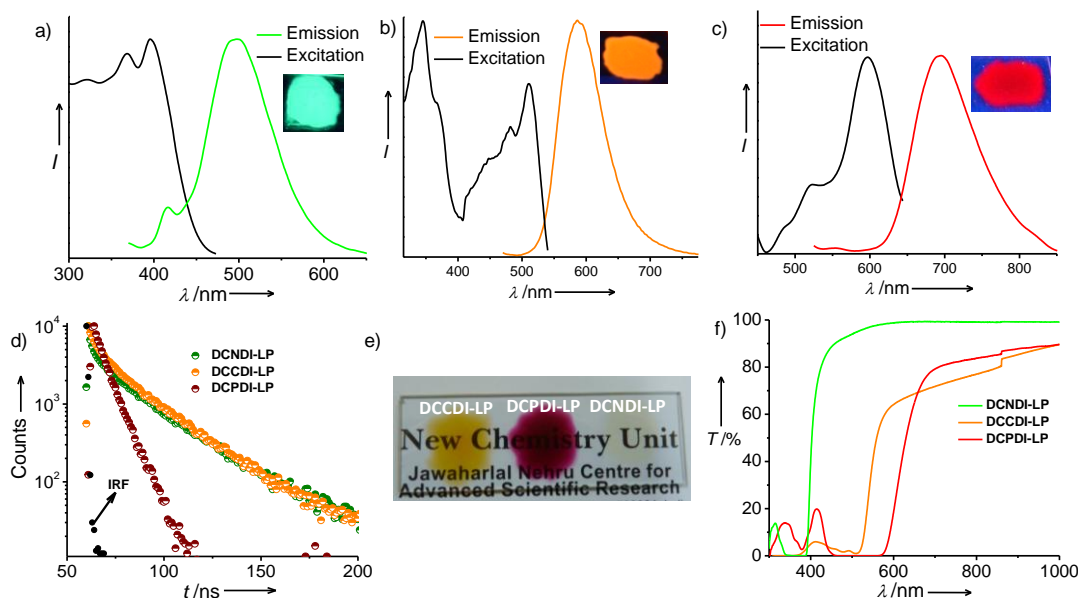


Figure 4.2.8. Normalized emission and excitation spectra of a) **DCNDI-LP** b) **DCCDI-LP** and c) **DCPDI-LP** xerogels and inset shows their photographs under 365 nm UV light ($\lambda_{exc} = 350$ nm (**DCNDI-LP**), 375 nm (**DCCDI-LP**) and 500 nm (**DCPDI-LP**)) and excitation spectra were monitored at 510 nm (**DCNDI-LP**), 600 nm (**DCCDI-LP**) and 700 nm (**DCPDI-LP**)). d) Nanosecond lifetime decay profiles of dye-LP hybrid xerogels where IRF is the instrument response function. e) Photograph of transparent dye-LP hybrid xerogels under ambient light and their f) transmittance spectra.

The mechanical strength of these hybrids indicates that they are soft in nature and hence can be solution processed to form films which is advantageous for many applications. In this regard, we have further investigated the molecular organization of these organic-inorganic hybrids in their xerogel state (Figure 4.2.8). The emission spectrum of film made from **DCNDI-LP** hybrid hydrogel showed excimer emission at 500 nm with negligible contribution from its monomer (~440 nm) compared to its gel state (Figure 4.2.8a). The corresponding excitation spectra collected at 510 nm, also showed strongly coupled J-aggregates of **DCNDI** chromophores. Similarly, films made from **DCCDI-LP** and **DCPDI-LP** hybrid hydrogels also showed J-aggregate emission without any signature of monomer, suggesting an efficient co-assembly in the film state. In case of **DCCDI-LP** xerogels, the excitation spectra collected at J-aggregate emission (600 nm) showed the J-aggregate absorption bands at 375 nm and 510 nm which are more significant than the corresponding gel state (Figure 4.2.8b). On the other hand, the xerogels of **DCPDI-LP**, exhibited red-shift of 20 nm (670-690 nm) in emission and 5 nm in excitation (collected at 700 nm) maxima compared to its gel state (Figure 4.2.8c). Fluorescence lifetime decay profiles on **DCNDI-LP** xerogels also showed major contribution from preassociated excimer with a lifetime of 26.6 ns (76.43%) (Figure 4.2.8d). Similarly, in case of **DCCDI-LP** xerogels, contribution from long lived preassociated excimer (24.3 ns (74.07%)) is significantly increased than their dilute solutions (24.5 ns (38.53%)) when monitored at 600 nm which further indicates enhanced aggregation at high concentrations (Figure 4.2.8d). However, **DCPDI-LP** xerogels showed only small increase in fluorescence lifetime from 4.5 ns to 6.8 ns compared to their dilute solutions. This might be due to the absence of preassociated excimer formation by **DCPDI-LP** hybrid J-aggregates (Figure 4.2.8d). The decrease or disappearance of monomer emission and strong J-aggregate features in the excitation spectra and increased contribution from aggregate lifetime for all the hybrids further indicate the enhanced J-aggregate formation in the film state than corresponding gel state. As shown in the photograph all films made from **LP-dye** hybrid hydrogels are visibly transparent with bright green, yellow and red emission under 365 nm UV irradiation (Figure 4.2.8e and insets of Figure 4.2.8a-c). Remarkably, the xerogel of **DCNDI-LP** displayed transmittance as high as 99.0% (above 850 nm) which is less (85%) for other two xerogels due to their relatively low solubility than **DCNDI-LP** hybrids in water (Figure 4.2.8f). Notably, the high concentration (5 mM) of dyes in these hybrids would be advantageous because, even thin films made from these hybrids can efficiently absorb the incident light while avoiding loss due to scattering owing to their high extinction coefficients and transparent nature.

4.2.7 Alternate Organic-Inorganic Hybrid Arrays

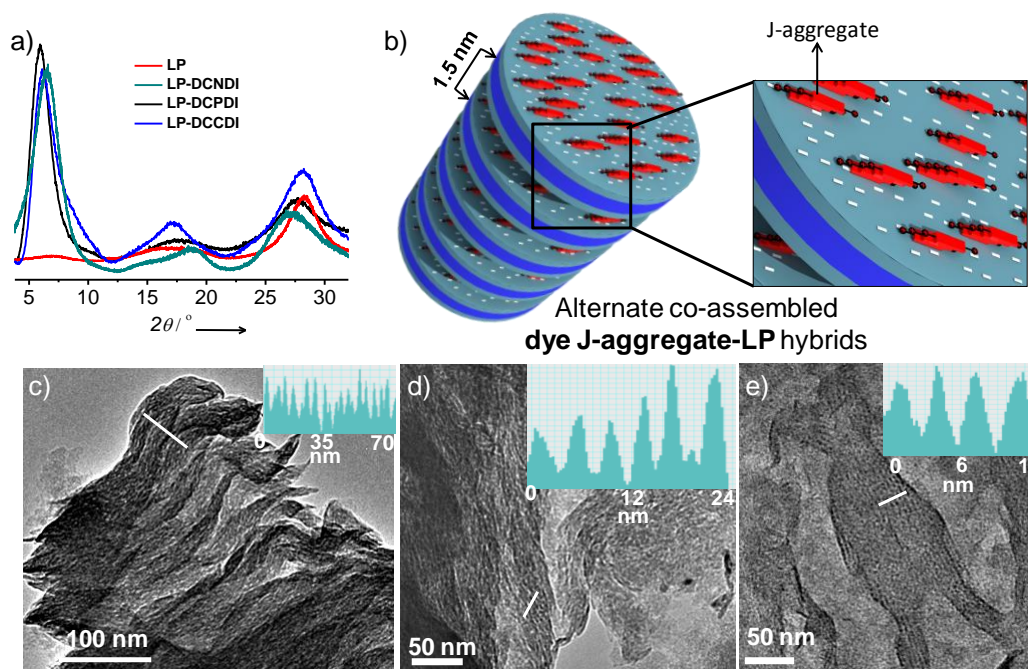


Figure 4.2.9. a) PXRD pattern of exfoliated **LP** particles in water and **dye-LP** hybrid hydrogel films. b) Proposed schematic representation for the co-assembly of cationic dyes and **LP** particles into alternate **dye J-aggregates-LP** organic-inorganic hybrids. TEM images of c) **DCNDI-LP**, d) **DCCDI-LP** and e) **DCPDI-LP** hybrid hydrogel films and corresponding intensity profiles are shown in the inset.

Since the J-aggregation of chromophores and hydrogel formation in **dye-LP** hybrids, indicates the formation of higher order aggregates, we have investigated powder XRD (PXRD) pattern and transmission electron microscopy (TEM) images of these soft-hybrids to get insight into the molecular packing and hierarchical organization (Figure 4.2.9). PXRD pattern of the films made from exfoliated **LP** particle solution showed two diffraction peaks between 17° - 28° (2θ) which are signatures for the crystalline lattice planes of **LP** particles. The absence of any peaks below 10° (2θ) is consistent with the exfoliated **LP** particles, hence ruling out the face-to-face stacking between **LP** particles (Figure 4.2.9a). Remarkably, films made from co-assembled **LP-dye** hybrid hydrogels displayed strong low angle reflections at $\sim 5.9^{\circ}$ (2θ) corresponding to the d -spacing of ~ 1.5 nm while without affecting the rest of the peaks corresponding to crystalline lattice planes of single **LP** particle. This unambiguously proves the face-to-face stacking of **LP** particles due to ionic interactions with J-aggregates (see above) of dicationic diimides, while forming an unprecedented alternate organization between **LP** particles and J-aggregates of dicationic diimides (Figure 4.2.9a and b). This is further supported by TEM analysis on these xerogels which showed the appearance of nanoscale striations with bright (organic) and dark (inorganic) contrasts due to the co-existence of both **dye J-aggregates** and **LP** particles (Figure 4.2.9c-e). Moreover, the final **dye-LP** hybrids resemble an

alternate (...ABAB...) organic-inorganic supramolecular co-polymer structure, which is quite unique to this hybrid system.

4.2.8 Conclusions

In conclusion we have demonstrated a simple non-covalent strategy to make luminescent soft-hybrids through controlled molecular organization of π -systems via ionic co-assembly with crystalline inorganic **LP** nanoparticles. Depending on the ratio between organic and inorganic components, the chromophores were organized on **LP** surface as fluorescent monomers or supramolecular J-aggregates. In the former organization, the **LP-dye** hybrids showed high fluorescence quantum yields in solution which also retained in solid-state due to fencing of dye monomers from aggregation through **LP** co-assembly. This approach was further extended to make luminescent hybrid hydrogels having strongly coupled fluorescent J-aggregates of n-type diimides. This highlights the unique feature of the hybrid co-assembly for solution processable luminescent hybrids as these dyes have a natural tendency to form non-fluorescent H-aggregates in solution or on the surface. Moreover, microscopy and PXRD showed the unprecedented alternate hierarchical organization between **LP** particles and dye J-aggregates. We propose that, these **LP-chromophore** soft-hybrid assemblies can be integrated into various sensory, photonic and photovoltaic devices in an environmental friendly manner owing to their ease of processability in water and tailor made optical functionality.

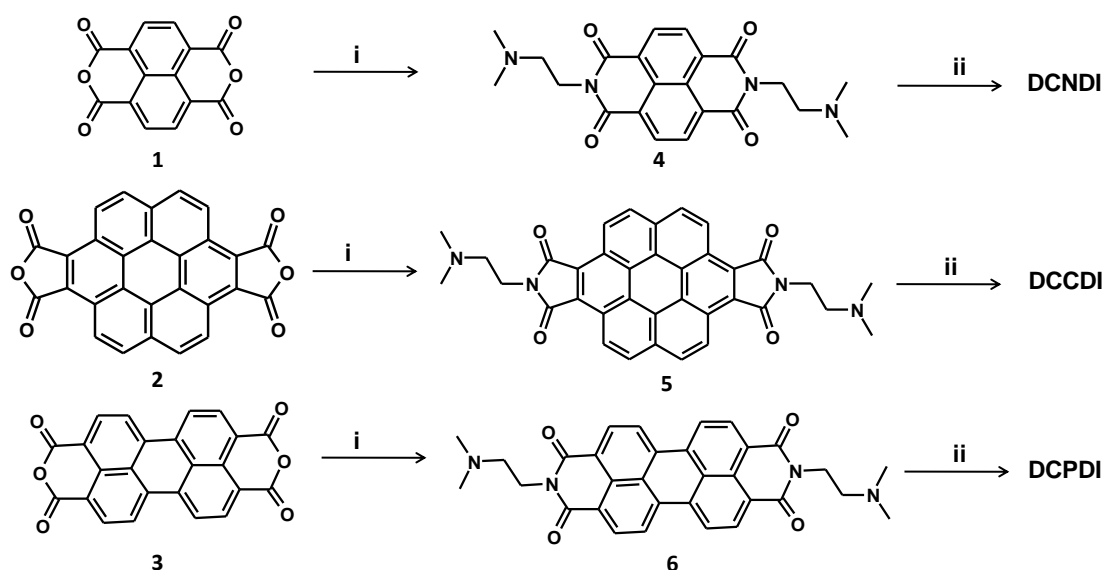
4.2.9 Experimental Section

General methods: TEM measurements were performed on a JEOL, JEM 3010 operated at 300 kV. Samples were prepared by placing a drop of the gels on carbon coated copper grids followed by drying at room temperature. Electronic absorption spectra were recorded on a Perkin Elmer Lambda 900 UV-Vis-NIR Spectrometer and emission spectra were recorded on Perkin Elmer Ls 55 Luminescence Spectrometer. UV-Vis and emission spectra were recorded in 1 mm path length cuvette. Fluorescence spectra of solutions, gels and films were recorded in front-face geometry to avoid self-absorption at high concentrations. Fluorescence quantum yields were calculated using 0.1 mM Rhodamine 6G in ethanol as a standard. Powder XRD pattern of the compounds were recorded by in Bruker D8 Discover (40 kV, 30 Ma) instrument using Cu K α radiation ($2\theta = 0.8\text{--}35^\circ$). $^1\text{H-NMR}$ measurements were performed on BrukerAvance 400 (400 MHz) spectrometer. Fluorescence lifetime measurements in solutions were performed on FLSP920 spectrometer, Edinburgh Instruments. A pulsed diode laser was used as excitation source ($\lambda_{ex} = 405\text{ nm}$). Fluorescence lifetime of films were measured using IBH (FluoroCube) time-correlated picosecond single photon counting (TCSPC) system. Films were excited with a pulsed diode laser (<100 ps pulse duration) at a wavelength of 375 and 500

nm (NanoLED-11) with a repetition rate of 1 MHz. The detection system consists of a microchannel plate photomultiplier (5000U-09B, Hamamatsu) with a 38.6 ps response time coupled to a monochromator (5000M) and TCSPC electronics (Data Station Hub including Hub-NL, NanoLED controller and preinstalled Fluorescence Measurement and Analysis Studio (FMAS) software). The fluorescence lifetime values were determined by deconvoluting the instrument response function using DAS6 decay analysis software. The quality of the fit has been judged by the fitting parameters such as χ^2 (< 1.2) as well as the visual inspection of the residuals. DLS measurements were carried out using a NanoZS (Malvern UK) employing a 532 nm laser at a back scattering angle of 173° . Rheological measurements were performed at 25°C on Anton Paar MCR 150, stress controlled rheometer having a cone and plate geometry with a plate gap of $100\ \mu\text{m}$.

4.2.9a Synthesis

LP XLG particles with low heavy metals content were purchased from Rockwood. Coronene dianhydride was synthesized according to the literature methods²³, perylene and naphthalene dianhydrides, and N,N-dimethyl ethylene diamine were purchased from Aldrich.



Scheme 4.2.2. Synthesis of dicationic diimides. i) N,N-dimethyl ethylene diamine, isobutanol, refluxing, 24 h. ii) methyl iodide, toluene, refluxing, 4 h.

General procedure for the synthesis of dicationic diimides: Dianhydrides (2.42 mmol) and N,N-dimethyl ethylene diamine (23.6 mmol) were taken in 40 mL of isobutanol and stirred at 90°C under N_2 atmosphere for 24 h. The resultant solution was filtered and washed with ethanol and water and dried. The obtained product was suspended in 30 mL of 5% NaOH and heated for 30 min at 90°C and filtered followed by several washings with water and ethanol

(only for compounds **5** and **6**). After drying under vacuum, diimides (**5** and **6**) were obtained in the form of powders. The obtained diimide (**4**, **5** or **6**) was taken in 50 mL of toluene with excess of methyl iodide and refluxed for 4 h. The obtained residue were filtered and dried under vacuum.

DCNDI: Yellow solid (yield 90 %); ^1H NMR (DMSO- D_6 , 400 MHz), δ (ppm) = 8.72 (s, 4H), 4.61 (t, 4H, $J = 7.2$ Hz), 3.65 (t, 4H, $J = 7.6$ Hz), 3.26 (s, 18H); HRMS (ESI): m/z calculated: 219.1128, observed 219.1143 [$\text{M}^{+2}/2$].

DCCDI: Orange solid (yield 70 %); ^1H NMR (DMSO- D_6 , 400 MHz, 80 °C), δ (ppm) = 9.95 (d, 4H, $J = 8.8$), 9.29 (d, 4H, $J = 8.8$), 4.47 (t, 4H, $J = 6.8$ Hz), 3.99 (t, 4H, $J = 6.8$ Hz), 3.39 (s, 18H); HRMS (ESI): m/z calculated: 305.1284, observed: 305.1272 [$\text{M}^{+2}/2$].

DCPDI: Brownish red solid (yield 70 %); ^1H NMR (DMSO- D_6 , 400 MHz, 80 °C), δ (ppm) = 9.01 (d, 4H, $J = 8.0$ Hz), 8.67 (d, 4H, $J = 8.0$ Hz), 4.55 (t, 4H, $J = 7.2$ Hz), 3.73 (t, 4H, $J = 7.2$ Hz), 3.27 (s, 18H); HRMS (ESI): m/z calculated: 281.1284, observed: 281.1273 [$\text{M}^{+2}/2$].

4.2.10 References

1. a) F. J. M. Hoeben, P. Jonkheijm, E.W. Meijer, A. P. H. J. Schenning, *Chem. Rev.* **2005**, *105*, 1491; b) K. J. C. van Bommel, A. Friggeri, S. Shinkai, *Angew. Chem. Int. Ed.* **2003**, *42*, 980; c) A. P. H. J. Schenning, E.W. Meijer, *Chem. Commun.* **2005**, 3245; d) N. Mizoshita, T. Taniab, S. Inagaki, *Chem. Soc. Rev.* **2011**, *40*, 789.
2. a) A. Ajayaghosh, V. K. Praveen, *Acc. Chem. Res.* **2007**, *40*, 644; b) F. Würthner, *Chem. Commun.* **2004**, 1564.
3. a) Q. Wang, J. L. Mynar, M. Yoshida, E. Lee, M. Lee, K. Okuro, K. Kinbara, T. Aida, *Nature* **2010**, *463*, 339; b) M. Liu, Y. Ishida, Y. Ebina, T. Sasaki, T. Aida, *Nat. Commun.* **2013** (DOI: 10.1038/ncomms3029).
4. C. Sanchez, P. Belleville, M. Popall, L. Nicole, *Chem. Soc. Rev.* **2011**, *40*, 696.
5. a) S. Inagaki, O. Ohtani, Y. Goto, K. Okamoto, M. Ikai, K. Yamanaka, T. Tani, T. Okada, *Angew. Chem. Int. Ed.* **2009**, *48*, 4042; b) N. Mizoshita, Y. Goto, T. Tani, S. Inagaki, *Adv. Mater.* **2009**, *21*, 4798.
6. a) G. Calzaferri, S. Huber, H. Maas, C. Minkowski, *Angew. Chem. Int. Ed.* **2003**, *42*, 3732; b) G. Calzaferri, K. Lutkouskaya, *Photochem. Photobiol. Sci.* **2008**, *7*, 879.
7. a) C. V. Kumar, A. Chaudhari, *J. Am. Chem. Soc.* **1994**, *116*, 403; b) S. Takagi, D. A. Tryk, H. Inoue, *J. Phys. Chem. B* **2002**, *106*, 5455; c) Y. Ishida, T. Shimada, D. Masui, H. Tachibana, H. Inoue, S. Takagi, *J. Am. Chem. Soc.* **2011**, *133*, 14280.

8. a) X. Zhang, M. A. Ballem, Z.-J. Hu, P. Bergman, K. Uvdal, *Angew. Chem. Int. Ed.* **2011**, *50*, 5729; b) X. Zhang, M. A. Ballem, M. Ahrén, A. Suska, P. Bergman, K. Uvdal, *J. Am. Chem. Soc.* **2010**, *132*, 10391; c) X. Zhang, Z.-K. Chen, K. P. Loh, *J. Am. Chem. Soc.* **2009**, *131*, 7210.
9. a) F. Würthner, T. E. Kaiser, C. R. Saha-Möller, *Angew. Chem. Int. Ed.* **2011**, *50*, 3376; b) A. Pron, P. Gawrys, M. Zagorska, D. Djuradoa, R. Demadrille, *Chem. Soc. Rev.* **2010**, *39*, 2577; c) M. Hasegawa, M. Iyoda, *Chem. Soc. Rev.* **2010**, *39*, 2420; d) X. Zhang, Z. Chen, F. Würthner, *J. Am. Chem. Soc.* **2007**, *129*, 4886.
10. F. Bergay, B. K. G. Theng, G. Lagaly in *Handbook of Clay Science, Vol. 1*, Elsevier, Amsterdam, **2006**.
11. A. J. Patil, Y.-C. Lee, J.-W. Yang, S. Mann, *Angew. Chem. Int. Ed.* **2012**, *51*, 733.
12. a) T. Yi, R. Clément, C. Haut, L. Catala, T. Gacoin, N. Tancrez, I. Ledoux, J. Zyss, *Adv. Mater.* **2005**, *17*, 335; b) P. Innocenzia, B. Lebeau, *J. Mater. Chem.* **2005**, *15*, 3821; G. De Luca, A. Romeo, V. Villari, N. Micali, I. Foltran, E. Foresti, I. G. Lesci, N. Roveri, T. Zuccheri, L. M. Scolaro, *J. Am. Chem. Soc.* **2009**, *131*, 6920.
13. a) K. V. Rao, K. K. R. Datta, M. Eswaramoorthy, S. J. George, *Angew. Chem. Int. Ed.* **2011**, *50*, 1179; b) M. M. Lezhnina, T. Grewe, H. Stoehr, U. Kynast, *Angew. Chem. Int. Ed.* **2012**, *51*, 10652.
14. K. V. Rao, K. K. R. Datta, M. Eswaramoorthy, S. J. George, *Chem. Eur. J.* **2012**, *18*, 2184.
15. L. Lu, R. M. Jones, D. McBranch, D. Whitten, *Langmuir* **2002**, *18*, 7706.
16. a) T. E. Kaiser, H. Wang, V. Stepanenko, F. Würthner, *Angew. Chem. Int. Ed.* **2007**, *46*, 5541; b) T. E. Kaiser, V. Stepanenko, F. Würthner, *J. Am. Chem. Soc.* **2009**, *131*, 6719; c) F. Würthner, C. Bauer, V. Stepanenko, S. Yagai, *Adv. Mater.* **2008**, *20*, 1695.
17. a) B. Wang, C. Yu, *Angew. Chem. Int. Ed.* **2010**, *49*, 1485; b) W. Wang, L.-S. Li, G. Helms, H.-H. Zhou, A. D. Q. Li, *J. Am. Chem. Soc.* **2003**, *125*, 1120.
18. a) F. Biedermann, E. Elmalem, I. Ghosh, W. M. Nau, O. A. Scherman, *Angew. Chem. Int. Ed.* **2012**, *51*, 7739; b) F. Schlosser, M. Moos, C. Lambert, F. Würthner, *Adv. Mater.* **2013**, *25*, 410; c) K. V. Rao, S. J. George, *Chem. Eur. J.* **2012**, *18*, 14286.
19. Y. Tang, Z. Zhou, K. Ogawa, G. P. Lopez, K. S. Schanze, D. G. Whitten, *Langmuir*, **2009**, *25*, 21.
20. a) M. Kumar, S. J. George, *Nanoscale*, **2011**, *3*, 2130; b) R. Zhang, D. Tang, P. Lu, X. Yang, D. Liao, Y. Zhang, M. Zhang, C. Yu, V. W. W. Yam, *Org. Lett.* **2009**, *11*, 4302.
21. K. V. Rao, S. J. George, *Org. Lett.* **2010**, *12*, 2656.
22. a) E. A. Appel, X. J. Loh, S. T. Jones, F. Biedermann, C. A. Dreiss, O. A. Scherman, *J. Am. Chem. Soc.* **2012**, *134*, 11767; b) E. A. Appel, F. Biedermann, U. Rauwald, S. T. Jones, J.

- M. Zayed, O. A. Scherman, *J. Am. Chem. Soc.* **2010**, *132*, 14251; c) K. V. Rao, K. Jayaramulu, T. K. Maji, S. J. George, *Angew. Chem. Int. Ed.* **2010**, *49*, 4218.
23. S. A-Fouet, I. Seguy, J.-F. Bobo, P. Destruel, H. Bock, *Chem. Eur. J.* **2007**, *13*, 1746.

PART-5

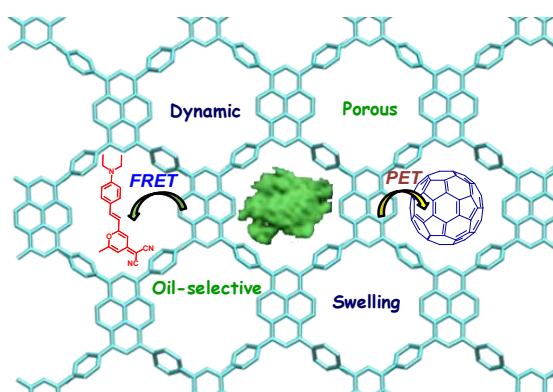
Conjugated Microporous Polymers

PART-5

Super-Absorbent Dynamic Microporous Polymers: Guest-Responsive Reversible Swelling, Enhanced Fluorescence, and Light-Harvesting*

Abstract

Synthesis and guest-responsive properties of two fluorescent microporous organic polymer networks (Py-PP and Py-BPP) rendered with pyrene chromophores are described. The structure of these polymers was fully characterized by various techniques. The hydrophobic nature of these porous networks allows the phase-selective swelling by the instantaneous absorption of a broad range of organic solvents and oils from their water mixtures at room temperature. Moreover the dynamic nature of these networks signals the swelling process with enhanced fluorescence. We have further explored the guest encapsulation in these microporous polymers for various photophysical processes. The dynamic swelling behaviour has been used for rapid encapsulation of various chromophoric guests such as C₆₀ and fluorescent dyes, and investigated for photoinduced electron/energy transfer process. This work holds a great promise on the design of smart porous organic solids from π -conjugated small molecules for sensing and separation.



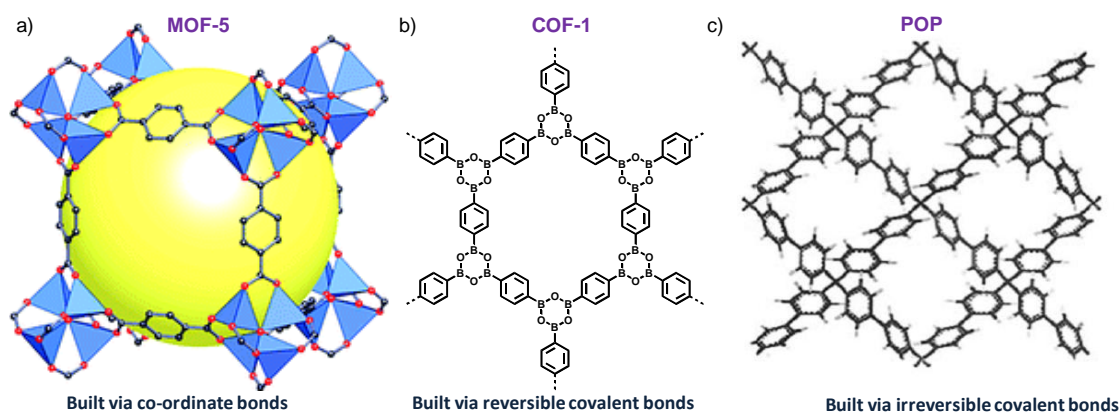
* Papers based on this work have appeared in *Chem. Eur. J.* 2012, 18, 4505; *Chem. Mater.* 2012, 24, 969; *J. Mater. Chem.* 2011, 21, 12958.

5.1 Introduction

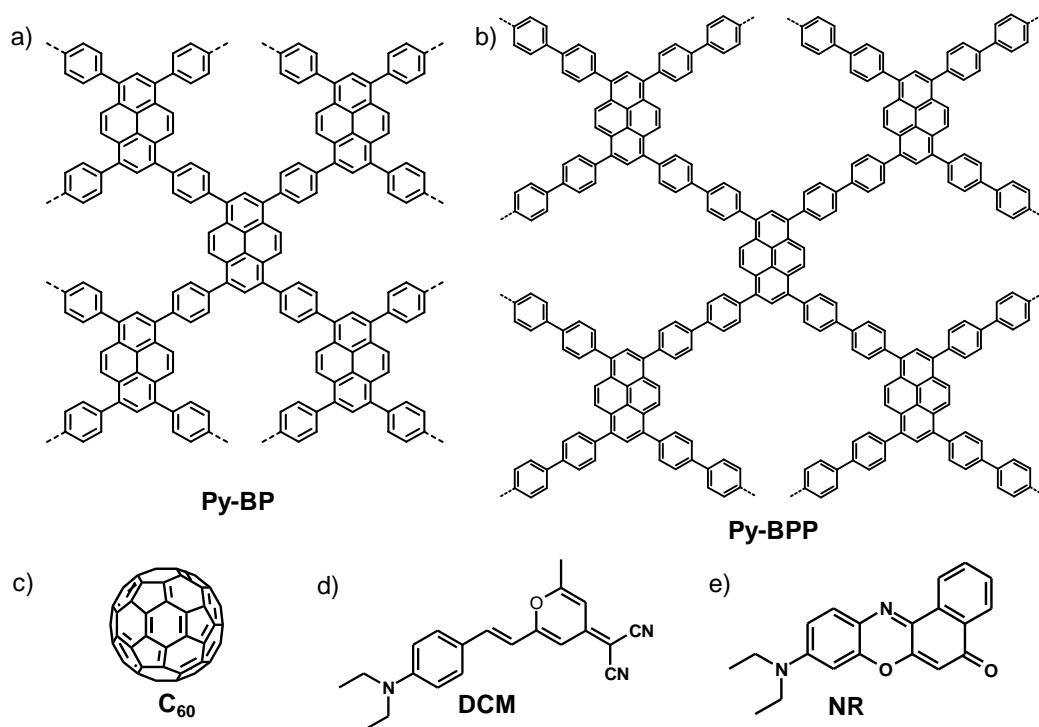
Luminescent porous materials, which combine the advantages of both porosity and guest-responsive (typically gases and solvent molecules) signalling, are the solid-state analogues of well studied photo-functional molecular cages in solution.¹ Recently, many crystalline materials like metal organic frameworks (MOFs), covalent organic frameworks (COFs) and periodic mesoporous silica have been constructed with chromophoric ligands, which showed remarkable guest-induced photo-electronic properties like energy transfer and photoconductivity.² On the other hand, polymeric and self-assembled systems that can swell or gel in presence of solvent guest molecules have been used as superabsorbents.³ Though the superabsorbent materials for water uptake have already been commercialized, the design of corresponding analogues for organic solvent uptake, which are of great importance for removing organic pollutants and for recovering oil from water due to spills,⁴ remains challenging as this requires selective, thermally stable and recyclable hydrophobic networks.⁵ Porous framework materials such as MOFs and COFs can be used as organic superabsorbent materials owing to their high surface areas. However, MOFs are chemically unstable and framework can degrade even with ambient humidity as they are built via metal-ligand coordination bonds (Scheme 5.1a). Though the coordination bonds are absent in COFs, the use of reversible covalent bonds in their synthesis to maintain crystallinity again make them chemically unstable (Scheme 5.1b).⁶ In this context, amorphous porous organic polymers (POPs)⁷ built via strong covalent bonds benefit from better thermal and chemical stabilities than MOFs and COFs (Scheme 5.1c). Moreover, with the realization that the crystalline order is not a prerequisite for controlling the functional properties of organic frameworks, POPs with an amorphous two or three-dimensional (2/3D) network have recently emerged as a new class of porous materials.⁸ Hence we envision that, an amorphous dynamic porous network⁹ with emissive backbones could provide multi-functions such as guest/solvent responsive swelling and signalling. In this respect, we find that the POPs with conjugated backbones would be appealing to integrate both the luminescent and dynamic functionality to the materials.¹⁰ Although, POPs have been extensively studied for gas adsorption,¹¹ the properties characteristic of π -conjugated segments or dynamic networks, such as fluorescence response, light-harvesting and solvent uptake, has not been adequately investigated to date.

Since artificial light-harvesting¹² has gathered immense attention in recent years due to its crucial role in photosynthesis and optoelectronic devices, we envision that luminescent dynamic polymers can also serve as versatile donor scaffold for excitation energy-transfer when loaded with appropriate guest molecules. However, encapsulation of guest molecules in POPs often requires tedious procedures owing to their non-dynamic backbone. This can be achieved under ambient conditions in POPs having dynamic framework. Even though light-harvesting

was shown in non-dynamic POPs absorbing in the UV-region,¹³ visible light-harvesting¹⁴ with rapid encapsulation of energy acceptor (guest) is hitherto unknown.



Scheme 5.1. Structure of a) MOF-5 [reproduced from ref. 2i] and b) COF-1. c) Structure of a POP built from tetraphenyl methane derivative [reproduced from ref. 11b].



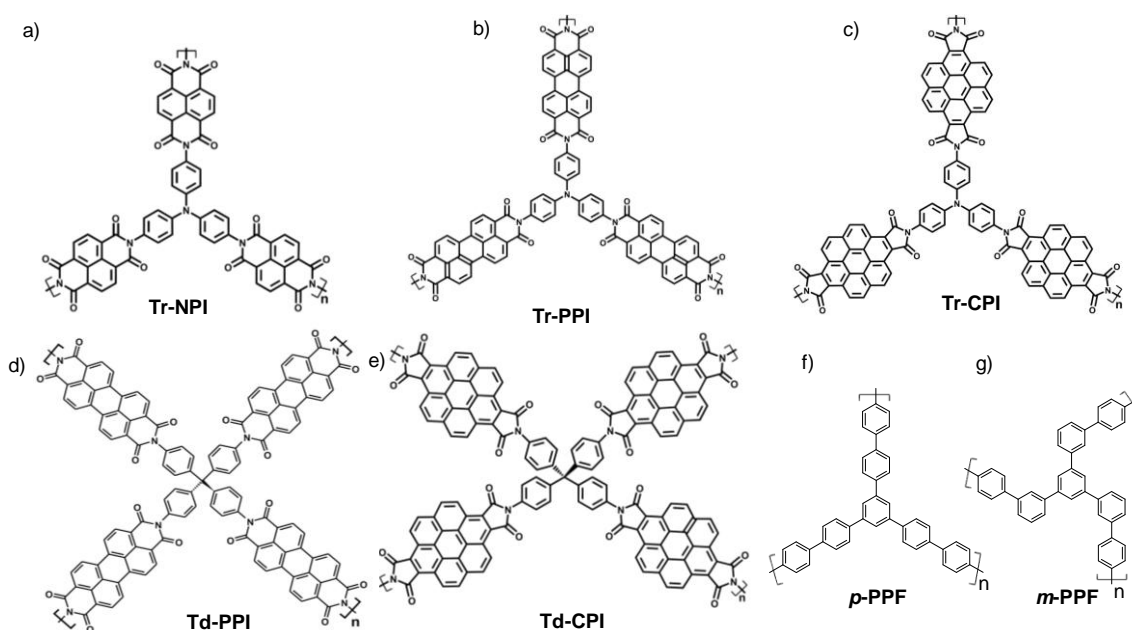
Scheme 5.2. Molecular structures of microporous polymers; a) **Py-PP** and b) **Py-BPP**. Molecular structures of guest molecules c) **C₆₀**, d) **DCM** and e) **NR** dye molecules.

In this Part, we describe the guest-responsive reversible swelling, fluorescence response and light-harvesting properties of two dynamic microporous polymer networks (**Py-PP** and **Py-BPP**) rendered with pyrene chromophores (Scheme 5.2a and b). The hydrophobic nature of these porous networks further allows the phase-selective swelling by the instantaneous absorption of a broad range of organic solvents and oils from their water mixtures at room temperature. We also demonstrate that, these hydrophobic microporous networks can

efficiently soak fullerene (C_{60}), Nile red (NR) and 4-(Dicyanomethylene)-2-methyl-6-(4-dimethylaminostyryl)-4Hpyran (DCM) through π - π and host-guest interactions (Scheme 5.2c-e). Detailed optical studies have shown electron/energy transfer from host network to the entrapped guest chromophores.

5.2 Preliminary Work on POPs

We have been working on microporous conjugated polymers consisting of polyaromatic components. In this direction, we have synthesized series of microporous organic polymers via imidation and Suzuki cross coupling reactions of various structure directing monomers (Schemes 5.2a and b, and 5.3). Though all the polymers have permanent porosity (Table 5.1), only conjugated polymers, poly(phenylene)s (*p*-PPF and *m*-PPF) and pyrene based polymers show fluorescence in the solid-state and only the pyrene based polymer frameworks display dynamic and superabsorbent nature in organic solvents. Polyimides are synthesized via the condensation of amines having trigonal (Scheme 5.3a-c) and tetrahedral (Scheme 5.3d and e) geometry with polyaromatic dianhydrides. Poly(phenylene)s (*p*-PPF and *m*-PPF) (Scheme 5.3f and g) are derived from triphenylbenzene derivatives with *para*- and *meta*-substituted tribromides as structure directing monomers in the Suzuki cross-coupling reaction with benzene-1,4-diboronic acid (BDA).



Scheme 5.3. Structures of a-c) trigonal and, d-e) tetrahedral polyimides and f-g) conjugated poly(phenylene)s.

Interestingly, both poly(phenylene)s and polyimides showed excellent surface area and high selectivity for CO_2 adsorption over N_2 (Table 5.1 and Figure 5.1). The presence of large aromatic π -clouds on the pore surface, small pore size and the polar end functional groups in

poly(phenylene)s are responsible for their selective CO₂ adsorption over N₂ (Figure 5.1a and b). On the other hand, the presence of large number of CO₂ phillic polar oxygen and nitrogen functionalities inside the porous network of polyimides are mainly responsible for their selective CO₂ adsorption (Figure 5.1c). Compared to poly(phenylene)s, polyimides posses high thermal stability and selectivity towards CO₂ at room temperature (293 K). Owing to the luminescent, dynamic and hydrophobic nature of pyrene derived porous polymers, we have exploited their functional properties such as super-absorbent nature for organic solvents and as light-harvesting scaffolds by non-covalent incorporation of various chromophoric guest molecules inside their porous networks (*vide infra*).

Table 5.1. Surface areas of various POPs synthesized in our group.

| POP | Tr-NPI | Tr-PPI | Tr-CPI | Td-PPI | Td-CPI | <i>p</i> -PPF | <i>m</i> -PPF | Py-PP | Py-BPP |
|----------------------------------|--------|--------|--------|--------|--------|---------------|---------------|-------|--------|
| Surface area (m ² /g) | 567 | 400 | 130 | 2213 | 210 | 269 | 229 | 1070 | 350 |

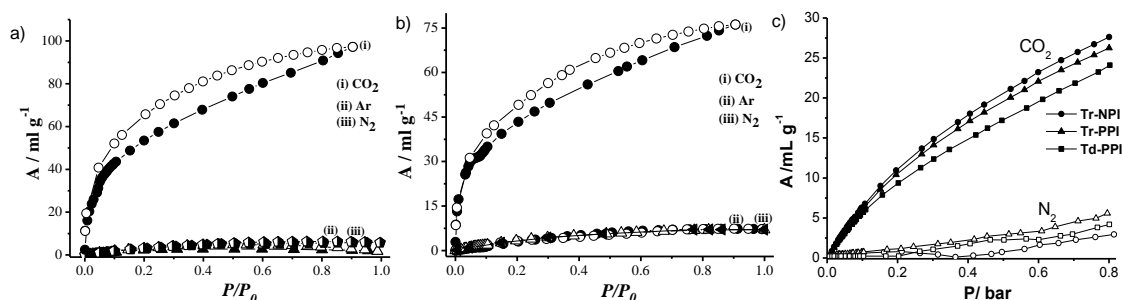


Figure 5.1. Sorption isotherms for a) *p*-PPF and b) *m*-PPF at 195 K (filled symbols shows adsorption, empty symbols shows desorption, P₀ is the saturated vapor pressure of the respective adsorbates). c) N₂ and CO₂ adsorption isotherms of Tr-NPI, Tr-PPI and Td-PPI at 293 K (Figure 5.1a and b, reproduced by permission of The Royal Society of Chemistry, <http://pubs.rsc.org/en/Content/ArticleLanding/2011/JM/c1jm11508a>).

In this Part, we restrict ourself to the pyrene based porous polymers keeping in mind the general theme of this thesis.

5.3 Functional Properties of Pyrene Based Microporous Polymers

5.3a Synthesis and Structural Characterization

Scheme 5.2a and b show the polymers, designed from tetra-phenyl substituted pyrene chromophores, which would impart both luminescence and hydrophobic interior to the frameworks. The porous model shown in Figure 5.2 is built on the energy minimized geometry of their structure repeating units which showed a twisted conformation for the phenyl rings that bridges the pyrene chromophores, which would result in an extended three-dimensional framework. Powder X-ray diffraction (PXRD) studies on both the polymers showed broad peaks characteristic of the amorphous nature of organic microporous polymers. The

orthogonally faced pyrene and phenylene rings would provide closed aromatic shells with hydrophobic cavities for the encapsulation of large molecules, through strong host-guest interactions.

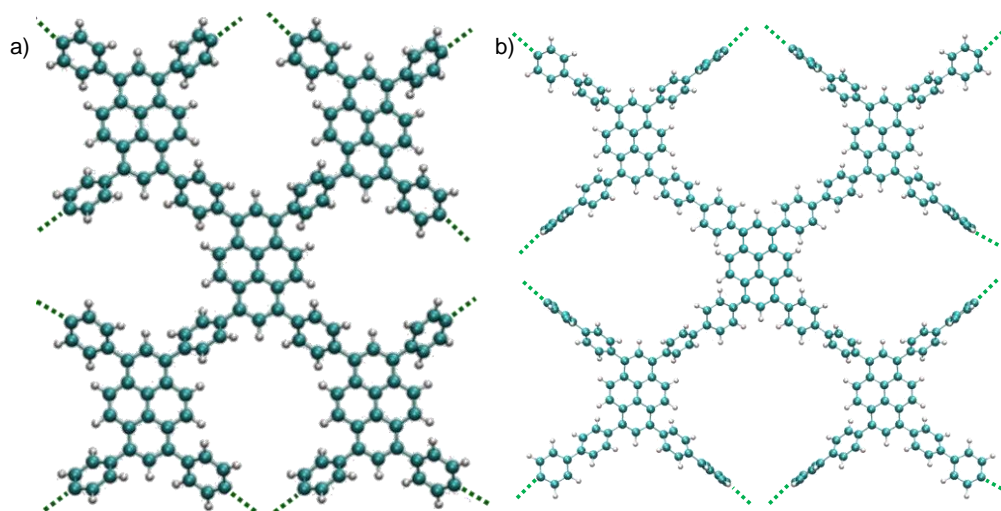


Figure 5.2. Extended molecular structures of a) **Py-PP** and b) **Py-BPP** based on their energy-minimised geometry of the basic structural units.

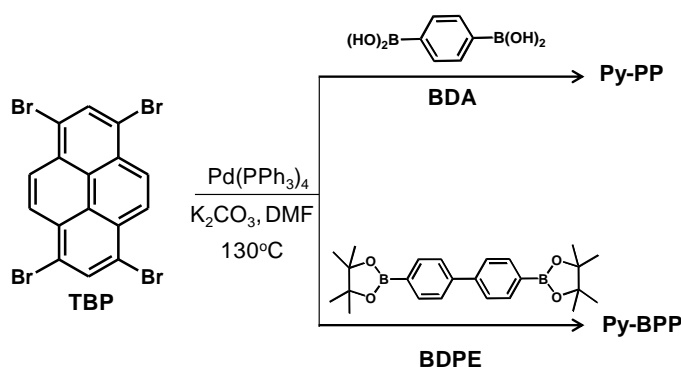


Figure 5.3. Synthetic scheme for **Py-PP** and **Py-BPP**.

Py-PP and **Py-BPP** were synthesized using Suzuki cross coupling reaction of 1,3,6,8-tetrabromopyrene (**TBP**) with benzene 1,4-diboronic acid (**BDA**) and 4,4'-Biphenyldiboronic acid bis(pinacol) ester (**BDPE**) respectively (Figure 5.3). The resulting polymers have been characterized by solid-state ^{13}C -CP TOSS NMR, FT-IR and Thermo gravimetric analysis (TGA) (Figure 5.4). Solid-state NMR of **Py-PP** showed three peaks at 138.4, 136.2, and 126.7 ppm corresponding to the two types of un-substituted and substituted phenyl carbon atoms, respectively (Figure 5.4a). **Py-BPP** also showed similar set of peaks at 139.5, 132.7, and 126.5 ppm (Figure 5.4b). The structures with the pyrene-phenylene linkages are also evident from the FT-IR measurements, which showed signals corresponding to aromatic C=C stretch (1595 cm^{-1}), C=C vibrational modes (1390 and 1480 cm^{-1}) of the substituted phenyl rings and aromatic C-H stretch ($3030\text{--}3010\text{ cm}^{-1}$). In addition, IR signals corresponding to trace amounts of the

end functional $\text{B}(\text{OH})_2$ or OH groups (3300 cm^{-1}) and $\text{C}-\text{Br}$ (1005 cm^{-1}) are also observed (Figure 5.4c and d). TGA profiles of both the polymers showed excellent thermal stability up to $500\text{ }^\circ\text{C}$ for **Py-PP** and $350\text{ }^\circ\text{C}$ for **Py-BPP**. Observed weight loss at the initial stages ($\sim 200\text{ }^\circ\text{C}$) for both the polymers is attributed to the trapped solvent molecules (Figure 5.4e). N_2 gas adsorption experiments (77 K) of the polymers, desolvated at 483 K , showed a typical type-I profile of the isotherms with steep uptake at low pressure regions, suggesting the microporous nature of the networks with a maximum N_2 uptake of 792 mL/g for **Py-PP** (Figure 5.5a). The increase in N_2 uptake at $P/P_0 > 0.8$ in the adsorption isotherms can be attributed to the interparticulate porosity associated with the meso- and macrostructures of the sample in the bulk.⁷ The BET (Brunauer–Emmett–Teller) surface areas evaluated for **Py-PP** and **Py-BPP** are $1070\text{ m}^2/\text{g}$ and $350\text{ m}^2/\text{g}$ respectively. Furthermore, greenish yellow emission ($500\text{--}700\text{ nm}$) was observed for **Py-PP** with maximum at 540 nm , whereas green emission ($470\text{--}650\text{ nm}$) was observed for **Py-BPP** with maximum at 517 nm (Figure 5.5b). The red-shifted absorption and emission of these polymers compared to tetraphenyl pyrene ($\lambda_{\text{abs}} = 320\text{ nm}$ and $\lambda_{\text{em}} = 450\text{ nm}$)¹⁵ indicates the presence of extended conjugation in the polymer. These results indicate that these polymers combines both the microporous and luminescent functionalities, consistent with their design.

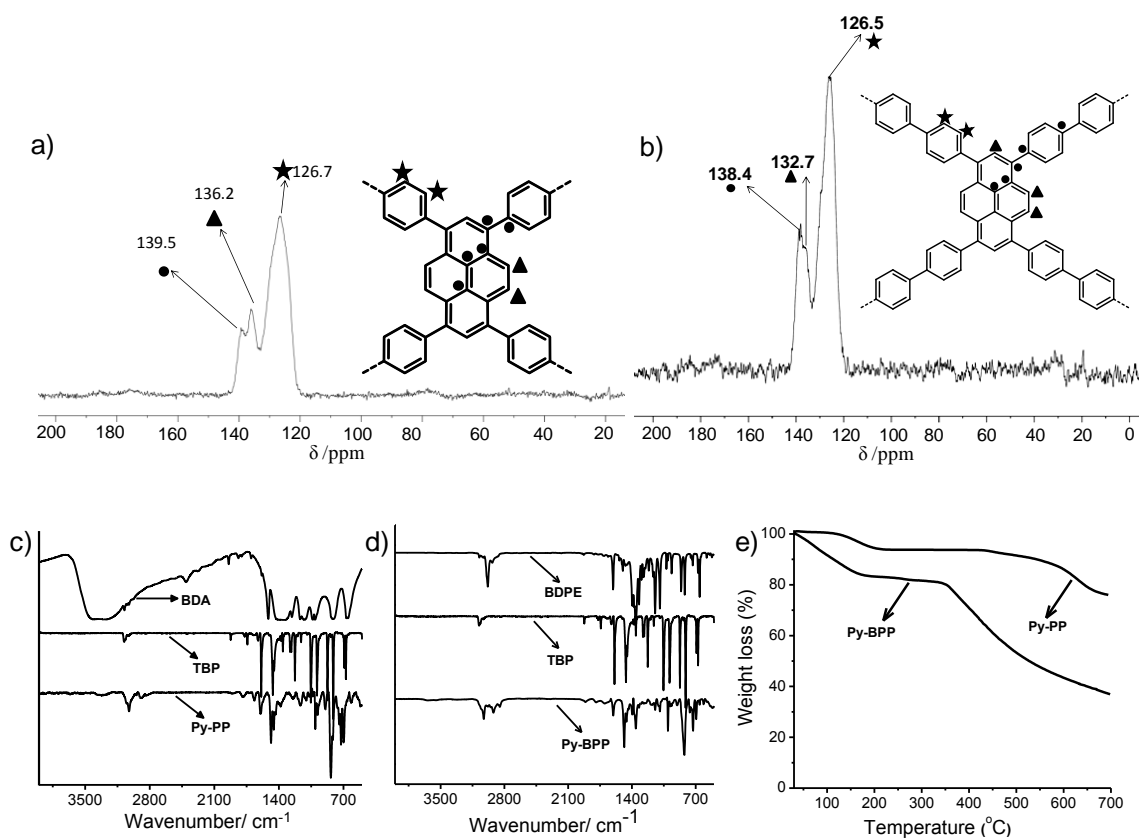


Figure 5.4. Solid state ^{13}C -CP TOSS NMR of a) **Py-PP** and b) **Py-BPP**. FT-IR spectra of c) **BDA**, **TBP** and **Py-PP**, and d) **BDPE**, **TBP** and **Py-BPP** measured in KBr . e) TGA profiles of **Py-PP** and **Py-BPP** measured under N_2 atmosphere.

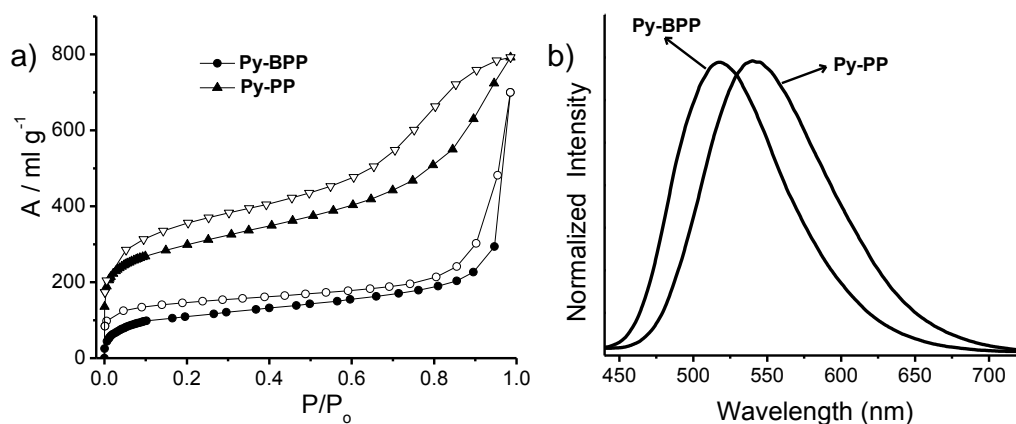


Figure 5.5. a) N_2 gas sorption isotherms (77 K) of the desolvated **Py-PP** and **Py-BPP** polymers (closed symbols show the adsorption and open symbols show the desorption). b) Solid-state emission spectra of **Py-PP** and **Py-BPP** powders.

5.3b Dynamic and Swelling Nature

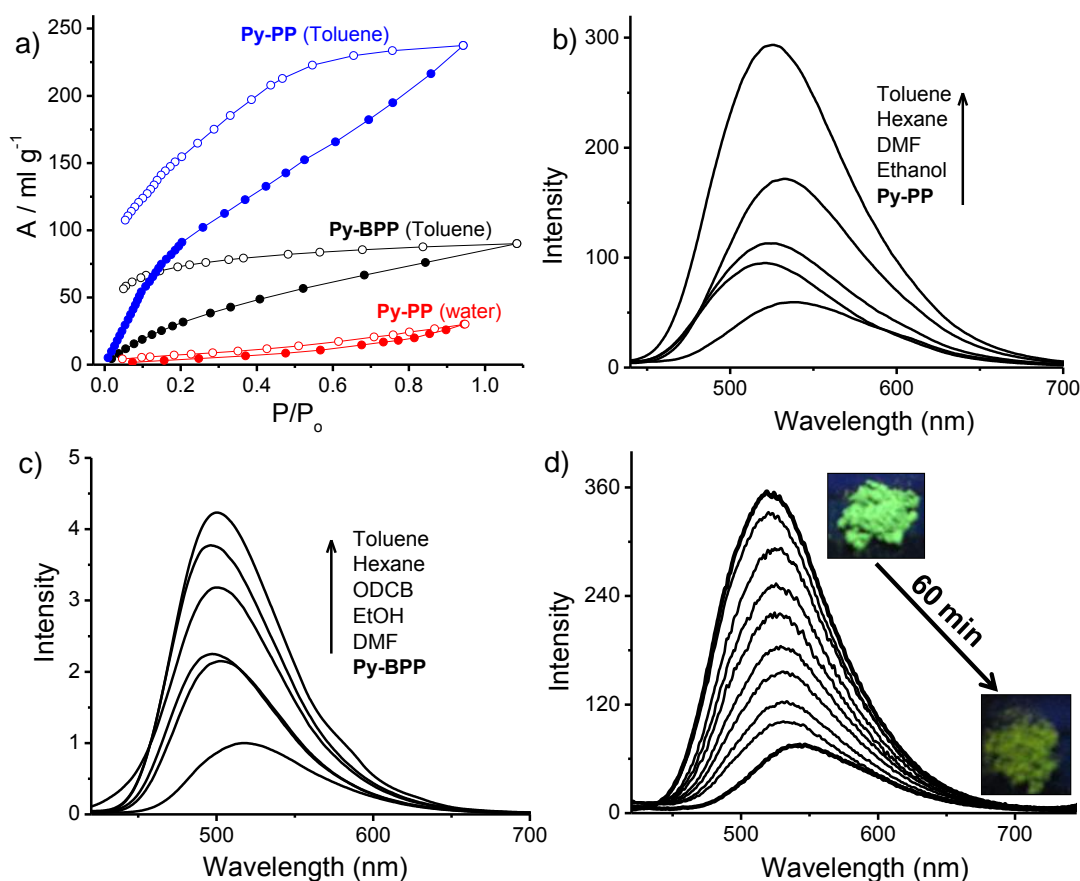


Figure 5.6. The dynamic nature of the polymers: a) Solvent adsorption isotherms of **Py-PP** and **Py-BPP** (toluene at 293 K and water at 298 K); the sample was degassed at 483 K before measurement and the equilibrium time was 500 s. Fluorescence enhancement of b) **Py-PP** and c) **Py-BPP** after treatment with different organic solvents. d) Time-dependent fluorescence response of **Py-PP** after treatment with toluene (inset: a photograph of the fluorescence change in **Py-PP**, 60 min after treatment with toluene, $\lambda_{exc} = 365$ nm). P_0 is the saturated vapour pressure of the respective adsorbates, fluorescence measurements were done with a front-face geometry, $\lambda_{exc} = 380$ nm.

The adsorption studies with toluene and water vapours (Figure 5.6) have provided insight into the dynamic nature and polarity of the both polymer networks. Though, the adsorption profiles showed significant uptake for toluene vapours, the pores were not accessible to water vapours (typical type II profile), which is consistent with the hydrophobic nature of the polymers (Figure 5.6a). The adsorption isotherms of toluene displays a rapid uptake at low relative pressures ($P/P_0 \sim 0.2$) followed by a monotonically increasing profile with the increase of pressure, which ended without saturation at $P/P_0 \sim 1$, indicating a structural transformation with gradual unfolding of the porous network. Furthermore, desorption isotherm does not retrace the adsorption resulting in a large hysteresis (Figure 5.6a). The incomplete desorption and large hysteresis suggests strong interaction of the toluene molecules with the pore surface and solvent-induced structural modification, thus unveiling the dynamic and soft characteristics of these polymers. Although ‘breathing’ in metal-organic frameworks upon gas uptake has been reported recently,⁹ this is the first time an amorphous porous polymers with solvent-responsive dynamic backbones, which would give interesting absorbent properties, have reported.

Table 5.2. Fluorescence lifetime data of **Py-PP** alone and with different organic guests.

| Sample Name | t_1 (ns) | t_2 (ns) | t_3 (ns) |
|------------------------|------------|------------|------------|
| Py-PP | 0.074 ns | 0.48 ns | 1.7 ns |
| Py-PP + Ethanol | 0.056 ns | 0.52 ns | 2.23 ns |
| Py-PP + DMF | 0.06 ns | 0.63 ns | 0.049 ns |
| Py-PP + Hexane | 0.1 ns | 1.2 ns | 3.5 ns |
| Py-PP + Toluene | 0.104 ns | 1.0 ns | 2.97 ns |
| Py-PP + ODCB | 0.1 ns | 1.17 ns | 3.5 ns |

Interestingly, both the polymers exhibited enhanced fluorescence with various organic solvents, reiterating the guest induced structural/conformational changes in its conjugated backbone (Figure 5.6b and c) and hence we have used their emission properties to further probe the dynamic nature of the network. In order to investigate this property, the desolvated polymers were exposed to various organic solvents and then emission spectra were recorded. In a typical experimental procedure, 20 mg of desolvated polymer was soaked in 1 mL of various anhydrous solvents for 5 minutes. The wet powder was then purged with nitrogen gas to ensure the removal of physically absorbed solvent molecules and finally the resultant powder sample was analyzed using a front-face fluorescent spectrometry setup ($\lambda_{exc} = 380$ nm). Solvent exposed powders of both the polymers showed visible color changes and bright green emission with an enhancement in fluorescence intensity with varying orders of magnitude depending on the solvent (Figure 5.6b and c). The emission spectra of the solvent-exposed

polymers showed a blue-shift (10-25 nm) with respect to the desolvated samples. The maximum fluorescence enhancement (4-5 times) was observed for aromatic non-polar solvent like toluene whereas the polar solvents like DMF and ethanol showed only 1.5-2 times enhancement in the emission. This was further supported by absolute quantum yield measurements on **Py-PP** and its solvent treated samples, which also showed a similar trend.¹⁶ For example, the percentage of absolute quantum yield of ODCB treated sample was 10%, which is nearly 8 times higher than that of the native **Py-PP** polymer (1.2%). Both the polymers did not show any fluorescence response with water, proving further the hydrophobic interior of the polymer. This guest-responsive emission could be attributed to reorganization in the framework due to reduced inter-molecular interactions induced by the hydrophobic solvent molecules. Time dependent steady-state fluorescence measurements of solvent exposed **Py-PP** showed that the emission maxima slowly (with in 1 h for toluene) shifts back to the red-shifted emission of desolvated framework clearly suggesting the reversibility of guest-induced breathing of the **Py-PP** framework (Figure 5.6d).¹⁷ Time-resolved decay emission measurements carried with **Py-PP** further proved the changes in local environment of pyrene chromophores on expansion of the network with guest molecules (Table 5.2). The decay profiles were best fitted by a tri-exponential function and significant increase in the lifetime was observed with non-polar solvents (*eg.* for toluene 0.1, 1.0 and 2.97 ns) which is consistent with the increase in emission intensity, compared to that of desolvated **Py-PP** (0.07, 0.48, and 1.7 ns). However, no significant changes in lifetimes were observed with polar solvents like DMF and ethanol.

The amorphous and dynamic porous features of these polymers promoted us to investigate their absorbent behaviour with solvent/guest molecules. Interestingly, both the polymers exhibited remarkable solvent uptake and resultant swelling in presence of various organic solvents. In addition, the solvent uptake is accompanied by a simultaneous increase in fluorescence of the frameworks, suggesting the crucial role of flexible backbone in the swelling process (Figure 5.7a and b). We have systematically studied the swelling behaviour of both the polymers in organic solvents of various polarities in terms of their equilibrium state of swelling parameter (Q%) and equilibrium solvent content (H%),^{3a} that are calculated from the weight of dried and swollen polymers (Figure 5.7c and d). Figure 5.7a and b shows the dried powder and swollen polymers in ODCB for **Py-PP** and in toluene for **Py-BPP** and their swelling parameters are summarized in Figure 5.7c and d. The swelling parameter and the solvents content varied between 900-3000 and 90-99 respectively, for various organic solvents under investigation suggesting the superabsorbent nature of both the polymers.³ Starting from the nonpolar hexane, the swelling degree increased with increasing solvent polarity, and the maximum swelling was observed for chloroform. The difference in the swelling parameters between relatively non-

polar solvents like hexane and toluene suggests that, size and shape of the guest molecules along with its π - π interaction with the aromatic host framework are crucial for efficient swelling. For example, **Py-PP** immobilizes ODCB to roughly 20 times to its own native weight whereas it can trap hexane only up to 9 times. Then, the swelling degree decreased with increasing solvent polarity and the polymer did not swell with water, which is consistent with the hydrophobic aromatic framework structure of the polymers. Noticeably, the swelling process was instantaneous compared to classical polymer absorbents and was stable for months. Furthermore, this process could be repeated many times using recycled polymers after the desolvation process under vacuum. In addition, we have observed that the swelling process was more efficient while sonication or stirring and green fluorescent gel-like, self-standing materials were formed within seconds, with only 4 wt% of **Py-PP** in ODCB and 10% of **Py-BPP** in toluene (Figure 5.7a and b). Although the micropores of these polymers are robust for the diffusion of small gas molecules (*vide supra*), solvation results in the structural re-organization of the aromatic frameworks, resulting in the observed macroscopic swelling. This instantaneous swelling and fluorescence enhancement are hitherto unknown features in microporous polymers and provides an opportunity to exploit these polymers as selective absorbent and sensory materials.

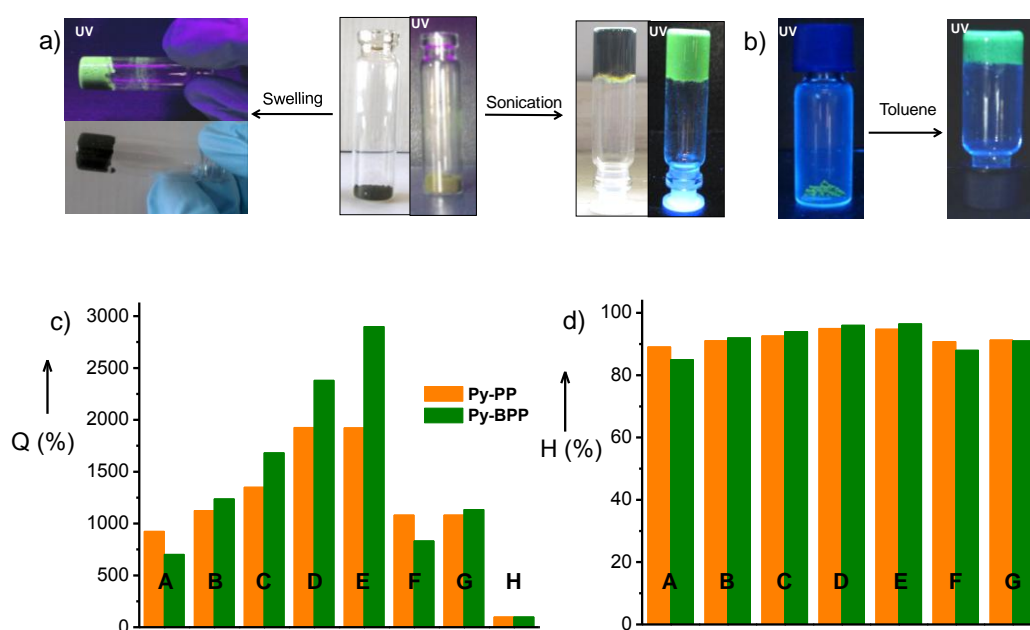


Figure 5.7. Swelling properties of the polymers; a) Photographs of the swelling of **Py-PP** powder without and with sonication in ODCB, under normal and 365 nm UV light. b) Photographs of the swelling of **Py-BPP** powder without and with toluene, under 365 nm UV light. Swelling behaviour of polymers expressed in terms of c) Q (%) and d) H (%), in various organic solvents with different polarities (A: hexane, B: diesel, C: toluene, D: ODCB, E: chloroform, F: ethanol, G: DMF, H: water).

5.3c Oil Removal and Recovery from Water

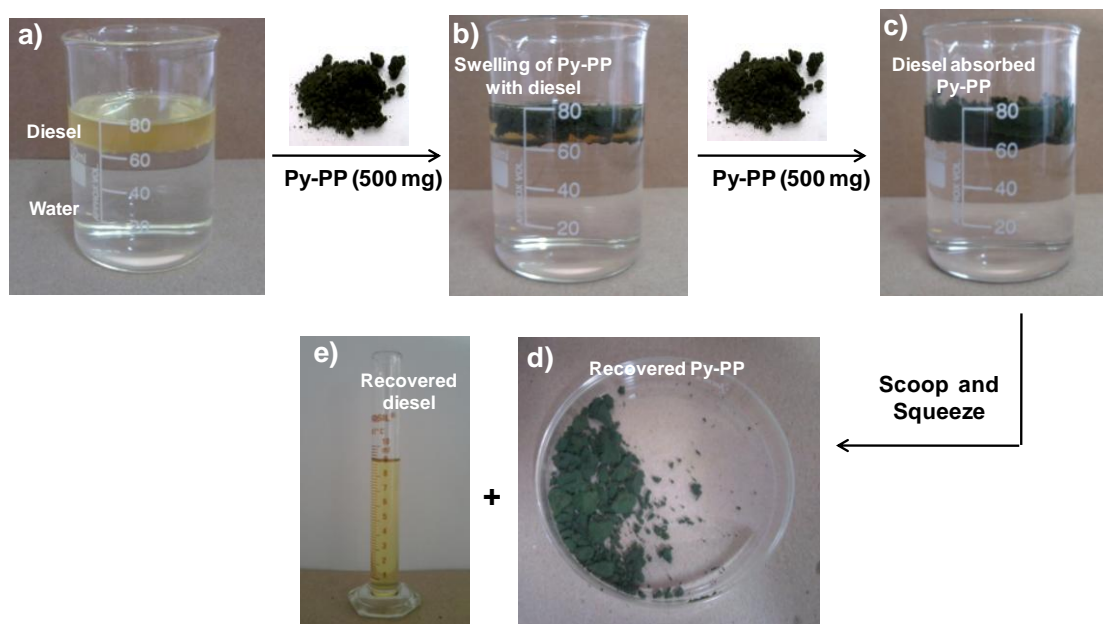


Figure 5.8. Phase-selective swelling of **Py-PP**; a-c) shows the swelling of diesel upon sequential addition of **Py-PP** (1 g) to a beaker containing diesel-water mixture. d) and e) shows the recovered polymer and diesel, respectively by simple squeezing of the scooped material. (Composition of the initial mixture: water = 62 mL, diesel = 18 mL).

Having understood their structural features, we were further interested in the functional aspects characteristic of its hydrophobic and dynamic pores. The significant uptake of diesel-oil by both the polymers motivated us to attempt the phase-selective capture of oil in presence of water, which is of great current technological interest for the cleaning up and recovery of oil from marine spills.¹⁸ This has been demonstrated with a prototype experiment performed with **Py-PP**. Remarkably, in a typical demonstration experiment, when **Py-PP** (1.0 g) was added into a diesel-water mixture (1:3.5 volume ratio), the uniformly spread polymer powder quickly absorbed the diesel and swelled while repelling the water (Figure 5.8). As shown in Figure 5.8, **Py-PP** showed uptake capacities up to 12 times its weight for the collection of diesel. Most importantly, the swelled polymer could be easily scooped out and both the polymer and diesel (50-60%) were recovered by simple mechanical squeezing, leaving the water without any traces of oil. Recovery of the diesel could be made almost quantitative when distillation procedure was adopted. We have also observed phase-selective swelling for other oils and hydrocarbon solvents. The instantaneous spreading and swelling action of **Py-PP**, would be very attractive as a simple room temperature strategy for oil recovery, without impractical heating and mechanical stirring procedures.

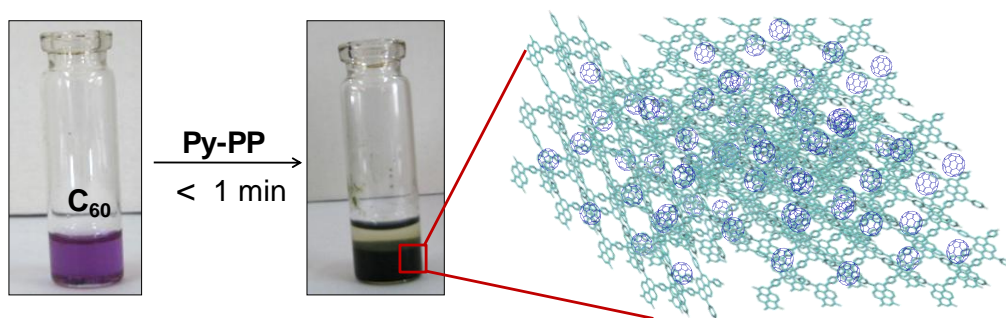
5.3d Encapsulation of C₆₀ and Photoinduced Electron Transfer

Figure 5.9. Photographs of saturated toluene solution of C₆₀ before and after treating with **Py-PP** and schematic representation of C₆₀ loaded **Py-PP** (Concentration of C₆₀ in toluene = 2 mg/mL).

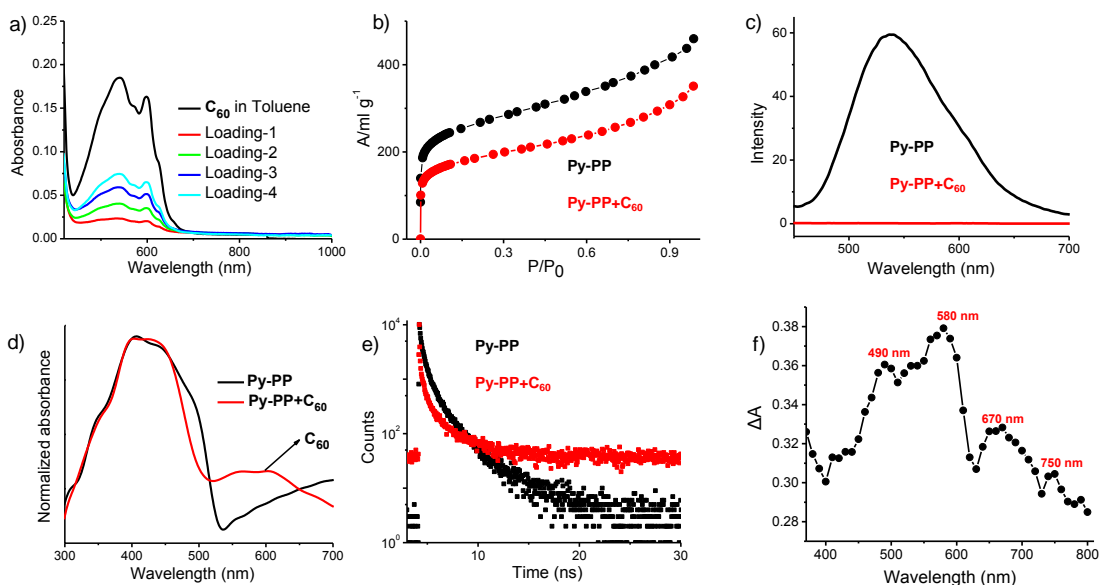


Figure 5.10. a) Absorption spectra of saturated toluene solutions of C₆₀ before and after sequential treatment with **Py-PP**. b) N₂ adsorption isotherms (77 K), c) solid-state emission spectra, d) absorption spectra and e) picosecond lifetime decay profiles (monitored at 540 nm) of **Py-PP** powder with (red line) and without (black line) C₆₀ (P_0 is the saturated vapour pressure of the gas at 77 K, fluorescence measurements were done with a front-face geometry, $\lambda_{exc} = 380$ nm). f) Nanosecond transient absorption spectrum of **Py-PP-C₆₀** adducts dispersion in chloroform. The 490 nm peak can be assigned to the pyrene radical cation and the broad absorption in the 500-700 nm could be due to the S_1-S_n transitions of pyrene.

The electron rich and curved π -surface of polymer porous backbones motivated us to investigate its encapsulation of convex-shaped fullerene (C₆₀), a well-known electron acceptor molecule. Several well-defined molecular and co-ordination cages have been extensively studied for the encapsulation of fullerene derivatives in solution, through specific host-guest interactions, which is often a slow process.^{1b,19} However, extended porous solids for C₆₀ uptake, which would provide an assembled array of fullerenes, are seldom reported.^{19a} We have demonstrated absorbing of C₆₀ molecules from toluene solution with **Py-PP** polymer.

Remarkably, when **Py-PP** was soaked in a pale purple coloured saturated toluene solution (~2.7 mM) of C_{60} , the solution immediately (< 1 min) became colourless, suggesting the efficient and instantaneous encapsulation of C_{60} molecules inside the porous network (Figure 5.9). This is further evident from the reduction in the absorbance of fullerene in the UV spectra of residual solution (Figure 5.10a). This process could be repeated 3-4 times with the same polymer sample to finally result in 15 wt% encapsulation of the C_{60} . Definitive proof for the C_{60} encapsulation was provided by the N_2 adsorption measurements of desolvated **Py-PP- C_{60}** adducts, which showed 20% decrease in the BET surface area against the pure **Py-PP** without guest molecules (Figure 5.10b). The corresponding pore volume decreases from $0.71 \text{ cm}^3/\text{g}$ of as-synthesized desolvated **Py-PP**, to $0.54 \text{ cm}^3/\text{g}$ in **Py-PP- C_{60}** adducts. The fluorescence of the fullerene encapsulated **Py-PP** was completely quenched, with no evidence for ground state charge-transfer interaction, suggesting the excited state electron/energy transfer process from pyrene to the C_{60} as reported in literature for many pyrene-fullerene conjugates (Figure 5.10c and d).²⁰ This is further evident from the quenching of fluorescence lifetime of the pyrene donor in presence of the C_{60} (Figure 5.10e, Table 5.3). Nanosecond laser flash photolysis studies on **Py-PP- C_{60}** dispersion, showed the presence of pyrene radical cation at 490 nm, indicating photoinduced electron transfer from the framework to the encapsulated C_{60} guest molecules (Figure 5.10f).²¹

Table 5.3. Picosecond lifetime data of **Py-PP** with and without C_{60} .

| Sample Name | t_1 (ns) | t_2 (ns) | t_3 (ns) |
|------------------------------------|-------------------|-------------------|-----------------|
| Py-PP | 0.074 ns (32.5 %) | 0.48 ns (36.8 %) | 1.7 ns (30.7 %) |
| Py-PP + C_{60} | 0.056 ns (24.5 %) | 0.038 ns (44.5 %) | 2.9 ns (30.0 %) |

5.3e Fluorescence as a Probe for Guest Encapsulation

The polymers with dynamic backbones should exhibit a blue shifted emission upon guest encapsulation (*vide supra*). We envisaged that if we could swell the network with a red shifted fluorescent dye molecule, we can clearly use the emission of host frameworks as a probe for guest encapsulation. For this purpose, we encapsulated both the frameworks with different wt% of **NR** and **DCM** in the same way as C_{60} . Interestingly, along with the continuous blue shift in the emission of **Py-BPP** there is a quenching in emission intensity was observed with increase of **NR** wt% from 0-1.0 (Figure 5.11). The fluorescence quenching is due to the energy transfer (*vide infra*) to the guest molecules and blue shift is due to the swelling of polymer network (*vide supra*). Initially a 13 nm blue shift in **Py-BPP** emission was observed with 0.1 wt% of **NR** loading which is further blue shifted to 36 nm with 0.5 wt% of **NR** and finally reached 40 nm with 1 wt% loading of **NR** (517 nm to 477 nm) (Figure 5.11a).

When **Py-BPP** treated with different solvents, maximum 15 nm blue shift was observed due to swelling. Similarly, blue shifts up to 45 nm were observed in case of **Py-PP** emission with 1 wt% of loading **NR** (Figure 5.11b).

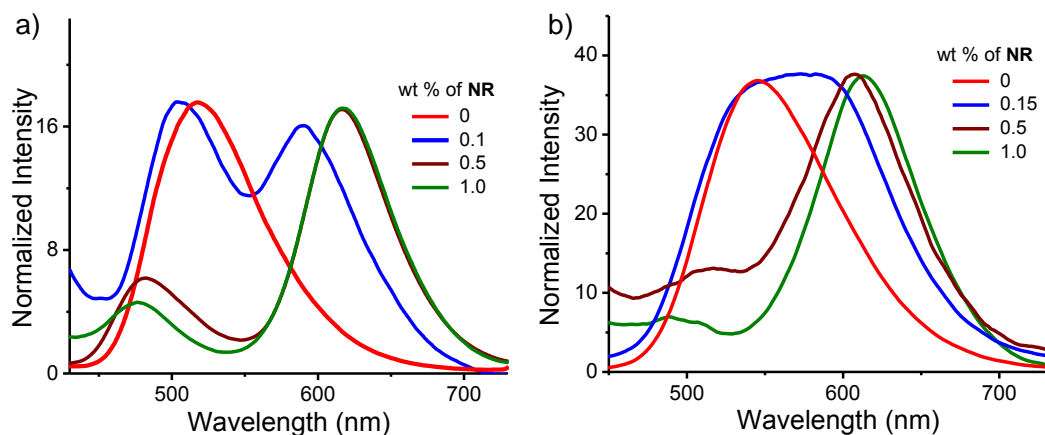


Figure 5.11. Normalized emission spectra of a) **Py-BPP** and b) **Py-PP** with different wt% of **NR** loading.

These studies suggest that pyrene derived dynamic frameworks are capable of encapsulating wide variety of guest molecules with varying emission response. Furthermore, their swelling behaviour was not only limited to small solvent molecules but they are also able to absorb photo-functional compounds such as **DCM**, **NR** and **C₆₀**. More interestingly, except water they could efficiently absorb a variety of solvents ranging from zero polar solvents (hexane and diesel oil) to highly polar solvents (DMF and Ethanol). The ability of these polymers to absorb wide variety of guest molecules, irrespective of their size and polarity is due to its dynamic porous framework which has the capability to reorganise. Further, they promote photoinduced energy or electron transfer processes with photoactive guests.

5.3f POPs as Light-Harvesting Scaffolds

The dynamic and guest responsive behaviour of these pyrene based polymers encouraged us to swell them with appropriate luminescent hydrophobic dyes to facilitate Förster type energy transfer (FRET) from the pyrene framework to the guest molecules. Energy transfer was shown in porous organic polymers in which non-covalent encapsulation of guest requires overnight stirring at high temperatures.^{2d} Since visible light-harvesting is preferred for many practical applications, we have used red emitting **DCM** as acceptor to harvest visible excitation energy from **Py-PP** and **Py-BPP**. In our case, the dynamic and swelling nature of these polymers allowed facile encapsulation of **DCM**. Toluene was used as a mediating solvent for guest encapsulation due to good solubility of **DCM** and excellent swelling behaviour of the polymers in this solvent. In a typical experimental procedure different amounts of dye were dissolved in 0.5 mL toluene and added to 30 mg of polymers. The resultant swelled polymer-

dye composites were kept at room temperature for 30 min and dried at room temperature as well as in vacuum to remove the toluene, completely. The resultant powders loaded with different wt% of **DCM** were used for optical measurements. The gradual luminescence changes in the polymer powders with increasing guest loading further confirm their encapsulation within the porous cavities of the polymers. Furthermore, we could achieve control over distribution of guest molecules as isolated and aggregated species, inside the porous networks of the polymers.

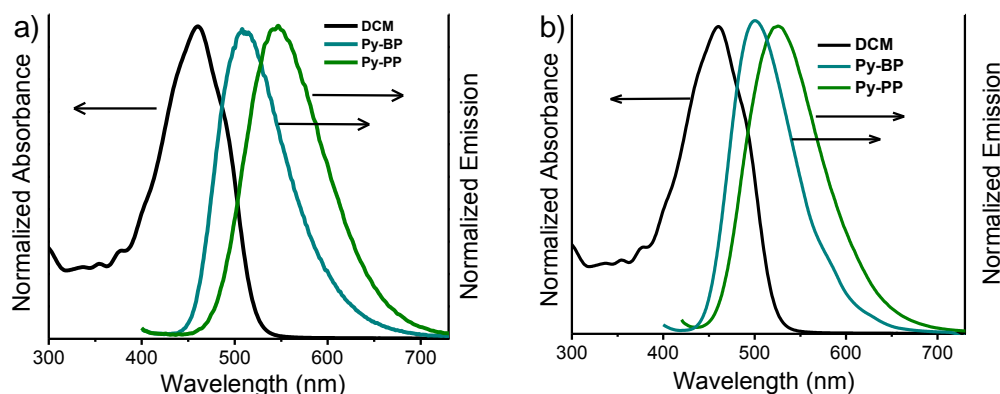


Figure 5.12. Normalized absorption spectra of **DCM** (in toluene) with the emission spectra of **Py-BPP** and **Py-PP** a) before, and b) after swelling in toluene.

The good spectral overlap between emission of **Py-BPP** and **Py-PP** polymer powders with the absorption of **DCM** dye indicates that it would be possible to make visible light-harvesting antenna using simple host-guest chemistry (Figure 5.12). Energy transfer experiments were performed with varying amounts of **DCM** loading (0-10 wt%) inside the porous network of the polymers. As the amount of encapsulated **DCM** (0-10.0 wt%) increases, gradual quenching in the emission of both the donor frameworks with concomitant increase in the **DCM** emission (600-700 nm) intensity was observed (Figure 5.13). This gives an indication of excitation energy transfer from host frameworks (**Py-BPP** and **Py-PP**) to the entrapped dye molecules. Moreover, the absence of vibronic features in the **DCM** emission when it was loaded into the pore channels of **Py-BPP** and **Py-PP** confirms the existence of orientational dipolar interactions between **DCM** and aromatic shells of host frameworks.²² These kinds of dipolar interactions are indeed important to achieve efficient Förster type energy transfer. This inherent property of **DCM** to show orientational dipolar interactions with aromatic and polar solvents is added advantage in addition to dynamic behaviour of **Py-BPP** and **Py-PP** in the construction of present visible light-harvesting antenna. In these host-guest systems, 2.0-2.5 wt% of guest was able to completely harvest the excitation energy from host frameworks (Figure 5.13a and b). The observed gradual red-shift in the emission maxima of encapsulated **DCM** molecules (up to 30 nm) with increasing its concentration are attributed to the formation of **DCM** aggregates inside the pores at higher amounts of loading (~10 wt%). Emission

spectra, collected for different wt% of **DCM** loaded polymers indicates that, at below 2wt% of **DCM** energy transfer is mainly to its isolated species (**DCM**, $\lambda_{\text{max}} = 570$ nm), where all **DCM** molecules are spatially distributed inside the pore channels (Figure 5.13a and b). Above 2 wt% of **DCM** loading leads to the energy transfer mostly to its aggregated species ($\lambda_{\text{max}} = 604$ nm). This was further rationalized by the observed amplified fluorescence of **DCM** by energy transfer in this host-guest system (Figure 5.13c and d). In case of **Py-BPP** loaded with 10 wt% of the **DCM**, excitation at 380 nm (indirect excitation) results in nearly 2 times higher **DCM** emission due to energy transfer, compared to its direct excitation at 500 nm (Figure 5.13c). Similarly 2.5 times amplification in the **DCM** emission was observed in case of **Py-PP** loaded with 2.5 wt% of **DCM** (Figure 5.13d). This clearly indicates that the enhancement in the emission of both isolated and aggregated **DCM** molecules inside the pores is indeed due to resonance energy-transfer.

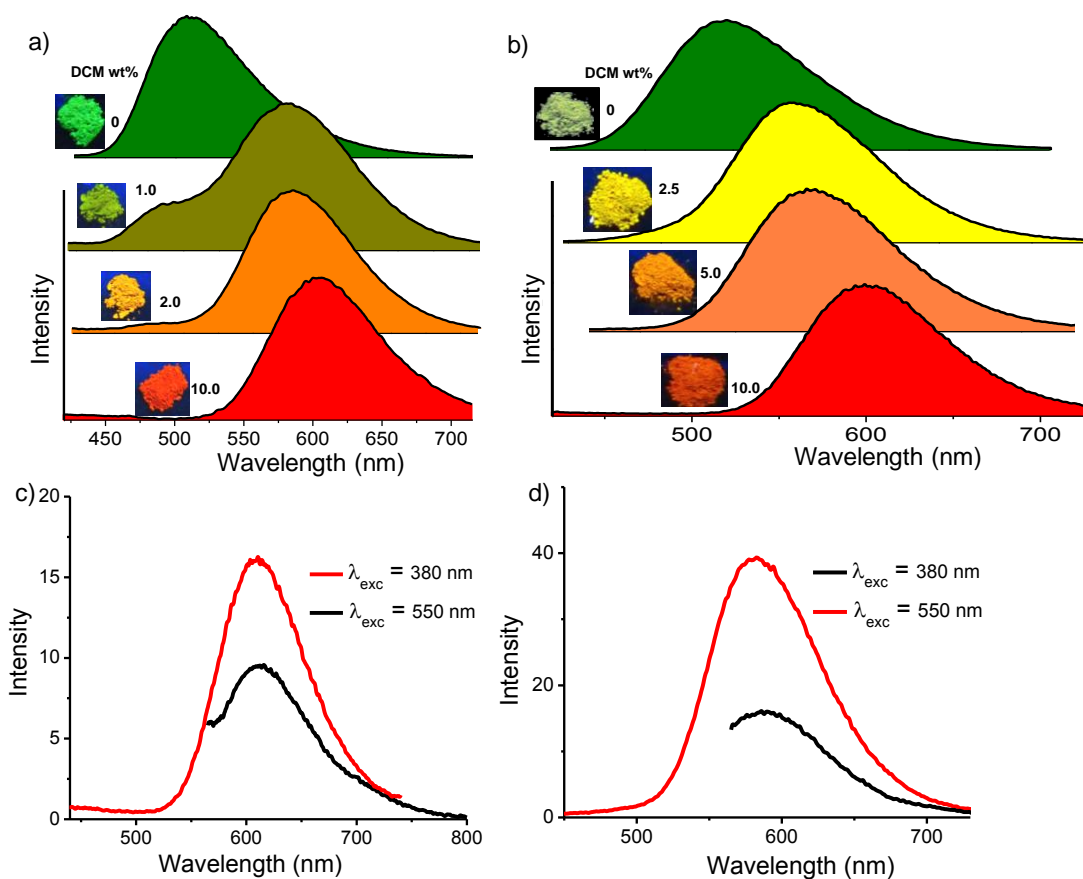


Figure 5.13. Normalized emission spectra of a) **Py-BPP** and b) **Py-PP** loaded with different wt% of **DCM**. Insets show the photographs of **Py-BPP** (inset of 5.13a) and **Py-PP** (inset of 5.13b) powders under 365 nm UV light loaded with different wt% of **DCM** (fluorescence measurements were done with a front-face geometry, $\lambda_{\text{exc}} = 380$ nm). Emission spectra of directly ($\lambda_{\text{exc}} = 380$ nm) and indirectly ($\lambda_{\text{exc}} = 500$ nm) excited c) **Py-BPP** loaded with 10.0 wt% and d) **Py-PP** loaded with 2.5 wt% of **DCM** dye.

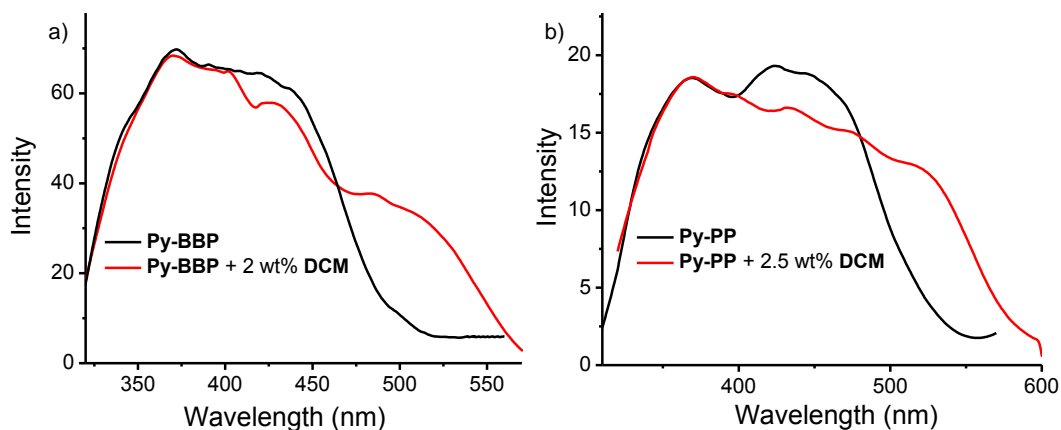


Figure 5.14. Excitation spectra of a) **Py-BBP** powder with (monitored at 650) and without (monitored at 540) **DCM**. Excitation spectra of b) **Py-PP** powder with (monitored at 650) and without (monitored at 560) **DCM**.

Energy transfer was further supported by excitation spectra collected at both polymers and **DCM** emission wavelengths (Figure 5.14). The appearance of absorption features of both polymer and **DCM** in the excitation spectra collected for both **Py-BBP-DCM** and **Py-BBP-DCM** host-guest systems at **DCM** emission (650) wavelength, where polymers have negligible emission, further supports population of **DCM** excited states via energy transfer from host polymers (Figure 5.14). Furthermore, the controlled loading of **DCM** molecules inside the polymers leads to the tunable emission from green to red followed by yellow. This is visually shown in the photographs taken under 365 nm UV-irradiation of **Py-BBP** and **Py-PP** powders loaded with different wt% of **DCM**. As shown in the insets of Figure 5.13a, **Py-BBP** alone is green emissive, with 1 wt% of **DCM** loading leads to greenish yellow, at 2 wt% it is yellow and finally at 10 wt% the polymer is orange-red emissive. Similar colour trends were seen in case of **Py-PP** loaded with different wt% of **DCM** in the insets of Figure 5.13b.

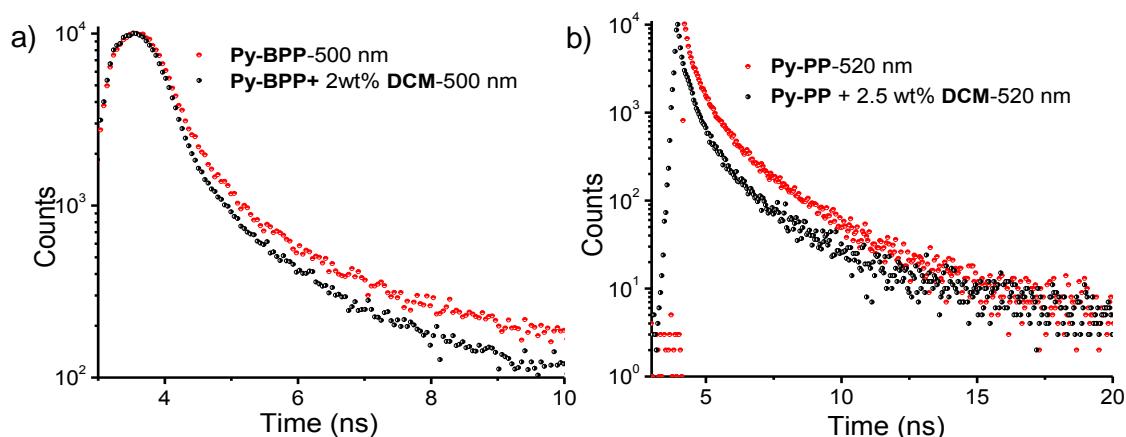


Figure 5.15. Lifetime decay profiles of a) **Py-BBP** and b) **Py-PP** alone and with **DCM** (lifetime measurements were done with a front-face geometry, $\lambda_{exc} = 380$ nm). Wavelengths in graphs indicate the where decay profiles were monitored.

Further investigation on fluorescence lifetime and absolute quantum yields of host-guest polymers provided decisive proof for the resonance energy transfer from host frameworks to the guest molecules without any radiation reabsorption process (Figure 5.15). The lifetime decay profiles were fitted with tri exponentials and average lifetime was considered for the analysis. **Py-BPP** framework with an average lifetime of 2.49 ns in its solid state, decreased to 2.1 ns (monitored at 500 nm) after loading with 2 wt% of **DCM** (Figure 5.15a). Similarly, the average lifetime of **Py-PP** also shortened from 0.72 ns to 0.58 ns (monitored at 520 nm) with 2.5 wt% of **DCM** loading (Figure 5.15b). This decrease in the excited state lifetimes of host frameworks upon encapsulation of **DCM** is a clear indication of excited state energy transfer mechanism for fluorescence quenching of host frameworks. Absolute quantum yield measurements further gave quantitative picture for the efficiency of energy transfer process. The high absolute quantum yield ($\phi = 0.56\%$) of **DCM** (2 wt%) loaded **Py-BPP** compared to the individual **Py-BPP** ($\phi = 0.31\%$) and **DCM** ($\phi = 0.24\%$) indicates efficient resonance energy transfer without radiation reabsorption process. The calculated energy transfer efficiency ($\eta_{ET} = 1 - \phi(0)/\phi(w)$) is 44 % where $\phi(w)$ and $\phi(0)$ are the absolute quantum yields of the **Py-BPP** with and without **DCM** respectively. Similarly, higher absolute quantum yield (0.83%) was observed for **Py-PP** loaded with **DCM** (2.5 wt%) than individual **Py-PP** (0.42%) and **DCM** (0.24%) with ~49 % energy transfer efficiency.

5.4 Conclusions

In conclusion this work introduces a novel class of multi-functional organic microporous polymers, in which the porous fluorescent frameworks can undergo swelling in presence of hydrophobic and aromatic guests. This remarkable guest-induced breathing of hydrophobic pores imparted unprecedented properties, such as super-absorbency and phase-selective swelling of oil from water, for these microporous organic polymers. Furthermore, the fluorescent and electron donor pyrene scaffold combined with the dynamic porosity facilitated guest-induced emission changes and encapsulation of C_{60} acceptor molecules and luminescent hydrophobic guests which holds great promise for applications in sensors. Efficient visible light-harvesting and band gap engineering was observed for these polymers with encapsulated red emitting **DCM** dye molecules. The unique ability of these polymers to encapsulate various guest molecules with fluorescence response behaviour holds a great promise in designing smart materials for sensing and separation.

5.5 Experimental Section

General methods: Electronic emission spectra were recorded on Perkin Elmer Ls55 Luminescence Spectrometer. Fluorescence spectra of solid powders were recorded in front-face

geometry with 380 nm wavelength. The absolute fluorescence quantum yield of the **Py-PP** and its solvent treated samples have been calculated according to the reference 16. Laser Flash photolysis was carried out using a Nd:YAG laser source producing nanosecond pulses (8 ns) of 355 nm light with the energy of the laser pulse being around 200 mJ. Dichroic mirrors were used to separate the third harmonic from the second harmonic and the fundamental output of the Nd-YAG laser. The monitoring source was a 150W pulsed xenon lamp, which was focused on the sample at 90° to the incident laser beam. The beam emerging through the sample was focused onto a Czerny-Turner monochromator using a pair of lenses. Detection was carried out using a Hamamatsu R-928 photomultiplier tube. Transient signals were captured with an Agilent infinium digital storage oscilloscope and the data was transferred to the computer for further analysis. Solid state ¹³C NMR CPTOSS measurements were performed on Bruker Avance 400 (400 MHz) spectrometer with MAS rate of 5 kHz. Infrared (IR) spectra were recorded on small amount of the samples embedded in KBr pellets using a Bruker FT-IR spectrometer. Thermogravimetric analysis (TGA) was carried out (Mettler Toledo) in nitrogen atmosphere (flow rate 50 mLmin⁻¹) in the temperature range 30–700 °C (heating rate 5 °C/min). CHNS analyses were carried out using Thermo Scientific Flash 2000 Elemental Analyzer. Powder XRD pattern of the compounds were recorded by in Bruker D8 Discover (40 kV, 30 Ma) instrument using Cu K α radiation ($2\theta = 0.8\text{--}60^\circ$).

Computational details: The tetraphenyl pyrene monomer was optimized using Gaussian-09 suite of programs.²³ The optimization was carried out within Density Functional Theory (DFT) using B3LYP³ hybrid exchange-correlation functional and 6-31G basis set. The optimised geometries were visualised using Visual Molecular Dynamics (VMD).²⁴

Adsorption measurements: N₂, adsorption study of the degassed samples of about 150 mg for a period of 18 hours under high vacuum (10⁻¹ pa), were carried out using QUANTACHROME QUADRASORB-SI analyzer at 77 K. The adsorbates were charged into the sample tube, and then the change of the pressure was monitored, the degree of adsorption was determined by the decrease of the pressure at the equilibrium state. All operations were computer-controlled and automatic.

H (%) and *Q (%)* of the polymers are calculated using following equations.

$$H(\%) = (W_{\text{wet}} - W_{\text{dry}}) / W_{\text{wet}} \times 100$$

$$Q(\%) = W_{\text{wet}} / W_{\text{dry}} \times 100$$

Where *W_{wet}* = Weight of the polymer after swelling in the solvents and

W_{dry} = Weight of the dry polymer

5.5a Synthesis

Compounds **TBP**, **BDA** and **BDPE** were purchased from Aldrich.

Synthesis of Py-PP: A mixture of **TBP** (0.19 mmol) and benzene 1,4-diboronic acid (**BDA**, 0.38 mmol) in DMF (20 mL) was degassed by four freeze-pump-thaw cycles. To this mixture 2M K₂CO₃ in water (2 mL) and tetrakis(triphenylphosphine)-palladium(0) (45 mg, 38.9 μmol) were added followed by degassing by four freeze-pump-thaw cycles. After that the resultant mixture was purged with Ar for 3 times and stirred at 150 °C in a schlenk flask for 36 h. After cooling to room temperature the mixture was poured into water and filtered. The precipitate was washed with methanol, dichloromethane and dried in vacuum. The precipitate was further purified by soxhlet extractions with methanol, dichloromethane, toluene and tetrahydrofuran for 12 h each to give the product as a dark green solid (150 mg). Solid-state ¹³C NMR (100 Mz, δ; ppm): 126.7, 136.2, 139.5; FT-IR (ν; cm⁻¹): 3325, 3060, 3010, 1595, 1480, 1450, 1390, 1175, 1051, 1004, 834, 702; Elemental Analysis (%) calculated for C₂₈H₁₄: C 95.617, H 4.383; found: C, 86.72; H, 4.34.

Synthesis of Py-BPP: A mixture of **TBP** (0.19 mmol) and 4,4'-Biphenyldiboronic acid bis(pinacol) ester (**BDPE**, 0.19 mmol) in DMF (20 mL) was degassed by four freeze-pump-thaw cycles. To this mixture 2M K₂CO₃ in water (2 mL) and tetrakis(triphenylphosphine)-palladium(0) (45 mg, 38.9 μmol) were added followed by degassing by four freeze-pump-thaw cycles. After that the resultant mixture was purged with Ar for 3 times and stirred at 150 °C in a schlenk flask for 36 h. After cooling to room temperature the mixture was poured into water and filtered. The precipitate was washed with methanol, dichloromethane and dried in vacuum. The precipitate was further purified by soxhlet extractions with methanol, dichloromethane, toluene and tetrahydrofuran for 12 h each to give the product as a green solid (140 mg). Solid-state ¹³C NMR (100 Mz, δ; ppm): 126.5, 132.7, 138.4; FT-IR (ν; cm⁻¹): 3025, 2913, 1602, 1485, 1359, 1145, 1095, 1004, 823, 728; Elemental Analysis (%) calculated for C₄₀H₂₂: C 95.617, H 4.383; found: C 89.47; H 4.42.

5.6 References

1. a) M. Yoshizawa, J. K. Klosterman, M. Fujita, *Angew. Chem. Int. Ed.* **2009**, *48*, 3418. b) K. Suzuki, K. Takao, S. Sato, M. Fujita, *J. Am. Chem. Soc.* **2010**, *132*, 2544; c) Y. Inokuma, M. Kawano, M. Fujita, *Nat. Chem.* **2011**, *3*, 349.
2. a) S. Wan, J. Guo, J. Kim, H. Ihee, D. Jiang, *Angew. Chem. Int. Ed.* **2009**, *48*, 5439; b) S. Wan, J. Guo, J. Kim, H. Ihee, D. Jiang, *Angew. Chem. Int. Ed.* **2008**, *47*, 8826; c) S. Inagaki, O. Ohtani, Y. Goto, K. Okamoto, M. Ikai, K. Yamanaka, T. Tani, T. Okada,

- Angew. Chem. Int. Ed.* **2009**, *48*, 4042; d) L. Chen, Y. Honsho, S. Seki, D. Jiang, *J. Am. Chem. Soc.* **2010**, *132*, 6742; e) X. Zhang, M. A. Ballem, M. Ahr, A. Suska, P. Bergman, K. Uvdal, *J. Am. Chem. Soc.* **2010**, *132*, 10391; f) X. Zhang, M. A. Ballem, Z.-J. Hu, P. Bergman, K. Uvdal, *Angew. Chem. Int. Ed.* **2011**, *50*, 5729; g) K. V. Rao, K. K. R. Datta, M. Eswaramoorthy, S. J. George, *Angew. Chem. Int. Ed.* **2011**, *50*, 1179; h) S. S. Babu, K. K. Kartha, A. Ajayaghosh, *J. Phys. Chem. Lett.* **2010**, *1*, 3413; i) S. S. Kaye, A. Dailly, O. M. Yaghi, J. R. Long, *J. Am. Chem. Soc.*, **2007**, *129*, 14176.
3. a) K. Matyjaszewski, K. L. Beers, A. Kern, S. G. Gaynor, *Journal of Polymer Science: Part A: Polymer Chemistry* **1998**, *36*, 823; b) T. K. Mudiyansele, D. C. Neckers, *Journal of Polymer Science: Part A: Polymer Chemistry* **2008**, *46*, 1357; c) T. Ono, T. Sugimoto, S. Shinkai, K. Sada, *Adv. Funct. Mater.* **2008**, *18*, 3936; d) W. Ni, F. Liang, J. Liu, X. Qu, C. Zhang, J. Li, Q. Wang, Z. Yang, *Chem. Commun.* **2011**, *47*, 4727; e) A. Ajayaghosh, V. K. Praveen, *Acc. Chem. Res.* **2007**, *40*, 644; f) F. J. M. Hoeben, P. Jonkheijm, E.W. Meijer, A. P. H. J. Schenning, *Chem. Rev.* **2005**, *105*, 1491; g) F. Würthner, C. Bauer, V. Stepanenko, S. Yagai, *Adv. Mater.* **2008**, *20*, 1695.
4. a) S. R. Jadhav, P. K. Vemula, R. Kumar, S. R. Raghavan, G. John, *Angew. Chem. Int. Ed.* **2010**, *49*, 7695; b) J. Yuan, X. Liu, O. Akbulut, J. Hu, S. L. Suib, J. Kong, F. Stellacci, *Nat. Nanotechnol.* **2008**, *3*, 332; c) S. Bhattacharya, Y. Krishnan-Ghosh, *Chem. Commun.* **2001**, 185; d) P. Dastidar, *Chem. Soc. Rev.* **2008**, *37*, 2699.
5. a) <http://www.nanowerk.com/spotlight/spotid=20215.php>; b) M.O. Adebajo, R. L. Frost, J.T. Klopogge, O. Carmody, S. Kokot, *Journal of Porous Materials* **2003**, *10*, 159; c) http://www.m2polymer.com/html/oil_absorbents.html.
6. a) L. M. Lanni, R. W. Tilford, M. Bharathy, J. J. Lavigne, *J. Am. Chem. Soc.* **2011**, *130*, 11872; b) E. Spitler, M. Giovino, S. White, W. Dichtel, *Chem. Sci.* **2011**, *2*, 1588; c) Y. Du, K. Mao, P. Kamakoti, P. Ravikovitch, C. Paur, S. Cundy, Q. Li, D. Calabro, *Chem. Commun.* **2012**, *48*, 4606.
7. J.-X. Jiang, F. Su, C. D. Wood, N. L. Campbell, H. Niu, C. Dickinson, A. Y. Ganin, M. J. Rosseinsky, Y. Z. Khimyak, A. I. Cooper, A. Trewin, *Angew. Chem. Int. Ed.* **2007**, *46*, 8574.
8. a) J. Weber, A. Thomas, *J. Am. Chem. Soc.* **2008**, *130*, 6334; b) J.-X. Jiang, F. Su, A. Trewin, C. D. Wood, H. Niu, J. T. A. Jones, Y. Z. Khimyak, A. I. Cooper, *J. Am. Chem. Soc.* **2008**, *130*, 7710; c) L. Chen, Y. Yang, D. Jiang, *J. Am. Chem. Soc.* **2010**, *132*, 9138; d) J. R. Holst, E. Stöckel, D. J. Adams, A. I. Cooper, *Macromolecules* **2010**, *43*, 8531; e) R. Dawson, A. Laybourn, Y. Z. Khimyak, D. J. Adams, A. I. Cooper, *Macromolecules* **2010**, *43*, 8524; f) J. H. Choi, K. M. Choi, H. J. Jeon, Y. J. Choi, Y. Lee, J. K. Kang, *Macromolecules*, **2010**, *43*, 5508; g) E. Stöckel, X. Wu, A. Trewin, C. D. Wood, R.

- Clowes, N. L. Campbell, J. T. A. Jones, Y. Z. Khimyak, D. J. Adams, A. I. Cooper, *Chem. Commun.* **2009**, 212; h) J. Lan, D. Cao, W. Wang, T. Ben, G. Zhu, *J. Phys. Chem. Lett.* **2010**, *1*, 978; i) L. Chen, Y. Honsho, S. Seki, D. Jiang, *J. Am. Chem. Soc.* **2010**, *132*, 6742.
9. For dynamic metal-organic frameworks, see; a) S. Kitagawa, K. Uemura, *Chem. Soc. Rev.* **2005**, *34*, 109; b) T. K. Maji, K. Uemura, H.-C. Chang, R. Matsuda, S. Kitagawa, *Angew. Chem. Int. Ed.* **2004**, *43*, 3269.
10. a) A. I. Cooper, *Adv. Mater.* **2009**, *21*, 1291; b) A. Thomas, *Angew. Chem. Int. Ed.* **2010**, *49*, 8328; c) J.-X. Jiang, F. Su, C. D. Wood, N. L. Campbell, H. Niu, C. Dickinson, A. Y. Ganin, M. J. Rosseinsky, Y. Z. Khimyak, A. I. Cooper, A. Trewin, *Angew. Chem. Int. Ed.* **2007**, *46*, 8574; d) J. Weber, A. Thomas, *J. Am. Chem. Soc.* **2008**, *130*, 6334; e) P. Kuhn, M. Antonietti, A. Thomas, *Angew. Chem. Int. Ed.* **2008**, *47*, 3450; f) J.-X. Jiang, A. Trewin, D. J. Adams, A. I. Cooper, *Chem. Sci.* **2011**, *2*, 1777; g) T. M. Figueira-Duarte, K. Müllen, *Chem. Rev.* **2011**, *111*, 7260.
11. a) L. Chen, Y. Yang, D. Jiang, *J. Am. Chem. Soc.* **2010**, *132*, 9138; b) T. Ben, H. Ren, S. Ma, D. Cao, J. Lan, X. Jing, W. Wang, J. Xu, F. Deng, J. M. Simmons, S. Qiu, G. Zhu, *Angew. Chem. Int. Ed.* **2009**, *48*, 9457; c) L. Chen, Y. Yang, Z. Guo, D. Jiang, *Adv. Mater.* **2011**, *23*, 3149; d) D. Yuan, W. Lu, D. Zhao, H.-C. Zhou, *Adv. Mater.* **2011**, *23*, 3723; e) W. Lu, D. Yuan, D. Zhao, C. I. Schilling, O. Plietzsch, T. Muller, S. Bräse, J. Guenther, J. Blümel, R. Krishna, Z. Li, H.-C. Zhou, *Chem. Mater.* **2010**, *22*, 5964; f) J. Weber, M. Antonietti, A. Thomas, *Macromolecules* **2008**, *41*, 2880; g) A. P. Katsoulidis, M. G. Kanatzidis, *Chem. Mater.* **2011**, *23*, 1818.
12. a) M. D. Ward, *Chem. Soc. Rev.* **1997**, *26*, 365; b) A. Adronov, J. M. J. Fréchet, *Chem. Commun.* **2000**, 1701; c) A. Ajayaghosh, V. K. Praveen, C. Vijayakumar, *Chem. Soc. Rev.* **2008**, *37*, 1090; d) C. Devadoss, P. Bharathi, J. S. Moore, *J. Am. Chem. Soc.* **1996**, *118*, 9635; e) D.-L. Jiang, T. Aida, *Nature* **1997**, *388*, 454; f) A. Ajayaghosh, S. J. George, V. K. Praveen, *Angew. Chem. Int. Ed.* **2003**, *42*, 332.
13. L. Chen, Y. Honsho, S. Seki, D. Jiang, *J. Am. Chem. Soc.* **2010**, *132*, 6742.
14. a) H. Takeda, Y. Goto, Y. Maegawa, T. Ohsuna, T. Tani, K. Matsumoto, T. Shimadabc, S. Inagaki, *Chem. Commun.* **2009**, 6032; b) Y. Maegawa, N. Mizoshita, T. Taniab, S. Inagaki, *J. Mater. Chem.* **2010**, *20*, 4399.
15. T. Oyamada, S. Akiyama, M. Yahiyo, M. Saigou, M. Shiro, H. Sasabe, C. Adachi, *Chem. Phys. Lett.* **2006**, *421*, 295.
16. M. S. Wrighton, D. S. Ginley, D. L. Morse, *J. Phys. Chem.* **1974**, *78*, 2229.
17. S. Srinivasan, P. A. Babu, S. Mahesh, A. Ajayaghosh, *J. Am. Chem. Soc.* **2009**, *132*, 15122.

18. a) L. Guterman, *Science* **2009**, 323, 1558; b) M. Gaskill, *Nature* **2011** (DOI:10.1038/news.2011.396); c) *Nature* **2011**, 475, 144.
19. a) Y. Inokuma, T. Arai, M. Fujita, *Nat. Chem.* **2010**, 2, 780; b) A. Sygula, F. R. Fronczek, R. Sygula, P. W. Rabideau, M. M. Olmstead, *J. Am. Chem. Soc.* **2007**, 129, 3842; c) T. Hasobe, A. S. D. Sandanayaka, T. Wada, Y. Araki, *Chem. Commun.* **2008**, 3372; d) L. Pirondini, D. Bonifazi, B. Cantadori, P. Braiuca, M. Campagnolo, R. De Zorzi, S. Geremia, F. Diederich, E. Dalcanale, *Tetrahedron* **2006**, 62, 2008; e) T. Iwamoto, Y. Watanabe, T. Sadahiro, T. Haino, S. Yamago, *Angew. Chem. Int. Ed.* **2011**, 50, 8342; f) N. Kishi, Z. Li, K. Yoza, M. Akita, M. Yoshizawa, *J. Am. Chem. Soc.* **2011**, 133, 11438.
20. a) D. M. Guldi, F. Spänig, D. Kreher, I. F. Perepichka, C. van der Pol, M. R. Bryce, K. Ohkubo, S. Fukuzumi, *Chem. Eur. J.* **2008**, 14, 250; b) S. Fujii, T. Morita, S. Kimura, *Langmuir* **2008**, 24, 5608.
21. a) Y. Hirata, N. Mataga, *J. Phys. Chem.* **1989**, 93, 7539; b) H. S. S. R. Matte, K. S. Subrahmanyam, K. V. Rao, S. J. George, C.N.R. Rao, *Chem. Phys. Lett.* **2011**, 506, 260.
22. S. L. Bondarev, V. N. Knyukshto, V. I. Stepuro, A. P. Stupak, A. A. Turban *J. Appl. Spectrosc.* **2004**, 71, 194.
23. a) M. J. Frisch, *et al.* Gaussian 09, Revision B.01, *Gaussian, Inc. Wallingford CT*, **2010**; b) A. D. Becke, *J. Chem. Phys.* **1993**, 98, 5648; c) C. Lee, W. Yang, R.G. Parr, *Phys. Rev. B* **1988**, 37, 785.
24. W. Humphrey, A. Dalke, K. Schulten, *J. Molec. Graphics* **1996**, 14, 33.

CURRICULUM VITAE



K. Venkata Rao was born on June 5, 1986 in Dronadula, Prakasam district, Andhra Pradesh, India. He completed B.Sc from Sri Nagarjuna Degree College (Affiliated to Acharya Nagarjuna University), Ongole in 2006. He then joined in School of Chemistry, University of Hyderabad, Hyderabad in 2006 and obtained a M.Sc degree in Chemistry in 2008. After that, he subsequently joined as an R&D assistant at Supramolecular Chemistry Laboratory, New Chemistry, JNCASR, Bangalore under the supervision of Dr. Subi J. George. From January 2009, he worked as a PhD student in the same laboratory. His research work at Supramolecular Chemistry Laboratory focused on the use of various non-covalent approaches to improve the optoelectronic functions of π -conjugated molecules. The most important results of this work are presented in this thesis.

LIST OF PUBLICATIONS**From Thesis**

1. Highly Pure Solid-State White-Light Emission from Solution Processable Soft-Hybrids, **K. V. Rao**, K. K. R. Datta, M. Eswaramoorthy, S. J. George, *Adv. Mater.* **2013**, *25*, 1713.
2. Supramolecular Alternate Co-Assembly Through a Non-Covalent Amphiphilic Design: Conducting Nanotubes with a Mixed D–A Structure, **K. V. Rao**, S. J. George, *Chem. Eur. J.* **2012**, *18*, 14286.
3. Perylene Based Porous Polyimides: Tunable, High Surface Area with Tetrahedral and Pyramidal Monomers, **K. V. Rao**, R. Haldar, C. Kulkarni, T. K. Maji, S. J. George, *Chem. Mater.* **2012**, *24*, 969.
4. Light-Harvesting Hybrid Assemblies, **K. V. Rao**, K. K. R. Datta, M. Eswaramoorthy, S. J. George, *Chem. Eur. J.* **2012**, *18*, 2184.
5. Guest-Responsive Reversible Swelling and Fluorescence Response in a Super-Absorbent, Dynamic Microporous Polymer, **K. V. Rao**, S. Mohapatra, T. K. Maji, S. J. George, *Chem. Eur. J.* **2012**, *18*, 4505.
6. Extended phenylene based microporous organic polymers with selective carbon dioxide adsorption, **K. V. Rao**, S. Mohapatra, C. Kulkarni, T. K. Maji, S. J. George, *J. Mater. Chem.* **2011**, *21*, 12958.
7. Light-Harvesting Hybrid Hydrogels: Energy Transfer Induced Amplified Fluorescence in Non-Covalently Assembled Chromophore-Organoclay Composites, **K. V. Rao**, K. K. R. Datta, M. Eswaramoorthy, S. J. George, *Angew. Chem. Int. Ed.* **2011**, *50*, 1179.
8. Supramolecular Hydrogels and High-Aspect-Ratio Nanofibers through Charge-Transfer-Induced Alternate Co-assembly, **K. V. Rao**, K. Jayaramulu, T. K. Maji, S. J. George, *Angew. Chem. Int. Ed.* **2010**, *49*, 4218.
9. Synthesis and Controllable Self-Assembly of a Novel Coronene Bisimide Amphiphile, **K. V. Rao**, S. J. George, *Org. Lett.* **2010**, *12*, 2656.
10. Organic-Inorganic Light-Harvesting Scaffolds for Luminescent Hybrids, **K. V. Rao**, A. Jain, S. J. George (submitted).
11. Autonomous Alignment of Charge-Transfer Fibers via Two-Dimensional Donor-Acceptor Self-Assembly, **K. V. Rao**, S. J. George (submitted, Part-3.1).
12. High Charge Carrier Mobility in Non-Covalently Tailored p-n Heterojunction Nanostructures, **K. V. Rao**, A. Saeki, S. Seki, S. J. George (Part-3.3).
13. Controlling the Molecular Organization of π - Systems via Hybrid Co-assembly: A Non-Covalent Strategy towards Solution Processable Luminescent Hybrids, **K. V. Rao**, A. Achari, M. Eswaramoorthy, S. J. George (submitted, Part-4.2).
13. Amphiphilic Self-Assembly of n-type Coronene Bisimides: Controllable Nanostructures with High Electron Mobility, **K. V. Rao**, S. P. Senanayak, K. S. Narayan S. J. George (Manuscript in preparation, Part-2.1).
14. Guest Induced Supramolecular Chirality and Self-Assembly Mechanism of Cationic Coronene Diimide Amphiphiles, **K. V. Rao**, S. J. George (Manuscript in preparation, Part-2.2).

15. **Kinetic Control over Chiral Amplification of Coronene Bisimide Amphiphiles**, **K. V. Rao**, S. J. George (Manuscript in preparation, Part-2.2).
16. **Light-Harvesting Soft-Hybrids: Controlled Molecular Organization and Dynamics of Donor/Acceptor Molecules**, **K. V. Rao**, K. K. R. Datta, M. Eswaramoorthy, S. J. George (Manuscript in preparation, Part-4.1).
17. **Visible Light-Harvesting Dynamic Microporous Polymers via Swelling Induced Rapid Guest Encapsulation**, **K. V. Rao**, R. Haldar, T. K. Maji, S. J. George (Manuscript in preparation, Part-5).
18. **Self-Sorting of Donor-Acceptor Molecules on Laponite Surface: Towards Multicolored Luminescent Soft-Hybrids**, **K. V. Rao**, A. Achari, M. Eswaramoorthy, S. J. George (Manuscript in preparation).
19. **Robust Microporous Polyimides Derived from Rylene Diimides with High CO₂ and H₂ Uptake Capacities**, **K. V. Rao**, R. Haldar, T. K. Maji, S. J. George (Manuscript in preparation).
20. **Dynamic Naphthalene Diimide and Laponite hybrids for humidity sensing**, **K. V. Rao**, A. Achari, M. Eswaramoorthy, S. J. George (Manuscript in preparation).
21. **Light-Harvesting Soft-Organic-Inorganic Hybrid Assemblies**, **K. V. Rao**, A. Jain, S. J. George (Manuscript in preparation).
22. **Wide-Range Cascade Energy-Transfer in Clay-Chromophore Derived Luminescent Soft-Hybrids**, **K. V. Rao**, M. Eswaramoorthy, S. J. George (Manuscript in preparation).
23. **Amphiphilic Design for Supramolecular Materials with Optoelectronic Functions**, **K. V. Rao**, A. Jain, S. J. George (Manuscript in preparation).

Other Publications

24. **A charge transfer single crystal field effect transistor operating at low voltages**, A. A. Sagade, **K. V. Rao**, S. J. George, A. Datta, G. U. Kulkarni, *Chem. Commun.* **2013**, 49, 5847.
25. **High-Mobility Field Effect Transistors based on Supramolecular Charge Transfer Nanofibers**, A. A. Sagade, **K. V. Rao**, U. Mogera, S. J. George, A. Datta and G. U. Kulkarni, *Adv. Mater.* **2013**, 25, 559.
26. **Exciplex Formation and Energy Transfer in a Self-assembled Metal-Organic Hybrid System**, R. Haldar, **K. V. Rao**, S. J. George, T. K. Maji, *Chem. Eur. J.* **2012**, 18, 5848.
27. **Fluorescent Coronene Monoimide Gels via H-bonding Induced Frustrated Dipolar Assembly**, A. Jain, **K. V. Rao**, C. Kulkarni, A. George, S. J. George, *Chem. Commun.* **2012**, 48, 1467.
28. **Dynamic Self-Assembly of Charge-Transfer Nanofibers of Tetrathiafulvalene Derivatives with F4TCNQ**, A. Jain, **K. V. Rao**, U. Mogera, A. A. Sagade, S. J. George, *Chem. Eur. J.* **2011**, 17, 12355.
29. **Metal Selective Co-ordinative Self-Assembly of π -Donors**, A. Jain, **K. V. Rao**, A. Goswami, S. J. George, *J. Chem. Sci.* **2011**, 123, 773.
30. **Quenching of Fluorescence of Aromatic Molecules by Graphene due to Electron Transfer**, H. S. S. R. Matte, K. S. Subrahmanyam, **K. V. Rao**, S. J. George, C. N. R. Rao, *Chem. Phys. Lett.* **2011**, 506, 260.

31. Non-Covalent Functionalization, Solubilization of Graphene and Single-Walled Carbon Nanotubes with Aromatic Donor and Acceptor Molecules, A. Ghosh, **K.V. Rao**, R. Voggu, S. J. George, *Chem. Phys. Lett.* **2010**, 488, 198.
32. A Simple Method of Separating Metallic and Semiconducting Single-Walled Carbon Nanotubes Based on Molecular Charge Transfer, R. Voggu, **K. V. Rao**, S.J. George, C. N. R. Rao, *J. Am. Chem. Soc.* **2010**, 132, 5560.
33. Non-covalent Functionalization, Exfoliation, and Solubilization of Graphene in Water by Employing a Fluorescent Coronene Carboxylate, A. Ghosh, **K. V. Rao**, S.J. George, C.N.R. Rao, *Chem. Eur. J.* **2010**, 16, 2700.
34. Confinement Induced Stochastic Sensing of Charged Coronene and Perylene Aggregates in α -Hemolysin Nanochannel, R. Shivanna, D. Pramanik, H. Kumar, **K. V. Rao**, S. J. George, P. K. Maiti, K. S. Narayan (Submitted).
35. Water-soluble coronene:europium polymer blends for downconversion of UV light, M. Planells, E. Klampaftis, M. Congiu, R. Shivanna, **K. V. Rao**, A. C. Jones, B. S. Richards, S. J. George, K. S. Narayan, N. Robertson (Submitted).
36. Nanoscale Luminescent Coordination Polymers of Coronene and Perylene Tetracarboxylates: Tunable Emission Based on Coordination Mode, K. Jayaramulu, **K. V. Rao**, S. J. George, T. K. Maji (To be submitted).
37. Charge-Transfer Nanostructures with Mixed Stack TTF-Viologen/Naphthalene Diimide Organization via Non-Covalent Amphiphilic Design, K. Jalani, **K. V. Rao**, S. J. George (Manuscript in preparation).
38. Adaptive Pores: Charge Transfer Modules as Supramolecular Handles for Reversible Pore Engineering of Mesoporous Silica, B.V.V.S. P. Kumar, **K. V. Rao**, S. J. George, M. Eswaramoorthy, *J. Am. Chem. Soc.* (Under revision).

Patents

1. Methods and compositions for the separation of single-walled carbon nanotubes, C. N. R. Rao, S. J. George, R. Voggu, **K. V. Rao**, US Patent (US 8246928 B1 20120821).
2. Hydrocarbon Sorbent Materials, S. J. George, **K. V. Rao** (Indian Complete Patent Application No. 2287/CHE/2012).
3. Polymer, Methods of Obtaining the Polymer and Applications Thereof, S. J. George, **K. V. Rao**, International Patent Application No. PCT/IB2012/055021.
4. Metal-free organic phosphorescent molecules as photo-active encapsulation for photovoltaic and thereof, K. S. Narayan, S. J. George, **K. V. Rao**, R. Shivanna (Under process).